Synthesis, Characterizations and applications of oxides materials based on CaCu3Ti4O12

Sara Kawrani

THÈSE POUR OBTENIR LE GRADE DE DOCTEUR DE L'UNIVERSITÉ DE MONTPELLIER

En Chimie et Physicochimie des matériaux

École doctorale Sciences Chimiques Balard (ED459)

Unité de recherche Institut Européen des Membranes (UMR 5635, CNRS, UM, ENSCM)

Synthèse, Caractérisations, et Applications des Matériaux Oxydes à base de $CaCu_3Ti_4O_{12}$

Présentée par Sara KAWRANI

Le 16 Décembre 2019

Sous la direction de David CORNU
La codirection de Madona BOULOS
et l'encadrement de Mikhael BECHELANY

Devant le jury composé de

Mme Mirvat ZAKHOUR, Professeur, Université Libanaise	Rapporteur
M. Lionel PRESMANES, Docteur, Université de Toulouse	Rapporteur
Mme Bérangère TOURY, Maitre de conférences, Université de Lyon	Examinateur
M. Marc Cretin, Enseignant-Chercheur, Université de Montpellier	Examinateur
M. David CORNU, Professeur, Université de Montpellier	Directeur
Mme Madona BOULOS, Professeur associé, Université Libanaise	Co-directeur
M. Mikhael BECHELANY, Chargé de recherches, CNRS	Encadrant

UNIVERSITÉ DE MONTPELLIER

A celui qui a sacrifié sa vie pour nous et qui nous a recommandé d'être toujours libres dans ce monde

Al-Hussein ibn Ali ibn Abi Talib

Remerciement

J'aimerais tout d'abord remercier Dieu, le miséricordieux mon guide tout au long du chemin pour tous ses enchères.

J'adresse mes remerciements aux membres du jury, les rapporteurs Pr. Mirvat ZAKHOUR de l'Université Libanaise et Pr. Lionel PRESMANES de l'Université de Toulouse, et les examinateurs Dr. Bérangère TOURY de l'Université de Lyon et Pr. Ahmad MEHDI de l'Université de Montpellier pour avoir accepté d'évaluer mon travail et pour leur présence.

Je tiens à remercier le directeur de laboratoire Professeur Philipe MIELE, pour son souriant accueil durant mes séjours au sein de l'institut. J'adresse mes chaleureux remerciements à tous les permanents de l'institut pour le respect que j'ai eu envers chacun d'entre eux, leurs aides et gentillesses, qui m'ont facilité mon séjour.

Je tiens à exprimer ma gratitude à mon directeur de thèse Professeur David CORNU de l'Université de Montpellier qui m'a accompagné durant ce travail, j'aimerais le remercier pour son soutien et ses conseils. Je remercie également ma co-directrice de l'Université Libanaise Dr. Madona BOULOS pour son suivi et sa présence toujours pour améliorer le travail. Je tiens aussi à remercier profondément mon encadrant Dr. Mikhael BECHELANY, pour m'avoir orienté dans ce travail malgré tout ce qu'on a eu comme entraves et difficultés, et m'avoir facilité le contact avec d'autres laboratoires. Je remercie Dr. BECHELANY pour me mettre toujours sous pression, ''il a bien su mes clés de travail'', pour son anti-stress attitude toujours, sa diplomatie qu'il a essayé de nous apprendre et son amitié. Je vous remercie de tout mon cœur.

Je voudrais remercier principalement les premiers que j'ai rencontré de l'équipe Danaé, Maryline, Habib, Mathieu et Sakthivel pour leurs aides et conseils à mon arrivée et la brésilienne Anna pleine d'énergie. Un spécial remerciement pour la blonde Espagnol Danaé qui était toujours à côté de moi quand j'en ai besoin, pour m'aider à s'intégrer avec nos collègues de l'institut et les beaux moments que je vais emporter avec moi après la fin de cette thèse.

Je n'oublierai jamais le respect de tous les amis pour les petits détails qui m'intéresse, la rencontre de nos différentes cultures a été une force qui nous rassemble, m'a permis d'être confiante et alaise avec vous, Hana, Mona, Thomas, Carole, Octavio, Quiké, Carlos, Cyril, Somaya et Socrates et tous que j'ai rencontré durant ces années pour ne pas oublier quelqu'un je vous remercie, vous allez me manquer énormément.

Un grand merci pour les amis Libanais, notre grande communauté à l'institut et ceux dispersés sur les territoires français, avec qui l'aliénation était rendu plus facile à passer, Loraine pour ta présence toujours pour m'aider commençant par les premiers feuilles administratifs et ça continue, Maya 'my drama queen', Syreina (et ses malheurs), Cynthia, Marleine, Ghenwa,

Georges, Joëlle, Ghady, Mohamed, Petros, Rania, Fatima, Ali, Ahmad, et Rana, j'arrête là pour ne pas oublier quelqu'un ! Je ne veux pas oublier le couple Egyptien ça fait plaisir de vous rencontrer, je remercie Amr pour ses aides et sa disponibilité. Je voudrais remercier mes amies qui m'attendaient au Liban et me suivent toujours Narjes, Jinane, Zaynab, Rim et Nour.

Un proverbe disait que la famille est comme les branches d'un arbre, nous grandissons tous dans de différentes directions, mais nos racines ne font qu'un. Maman, Papa je crois que quelques mots de remerciement ne suffisent jamais vos bienfaits, je vous remercie de toujours avoir cru en moi, pour votre confiance et votre amour, ma sœur, mes frères vous êtes les meilleurs, je n'aurais jamais pu continuer sans vos soutiens, je vous aime énormément.

Table of Contents

Abbreviations list

1BN	CCTO with 1%h-BN
1GO	CCTO with 1%GO
3BN	CCTO with 3%h-BN
3GO	CCTO with 3%GO
6BN	CCTO with 6%h-BN
6GO	CCTO with 6%GO
C1BN	CCTO with 1% of h-BN
C1GO	CCTO with 1% of GO
C3BN	CCTO with 3% of h-BN
C3GO	CCTO with 1% of GO
C6BN	CCTO with 6% of h-BN
C6GO	CCTO with 1% of GO
CCTO	$CaCu_3Ti_4O_{12}$
CV	Cyclic Voltammetry
EIS	Electrochemical Impedance spectroscopy
GO	Graphene Oxide
h-BN	Hexagonal Boron Nitride
IS	Impedance spectroscopy
LV	Linear Voltammetry
OER	Oxygen Evolution reaction
ORR	Oxygen reaction reduction
PEC	Photoelectrochemical cell
PL	Photoluminescence spectroscopy
SEM	Scanning electron microscopy
tan δ	Dielectric loss
UV-Vis	Ultraviolet-Visible Diffuse reflectance spectroscopy
XPS	X-ray photoelectron spectroscopy
XRD	X-ray diffraction
ε'	Permittivity

List of Tables

List of Figures

General Introduction

General introduction

Perovskite materials are widely used due to their interesting properties that allow them to be involved in different technological applications (e.g. Capacitors, solar cell, fuel cell, antennas). The ideal structure of the perovskite is a cubic lattice. Few compounds have this ideal instable structure such as Strontium Titanate ($SrTiO_3$) and Barium Titanate ($BaTiO_3$). Many oxides have slightly distorted variants with lower symmetry (e.g., orthorhombic or hexagonal). In the unit formula of perovskite structure ABO_3, A is the larger cation and B is the smaller one. $CaCu_3Ti_4O_{12}$ (CCTO) is an ideal perovskite with a cubic lattice stable at a large temperature scale, where A site is occupied by Ca^{2+} and Cu^{2+} and B site is occupied by Ti^{4+} cation. These cations arrangements create a distortion of TiO_6 octahedron, and give CCTO perovskite specific properties.

Due to its specific structure CCTO is a material that can have applications in different fields such as photoelectrochemical cells for hydrogen production, energy storage (capacitors) and magnetic field for GPS or antennas applications.

Energy deficiency and environmental issues of combustible fuels forced researchers to find a new energy strategy. Among several energy strategies, constructing a device for hydrogen production from water splitting is studied as a source of clean and renewable energy. The photoelectrochemical cells (PEC) or photoelectrolytic cells are devices that uses light incident on a photosensitizer, semiconductor, or aqueous metal immersed in an electrolytic solution to directly cause a chemical reaction (produce hydrogen via electrolysis of water).

The photoelectrochemical cells are mainly limited by the nature of the material used for electrodes. It is known that 4% part of the visible light covers UV light and since the majority of catalysts are active under UV light irradiation, it is necessary to develop visible light active photocatalyst. For more efficiency in the hydrogen production process, visible light active electrodes should be used.

Perovskite ABO_3 is known as complex oxides composed from at least two different oxides with specific optical properties. CCTO lattice involved TiO_2 with a narrow band gap energy active in

ultraviolet region, and CuO compound able to absorb visible light. In CCTO every oxygen atom has strong covalence bonding with A'-Cu^{2+} ion and two B-Ti^{4+} ions. Therefore, the charge transfer between A'-Cu and B-Ti ions plays main role in electrocatalytic activity. It is reported that the activity of CCTO under visible light irradiation is governed by the square-planar (octahedral) structure, in which Cu (Ti) e_g and O 2p orbitals are superposed. As mentioned above CCTO exhibits different applications, one of its interesting properties is the high dielectric constant.

$CaCu_3Ti_4O_{12}$ was described for the first time as a dielectric material with high dielectric constant, stable at large scale of frequency and temperature. Investigations explained the colossal dielectric permittivity by the Internal Barrier Layer Capacitance Model (IBLC), consisting on the presence of conducting grains separated by insulating grain boundaries. In parallel of the high dielectric permittivity, CCTO showed a high loss factor which limits their industrial use in energy storage application. The dielectric properties (permittivity and loss) increase and decrease proportionally, thus studies focused on decreasing the dielectric loss with maintaining a high permittivity. Another interesting property that was investigated for CCTO is its magnetic behavior.

Magnetic properties of $CaCu_3Ti_4O_{12}$ were studied basing on the concept of orbital ordering. In this theory the crystallographic ordering and the magnetic properties are strongly connected. CCTO showed a magnetic phase transition due to the ordering of Cu^{2+} ions ($\boldsymbol{s} = \frac{\mathbf{1}}{\mathbf{2}}$), in which the spins are connected together through the non-magnetic element Ti^{4+} (Cu-O-Ti-O-Cu). The copper spin sublattice develops a long-range magnetic order below Neel temperature ~25 K.

On the other hand two-dimensional nanosheets materials (2D) including hexagonal boron nitride (h-BN) and graphene oxide (GO) were widely used due to their specific properties. They are known as high specific surface materials with particular electrical properties.

The aim of this work is to prepare composite materials based CCTO in order to study their properties for different applications such as photoelectrodes for water splitting applications, energy storage and magnetic compounds. 2D nanosheets materials (boron nitride and

graphene oxide) with different weight percentages were added to CCTO. Those two materials were chosen due to their high surface activity and their electronic structure that can improve the properties of CCTO.

This thesis manuscript is divided into five parts.

Firstly $CaCu_3Ti_4O_{12}$ perovskite as a specific ferroelectric material with cubic lattice and its different synthesis method is described. In this review, we presented the recent investigations done to decrease the dielectric loss by doping, co-doping, and using different synthesis techniques. At the end of this review we summarized the photocatalytic, electrocatalytic and magnetic applications of CCTO and their derived materials.

In the second chapter, we introduced all the analysis techniques used during this work. The detailed experimental work to synthesize calcium copper titanate CCTO and 2D nanosheets materials (boron nitride and graphene oxide) composites were also presented.

The third and fourth sections focused on CCTO based material with 2D nanosheets materials obtained by solid-state reaction and their enhanced photoelectrochemical properties. In a first study, hexagonal boron nitride nanosheets were incorporated in CCTO material in order to insert B and N atoms in TiO_2 lattice. In a second study, graphene oxide nanosheets were added, for Ti^{4+} and Cu^{2+} reduction and to create oxygen vacancy.

Finally, in the last section, we studied the dielectric and magnetic properties of prepared composites. The thesis ends by a general conclusion and some perspectives.

Part I : Bibliography

Part I: From synthesis to applications: Copper calcium titanate (CCTO) with outstanding properties

***Table of contents entry**: In this review, the synthesis and the sintering approaches, the dopant elements used as well as the applications of Copper calcium titanate (CCTO) will be reported. In addition to the dielectrical properties useful to energy storage devices; CCTO could serve as magnetic materials as well as photo- and photoelectro-catalytic materials with a very good performance in visible light.*

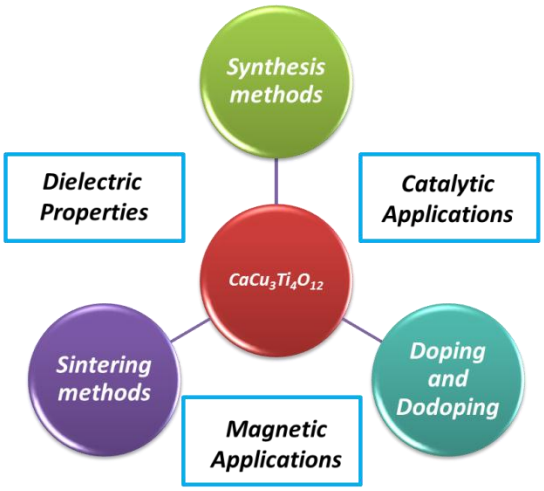

Abstract

Investigations focusing on electrical energy storage capacitors especially the dielectric ceramic capacitors for high energy storage density are attracting more and more attention in the recent years. Ceramic capacitors possess a faster charge-discharge rate and improved mechanical and thermal properties compared with other energy storage devices such as batteries. The challenge is to obtain ceramic capacitors with outstanding mechanical, thermal and storage properties over large temperature and frequencies ranges. ABO_3 as a type of perovskites showed a strong piezoelectric, dielectric, pyroelectric, and electro-optic properties useful as energy storage and environmental devices. $CaCu_3Ti_4O_{12}$ (CCTO) perovskite with cubic lattice (Im3 symmetry) was discovered to have a colossal dielectric constant (10^4) that is stable over a wide range of frequencies (10Hz-1MHz) and temperature independence (100-300K). The origin of this high dielectric constant is not fully established, specially because it is the same for single crystal and thin films. In this review, the history of CCTO will be introduced. The synthesis and the sintering approaches, the dopant elements used as well as the applications of CCTO will be reported. In addition to dielectrical properties useful to energy storage devices; CCTO could serve as photocatalytic materials with a very good performance in visible light.

I.1 Introduction:

Ferroelectric materials consist of domains with a spontaneous polarization in the absence of an external electric field, and in which this polarization is reversible under the application of an electric field of magnitude less than the dielectric breakdown of the material itself. Spontaneous polarization is the value of charge per unit area on the surface perpendicular to the axis of spontaneous polarization[1]. The magnitude of the net spontaneous polarization possessed by a ferroelectric material starts to decrease while increasing the temperature or the pressure. A phase transition from ferroelectric state to a non-polar paraelectric state took place above a critical temperature T_c (and a critical pressure P_c), called the Curie temperature in which the spontaneous polarization disappears. The structural phase transition from paraelectric to ferroelectric phase is due to the displacement of both cations occupying the A and B sites in the perovskite. This transition may cause a change in dielectric, thermal and other properties of the material.

Ferroelectric materials are divided into four groups; one of these groups is the perovskite. A perovskite is a material with the same crystal structure as calcium titanium oxide ($CaTiO_3$). Perovskites have the general formula ABO_3, where A and B are metal cations (ion radius of A is larger than that of B). An ideal structure is cubic with space group symmetry Pm3m, and it is the simplest example of a structure containing two different cations. Due to the relative sizes of the A and B cations, three types of distortions appear in the simple cubic perovskite structure:

- Distortions of the octahedral units (Jahn-Teller distortion)

- B-cation displacements within the octahedral leading to either a ferroelectric (if all the B atoms move in the same direction) or antiferroelectric (if the B atoms move in opposite directions) structure.

- The relative titling of one octahedral to another. The size of the unit cell increase while reducing the A-site size and no changes in the B-cation environment in such titling [2]. Goldschmidt examined the octahedral titling disordered [3]. In order to determine the stability

of perovskite phases, he was based on a formula to define the tolerance factor *t* in the following equation:

$$t= (R_A+R_B)/\sqrt{2}(R_B+R_X) \quad (1)$$

Where R_A, R_B and R_X are the ion radii of the A-site and B-site cations and the X-site anion respectively in an ABX_3 perovskite. The average ionic radius of the ions occupying each site is considered in cases of complex perovskites. The deviation of t values indicates the degree of distortion of a perovskite from the ideal cubic structure.

Barium titanate is a model of ferroelectric materials and belongs to the perovskite group with high dielectric properties. It has been seen that even the crystal structure of calcium titanate ($CaTiO_3$) and barium titanate $BaTiO_3$ is not truly cubic, it is slightly modified [4]. The crystalline phases of barium titanate varied at different temperatures. It is paraelectric at high temperature with a cubic phase, tetragonal and [100] polarized below its Curie temperature (T_c=120°C), orthorhombic and [110] polarized below 5°C, and rhombohedral and [111] polarized below -90°C.

For the miniaturization of electronic devices, high dielectric constant materials are highly useful. Barium titanate and Lead titanate ($PbTiO_3$) perovskites were used widely; they showed different crystalline phases at different temperatures which leads to dielectric properties variation. In addition to that, both $BaTiO_3$ and $PbTiO_3$ showed important dielectric properties useful for capacitor application, but they contain materials which are severally toxic for human body and therefore are non-environment friendly materials [5], so searching a perovskite with stable properties is important to such applications.

Many researches have been recently investigated the synthesis and characterization of the pseudo-cubic perovskite $CaCu_3Ti_4O_{12}$ (commonly called CCTO), because of its unusual electrical properties. The high dielectric constant 1 KHz for this type of oxides was first reported in 2000 by Subramanian *et al.* [6]. Calcium copper titanate was synthetized for the first time using conventional powder-sintering technique. Highly pure starting materials were used (99%) of oxides (CaO, TiO_2 and CuO). The mixed powder was calcined at 900-1000°C for 8h, and then

the calcined powder was reground and pressed into disks. The disks were sintered in air at 1000-1200°C [6].The structure of CCTO (space group I*m3*) can be derived from an ideal cubic perovskite structure ABO_3 by superimposing a body centered ordering of Ca^{2+} and Cu^{2+} that share the A site, and Ti^{4+} is on B site. Due to the different ionic radius between Cu and Ca atoms, a tilting of TiO_6 octahedral planar appears [7]. This distortion forms a square planar oxide environment convenient to Jahn-Teller distorted Cu^{2+} [8] (Figure I-1).

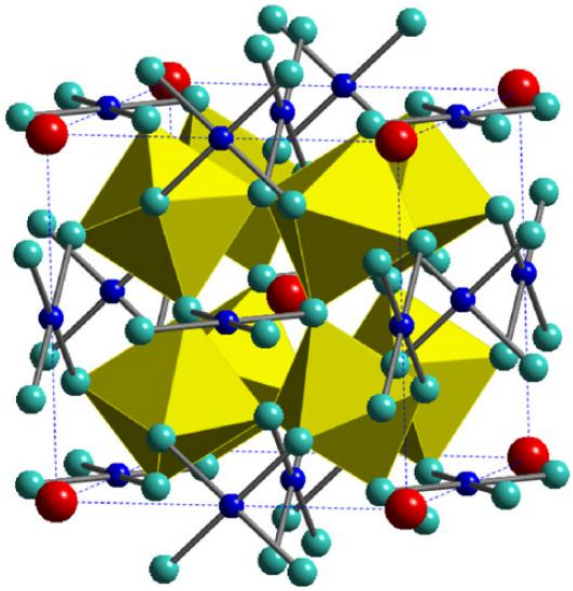

Figure I-1: Structure of the cubic pseudo-perovskite (Im3) $CaCu_3Ti_4O_{12}$ with TiO_6, Cu in square planar coordination (small black spheres) about O (small light grey spheres) and Ca at the origin and cube center (medium size grey spheres).Reprinted with permission from (Subramanian et al.,2009). Copyright 2009 Elsevier. [9]

CCTO has been found as a material that shows an outstanding dielectric permittivity (up to 10^4) at low frequency and stable at a large frequency scale (10^2Hz-10^6Hz). It has been noticed that this giant dielectric permittivity is temperature independent over a wide temperature range between 100 and 600 K [9] which makes this oxide very attractive for technological applications. Despite the high permittivity, CCTO loss tangent still high and constitute an obstacle for commercial applications [10,11]. The origin of this important permittivity is not fully understood and many hypotheses based on intrinsic and extrinsic properties were suggested. Subramanian *et al.* suggested an intrinsic origin for this high permittivity explained

by a ferroelectric relaxation that affects the rearrangement of Ti^{4+} ions [6], Sinclair *et al.* [7,12–14] showed that the high permittivity is due to an internal barrier layer capacitor and not to an intrinsic feature of the bulk crystal structure. They demonstrated that CCTO ceramics are formed from semiconducting grains separated by insulating grains boundaries and they suggested an electrical model that consists of two parallel capacitance-resistance (RC) elements, R_gC_g and $R_{gb}C_{gb}$ representing semiconducting grains and insulating grains boundaries respectively, both connected in series [7] (Figure I-2). It is now fully accepted that the origin of the exceptional electrical properties of CCTO ceramics are due to an internal barrier layer capacitance (IBLC) origin.

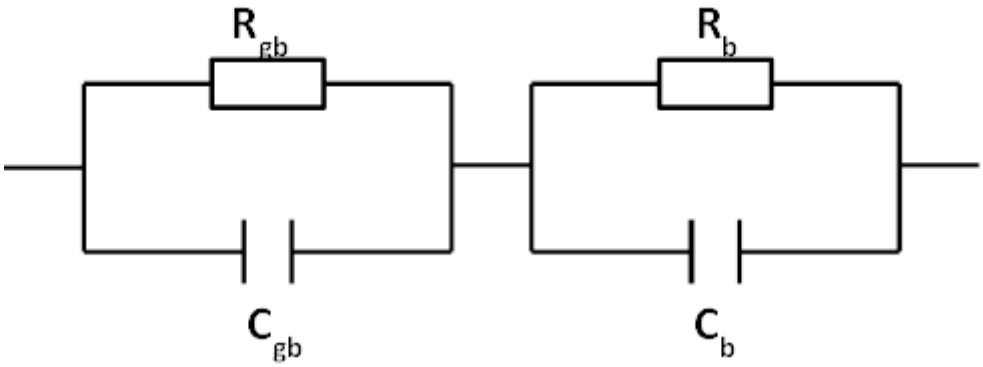

Figure I-2: simplified equivalent circuit consisting of two parallel RC elements connected in series. Updated from reference [15]

Basing on the experimental results, it has been possible to use CCTO for fabricating an efficient energy storage device (EDS), and can be used for the evolution of solid state capacitors of class II type. In addition to that, CCTO is a wide gap n-type semiconductor material and can be used for high temperature electronics, basing on studies of the resistivity at high temperature[16].

However decreasing dielectric loss with maintaining a high dielectric constant is the challenge. Many investigations have been done to understand the origin of these dielectric properties and their relation with CCTO crystal structure.

Several reviews focusing on different perovskite materials and their dielectric properties such as barium titanate ($BaTiO_3$) [17] and Lead titanate ($PbTiO_3$) [18] have been reported recently. In

2016, Ahmadipour *et al.* reported CCTO ceramics and films fabrication, factors influencing its dielectric properties and its sensing applications [19]. In this review, an overview on the influence of experimental conditions such as synthesis method, sintering approaches and doping elements on the structures and dielectric properties of CCTO will be investigated. The new trend in this field (since 2016) will be mainly discussed. This review will focus, in addition to electrical properties, on the photocatalytic and the magnetic applications of CCTO, two interesting properties that have not been reviewed before.

This review is composed from five sections. In first section, the synthesis methods are discussed. The following section will report the sintering approaches and their influence on dielectric properties. In the third part, different doping elements as well as their influence on the morphology and the dielectric properties of CCTO will be discussed. Finally the new properties of CCTO such as magnetic and photocatalytic properties will be reviewed.

I.2 Synthesis methods

In this section the synthesis methods used to design calcium copper titanate such as solid state route (solid-solid, mechanosynthesis method), wet chemistry method or soft chemistry (sol-gel, coprecipitation, hydrothermal method), microwave synthesis and combustion synthesis techniques will be reported.

I.2.1 Solid state route

Solid state route is the first method used to prepare oxide. It is a mixing of solid starting materials. Since those solids do not diffuse in each other at room temperature to form the final compound, an additional step of heating at high temperature is necessary. Solid-state route is divided into two groups, solid-solid by mixing manually the powders in an agate mortar and mechanosynthesis method by using a ball mill machine to mix the precursors.

The CCTO, for dielectric applications, is very largely prepared by the “solid-solid” route. This method consists in making an intimate mixture of oxide powders or precursors of oxides (carbonates, hydroxides or nitrates) of calcium, copper and titanium. Subramanian *et al.* [6]

used oxides and carbonates precursors which they calcined at 1000°C. Unfortunately in order to obtain at the end a proper, homogeneous and single phase material, several steps of grinding and calcination at high temperature are required. This is the reason why finding new methods that are rapid and environmentally safe was developed later.

The mechanochemical synthetic route (Figure I-3) is a simple and rapid method that allows the direct synthesis of the single phase oxides at low temperatures. One of the most important advantages of this technique is that the starting materials can react together by a simple diffusion mechanism at room temperature. The diffusion mechanism is due to the mechanical stress applied on the precursors during the synthesis. In addition the grains size is reduced during this process [20].

The chemical reaction during the solid-solid and a mechanochemical reaction method for the synthesis of CCTO is shown in equation I.2:

$$CaCO_3 + 3CuO + 4TiO_2 \rightarrow CaCu_3Ti_4O_{12} + CO_2 \uparrow \quad \textbf{(I.2)}$$

Recently mechanical alloying method is used to prepare CCTO by mixing $CaCO_3$, TiO_2 and CuO with or without solvent, followed by a calcination step to synthetize single pure phase of CCTO [14,21–23].

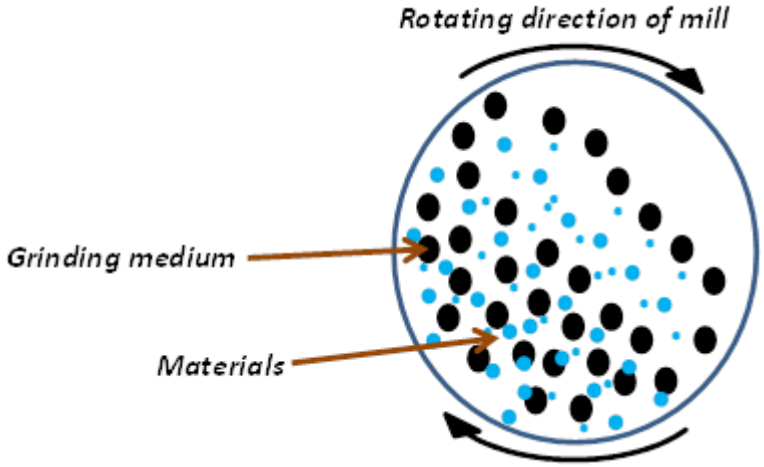

Figure I-3: Schematic diagram of a ball mill

Thirpathy *et al.* [24] mixed a stoichiometric amount of $CaCO_3$, TiO_2 and CuO into acetone (as a dispersant agent) using a ball mill in a sealed plastic bottle with zirconium beads. Powders were calcined at different temperatures from 900°C to 1050°C for 10h. Pellets were then sintered at 1100°C for 8h. XRD patterns (Figure I-4a) showed that the pure phase of CCTO is given at 1050°C of calcination. As seen in SEM images, (Figure I-4b) large grains are surrounded by small ones at the junction for sintered pellets.

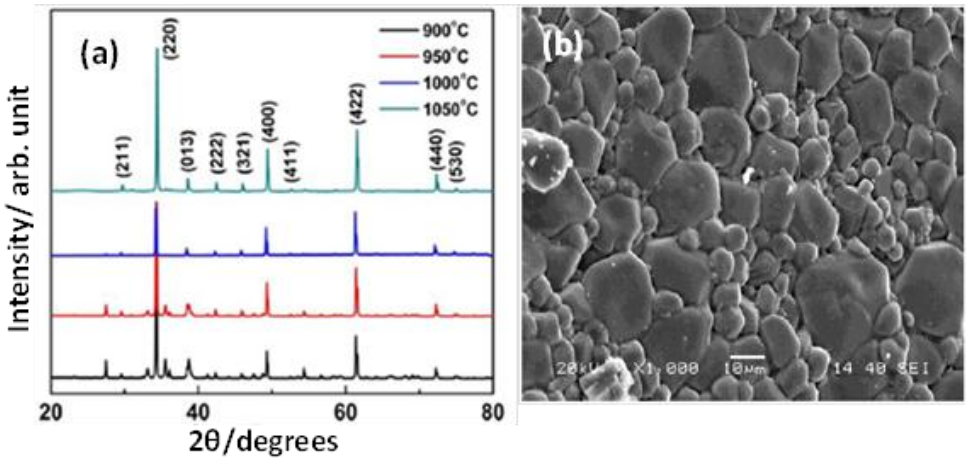

Figure I-4: (a) X-ray diffraction patterns of CCTO powder calcined at different temperature and (b) SEM micrograph of CCTO pellet. Reprinted with permission from (triphathy et al. 2016). Copyright 2016 Creative Commons CC [24]

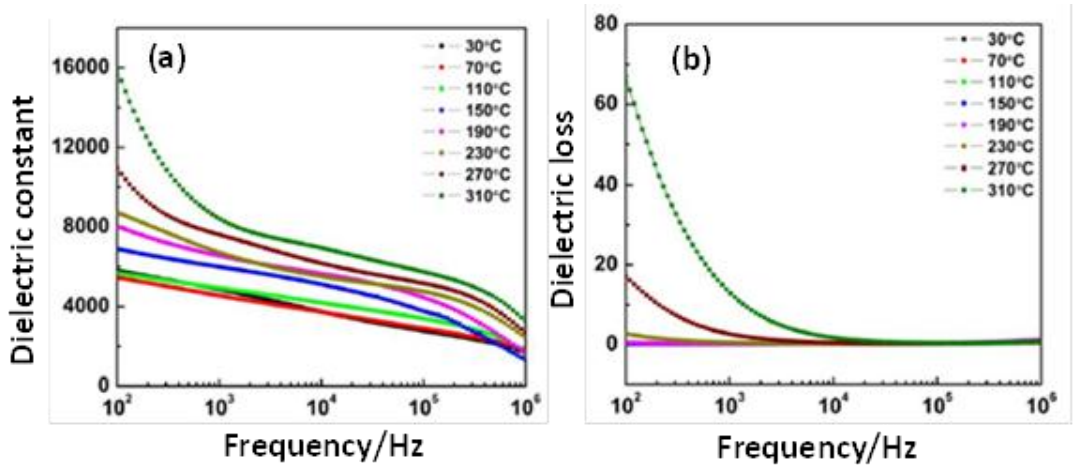

Figure I-5: (a) Frequency dependence of dielectric constant of CCTO pellet at different temperatures and (b) Frequency dependence of dielectric loss of CCTO pellet at different temperatures. Reprinted with permission from (triphathy et al. 2016). Copyright 2016 Creative Commons CC. [24]

Figure I-5 (a) showed the frequency dependence of dielectric constant as the function of temperature (30°C-310°C). The permittivity (ε') value decreases with increasing the frequency, and at some point, ε' increases while increasing temperature. This behavior could be related to the accumulation of charge on interface. Figure I-5 (b) showed that the dielectric loss is stable at high frequencies and increases at low frequencies and high temperature, this phenomenon is might due to the increase of conductivity with temperature.

Even if these methods are easy and simple to perform, they suffer from the need of repetitive grinding and the use of a very high temperature for calcination.

I.2.2 Wet synthesis or soft chemistry

Over the past thirty years, new methods improperly called "chemical" have been proposed to develop ceramic oxide powders of higher quality than those obtained by the solid route. Greater purity, better granulometric characteristics and higher reactivity, were reported thus leading to significantly lower sintering temperatures. Among these methods, there are two main categories: (i) wet synthesis methods under normal atmospheric pressure such as sol-gel and coprecipitation methods and (ii) hydrothermal methods.

I.2.2.1 Sol-gel method

Sol-gel method is one of the well-established synthetic approaches to prepare novel metal oxides nanoparticles. This method has potential control over the textural and surface properties of the materials. Sol–gel method mainly undergoes in few steps to deliver the final metal oxide protocols and those are hydrolysis, condensation, and drying process. The control of kinetics of hydrolysis and condensation of the titanium ions is sought in this type of synthesis. The basic idea is to slow down the formation of Ti-O-Ti sequences to favor the formation of Ti-O-Ca and Ti-O-Cu sequences which prefigure the crystalline structure of calcium cupper titanate instead of TiO_2. The slowing down of the Ti-O-Ti linkages is caused by a low water supply or by titanium ion fixation of groups such as acetate. The kinetics can also be slowed down by simply lowering the temperature.

The precursors used in this method are metal alkoxide, metal citrate or nitrate. Micrometers particles are distributed by mechanical mixing in a liquid, to form colloidal or sol solution with adjusted pH (Figure I-6). Some difficulties are associated with the key steps of this method such as hydrolysis, condensation and drying, which affect directly the morphology of the material.

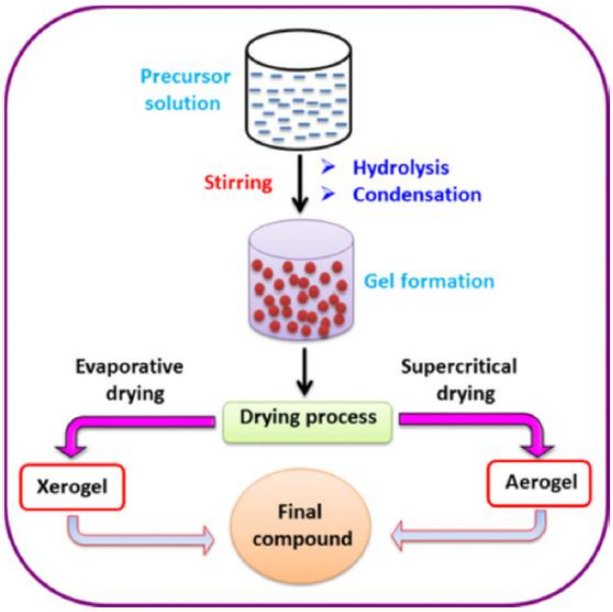

Figure I-6 : The Reaction Pathway for the Production of Metal Oxide Nanostructures in the Sol–Gel Method. Reprinted with permission from (Rao et al. 2017). Copyright 2017 Elsevier [25]

Mao *et al.* [26] have synthesized CCTO using calcium nitrate $Ca(NO_3)_2.4H_2O$, copper nitrate $Cu(NO_3)_2.3H_2O$, titanium isopropoxide ($Ti(C_3H_9O)_4$, citric acid ($C_6H_8O_7$) and ethylene glycol ($C_2H_6O_2$) as starting materials. A stoichiometric amount of $Ca(NO_3)_2.4H_2O$ and $Cu(NO_3)_2.3H_2O$ were dissolved in ethanol and the pH was adjusted by the addition of citric acid to form solution (A). Solution (B) is formed by mixing $Ti(C_3H_9O)_4$ and ethanol for 1h, then solutions (A) and (B) were mixed together with ethylene glycol at room temperature for 1h to obtain a clean and transparent sol solution. In order to obtain a viscous blue gel, this solution was heated at 90°C in a drying oven, then heated to 120°C and kept for 12h in the drying oven to gain fluffy precursor powders. The precursor powders labeled CCTO from 1 to 6 were calcined at 650°C, 700°C, 750°C, 800°C, 850°C and 900°C for 3h respectively then pressed to form pellets and sintered at 1050°C/10h.

The XRD patterns for the obtained powders and ceramics are shown in (Figure I-7). It is clear that CCTO is formed and well crystallized. However traces of CuO and TiO_2 phases are observed in powders calcined at 900°C.

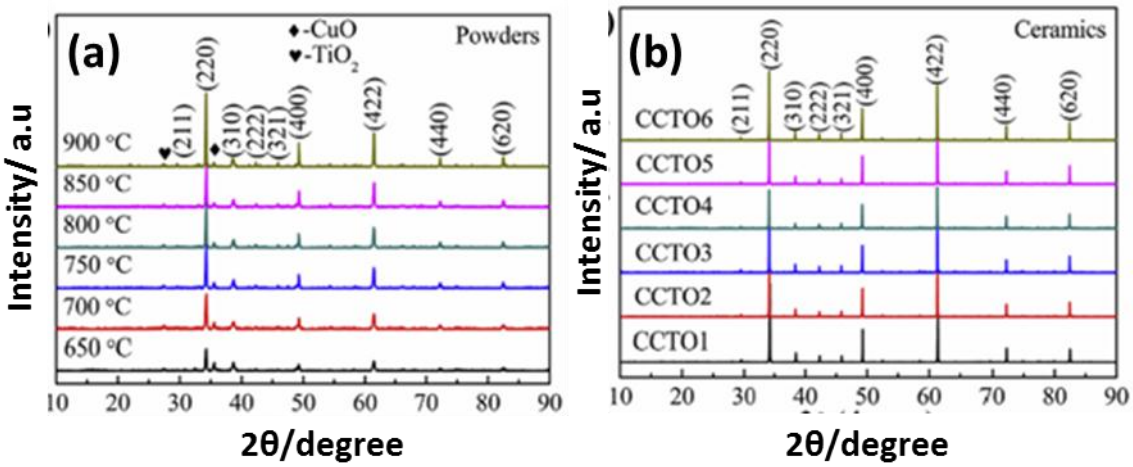

Figure I-7 : XRD patterns of the CCTO powders calcined at different temperature (a) and the sintered CCTO ceramics at 1050°C for 10 h (b). Reprinted with permission from (Mao et al.,2019). Copyright 2019 Elsevier [26]

From SEM images they concluded that the grain size distribution depends on the calcination. CCTO labeled 1, 2 and 3 ceramics had homogeneous microstructures, for CCTO labeled from 4 to 6 ceramics large grains are obtained. This could be attributed to the presence of small grains absorbed by large grains. Grain boundaries of CCTO 5-6 ceramics are heterogeneous and large grains are formed.

At low frequency (10^2 Hz) the permittivity and the dielectric loss increase with increasing calcination temperature, and the increasing of the grain size. Thus, the CCTO6 had the highest value for permittivity and tanδ. At medium frequency (10^3-10^5 Hz) it has been observed that CCTO5 exhibit the lowest value of tanδ (0.091).

Compared with the solid route where the homogeneity scale is rarely better than 0.5 µm, the sol gel method showed considerable advantages, including excellent chemical stoichiometry, compositional homogeneity, and lower crystallization temperature.

I.2.2.2 Co-precipitation

Co-precipiation is one of the most convenient techniques for the preparation of nanomaterials with a narrow size distribution. The co-precipitation technique does not require costly equipment, stringent reactions or complex procedures. This method is based on mixing stoichiometric amounts of soluble salts of metals to form a precipitate of hydroxides, oxalates, or citrates and then the mixture is filtered, dried and heated to form the final product.

Zhu *et al.* [27] used co- precipitation method to synthetize CCTO powders. They started by dissolving 0.2 mole of oxalic acid in ethanol, the pH of the obtained solution was adjusted to 2.5 - 3 using ammonia. At this point, 0.1 mole of $Ti(OCH_4H_9)_4$ were added. On the other hand a stoichiometric amount of calcium nitrate (0.025 moles) and copper nitrate (0.075 moles) were dissolved in distilled water. After few minutes, the metal nitrates solution and the oxalic solution were mixed and kept overnight to complete the reaction. The precipitate was filtered, dried then calcined. Pellets were pressed and sintered by spark plasma sintering at 1000°C for 2h.

Figure I-8a shows the XRD patterns of the powders obtained at different calcination temperatures. They confirm the formation of pure CCTO at 700°C calcination temperature.

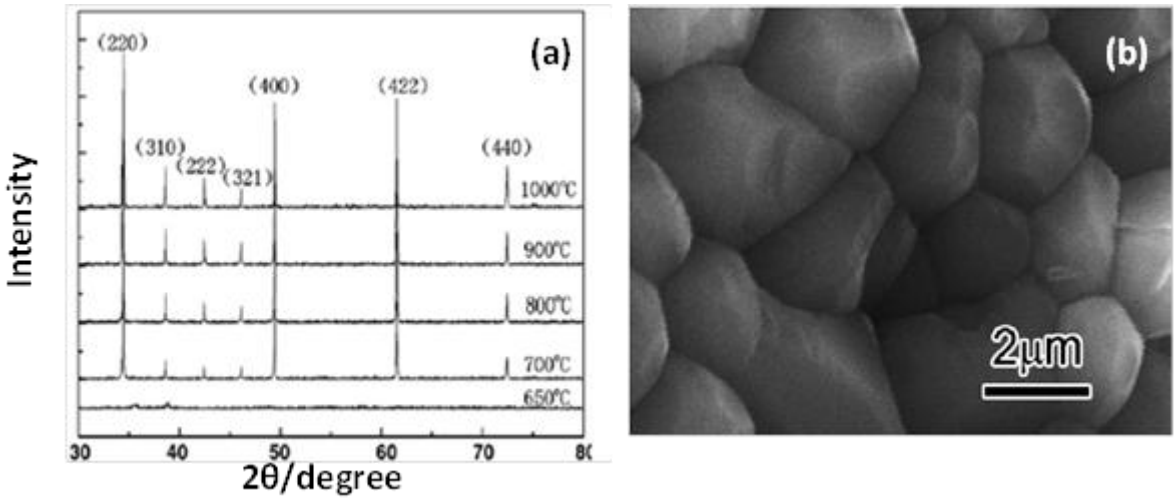

Figure I-8 : a) XRD patterns of CCTO calcined in air at various temperature,(b) the SEM photograph of CCTO ceramic bulk. Reprinted with permission from (Zhu et al.,2009). Copyright 2009 Elsevier [27]

SEM image of the obtained ceramic (Figure I-8b) showed a dense microstructure with an average grain size between 2 and 5µm. The sintered pellets showed a high dielectric constant > 10^4, that increases with frequency from 1 KHz to 1MHz due to IBLC model effect. Using coprecipitation method will help to obtain CCTO at low calcination temperature.

I.2.3 Microwave synthesis

Microwave energy was originally applied for heating food. Recently it has been used to accelerate chemical synthesis. Thus, the microwave energy replaces the calcination step to obtain the pure phase of CCTO powders. The heating effect utilized in microwave assisted synthesis is mainly due to dielectric polarization. This method is based on the emission of a radiation into a solution. If the solution contains charged particles, this particle will move under the influence of a field and produce an oscillating electric current. If the particles in the solution are not charged, the electric field component will cause them to align the dipole moments and this is the dielectric heating. To use the microwave heating techniques, the compound must contain at least one molecule that can absorb the radiation or must be surrounded by an absorbent molecule to absorb microwave radiations.

Kumar *et al.*[28] used the microwave flash combustion technique to synthetize CCTO, involving microwave irradiation on aqueous solution containing $Ca(NO_3)_2.4H_2O$, $Cu(NO_3)_2.4H_2O$,

$TiO(NO_3)_2$ as an oxidizer and urea (CH_4N_2O) as a fuel. They prepared an aqueous solution of two precursors $Ca(NO_3)_2.4H_2O$ and $Cu(NO_3)_2.4H_2O$ separately, then they mixed these solutions with an stoichiometric amount of urea fuel and oxidizer agent ($TiO(NO_3)_2$). At the end, they obtained a blue gel. This gel is kept in an alumina crucible and put into a microwave costumed oven operating at 2.45 GHz and 1.1KW power. The combustion takes around 30s to be completed. It is accomplished by a flash of light followed by discharge of gaseous mixture (O_2, N_2, H_2O) and a porous dark-brown residue is obtained. This residue was crushed then calcined at 800°C and 900°C for 5h to obtain CCTO. XRD patterns (figure I-9a) showed that the pure phase of CCTO is obtained after calcination at 900°C/5h.

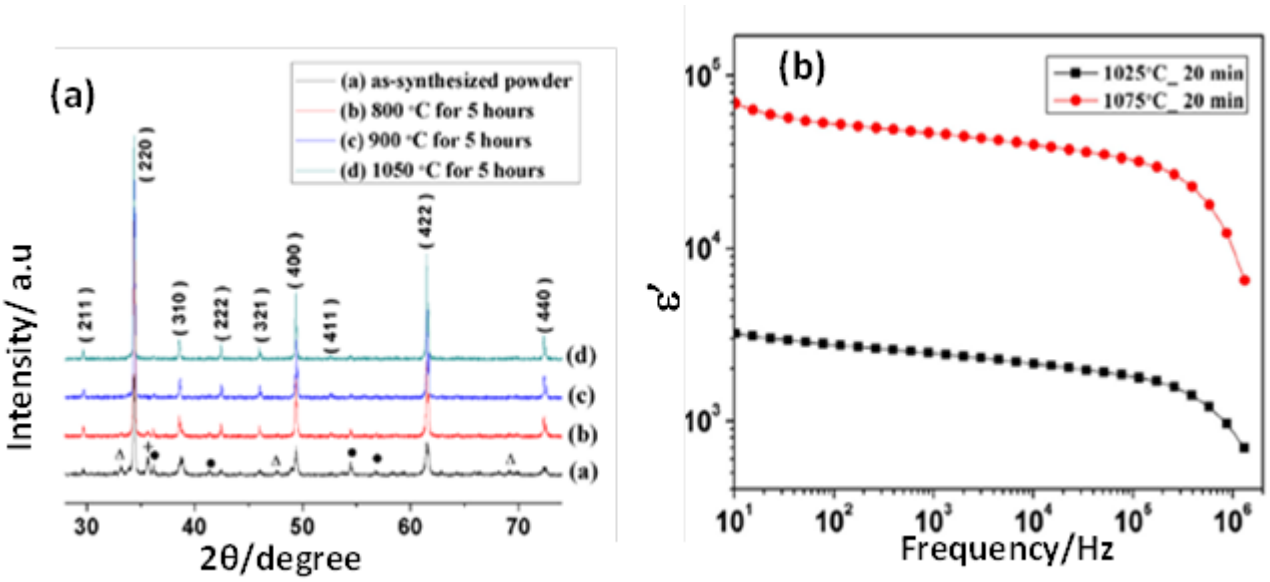

Figure I-9 : (a) XRD patterns of CCTO powder samples: (a) as-synthesized, (b) calcinated at 800 °C for 5 h, (c) calcinated at 900 °C for 5 h, and (d) sintered pellet at 1050 °C for 5 h. The symbols Δ, +, and • correspond to the trace of secondary phases $CaTiO_3$, CuO, and TiO_2, respectively, (b) Frequency dependence of the dielectric constant and tan δ of sintered CCTO samples sintered at 1050 °C for 5 h. The inset shows the variation of the real part of the impedance with frequency. Reprinted with permission from ref [28]. Copyright © 2015 American Chemical Society

Dielectric properties (Figure I-9b) were studied on CCTO pellet (sintered in air with conventional method at 1050°C/5h) and showed that at low frequencies dielectric constant increases, that

maybe due to the ceramic-electrode interface effect or to a relaxation dipole at the grain boundaries. However higher dielectric constant and dielectric loss appear at high frequency (0.5-8MHz). This value of dielectric loss is maybe due to that at high frequency just the response of grains is considered and there is charge carriers generated in grains during sintering by reduction of Cu^{2+} to Cu^{+} and by oxygen loss.

Despite that this approach is very elegant, the final compound cannot be formed after heating into a microwave and a second step of calcination is always needed.

I.2.4 Combustion synthesis technique

By this method, single homogenous nanopowders and single-phase material can be produced; ceramics, catalysis composites alloys and nanomaterials are synthetized and proceeded. A reaction is maintained between a fuel and an oxidant present in the precursor solution. Oxidant are the nitrates of different metals and the fuel generally are citric acid, urea, ethyl glycol or it can be added with some chelating agents such as acetic acid, to form complexes with the metal ions present in the precursor solution. The dehydration of this complex produces a viscous gel, that after self-heating produce a huge quantity of gazes which leads to the formation of pores. The final step is the calcination at high temperature of this gel to have a final product.

Patra *et al.* [29] used an appropriate amount of $TiO(NO_3)_2$, $CaCO_3$, CuO, citric acid monohydrate and ammonium nitrate. The pH of the solution was adjusted using NH_4OH, the solution was kept on a hot plate at 80-90°C. A viscous gel is developed due to the dehydration of the mixed solution during heating. This gel self-ignites resulted from heating is followed by swelling of the gel. A voluminous black precipitate was obtained from this ignition, and then calcined at 800°C to obtain pure CCTO phase.

Lopera *et al.* [30] used sol-gel method associated with auto-combustion to synthetize Sm-doped $CaCu_3Ti_4O_{12}$. They used ($Cu(NO_3)_2$), ($Ca(NO_3)_2$) Ti-isopropoxide ($Ti[OCH(CH_3)_2]_4$,) Samarium nitrate ($Sm(NO_3)_2$), and acid citric ($C_6H_8O_7H_2O$). In order to have $Ca_{1-x}Sm_xCu_3Ti_4O_{12}$ (for x=0, x=0.2,x=0.3), starting materials were mixed in distilled water solution then heated on a hot plate magnetic stirrer at 70°C until the auto-combustion is achieved. Precursor powders are

sintered at 1050°C/10h. XRD patterns (Figure I-10) showed that a pure phase of CCTO is formed with almost the same lattice parameter 7.392Ä, 7.394Ä and 7.395Ä for CCTO (x=0), CCTO2 (x=0.2) and CCTO3(x=0.3) respectively. SEM images showed that grain growth was inhibited after doping by Sm^{3+}, and the permittivity at 100 kHz decrease from 15.747 for undoped CCTO to 4126 for CCTO3.

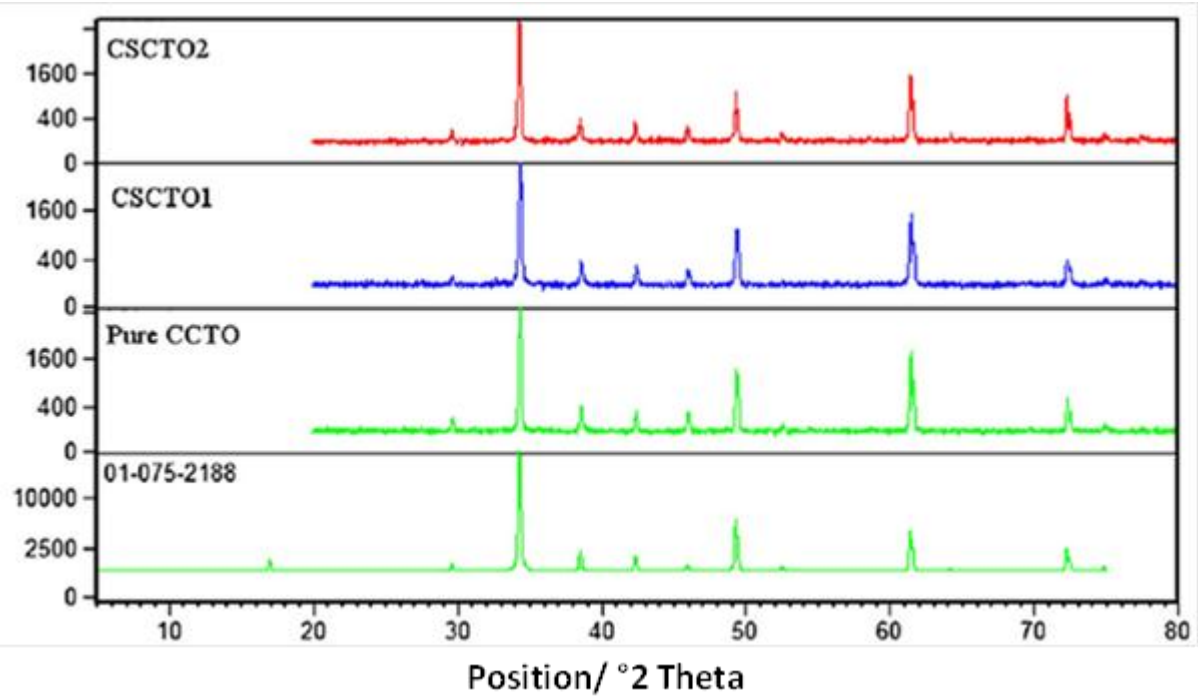

Figure I-10 : X-ray diffraction patterns for $Ca_{1-x}Sm_xCu_3Ti_4O_{12}$ the system CSCTO2 (x = 0.2), CSCTO1 (x = 0.3), and CCTO (x = 0.0). Reprinted with permission from (Lopera et al.,2014). Copyright 2014 Elsevier [30]

Autocombustion method is a rapid process with low-cost and low-temperature. There is a possibility to have multicomponent oxides with single phase and high surface area. It is an exothermic reaction that makes the product almost instantaneously. The disadvantages of this process are the possibility of contamination with carbonaceous residue and the poor control of morphology.

I.2.5 Hydrothermal method

Hydrothermal method is used in order to synthetize nanosized ceramics. To carry out the reaction under high temperature and pressure, precursors are placed into an autoclave filled with water.

Classically to synthesize CCTO by hydrothermal method [$Ti(OC_3H_7)_4$], $CaCO_3$, $Cu(NO_3)_2{\cdot}2.5H_2O$ and potassium hydroxide (KOH) are used as starting materials. In deionized water, an appropriate amount of titanium isopropoxide and calcium carbonate was dissolved, the same for copper nitrates, then the two solutions were mixed together with 50 mL from KOH (mineralizer). An amorphous precipitate of $Ti(OH)_2$, $Ca(OH)_2$ and $Cu(OH)_2$ is formed. In order to avoid the formation of calcium carbonate as second phase, nitrogen gas was constantly bubbled to the system. The mixture is transferred to a Teflon autoclave.

Masigboon *et al.* [31] synthetized $CaCu_3Ti_4O_{12}$ using the hydrothermal method. In aqueous medium, precursors $Ca(NO_3)_2.4H_2O$, $Cu(NO_3)_2{\cdot}3H_2O$, $Ti(OC_3H_7)_4$ and freshly extracted egg white (ovalbumin) were mixed. Egg white protein was used due to his gelling, foaming and emulsifying characteristics. It was no need to pH adjustment with this process. Mixed solutions were treated hydrothermally in autoclave at 150°C and 200°C for 8h. They dry the precursor at 70°C-80°C then it was calcined at 800°C, 900°C and 1000°C/8h.

XRD patterns (Figure I-11) showed that the pure phase of CCTO appears after 800°C of calcination with second phases $CaTiO_3$, TiO_2 and CuO. $CaTiO_3$ appears when there is non-stoichiometric amount of Titanium and calcium. As seen in TEM images (Figure I-12), CCTO had a nanocrystalline structure, in which grain size increases with calcination's temperature. They conclude that with hydrothermal method, CCTO powders can be produced in order to study their dielectric properties.

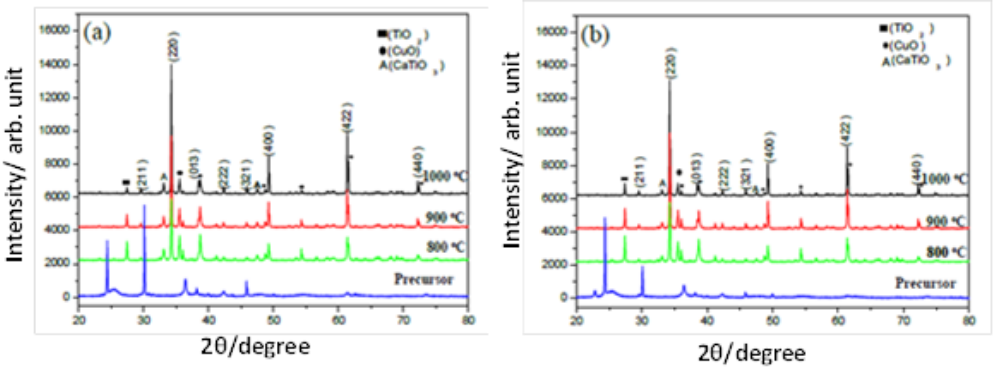

Figure I-11 : XRD patterns of CCTO base-powders prepared by hydrothermal process at (a) 150°C/8h and (b) 200°C/8h, respectively. All powders calcined in air for 8 h at 800, 900 and 1000 °C. Reprinted with permission from (Masingboon et al. 2017). Copyright 2017 Creative Commons CC.[31]

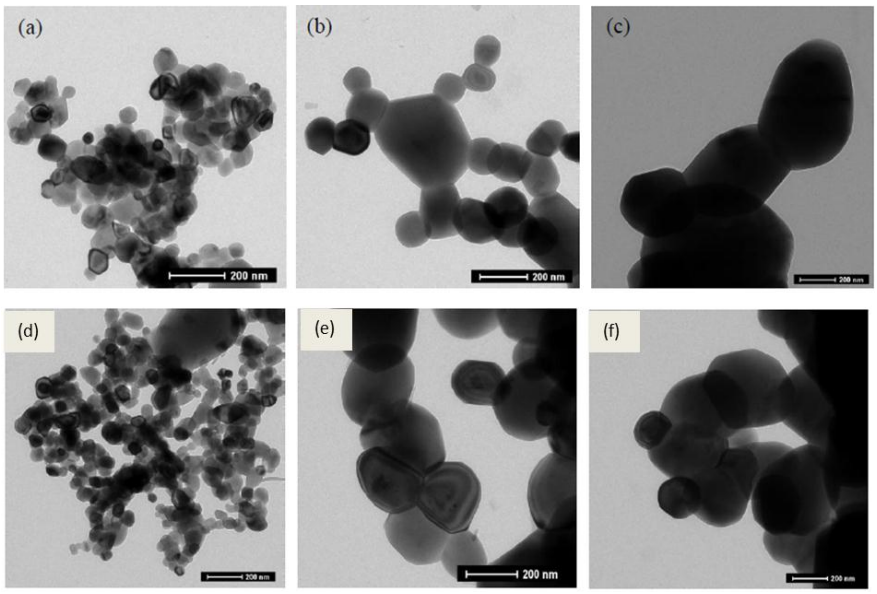

Figure I-12 : TEM images of CCTO powders, which prepared by hydrothermal process at 150 °C/8h calcined in air for 8 h at (a) 800, (b) 900 and (c) 1000 °C, and at 200 °C/8h calcined in air for 8h at (d) 800 , (e) 900 and (f) 1000 °C, respectively. Reprinted with permission from (Masingboon et al. 2017). Copyright 2017 Creative Commons CC [31]

In order to prepare calcium copper titanate, different synthesis methods are used. The aim of using these methods (apart solid state route) was to obtain the final compound at lower calcination temperature and with a homogeneous microstructure in order to maintain a high permittivity and a low dielectric loss. In Table I-1, some selected examples for these different synthesis methods are showed as well as their influence on permittivity (ε') and loss tangent ($\tan \delta$). From Table I-1, microwave synthesis showed the highest value of dielectric constant (ε'=53,300) but at the same time the highest dielectric loss ($\tan\delta$=0.2), which limit its industrial application. In the next section, the different approaches used for the sintering of CCTO will be reviewed.

Table I-1 : Resumed comparison between synthesis method and their influence on dielectric properties permittivity (ε'), and dielectric loss (tan δ)

Synthesis Method	Precursors	ε'	tan δ	References
Solid-solid	CaO,CuO and TiO_2	10,286	0.067	**[6]**
Mechanosynthesis	$CaCO_3$, CuO, TiO_2	~5000	0.14	**[21]**
Sol-gel	$Ca(NO_3)_2.4H_2O$, $Cu(NO_3)_2.3H_2O$, $Ti(C_3H_9O)_4$, $C_2H_6O_2$, $C_6H_8O_7$	$3*10^4$	0.091	**[25]**
Microwave synthesis	$Ca(NO_3)_2.4H_2O$, $Cu(NO_3)_2.4H_2O$, $TiO(NO_3)_2$, CH_4N_2O	53,300	0.2	**[27]**
Autocombustion	$Ca(NO_3)_2$, $Cu(NO_3)_2$, $Ti[OCH(CH_3)_2]_4$, $C_6H_8O_7H_2O$	15,474	-	**[29]**
Coprecipitation	$H_2C_2O_4.H_2O$, $Ca(NO_3)_2.4H_2O$, $Cu(NO_3)_2.3H_2O$, $Ti(OC_4H_9)_4$	10^4	0.09	**[26]**
Modified sol-gel with hydrothermal process	$Ca(NO_3)_2.4H_2O$, $Cu(NO_3)_2.4H_2O$, $TiO(OC_3H_7)_4$	-	-	**[30]**

I.3 Sintering and dielectric properties

Sintering (Figure I-13) is a well-established process used to consolidate powders by heating green bodies at high temperatures below the melting temperature of the powder. It is a thermal treatment for bonding particles into a coherent, predominantly solid structure via mass transport events that often occur on the atomic scale. The bonding leads to improve strength and lower system energy. Most industrial sintering is pressure less and performed without any external applied pressure. Pressure assisted sintering techniques include many processes: hot isotactic pressing, hot pressing, flash sintering and Spark Plasma sintering.

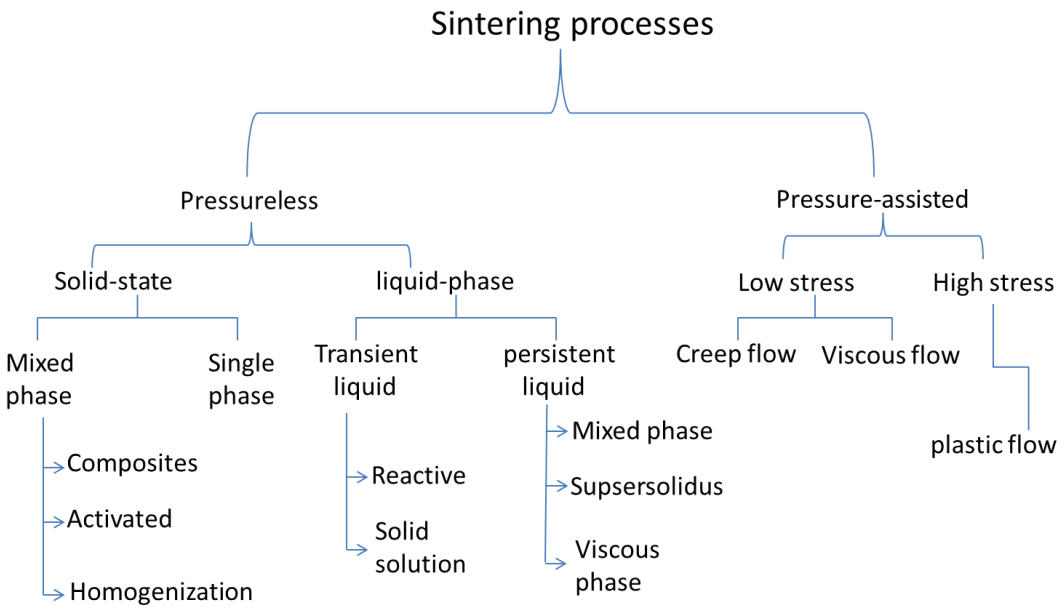

Figure I-13 : the taxonomy of sintering, showing process differentiation by various branches, starting with the application of pressure-assisted versus pressureless sintering. Adapted from [32]

There are challenging demands from all the industries involved in nanotechnology for new and improved sintering process with fine microstructure and enhanced mechanical, electrical, optical and physical properties. The aim of modern ceramic technologies is obtaining dense ceramic with nanostructured grains. That is why there are many factors to be optimized during the sintering process, starting from powders (shape and size of grains), green bodies manufacturing (dimensional changing during compacting which is dependent from the pressure) and sintering type and time [33]. In this review, we will present four main methods of sintering used to obtain dense ceramic of $CaCu_3Ti_4O_{12}$ such as conventional sintering, microwave sintering, and spark plasma sintering and thermobaric treatment.

I.3.1 Conventional sintering

The conventional sintering process consists of heating a preformed powder (raw or blended materials) at high temperatures, lower than the melting point, during minutes to hours. The driving force for sintering comes from the high surface energy and curved surface inherent to a powder. There are different “stages” for sintering. A “stage” of sintering can be described as an

interval of geometric change in which the pore shape change is totally defined or an interval of time during which the pore remains constant in shape while decreasing in size. The sintering process can be divided into three different stages:

- **The initial stage:** Sintering initially causes the particles that are in contact to form grain boundaries at the point of contact through diffusion. The neck and grain boundaries are formed during this stage. Neck formation is driven by the energy gradient resulting from the different curvatures of the particles and the neck. Surface diffusion is usually the dominant mass-transport mechanism during the early stages of neck growth, as the compact is heated to the sintering temperature. A smoothing in the surface occurs.
- **The intermediate stage:** During this stage, there is the creation of isolated pore structures. Grain growth and densification occur at this stage too. Densification is assumed to result from pores simply shrinking to reduce their cross section. The intermediate stage normally covers the major part of the sintering process, and it comes to an end when the density of the porous body reaches close to 90 % of the fully dense body.
- **The final stage:** Final stage sintering is much slower than the initial and intermediate stages. During this stage, pore shrinkage and closure happen. Pore shrinkage is one of the most important stages in the sintering process. For this shrinkage to occur solids must be transported into the pores and the gas present inside the pore must escape to the surface. In the final stage, grain growth occurs.

CCTO was widely prepared by conventional sintering and the electrical properties of the obtained ceramics were extensively studied. Different furnaces types were used to a conventional sintering such as refractory type electrical resistance furnace, induction furnace or fossil fuel furnace. High temperature and long sintering duration are maintained during sintering process. During heating, the temperature is distributed between elements by the mechanism of conduction, radiation and convection. First the material surface is heated then heat is transferred into material leading to a temperature differences between the surface and inside the material [34].

Sinclair *et al.*[7] prepared the CCTO powders via the mixed oxide route using $CaCO_3$, CuO and TiO_2 as starting materials. Pellets were prepared by sintering cold-pressed compacts in air at 1000-1100°C and were 89 to 90% of the theoretical density. The obtained ceramics showed values for permittivity higher than 10 000. The authors explained that the electrical properties of $CaCu_3Ti_4O_{12}$ ceramics depend on many variables, including ceramic microstructure (average grain size and pellet density) and processing conditions (oxygen partial pressure, sintering temperature and cooling rate).

Barbier *et al.*[35] prepared CCTO ceramics by adding an organic binder to the powder and the obtained mixture was pressed into pellets of 6 mm in diameter and 1.5 mm thick, at a pressure of 620 MPa. The obtained pellets were sintered in air at 1100°C for 24 h. The density of the samples was approximately 4.8 g cm^{-3}. The pellets exhibited a bimodal grain size distribution (Figure I-14).

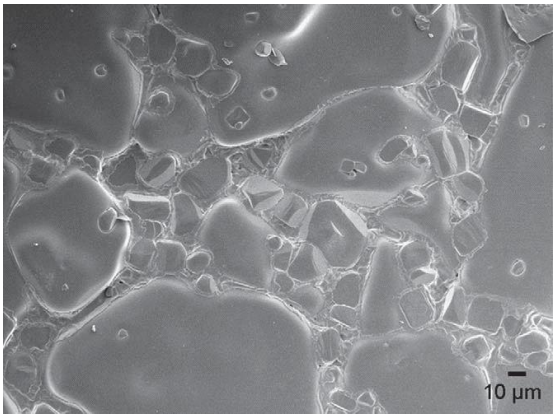

Figure I-14 : FEG-SEM micrograph of a 6mm diameter CCTO pellet sintered at 1100 ◦C for 24 h. Reprinted with permission from (Barbier et al.,2009). Copyright 2009 Elsevier [35]

High values of dielectric permittivity and low losses were observed whatever the electrode (ε_r = 1.4×10^5 and tg δ ~0.16 at 1 kHz). Lukenheimer *et al.* [36] studied the origin of the colossal dielectric constants of CCTO ceramics prepared by conventional sintering. They performed detailed dielectric measurements on various CCTO samples subjected to different surface and heat treatments. The ceramics were sintered at 1000°C in air for up to 48h. The authors concluded that there must be two different types of insulating layers in CCTO.

Ferrarelli *et al.* [37] undertook impedance spectroscopy study of CCTO single crystals and CCTO ceramics. The authors mentioned that the impedance spectroscopy is a useful technique to characterize electrically heterogeneous materials and can, in many circumstances, be used to identify and separate intrinsic (e.g. bulk) and extrinsic (e.g. grain boundary, non-ohmic electrode contact) effects. The CCTO ceramics were prepared by uniaxially cold pressing of the CCTO powder into 5 mm compacts under an applied pressure of 50 MPa, followed by pressing at 200 MPa in a Flow Autoclave System model 32330 cold isotactic press. Resulting green body compacts were placed on Pt foil and sintered at 1100 °C for 6 h. Heating and cooling rates of $5°C.min^{-1}$ were used for both the powder production and for sintering pellets. CCTO ceramics with a theoretical density of 96 % were obtained. The authors observed a predominantly grain boundary effect (IBLC) for ceramics and an extrinsic electrode – sample interface effect for single crystals.

Fiorenza *et al.* [38] used the combination of scanning impedance microscopy and conductive atomic force microscopy on single crystals of the perovskite-type oxide $CaCu_3Ti_4O_{12}$ (CCTO) in order to provide a local dielectric characterization on ingot sections. The authors sintered the single crystals in air for 12h at 1000°C. They demonstrated the presence of insulating inclusions in $CaCu_3Ti_4O_{12}$ single crystals, identified to be $CaTiO_3$. The $CaTiO_3$ secondary phase could block/restrict conduction within $CaCu_3Ti_4O_{12}$ crystals and could participate in the macroscopic conduction mechanisms.

Schmidt *et al.* [39] synthesized powders of various compositions within the ternary CaO–CuO–TiO_2 phase diagram from different amounts of dried high purity reagents of $CaCO_3$, CuO and TiO_2. For each composition, pellets were pressed from freshly crushed and ground powders using a uniaxial hydraulic press (1 ton) and all were simultaneously sintered at 1100 °C on Pt foil for 12 h. The authors observed an abnormal increase of the CCTO bulk dielectric permittivity in the absence of CuO secondary phase in the ceramics. Compositions containing CuO phase exhibit increased resistivity.

Turky *et al.* [40] demonstrated that without any dopant, only by controlling the chemistry and engineering, the interfacial regions at the grain boundaries, the dielectric loss can be suppressed remarkably while retaining the giant dielectric constant.

Finally, chung *et al.* [41] prepared pellets sintered in a tube-type furnace at 1100 °C in air for 3 to 20 h and removed immediately to room temperature without any furnace-cooling.

With conventional sintering method, CCTO can be produced in one step of heating, but the use of very high temperature is necessary which is costly in energy domain and non-environmentally.

I.3.2 Microwave sintering

Microwave sintering is a newly developed technique used for the sintering of materials that has shown many advantages against the conventional sintering process. Microwaves are a form of electromagnetic radiation with wavelengths ranging from about one meter to one millimeter; with frequencies between 300 MHz and 300 GHz. Originally, microwaves were used for communication. Heating of materials with the use of microwave energy got established in 1950. Thus, the microwave heating gained very fast popularity for processing of ceramics, polymers, metallic based materials and advanced materials.

The processing of material using microwaves depends on its dielectric and magnetic properties as the electric field and the magnetic field of the electromagnetic radiation interact with the material during irradiation. The dielectric interaction of materials with microwaves is characterized by two factors: The absorbed power (P) and the depth of microwave penetration (D). The absorbed power in a material is the dissipated power due to the electric and magnetic fields of microwave energy which could be represented as energy converted inside a heated material. Thus, the power absorbed by a material is significantly influenced by the depth up to which the radiations penetrate into it. However, microwaves cannot penetrate inside in the similar fashion in all materials.

Transparent or low dielectric loss materials let the microwaves pass through them without any loss. Opaque or conductive materials reflect the microwaves not allowing them to penetrate. Absorbing or high loss materials where microwaves are absorbed depending on the value of the dielectric loss factor (Figure I-15) [34,42].

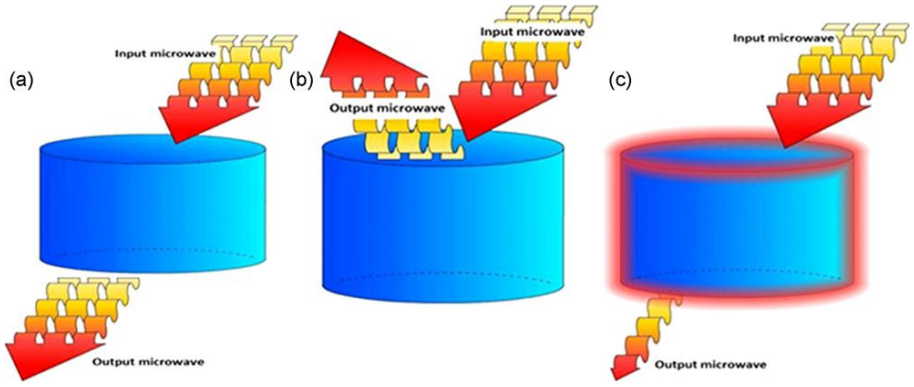

Figure I-15 : Three kinds of materials according to the interaction with microwaves: (a) transparent, (b) opaque (conductor) and (c) absorber. Reprinted with permission from (Oghbarir et al.,2010). Copyright 2010 Elsevier [34]

The Basic difference between conventional sintering and the microwave sintering resides in the heating mechanism. (Figure I-16) shows the temperature profile for both methods:

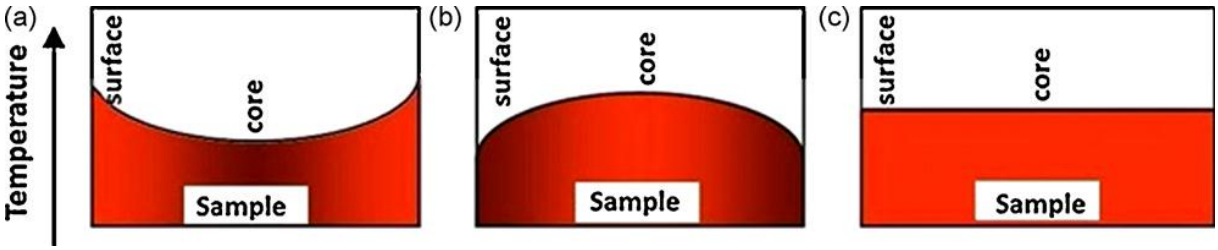

Figure I-16 : Temperature profile within the sample in: (a) conventional heating, (b) microwave heating and (c) microwave hybrid heating. Reprinted with permission from (Oghbarir et al.,2010). Copyright 2010 Elsevier [34]

For conventional sintering, heat is generated by heating elements and transferred to samples via radiation, conduction, and convection. In microwave sintering, however, the materials themselves absorb microwave energy, and then transform it into heat within their bodies [34]

The microwave sintering shows many advantages against the conventional sintering process:

- Increased density and more uniform grain sized distribution since it can promote the forward diffusion of ions.
- Lower energy consumption in microwave sintering because the use of microwaves facilitates the transfer of energy directly into the materials, providing volumetric heating.
- Reduced sintering time since microwaves directly interact with the particulates within

the green pellets rather than being conducted into the specimen from an external heat source, thereby provide rapid volumetric heating [34].

Recently many researchers have been using the microwave sintering process to prepare CCTO ceramics [43,44]. In 2016, Kumar *et al.* [43] demonstrated the effect of microwave heating rate on the sintering of CCTO. The higher is the heating rate (50°C/min) the more uniform and dense is the structure. Conductivity of the obtained ceramics was found to increase with increasing heating rate. They prepared nanocrystalline powders of CCTO by microwave flash combustion technique, the obtained powders were sintered by microwave sintering method. The sintering temperatures were optimized to 1025-1075°C and the duration to 20 minutes. Figure I-17 shows the SEM of the obtained ceramics obtained by microwave sintering.

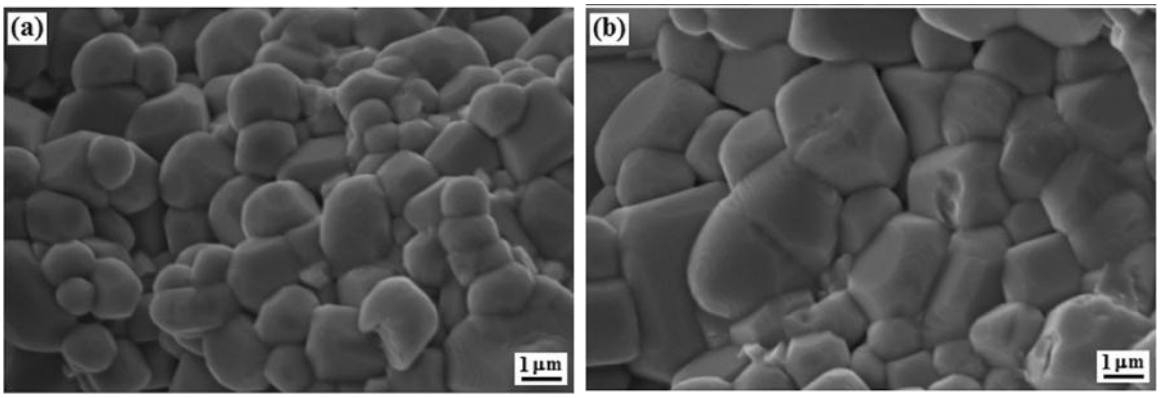

Figure I-17 : SEM image of CCTO sample sintered by microwave for 20 min at (a) 1025 °C and (b) 1075 °C. Reprinted by permission from (Nature/springer/Journal of Electroceramics) (Kumar et al.) Copyright (2018) [43]

Thus, the CCTO microstructure has well developed grains and grain boundaries. The grain boundaries are very thin as compared to that of grains. The authors showed that increasing the sintering temperature increases the grain growth in the ceramic as well as the densification (from 94 to 97%). At room temperature, a giant dielectric constant of 53300 and a small loss tangent of 0.2 at 100 Hz were found in CCTO sample sintered at 1075 °C for 20 min. It was found that CCTO microstructure was electrically heterogeneous due to grain resistance of 8 Ω and grain boundary resistance of 350000 Ω. This confirms that giant dielectric constant in CCTO is related to inter-barrier layer capacitance.

Ouyang *et al.* [44] used microwave sintering in order to obtain CCTO ceramics. The authors explained that the fundamental difference between conventional sintering and microwave sintering is the difference of the heating mechanisms. The dielectric properties of the ceramics depend on their microstructure. In the microwave sintered samples, an increase in the sintering time decreases the value of the relative permittivity and the electrical loss. While for conventional sintering ceramics, an increase in the time of sintering increase the values of the permittivity and dielectric loss. This difference in behavior between microwave and conventionally sintered ceramics was attributed to the difference in the microstructure.

Raval *et al.*[45] prepared three sets of samples; all of them sintered at 1223 K for 12 h then at 1423 K for 18 h. The first set was slowly cooled, the second one was quenched from the high temperature to liquid nitrogen and the third one was slowly cooled then treated in a domestic microwave (2.45 GHz) for 1h. They analyzed J-E graphs to investigate the I-V properties of different surfaces resulting from different treatments. They noticed that the maximum current density (J_{max}) decreases from 327 mA/cm^2 for the slowly cooled sample to 254 mA/cm^2 and 234 mA/cm^2 for the quenched and the microwave samples respectively. This behavior was attributed (i) to the relation between surface morphologies (grain size and secondary phases) after quenching and microwave treatment and (ii) to the varistor property.

I.3.3 Spark Plasma sintering

Field assisted sintering techniques have become recently very important for the rapid preparation of fully dense ceramic powders. Among them, the novel technique of Spark Plasma Sintering is used for the superfast densification of ceramic nanoparticles within a few minutes. Spark plasma sintering (Figure I-18) is a modified hot-pressing process where the ceramic powder compact is placed within a conducting die (mainly graphite), which is in turn heated via high DC or AC electric current density [46].

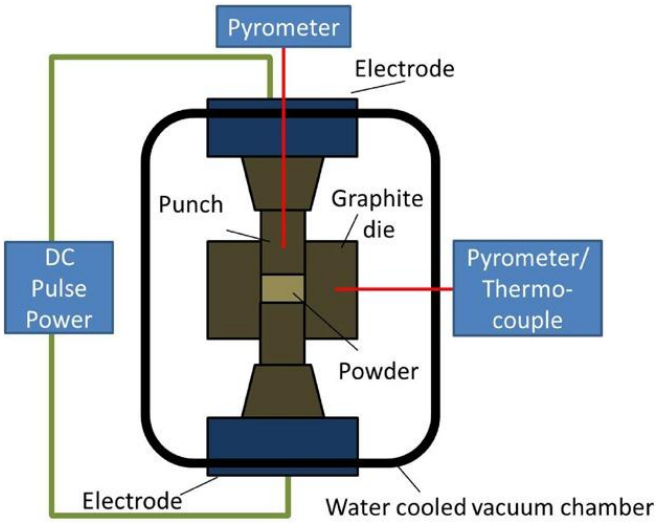

Figure I-18 : SPS system configuration. Reprinted with permission from (Guillon et al.,2014). Copyright 2014 Creative Commons CC [46]

The SPS process is performed in partial and low vacuum (* 3 Pa) in order to avoid oxidation of the graphite die at high temperatures. During the process, the sample placed in a conductive matrix and subjected to uniaxial pressure. In this sintering mode, series of DC pulses (pulse duration 3.3 ms, current 0.5 to 8 kA, voltage ≤ 10 volts) are applied during the sintering cycle. By this process it is possible to reach the sintering temperature extremely rapidly with temperature rise rates of up to 600 ° C. min^{-1} maximum. As a result, grain growth is strongly inhibited and dense materials of submicron grains can be expected to be obtained at temperatures of about 100 degrees lower than the temperatures required for conventional sintering methods.

Three mechanisms affect the spark plasma sintering, such as enhancement of grain boundaries diffusion process by pulsed current, pressure application and resistance sintering. These three mechanisms have to be optimized in order to obtain a compact structure with grain-to-grain contact [33].

Kumar *et al.* [47] prepared CCTO ceramics by sintering CCTO powders using the SPS method. The sintering temperature used is 1050°C and the duration of sintering is 10 min under uniaxial pressure of 50 MPa. The morphology of the particles in the sintered pellet is shown in the figure I-19.

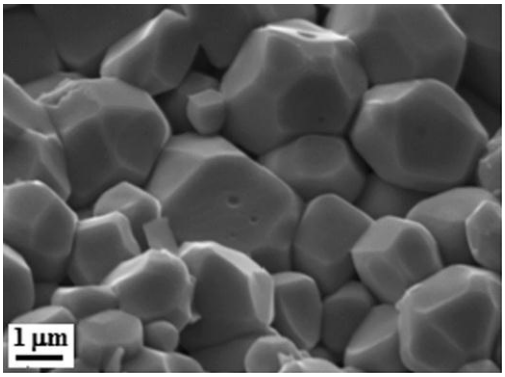

Figure I-19 : SEM image of CCTO pellets sintered at 1050 °C for 10 min using spark plasma sintering. Reprinted by permission from (Nature/springer/Journal of Materials science, Materials in Electronics) (Kumar et al.)- doi.org/10.1007/s10854-015-3275-x Copyright (2015) [47]

In 2017, Kumar *et al.* [48] obtained spark plasma sintered ceramics using a temperature of sintering of 1050°C and a duration of 30 minutes. The microstructure of the sintered ceramics (Figure I-20a) showed that microstructure has highly compacted grains with grain boundaries. The average grain size is in range of 12–15 µm. The density of sintered sample is measured to 97.5 % of theoretical density.

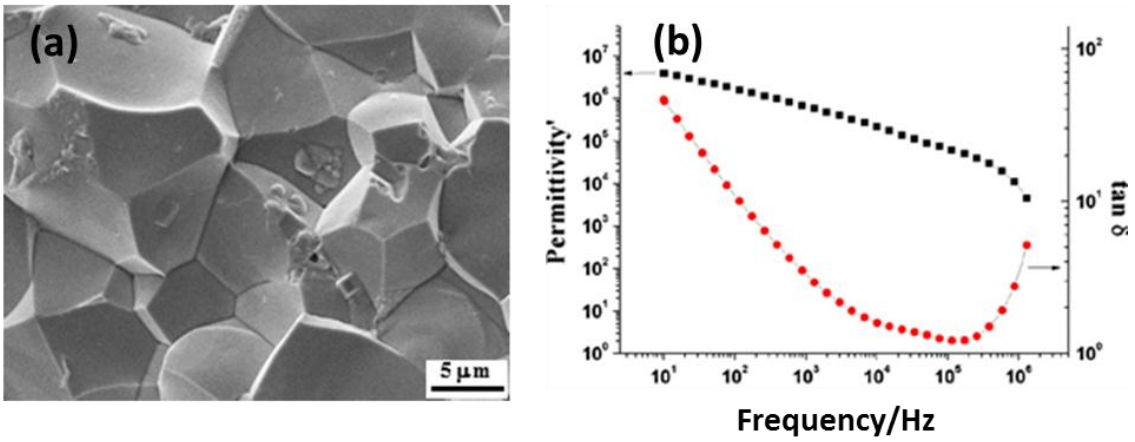

Figure I-20 : (a) SEM image of fractured CCTO pellet sintered by spark plasma at 1050 °C for 30 min,(b) Frequency dependence of the dielectric constant and tanδ of spark plasma sintered CCTO samples. Reprinted by permission from (Nature/springer/Journal of Materials science, Materials in Electronics) (Kumar et al.)- doi.org/10.1007/s10854-016-4418-4 Copyright (2016) [48]

The frequency dependence of the dielectric constant and loss tangent of SPS sintered ceramics are shown in the following Figure I-20b:

Dielectric constant and loss tangent of sintered samples was measured to 1.7×10^6 and 11 at 100 Hz respectively. Using the impedance spectroscopy, the resistance of grain and grain boundary was calculated to be 10 and 190Ω, respectively. These resistances form the internal resistive barrier that result in a giant dielectric constant in CCTO.

They noticed an increase in grain boundaries resistance. The conductivity shows a nonlinear I-V response that confirmed the non-ohmic electrical grain boundaries properties of CCTO. A polarization is applied between two adjacent CCTO grains (Schottky diode), one of Schottky is forward polarized (semiconductor-insulator) in which the depletion contribution is reduced, and the second one is polarized in reverse (insulator-semiconductor) in which the depletion contribution is enhanced. These two depletions are unequal. By dropping the applied voltage, the reverse side keeps expanding while the forward one is fasten and this behavior results in an increase in width of the depletion region. The decrease of grain boundaries capacitance is induced by the increasing of the width of depletion region and thus non-ohmic electrical grain boundaries properties appears.

Ni *et al.* [49] prepared CCTO spark plasma sintered ceramics and compared them to conventionally sintered CCTO ceramics. In the SPS method, the obtained powders were added in to a graphite die with 12 mm diameter and sintered at temperatures from 750°C to 950°C for 5 min under a vacuum of 6 Pa. During the period of heating and soaking, a pressure of 30 MPa was applied to the sample. Then the as-sintered samples by SPS were polished and annealed in air at 800°C for 2 h to remove the residual carbon on the surface of samples. After annealing, the samples were polished again from both sides to remove the residue from outer layers.

The authors showed that the SPS ceramics showed a higher dielectric constant compared to conventionally sintered ceramics and they attributed this to the higher densification the sintered samples.

Lin *et al.* [50] prepared four different ceramic series that were SPS sintered at 900°C for 5 min, 900°C for 20min, 950°C for 5min and 950°C for 20min. Figure I-21 shows the microstructure of the different ceramics obtained by SPS.

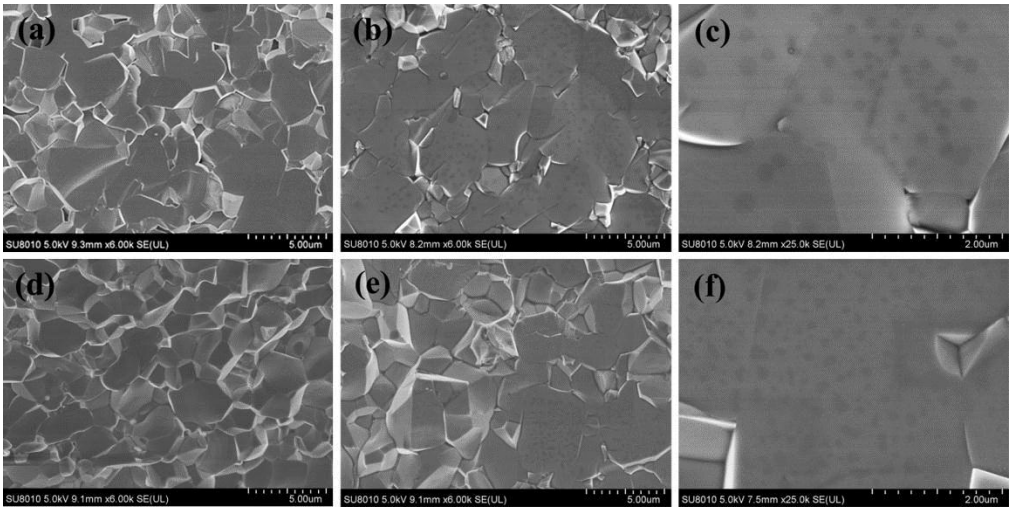

Figure I-21 : SEM images of fractured cross-sections of CCTO ceramics prepared by SPS method: (a) SPS-900-5, (b) SPS-900-20, (d) SPS-950-5, (e) SPS-950-20 samples; the high magnifications for (c) SPS-900-20 and (f) SPS-950-20 samples with small inclusions. Reprinted with permission from (Lin et al.). Copyright 2018 Elsevier [50]

The authors concluded that the ceramics sintered at 900°C for 5 min have the largest E_b (~9.28 kV/cm) and α (~21.5) value, which can be attributed to the synergistic effects of enhanced barrier height, large activation energy at grain boundaries, and the evolution of microstructure. Spark plasma sintering is an efficient method used to obtain a well and defined structure of CCTO ceramics; however it is a very costly method and not used widely.

I.3.4 Thermobaric treatment

High-pressure experimental techniques have been widely used in such fields as mineralogy, petrology, geophysics, and material science. Generally, there are three major high-pressure devices used in high-pressure experimental studies for the Earth and planets, including the piston-cylinder apparatus, the multianvil apparatus (MAA), and the diamond-anvil cell (DAC). Each apparatus has its own advantages and unique applications [51]. High pressure and high temperature sintering methods have been recently used to prepare CCTO ceramics [52,53]**.**

In order to study the properties of the CCTO ceramics prepared by thermobaric treatment, Xu *et al.*[52] prepared quenched CCTO at 1000°C/10 min after it had been subjected to a high quasihydrostatic pressure of 9 GPa. Such high pressure and high temperature treatment (HPT) result in significant changes of the crystallochemical parameters. The microstructures of the obtained ceramics are shown in Figure I-22 (a,b,c,d):

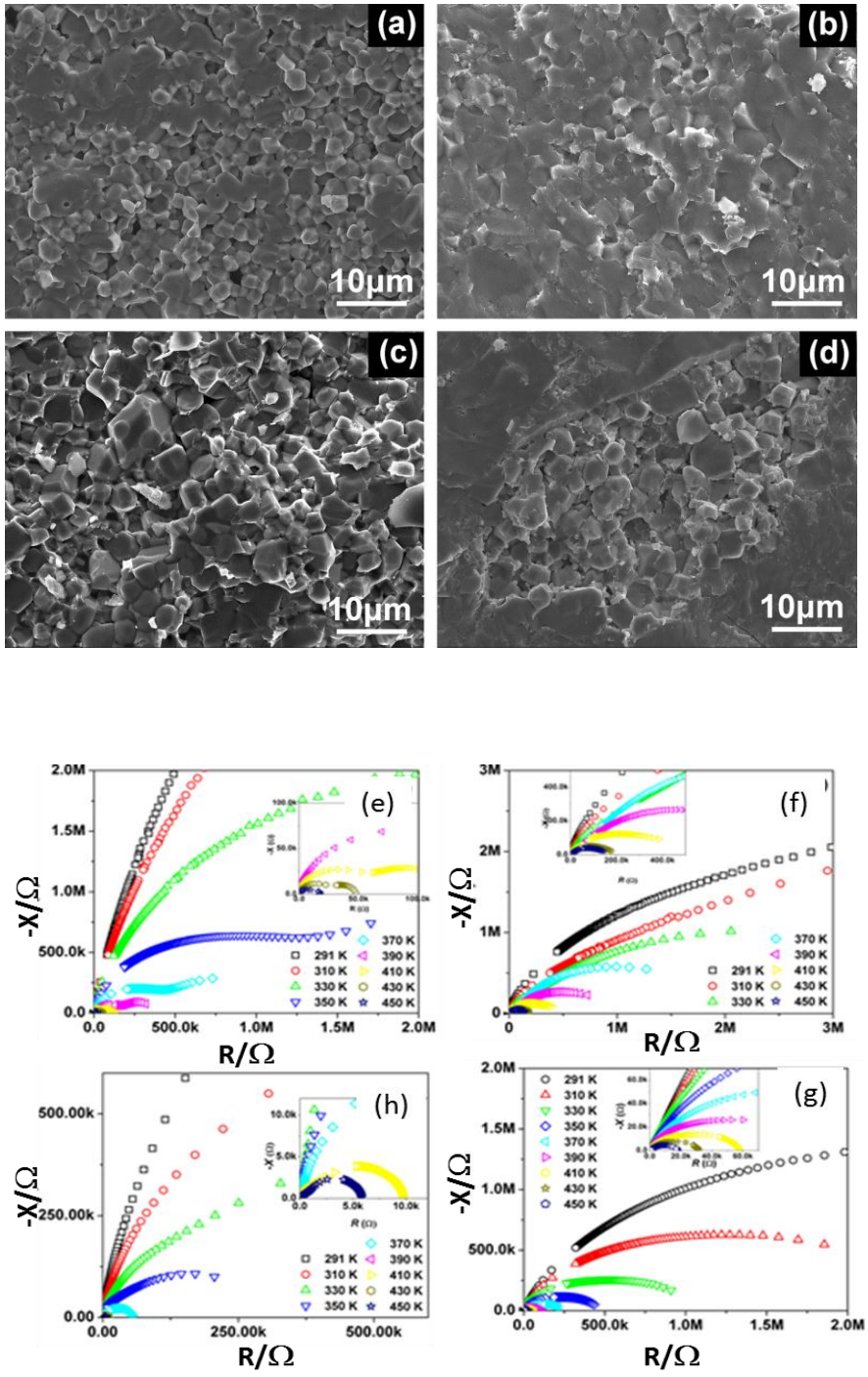

Figure I-22 : Fracture view field-emission scanning electron microscopy micrographs of (a) O2-CCTO, (b) O2-TBT-LN2, (c) LV-CCTO and (d) LV-TBT-LN2, Complex impedance spectra of CCTO ceramics in the frequency range of 20 Hz–3 MHz at various high temperatures: (e) O2-CCTO, (f) O2-TBT-LN2, (g) LV-CCTO and (h) LV-TBT-LN2. Reprinted with permission from (Xu et al.). Copyright 2018 Elsevier [52]

The samples sintered in vacuum show a little larger grain size of ~10µm than the others, whereas the oxygen sintered samples have more uniform and much finer grain size of about 3–5µm. Gain boundaries tend to become blurred after thermobaric treatment (TBT).

Figure I-23 (e,f,g,h) shows an example of the impedance study done on the ceramics obtained by TBT.

The authors concluded that the grain boundary relaxation is responsible for the abnormal dielectric behaviors of TBT CCTO ceramics. It is affected by the sintering condition and especially TBT processing.

Mao *et al.* [53] prepared the Calcium copper titanium oxide (CCTO) ceramics using the following procedure: Ceramics were quenched in air and liquid nitrogen separately after being subjected to sintering in low vacuum and thermobaric treatment (TBT) at 9 GPa and 1000 °C for 10 min. The microstructures of the obtained ceramics are shown in Figure I-23:

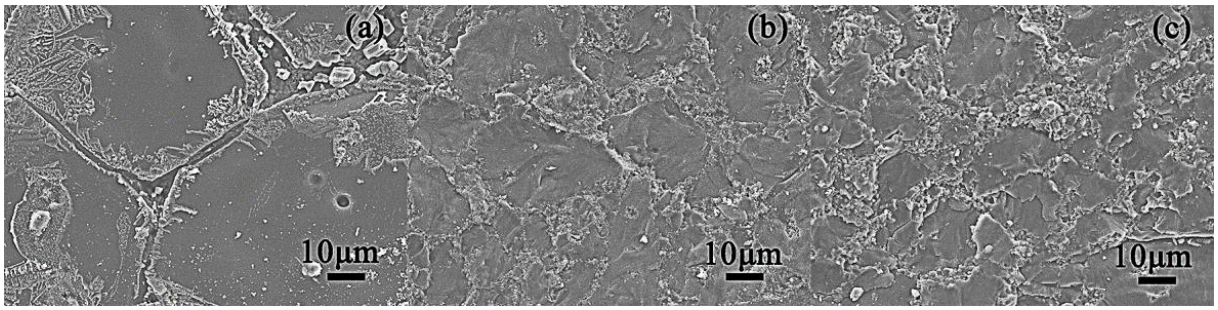

Figure I-23 : FEG-SEM cross-section images of (a) CCTO, (b) CCTO-TBT-LN2 and (c) CCTO-TBT-Air ceramics. Reprinted with permission from (Mao et al.). Copyright 2018 Elsevier [53]

The authors observed that after TBT and quenching the grain size decreases tremendously and the grain boundary becomes fuzzy. From impedance study, the authors concluded that the dielectric relaxation of CCTO should be originated with the grain boundary that can be apparently affected by the extreme conditions of TBT and quenching.

It is clear from this section that using different sintering method lead to different microstructures and different dielectric properties as shown in Table I-2. Despite the long duration and the high energy used for conventional sintering, this method gives best results of

dielectric properties comparing with others, especially for dielectric loss. After reporting the manufacturing methods of CCTO; next section will discuss the insertion of one or two elements into the crystalline lattice in order to investigate their effects on dielectric properties.

Table I-2 : Resuming the sintering method, different temperature and duration used and their influence on permittivity (ε') and dielectric loss (tanδ)

Sintering method	Precursors	Temperature	ε'	tanδ	References
Conventional Sintering (CS)	$CaCO_3$, TiO_2, CuO	1100°C/12h	$\sim 10^4$	-	**[38]**
Microwave Sintering	$Ca(NO_3)_2.4H_2O$, $Cu(NO_3)_2.3H_2O$, $C_{16}H_{36}O_4Ti$	950°C (2.54GHz,1.25KW)	3.14×10^3	0.161	**[42]**
Spark Plasma Sintering	$CaCO_3$, TiO_2, CuO	900°C/5min	10^5	-	**[46]**
Thermobaric Treatment (TBT)	$CaCO_3$, TiO_2, CuO	CS: 1100°C/24h TBT:1000°C/10m in (9GPa)	10^3	~ 10	**[50]**

I.4 Doping of CCTO

The first part of this review has shown that copper calcium titanate is a material of choice for the fabrication of ceramic capacitors because it has an extremely high dielectric constant. The doping of this material by different types of ions can change its electrical properties (relative permittivity, losses, Curie temperature) and lead to other uses. The copper calcium titanate may allow the partial exchange of one, two or three cations by other cations of the same or different valences. It is necessary that the size, charge, and mass of the surrogate ions be compatible with the host site. Doping element or dopant is like an impurity inserted into the element in low concentration to alter some electrical or optical properties, in crystalline materials. These dopants enter into the crystal lattice and take a place of a basic element. Many studies have been performed on the doping of CCTO by different elements and most recently the co-doping of CCTO by two different elements at the same time. This section is divided into two parts, the first one treated the one element doping CCTO and the second part treated the

two elements doping.

I.4.1 Doping of CCTO by one element:

Doping is crucial for determining physical properties and applications for various materials especially semiconductors. Fundamentally, a good dopant should achieve an ideal solubility in its host material and should exhibit a shallow defect level. However, there exist some fundamental doping bottlenecks, which strongly affect the device performance.

In order to enhance dielectric properties, doping CCTO was one of the investigations; it is an insertion of an atom into the structure lattice. Lee *et al.* [54] studied the effect of silver doping on the sintering temperature of CCTO. Ag dopant was added to $CaCu_3Ti_4O_{12}$ powders to reduce the sintering temperature in order to lower the fabrication costs. SEM figures of ceramics obtained from Ag-doped CCTO sintered at different temperatures are presented in Figure I-24.

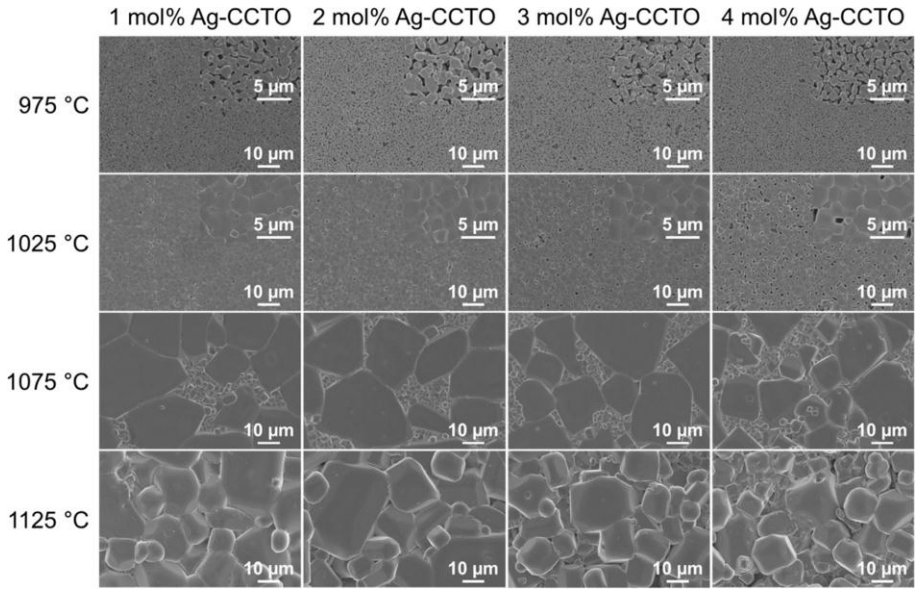

Figure I-24 : Surface morphologies of 1–4 mol% Ag-doped $CaCu_3Ti_4O_{12}$ ceramics sintered from 975 to 1125 °C for 12 h. Reprinted with permission from (Lee et al.). Copyright 2017 Elsevier [54]

The SEM results indicate that a higher sintering temperature contributes to grain growth and densification, except for the Ag-doped CCTO ceramic specimens sintered at 1125 °C. Ag is believed to behave as a liquid-phase sintering aid. The authors found that the sintering temperature needed for obtaining highly densified ceramics was decreased from 1125°C to

1075°C. The relative permittivity of the 2% Ag ceramic increased compared to the undoped CCTO ceramic.

The dependence of current density (J) as the function of the electric field (E) is investigated (Figure I-25). They conclude that the leakage of current density increases while doping with Ag atoms (sintered at 1075°C). At 100 mV, the current density is 1.63 and 0.17 mA/cm^2 for 2% Ag dopant and undoped CCTO respectively.

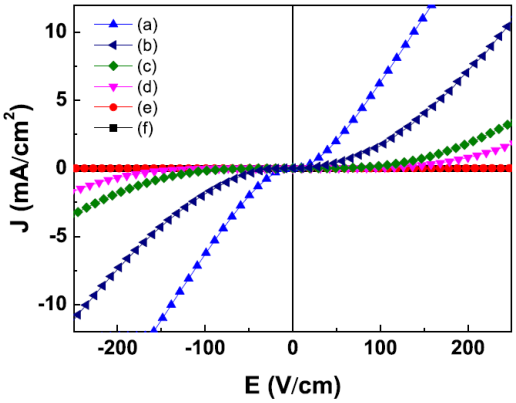

Figure I-25: Current density against electric field of (a) 2 mol% Ag-doped $CaCu_3Ti_4O_{12}$ based on nanoparticles sintered at 1075 °C, (b) 2 mol % Ag-doped $CaCu_3Ti_4O_{12}$ sintered at 1075 °C, (c) undoped $CaCu_3Ti_4O_{12}$ sintered at 1125 °C, (d) 2 mol% Ag-doped $CaCu_3Ti_4O_{12}$ sintered at 1125 °C, (e) 2 mol% Ag-doped $CaCu_3Ti_4O_{12}$ sintered at 1025 °C, and (f) 2 mol% Ag-doped $CaCu_3Ti_4O_{12}$ sintered at 975 °C. Reprinted with permission from (Lee et al.). Copyright 2017 Elsevier [54]

Xu *et al.* [55] studied the effect of bismuth doping on the electrical properties of CCTO. $Ca_{1-3x/2}Bi_xCu_3Ti_4O_{12}$ (x = 0:0, 0.1, 0.2 and 0.3; BCCTO) ceramics were prepared by traditional solid-state sintering method. They observed a drastic grain size reduction with bismuth doping.

The doping of CCTO by Cobalt was studied by Mu *et al.* [56], Kafi *et al.* [57] and Wang *et al.* [58].

Mu *et al.* [56] prepared $CaCu_3Ti_{1-x}Co_xO_{12}$ (x = 0, 0.2, 0.4) ceramics by a conventional solid state reaction. Both X-ray diffraction and energy dispersive X-ray spectroscopy confirmed the presence of Cu and Co rich phase at grain boundaries of *Co*-doped ceramics (Figure I-26)

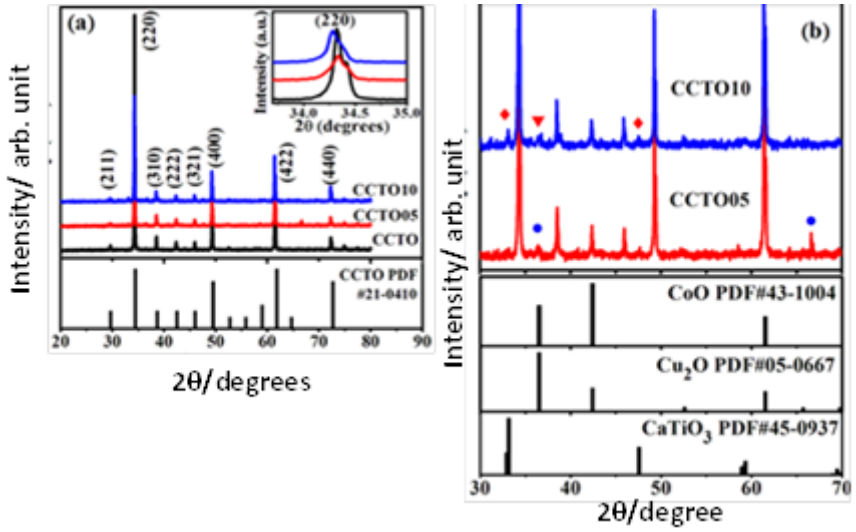

Figure I-26 : X-ray powder diffraction patterns of (a) CCTO, CCTO05, and CCTO10 ceramics, the top right inset is an expanded view of (220) peaks; (b) expanded XRPD patterns at 2h¼30–70for CCTO05 and CCTO10 ceramics. Reprinted from (Mu et al.) with the permission of AIP publishing [56]

The authors explained that the cobalt can exist in (II) and (III) oxidation states, and can occupy Cu^{2+} and Ti^{4+}, depending on its oxidation state. As compared with Ti^{4+} (r =0.61 A°), Cu^{2+} (r = 0.57 A°), and Co^{3+} (r = 0.55A°), Co^{2+} has larger ionic radius (r = 0.75A ° for high spin state). According to the XRD patterns, the authors explained that the Cobalt is replacing the titanium.

Scanning electron microscopy micrographs of Co-doped samples showed a striking change from regular polyhedral particle type in pure $CaCu_3Ti_4O_{12}$ (CCTO) to sheet-like grains with certain growth orientation. The authors showed that the dielectric constant value was slightly changed by 5% and 10% Co doping concentration, whereas the second relaxation process was clearly separated in low frequency region at room temperature. A multi-relaxation mechanism was proposed to be the origin of the colossal dielectric constant.

Kafi *et al.* [57] prepared $CaCu_{3-x}Co_xTi_4O_{12}$ (CCCTO, x = 0, 0.2, 0.4 and 0.6) ceramics using a semi wet method. Their results showed that the dielectric constants of the as-prepared samples in the frequency range of 50 Hz-200 kHz, at room temperature, are reasonably high ($1.7 \times 10^4 \leq \varepsilon \leq 6 \times 10^4$). It was also found out that the dielectric loss ($\tan\delta$) of the prepared samples decreased by increasing the cobalt concentration at low and middle frequencies.

Wang *et al.* [58] showed that the doping of CCTO by 5% of Co improved the dielectric

properties and gave dielectric constant ε' ≈7.4 × 10^4 and dielectric loss tanδ ≈ 0.034 at room temperature and 1 KHz. The authors explained that the Cobalt replaces the Copper ion in the CCTO structure (Figure I-27)

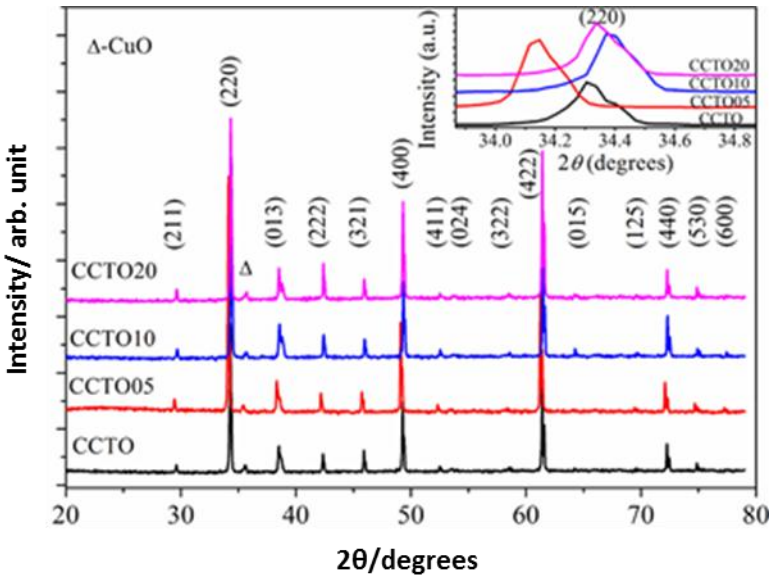

Figure I-27 : XRD patterns of the pure and various Co-doped CCTO ceramics. Inset shows the enlarged view of the diffraction strongest (220) peak. Reprinted with permission from (Wang et al.) by Oxford University Press and Copyright Clearance Center 2018 [58]

The main XRD peaks correspond to a body-centred cubic CCTO structure with space group Im3 indexed. The secondary-phase peak at ~35.5° ascribed to CuO phase is observed in all tested samples, indicating the precipitation of the liquid CuO-rich phase at GBs. Furthermore, because the absence of CuO phase in CCTO ceramic with 5% Cu deficient is reported elsewhere, the presence of CuO phase in Co-doped CCTO samples preliminarily confirms that the doped Co initially prefers to substitute at the Cu site.

Swatsitang *et al.* [59] prepared $CaCu_{3-x}Cr_xTi_4O_{12}$ (x=0-0.2) via a polymer pyrolysis route. Best values for the relative permittivity and the loss tangent were obtained for the composition x = 0.08 with a dielectric constant value of 7156 and a low dielectric loss value of 0.092. These values are due to the increase in the grain boundaries resistance caused by the reduction of oxygen vacancies.

The influence of Erbium doping on the electrical behavior of $CaCu_3Ti_4O_{12}$ was studied by Sakthisabarimoorthi *et al.* [60]. They prepared pure and Er doped CCTO ceramics by simple sol-gel method. The XRD pattern obtained confirmed that the addition of Er did not affect the crystallinity of CCTO. High dielectric constant (ε_r=26.749) was found for Er doped $CaCu_3Ti_4O_{12}$ ceramics.

Li *et al.* [61] reported the effect of Europium (Eu) on the dielectric properties of $CaCu_3Ti_4O_{12}$. The experimental results show that the doping of Eu on a calcium (Ca) site improves the dielectric loss and decreases the dielectric constant of CCTO. The authors explained this result because of the lack of the oxygen vacancies in the samples.

An enhancement of grain growth is produced with F^- doping CCTO studied by Jumpatam *et al.* [62] as shown in Figure I-28.

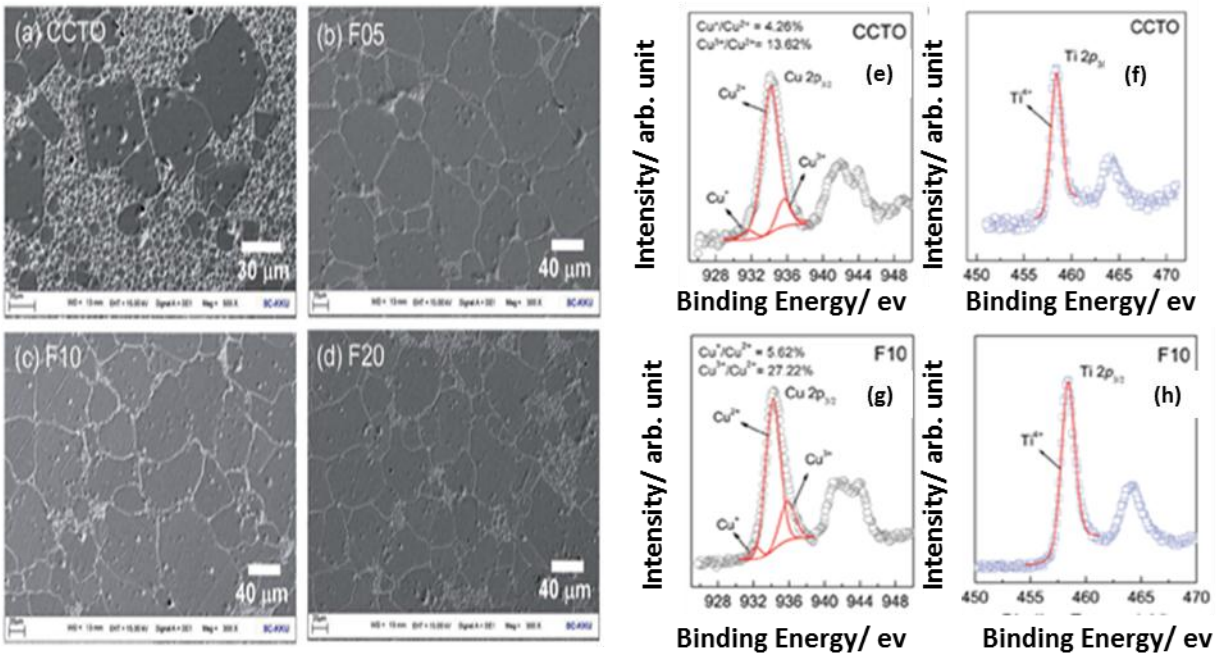

Figure I-28 : SEM images of polished surfaces of (a) CCTO, (b) F05, (c) F10 and (d) F20 samples, XPS spectra of CCTO and F10 samples: (e, f) Ti 2p regions and (g, h) Cu 2p regions. Reprinted from ref [62]. Copyright © 2017 Royal Society of chemistry.

The increase in the dielectric permittivity (98396 for F20) and the decrease of dielectric loss for a factor of 5 (tan=0.1) is attributed to the effect of F^- that enhances the Schottky barrier height

at grain boundaries, in addition to the increase in Ti^{3+} and Cu^{+} concentrations (Figure I-28 e,f,g,h) as a result of charge compensation leading to a large charge polarization space at grain boundaries.

Late *et al.* [63] have investigated the effect of Hf doping on the structural, dielectric and optical properties of CCTO. The authors considered that Hf substitute to Ti sites. From the XRD patterns, they deduced that when the Hf doping exceeds 2% some amount of HfO_2 remains un-reacted in the sample. Furthermore, with in Hf doping both lattice parameters and structural coherency of CCTHO samples increases due to the higher ionic radius of Hf^{4+} compared to the ionic radius of Ti^{4+}. The authors studied the electrical properties using impedance spectroscopy; the obtained results are shown in Figure I-29.

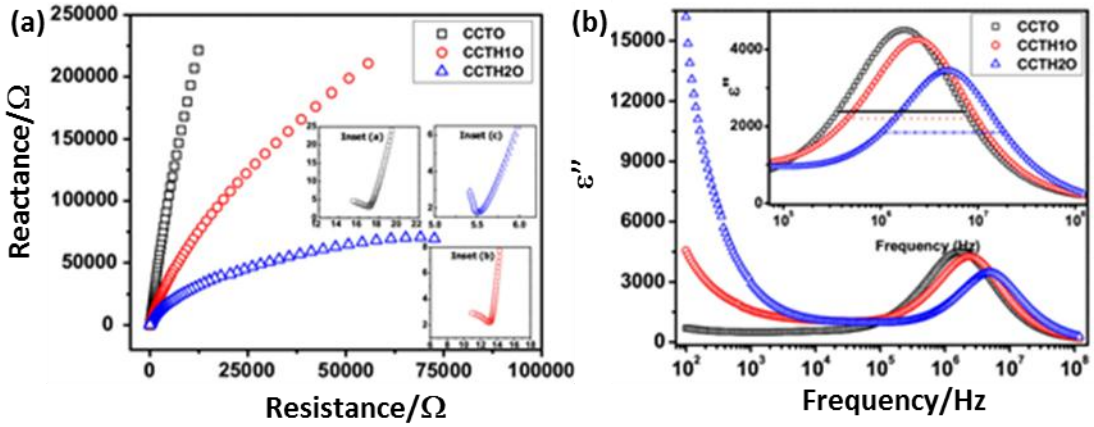

Figure I-29 : a) Complex impedance plot for all samples. Inset a is showing magnified view of semicircular arcs corresponding to grain contributions (i.e. corresponding to highest probing frequencies) for CCTO, Inset b for CCTH1O and Inset c for CCTH2O. b) Variation of imaginary part of dielectric constant (ε'') as a function of frequency for all samples. Reprinted by permission from (Nature/springer/Journal of Materials science, Materials in Electronics) (Late et al.)- doi.org/10.1007/s10854-016-4505-6 Copyright (2016) [63]

They observed that with Hf doping overall grain boundary resistance decreases compared to that of pure CCTO compound. Further, Hf substitution increases dispersion of resistances between grain and the grain boundary. The authors concluded that the shift of relaxation frequency to higher values may be recognized to the decrease in the grain, grain boundary resistance and mean relaxation time. The improved dielectric properties with Hf doping may be

credited to the improved structural coherency, increased grain size and optical band gap of these samples. The results agree well with the IBLC model.

The influences of K^+ doping and sintering conditions on the microstructures and dielectric properties were analyzed and discussed by Wang *et al.* [64].The authors observed that the grain size increases with the increasing sintering temperature and K^+ doping concentration.

The authors obtained giant ε′ of ~2.3×10^4 as well as relatively low tanδ of ~0.039 that can be observed in $Ca_{0.99}K_{0.02}Cu_3Ti_4O_{12}$ ceramics sintered at 1060 °C for 8 h measured at RT and 1 kHz.

Chen *et al.* [65], Srivastava *et al.* [66] and Huang *et al.* [67] studied the effect of Lanthanum doping on CCTO. Chen *et al.* [65] employed the rare earth element La to replace Ca site and studied the La doping effects on the microstructure and the non-Ohmic properties of La-doped CCTO. From microscopic observations, the authors deduced that the low content of La ions ($x \leq 0.015$) doping hardly affects the crystal structure and the grain size. However, the significant change in microstructure is clearly revealed as $x \geq 0.02$. With the increase of La content, the grain size is remarkably reduced to about 5 μm and the grain boundaries are blurred to obscurity.

The authors also concluded that the nonlinear behavior of CCTO system is not only influenced by the grain size, but also controlled by the local electron density which would affect the chemical environment of defects.

Srivastava *et al.* [66] prepared a 1% La doped CCTO via semi wet route. La doped CCTO showed a slight increase in the value of the dielectric constant compared to undoped CCTO (5000 for undoped CCTO and 7000 for La doped CCTO) at room temperature. Permittivity and dielectric loss increase with increasing temperature for both undoped and doped CCTO. The effects of La^{3+} doped in calcium copper titanate (CCTO) at Ca^{2+} site and Cu^{2+} site were examined by Huang *et al.* [67]. The doped compositions, $La_{0.1}Ca_{0.85}Cu_3Ti_4O_{12}$ (LCCTO) ceramics and $CaLa_{0.1}Cu_{2.85}Ti_4O_{12}$ (CLCTO) ceramics were prepared by the solid-state method. Ceramics were prepared under sintering temperatures ranging from 1040 to 1100°C. The microstructure of LCCTO ceramics presented a bimodal grain growth model (Figure I-30).

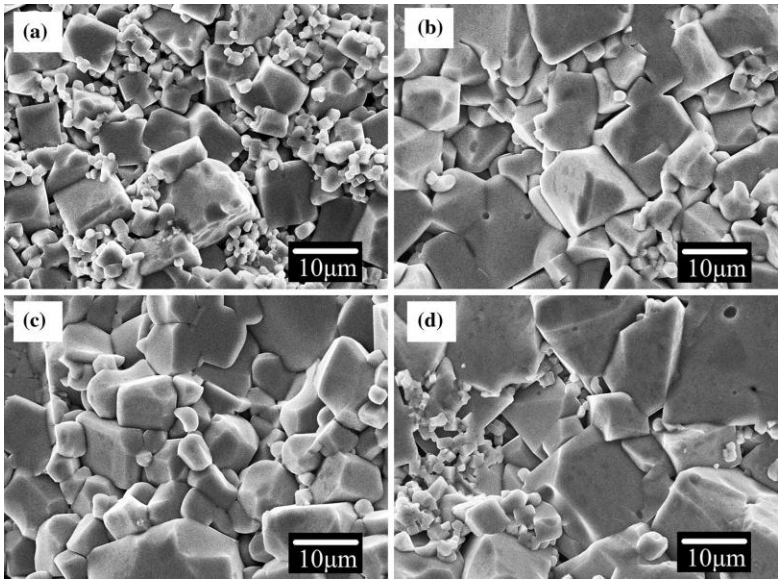

Figure I-30 : SEM images of the surface morphologies of LCCTO sintered at a 1040 ℃, b 1060 ℃, c 1080 ℃, d 1100 ℃ for 10 h. Reprinted by permission from (Nature/springer/Journal of Materials science, Materials in Electronics) (Huang et al.)- doi.org/10.1007/s10854-016-5244-4 Copyright (2016 [67].

It was found that La^{3+} doped at Ca^{2+} site achieved lower sintering temperatures than that doped at Cu^{2+} site in CCTO ceramics. The dielectric loss (tan δ) of LCCTO ceramics was about 0.05 at 40 kHz when the sample was sintered at 1080 °C. Dielectric constant (ε') of LCCTO ceramics was about 3.2×10^4 when the sample was sintered at 1100 °C, which was larger than CLCTO ceramics examined under the same process condition with different sintering temperature.

Mg doped CCTO was studied by Sun *et al.* [68] and Swatsitang *et al.* [69]. Sun *et al.* [68] prepared $CaCu_{3-x}Mg_xTi_4O_{12}$ ceramics with high ε' and very low tanδ by the sol–gel method. Very high values of relative permittivity and low values for dielectric loss were obtained for Mg doped CCTO ceramics : ε′ of 2.52×10^4 and tanδ of ~0.017 at 1 kHz and RT have been achieved for ceramics sintered at 1080°C for 8 h in the air atmosphere.

Swatsitang *et al.* [69] prepared the nominal $CaCu_{3-x}Mg_xTi_{4.2}O_{12}$ (0.00, 0.05 and 0.10) ceramics by sintering pellets of their precursor powders obtained by a polymer pyrolysis solution method at 1100 °C for different sintering times of 8 and 12 h. Very low loss tangent (tanδ) < 0.009–0.014 and giant dielectric constant (ε') ~ 1.1×10^4–1.8×10^4 with excellent temperature coefficient ($\Delta\varepsilon'$) less than ± 15% in a temperature range of − 60 to 210 °C were achieved. It was found that tanδ values decreased with increasing Mg^{2+} dopants due to the increase of grain

boundary resistance (R_{gb}) caused by the very high density of grain, resulting from the substitution of small ionic radius Mg^{2+}dopants in the structure.

Wang *et al.* [70] accomplished a comparative study on the colossal dielectric constant behavior of the pure and Mn-doped $CaCu_3Ti_4O_{12}$ ceramics over a wide range temperature aiming at deeply understanding the role of the Mn doping effects on the physical origin of the colossal dielectric constant behavior. The nominally pure and doped CCTO ceramics by substituting 2% and 4 % Mn at Ti sites (abbreviated as CCTO, CCTMO-2, and CCTMO-4, respectively) were prepared using the conventional solid-state reaction method. The resultant materials were sintered at 1100°C for 10 h. XRD patterns showed a decrease in the lattice parameters and SEM micrographs showed that Mn doping is beneficial for grain growth (Figure I-31).

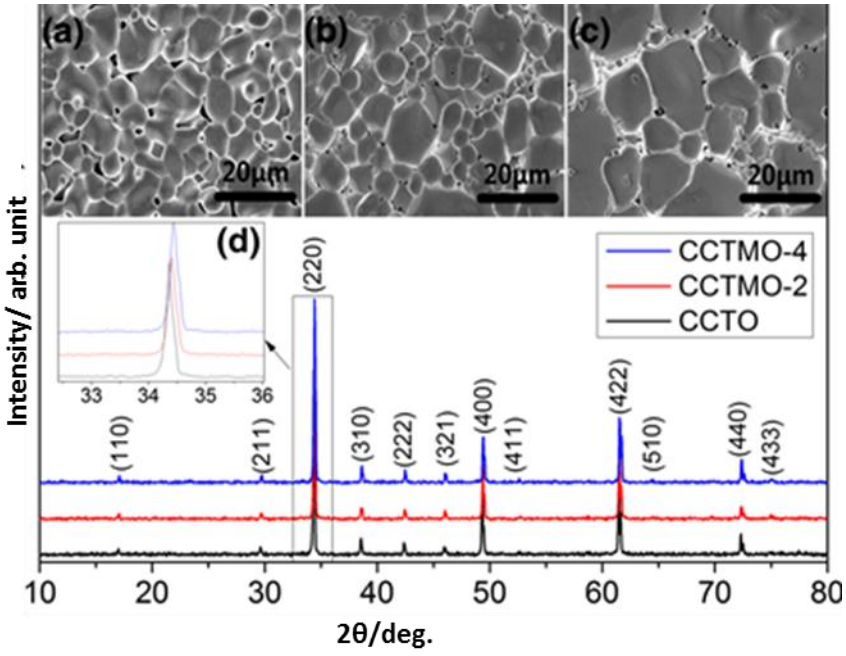

Figure I-31 : XRD patens of CCTO, CCTMO-2, and CCTMO-4 ceramics. Inset shows the SEM micrographs of (a) CCTO, (b) CCTMO-2, (c) CCTMO-4, and (d) the enlarged view of the (220) reflection peaks. Reprinted by permission from (Nature/springer/Journal of Electroceramics) (Wang et al.) doi.org/10.1007/s10832-016-0024-3 Copyright (2016) [70].

Concerning the dielectric studies, the authors concluded that Mn doping is harmful for the CDC behavior and they attributed this to the decrease in the ratios of Ti^{3+}/Ti^{4+} and Cu^{3+}/Cu^{2+} and the concentration of oxygen vacancies. Their results confirm the multi-relaxation mechanism for the CDC behavior in CCTO and the CDC behavior is mainly dominated by Maxwell-Wagner contribution.

The perovskite-type $CaCu_3Ti_4O_{12}$ (CCTO) doped by molybdenum (Mo) and its dielectric properties and the temperature dependence of Electron Spin Resonance (ESR) has been investigated by Kouassi *et al.* [71] Substitution on Ti-site by Mo helps to increase the grain size of samples and therefore increase the dielectric constant according to the IBLC theory. There is no great difference between the ESR spectra of pure CCTO and CCTO doped by Molybdenum as a function of temperature (Figure I-32).

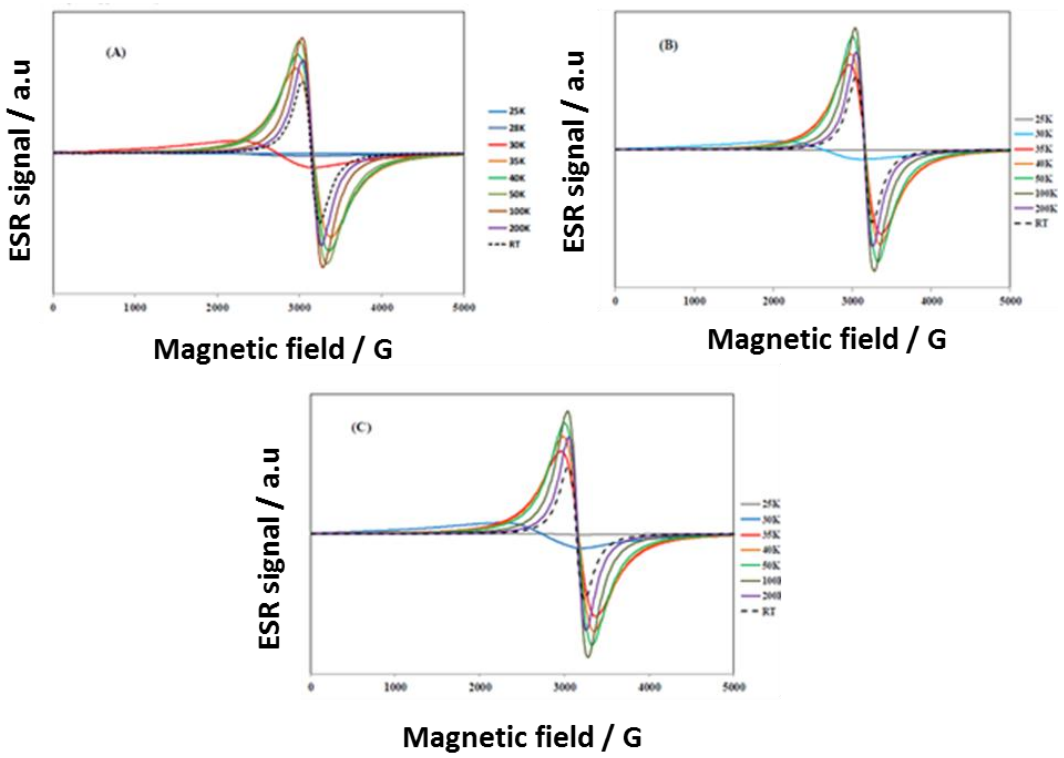

Figure I-32 : Temperature dependence of ESR for pellets sintered at 1050°C of M0 (a), M0.05 (b) and M0.1 (c). Reprinted from (Kouassi et al.). Copyright © 2017Creative commons [71]

Nickel doped CCTO were prepared and studied by Senda *et al.* [72], Wang *et al.* [73], Boonlakhorn *et al.* [74] and Sun *et al.* [9].

In the aim of increasing the relative permittivity and decreasing the dielectric loss of CCTO, Sun *et al.* [9] prepared $CaCu_{3-x}Ni_xTi_4O_{12}$ (x = 0, 0.05, 0.1, 0.2) powders by the sol-gel method. The pellets were sintered at 1000 - 1060°C for 8h. A very low tanδ value ~0.025 was found at the $CaCu_{2.95}Ni_{0.05}Ti_4O_{12}$ ceramic sintered at 1060 °C for 8h with ε'~4.2×104 at about 1 kHz. Senda *et al.* [72] studied the influence of Ni doping on $CaCu_{3-x}Ni_xTi_4O_{12}$ (x=0,0.05,0.075,0.1,0.2,0.3) ceramics sintered at 1100°C for 6, 12 and 24h in air. After sintering for 12h, they obtained for $x \leq 0.2$ the pure phase and for x>0.2 $CaTiO_3$, TiO_2 and CuO as a secondary phase. The highest dielectric permittivity was recorded to the composition x = 0.2 (10^5) with a slight decrease in loss tangent. Doping element enhance the cubic grain growth as shown in (Figure I-33). Dielectric properties of all composition showed a dependence of frequency range. At high frequency (1 kHz) the permittivity and loss tangent decrease.

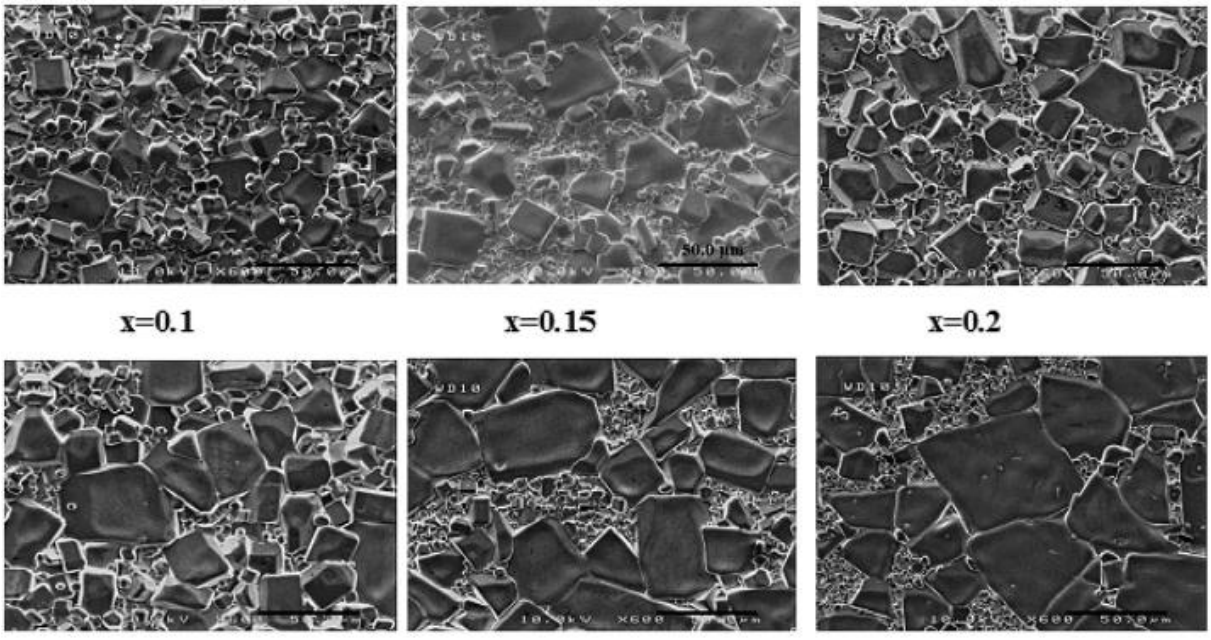

Figure I-33 : SEM images of surface morphologies of pure and Ni doped samples sintered at 1100°C for 12 h. Reprinted from (Senda et al.). Copyright 2017 Elsevier[72]

Wang *et al.* [73] reported good dielectric properties, a dielectric permittivity of ~1.5×10^5 and a low loss tangent of ~0.051, were obtained by optimization of dopant levels ($CaCu_{2.80}Ni_{0.20}Ti_4O_{12}$) and sintering conditions (1100 °C for 3 h). Boonlakhorn *et al.* [74] found that doping CCTO with Ni^{2+} caused a great increase in its dielectric permittivity, by a factor of ~3.

Li *et al.* [75] fabricated $CaCu_{3-x}Ru_xTi_4O_{12}$ (x = 0, 0.03, 0.05 and 0.07) electronic ceramics. They noticed an inhibition of grain growth after doping with Ru. In general, during the sintering treatment, a liquid phase of Cu is formed at grain boundaries and ions diffuse through it to form a large grain. The authors performed EDX analysis on the grain boundaries, and they found that for pure CCTO, Ti, Ca, O and Cu ions are present in excess in the grain boundary region, while for Ru-doped CCTO, Ti and Ca atoms were the ones present in excess. It is well known that TiO_2 and CaO have high melting point and inhibit the formation of a liquid phase during the sintering process.

When doped with proper amount of Ru (x = 0.05), CCTO displays low dielectric loss (tan δ < 0.05), while simultaneously maintains a decent dielectric constant (ε > 80).

Cortes *et al.* [76] focused on CCTO doped with Sn^{4+}, $Ca_2Cu_2Ti_{4-x}Sn_xO_{12}$ ($0.0 < x < 4.0$). They reported that the materials with low Sn^{4+} contents (x = 0.1 and 0.2) presented giant dielectric permittivity values, 166381 and 140845 respectively. They associated this to insulating grain boundaries with activation energies of 0.58 eV and 0.30 eV respectively, as well as conductive grains with activation energies of 0.04 eV and 0.08 eV.

Sahu *et al.* [77] investigated the effect of doping type on conduction and dielectric phenomena in 15% Sr doped CCTO. The Maxwell–Wagner model and interfacial polarization explains the higher dielectric constant of the material at higher temperatures.

Amhil *et al.* [78] recently prepared 0.05 Sr doped CCTO via a semi wet chemical route. Microstructural study showed that Sr concentration promotes grain growth in CSCTO ceramics. The dielectric properties were enhanced by the doping.

Tungsten doped CCTO was investigated by Singh *et al.* [79] $CaCu_3Ti_{4-x}W_xO_{12}$ (x = 0.01, 0.03, and 0.05) ceramics were prepared by flame synthesis method. The dielectric property measurement

shows that the relative permittivity (ε_r)and dielectric loss (tanδ) values in the measured frequency range at 328 K for W-doped ceramics were increased with increasing W content.

Kouassi *et al.* [80] again studied the effect of vanadium doping on the microstructure and dielectric properties of CCTO. They reported that the vanadium doping of CCTO system results in an increase of grain size, the grains being surrounded by melted-like grain boundaries. They added that in doped samples, above 1 kHz, a relaxation appears which is evidenced by a drop of real part of permittivity and a peak of its imaginary part. This relaxation phenomenon is very significant at relatively low doping rates and then decreases again as vanadium content increases.

Tang *et al.* [81] focused on the enhancement of dielectric properties of Y^{3+} donor doped CCTO. Grain growth in $Ca_{1-x}Y_xCu_3Ti_4O_{12}$ was suppressed with increasing the concentration of dopant element.

The permittivity increases (8.03×10^4) for x = 0.05 at 1 kHz and loss tangent decrease to 0.05 for x=0.03 in a frequency range between 1.5 kHz and 60 kHz. Figure I-34 presents the relationship between dielectric constant and grain resistance in CYCTO ceramics in order to explain the dependence of increasing the dielectric constant and the grain growth.

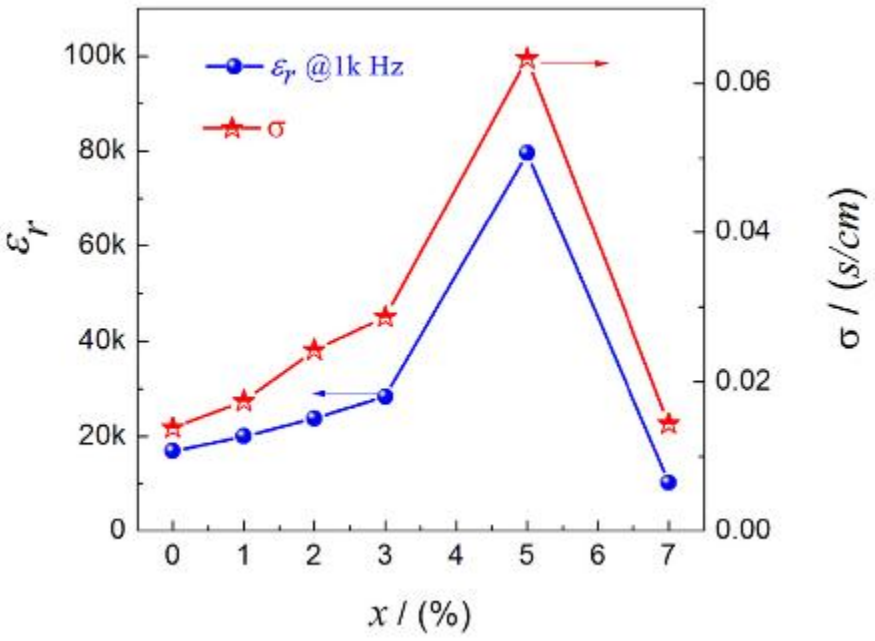

Figure I-34 : Relationship of dielectric constant (1 kHz) and Grain resistance in $Ca_{1-x}Y_xCu_3Ti_4O_{12}$ ceramics. Reprinted from (Tang et al.). Copyright 2018 Elsevier [81]

Xue *et al.* [82] studied the doping of CCCTO by different elements such as Y, Ta and Zr. They found that the grain growth changed with different doping element (Figure I-35) even the dielectric properties are different. For Y^{3+} doped CCTO, the dielectric constant increases and nonlinear property decreases while doping with La^{+} leads to inverse results. Doping by Zr^{2+} leads to the same results given for pure CCTO.

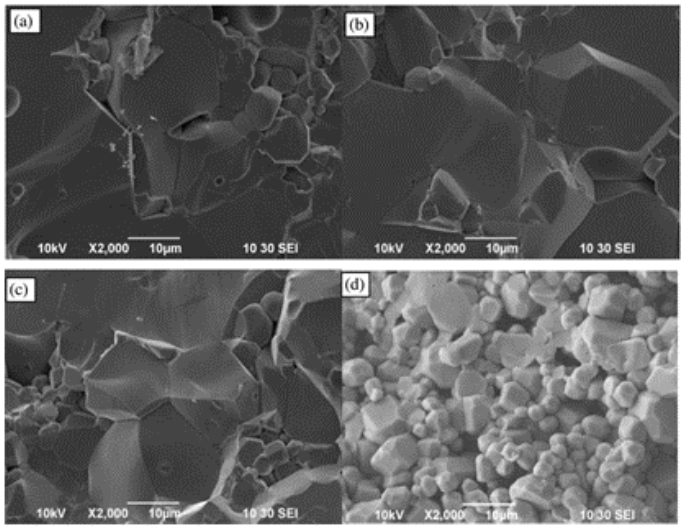

Figure I-35: SEM images of fracture morphologies for (a) pure CCTO, (b) Y-doped CCTO, (c) Zr-doped CCTO, (d) Ta-doped CCTO. Reprinted from (Xue et al.). Copyright 2016 Elsevier [82]

Gonzales *et al.* [83] presented the results of Zr oxide doping of a $CaCu_3Ti_4O_{12}$ (CCTO) ceramic prepared by a solid-state reaction. Zr-doping controls the grain size growth, leading to a reduction of the grain size. For both dopant concentrations of 0.5 and 1 wt.% , all of the samples exhibited lower dielectric loss and a smaller dielectric constant than those of undoped CCTO. The sample doped with 0.5% of the non-stoichiometric ZrO exhibits a dielectric constant over 3200 and a dissipation factor of 0.02 at 1 kHz.

Xu *et al.* [84] reported a very high dielectric permittivity value of 7591 and a very low tanδ value of 0.023 at 1 kHz for $CaCu_3Ti_{3.8}Zr_{0.2}O_{12}$.

All obtained results are resumed in Table I-**3**. Based on these results, F^- dopant element exhibits the highest dielectric properties where ε=81,306 and tanδ=0.07. These can be caused due to the increase of grain boundaries resistivity and decrease of grains resistivity. Improvement of dielectric

properties can be explained by the presence of free charge carrier concentration inside the semiconducting grains and Schottky barrier height at the grain boundaries respectively. A stronger intensity of interfacial polarization (Maxwell-Wagner polarization) is due to high charges concentration accumulated at the interface between grains and grain boundaries under an applied electric field [62].

Table I-3 : dopant element, concentration, permittivity, loss tangent (tanδ) and grain size of doped CCTO ceramic

Dopant	Concentration	ε_r (10^3Hz)	tanδ (10^3-10^6)	Grain size	References
Ni	x=0.2	$>10^5$	10^{-1}	50 μm	[85]
Cr	x=0.08	7,156	0.092	60.3 μm	[59]
Y	x=0.5	$8.03*10^4$	~ 0.01	2-4 μm	[81]
Co	5%	$7.4*10^4$	0.034	48.5 μm	[58]
Er	x=0.1	26,749	-	200 nm	[60]
Sr	x=0.2	$>10^4$	~ 0.3	~20 μm	[86]
Co	x=0.6	6×10^4	0.15	75 μm	[57]
SnO_2	2mol%	~21,250	0.04	3-5 μm	[87]
Mg	x=0.1	$\sim2.52\times10^4$	0.017	~2-20 μm	[68]
Y	x=0.05	~31,125	~ 0.14	~55 μm	[82]
Zr	x=0.05	~22,260	~ 0.02	~32 μm	[82]
Ta	x=0.05	~17,500	~ 0.01	~4μm	[82]
Mg	x=0.05	$\sim3\times10^4$	~ 0.013	~45.65 μm	[88]
Y	x=0.05	$\sim 8\times10^3$	~ 0.013	~2.52 μm	[88]
Sn	x=0.2	140,845	0.71	4.17 μm	[76]
Nb	x=0.025	4.8×10^5	0.566	~20.2 μm	[89]
Al	x=0.025	2.1×10^5	0.129	~129.6 μm	[89]
Y	x=0.02	32,000	0.05	1-2 μm	[90]
Sr	x=0.4	$\sim2\times10^4$	~1.0	2.7 μm	[91]
La	x=0.15	$\sim5\times10^3$	~0.1	3.9 μm	[91]
Zr	x=0.5	3,200	0.02	3.6 μm	[83]
F^-	x=0.1	81,306	0.077	~40-100 μm	[62]
Ru	x=0.7	$\sim6.0\times10^3$	~0.4	2-4 μm	[75]
LiF	0.5%	34,994	0.68	2.1 μm	[92]
Mn	2%	3.0×10^3	-	7-9 μm	[70]
K	x=0.01	2.3×10^4	0.039	4.28 μm	[64]
Yb-6h	x=0.05	9,832	0.014	~2-6 μm	[93]
Yb-12h	x=0.05	16,033	0.015	20-50 μm	[93]

I.4.2 Co-doping of CCTO by two elements:

In general, co-doping can be efficient for increasing the dopant solubility, increasing the activation rate by lowering the ionization energy of acceptors and donors, and increasing the carrier mobility [94]. CCTO was largely doped with single elements but most of the heteroatomic substitutions that are employed to improve a dielectric property of the CCTO always worsen simultaneously another dielectric performance. This is the reason why many researchers are trying to perform co-doping on CCTO.

Boonlakhorn *et al.* [88] improved the dielectric properties of $CaCu_3Ti_4O_{12}$ by co-doping with Y^{3+} and Mg^{2+} to simultaneously control the geometric and intrinsic properties of grain boundaries (GB), respectively. The authors found that the substitution of these dopants strongly suppressed the grain growth while enhancing the resistivity of an individual GB, respectively. This led to a great decrease in the loss tangent ($\tan\delta \sim 0.013$).

The authors prepared $Ca_{0.925}Y_{0.05}Cu_{2.95}Mg_{0.05}Ti_4O_{12}$ (Y-Mg05) using a modified sol-gel method. The obtained compacted powders were sintered in air at 1070°C for 6h using heating and cooling rates of 5°C/min.The authors deduced that the resistance of the grain boundaries is increased by the addition of dopants.

The same authors doped CCTO by both Al^{3+} and Nb^{5+} [89]. They found that the substitution of (Al^{3+}, Nb^{5+}) co–dopants into TiO_6 octahedral sites of $CaCu_3Ti_4O_{12}$ ceramics, which were prepared by a solid state reaction method and sintered at 1090°C for 18 h, can cause a great reduction in a low–frequency loss tangent ($\tan\delta \approx 0.045–0.058$) compared to those of Al^{3+} or Nb^{5+} single–doped $CaCu_3Ti_4O_{12}$.

The authors deduced that the doping with Nb^{5+} reduces the grain size while doping with Al^{3+} results in a large increase in the mean grain size. Alternatively, the mean grain sizes of the co–doped NA025 and NA05 ceramics were between the mean grain sizes of the single–doped Al025 and Nb025 ceramics and not much different that of the un–doped CCTO ceramic. They concluded that the simultaneous substitution of both Al^{3+} and Nb^{5+} ions can balance the driving and restorative forces for grain boundary (GB) migration.

The ε' values of the single–doped Al025 and Nb025 ceramics are larger than those of the co–doped NA025 and NA05 ceramics. Nevertheless, ε' values of both co–doped ceramics are still too large (> 10^4). Interestingly, over the measured frequency range, the tanδ values of both co–doped ceramics are much lower than those of the single–doped ceramics as well as the un–doped CCTO ceramic.

The co-doping of CCTO by Al^{3+} and Nb^{5+} was also studied by Wen *et al.* [95] The authors concluded again a decrease in the dielectric loss of ceramics after codoping.

Boonlakhorn *et al.* [96] studied the dielectric properties of Sm and Zn codoped $CaCu_3Ti_4O_{12}$ ceramics. The values of the electrical permittivity and the loss tangent obtained for the different ceramics are shown in Table I-4.

The authors observed that the ε' and tan δ values of the Sm05, SmZn05 and SmZn10 ceramics were lower than that of the CCTO ceramic over the measured frequency range. It should be noted that the low-frequency tanδ value of the single-doped Sm05 ceramic was much higher than that of the un-doped CCTO ceramic, while simultaneous substitution of Sm and Zn dopants into CCTO ceramics caused a great decrease in tanδ over the measured frequency range.

Ren *et al.* [97] co-doped $CaCu_3Ti_4O_{12}$ by Al^{3+} and Bi^{3+} elements to improve the electrical properties and enhance the varistor property of CCTO. The authors observed that the grain size homogenization was enhanced with co-doping. Although the average grain size shows not much difference, the grain size distribution of co-doped sample is much more uniform with smaller variance. The authors reported an enhancement of dielectric properties and varistor properties for 1mol% doping concentration. An increase of dielectric permittivity and decrease of dielectric loss to 0.04 at low and medium frequencies could be attributed to an increase of activation energy of dc conductance at grains boundaries as well as improvement in grains boundaries resistivity.

Bai *et al.* [98] prepared the $CaCu_3$ $(Ti_{1-x}Fe_{x/2}Nb_{x/2})_4O_{12}$ (x = 0.00, 0.50, 0.53, 0.57, 0.60) ceramics through the solid state reaction method with the pre-synthesis of the monoclinic precursor $FeNbO_4$.

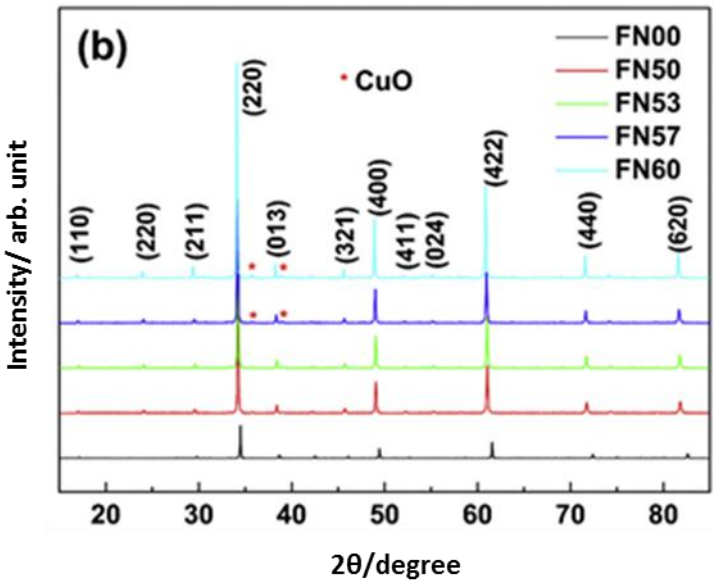

Figure I-36 : XRD patterns of $CaCu_3$ $(Ti_{1-x}Fe_{x/2}Nb_{x/2})_4O_{12}$ powders with different percentage of codoping. Reprinted from (Bai et al.). Copyright 2016 Elsevier [98]

From figure I-36, it has been noticed that the $CaCu_3$ $(Ti_{1-x}Fe_{x/2}Nb_{x/2})_4O_{12}$ powders kept single phase up to a codoping concentration of $(Fe_{1/2}Nb_{1/2})^{4+}$ complex ions as high as 60%. The dielectric frequency spectra of $CaCu_3$ $(Ti_{1-x}Fe_{x/2}Nb_{x/2})_4O_{12}$ ceramics reveals the existence of Debye-type relaxations in measurement frequency range.

The effect of the addition of La and Zn on the dielectric properties of CCTO was studied by Rani *et al.* [99].They prepared $Ca0_{.95}La_{0.05}Cu_{3-x}Zn_xTi_4O_{12}$ (x=0.01, 0.025, 0.05 & 0.10) by conventional solid state technique. The ceramics were sintered at 1080°C for 6 hours with 5°C/min rate of heating and cooling. The microstructure of the prepared ceramics was shown to be highly affected by the codoping. The grain size of the composition was decreased with the increase in Zn^{2+} concentration. The electrical studies showed that Zn^{2+} substitution at Cu^{2+} site resulted in enhancement in grain as well as grain boundary resistance, consequently IBLC effect is destroyed.

Gonzalez et al. [91] studied the influence of Sr and La replacing Ca and Cu, respectively, on the intrinsic properties of CCTO. The powders $Ca_{0.6}Sr_{0.4}Cu_3Ti_4O_{12}$, $CaCu_{2.85}La_{0.15}Ti_4O_{12}$, $Ca_{0.6}Sr_{0.4}Cu_{2.85}La_{0.15}Ti_4O_{12}$ and, pure $CaCu_3Ti_4O_{12}$ were prepared by mechanical alloying. The

microstructure analyzed by SEM showed a smaller grain size for the co-doped CCTO (Figure I-37).

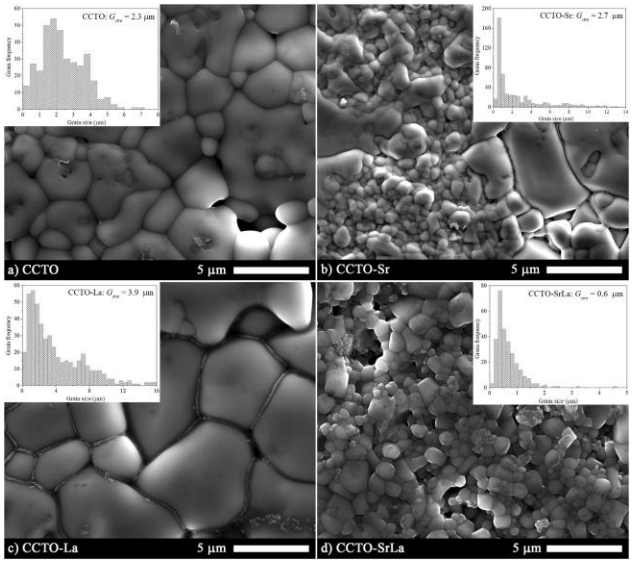

Figure I-37 : SEM micrographs of pure and doped CCTO: a) Pure CCTO, b) CCTO-Sr, c) CCTO-La, d) CCTO-Sr La. Insert plots: Grain size distribution for each sample. Reprinted from (Gonzalez et al.). Copyright 2018 Elsevier [91]

They also reported that the co-doped CCTO-Sr La ceramic showed the smallest tan(δ) of 0.039 at 26.8 kHz compared to pure CCTO and single-doped ceramics. The co-doped sample reached a higher dielectric permittivity compared to the single-doped ceramics.

The effect of the codoping with Li^+ and Al^{3+} on the dielectric properties of CCTO was studied by Sun *et al.* [100]. The codoped CCTO ceramics ($CaCu_{3-2x}Li_xAl_xTi_4O_{12}$, x = 0.05, 0.1, 0.15) were prepared by a sol–gel method and were sintered at 1020 –1080 °C for 8 h. The authors deduced that a very high dielectric constant of 1×10^5 with good dielectric-frequency as well as dielectric-temperature stability can be achieved in $CaCu_{2.8}Li_{0.1}Al_{0.1}Ti_4O_{12}$ ceramic sintered at 1060 °C. The average grain sizes, resistivity and the non-Ohmic properties are also improved compared to pure $CaCu_3Ti_4O_{12}$.

The effects of co-doping on dielectric and Electrical responses of $CaCu_3Ti_{4-x}$ $(Nb_{1/2}In_{1/2})_x$ O_{12} Ceramics were studied by Boonlakhorn *et al.* [101]. $CaCu_3Ti_{4-x}$ $(Nb_{1/2}In_{1/2})_x$ O_{12} ceramics, where x = 0, 0.025, 0.05, 0.10, and 0.20, were prepared via a solid state reaction method. All the green

bodies were sintered at 1090° C for 18 h. The mean grain size of CCTO was decreased by doping with Nb^{5+} and In^{3+}. Surprisingly the authors observed an increase in tanδ with the increase of x. They explained this by the change of microstructure and grain resistance.

Rani *et al.* [102] prepared $Ca_{0.95}Nd_{0.05}Cu_3Ti_{4-x}Zr_xO_{12}$ (x = 0.01, 0.03 & 0.10) via solid method. SEM images demonstrated that grain size of the modified CCTO ceramics was controlled by Zr^{4+} ions due to solute drag effect. The mean grain size of the doped CCTO was decreased with the increase in subsequent concentrations of Zr^{4+} ions (Figure I-38).

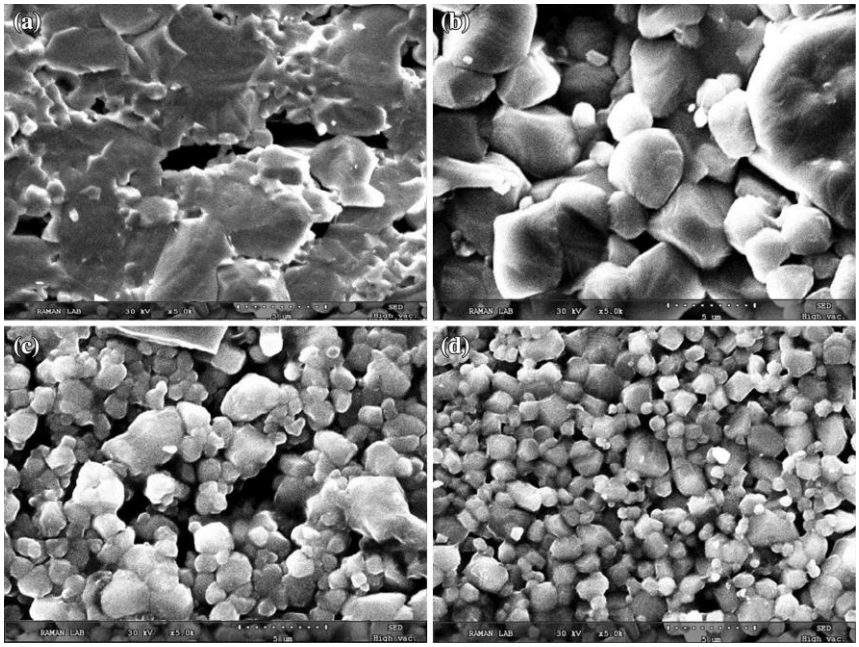

Figure I-38 : SEM images of fractured surfaces of a CCTO, b CCTO1, c CCTO2 and d CCTO3, ceramics. Reprinted by permission from (Nature/springer/Journal of Materials science, Materials in Electronics) (Rani et al.)- doi.org/10.1007/s10854-018-9150-9 Copyright (2018) [102]

A huge value of dielectric permittivity (ε_r ~ 16,902) with nominal dielectric losses (tan δ ~ 0.067 at 1 kHz) was observed in a broad frequency range from 10^3 to 10^5 Hz for CCTO3 (x=0.03) ceramic. Thus, it is concluded that the both dopant ions have played an independent role to improve the dielectric performance of CCTO system.

The same authors [103] focused on the Sr and Zn codoped CCTO. They prepared $Ca_{0.95}Sr_{0.05}Cu_3Ti_{4-x}Zn_xO_{12}$ (x = 0.01, 0.025, 0.05 & 0.10) powder by solid state method. They observed that the Zn ion has the same effect as the Zr ion and that grain size of the modified

CCTO ceramics was controlled by Zn^{2+} ions due to solute drag effect. Dielectric parameters observed to be improved for higher Zn/Sr ratio in the studied compositions. The $Ca_{0.95}Sr_{0.05}Cu_3Ti_{3.9}Zn_{0.1}O_{12}$ ceramic composition shows a colossal dielectric permittivity of ~37,788 and loss ~ 0.049, which are stable within a broad frequency region. Reduced tanδ over a broad range of frequency was well ascribed to the highly insulating grain boundaries.

Guo *et al.* [104] showed that the co-doping of CCTO by Ni^{2+} and Zr^{4+} by sol gel method can affect the microstructure of the ceramics and their dielectric properties. The grain size increases with the increase in the dopant concentrations. The authors also mentioned that they obtained a very low tanδ of 0.026 for the $CaCu_{2.95}Ni_{0.05}Ti_{3.9}Zr_{0.1}O_{12}$ ceramic sintered at 1060 °C for 8 h with a very high ε' value ~ 9.9×10^4 at about 9 kHz.

Du *et al.* [105] focused on the study of the codoping of CCTO by Y^{3+} on the A site and Al^{3+} on the B site in order to reduce the dielectric losses and simultaneously enhance the dielectric constants. Samples $Ca_{1-x}Y_xCu_3Ti_{4-x}Al_xO_{12}$ with different doping concentrations x = 0, 0.01, 0.02, 0.03, 0.05 and 0.07 have been prepared. No secondary phases were detected by XRD.

The dielectric properties showed that the dielectric losses of the doped ceramics are generally reduced and their dielectric constants are simultaneously enhanced across the frequency range up to 1 MHz. The doped sample with x = 0.05 exhibits the highest dielectric constant, which is well over 10^4 for frequency up to 1 MHz and is about 20% higher than the undoped sample.

Xu *et al.* [106] found that dielectric properties of CCTO were enhanced by its codoping with yttrium and zirconium. $CaCu_3Ti_{3.95}Zr_{0.0}\ O_{12}$ (CCTZO), $CaCu_3Ti_{3.97}Y_{0.03}O_{11.985}$ (CCTYO), and $CaCu_3Ti_{3.92}Y_{0.03}Zr_{0.05}O_{11.985}$ (CCTYZO) samples were prepared by citrate-nitrate combustion derived powders method. The SEM micrographs showed that Y_2O_3 and ZrO_2 additive can inhibit grain growth. The authors explained that the smaller grain sizes of Zr doped CCTO may be due to the slow diffusion of the larger Zr^{4+} ion substitutes of smaller Ti^{4+} ion , another possible explanation is that addition to larger Zr^{4+} ion, a high level of residual stress induced in the grain suppresses the grain growth of CCTO . Y doped CCTO also exhibits a smaller grain size, it may be due to the ability of Y^{3+} ion that suppresses the grain growth rate of CCTO ceramics, and rear-earth oxides could stop the grain boundaries from moving, which lead to fine grains .

A much better temperature and frequency stability of dielectric properties were realized in CCTYZO ceramics, and a low tan δ of 0.039 was observed at room temperature and 10 kHz for CCTYZO ceramics.

Dielectric properties of $Ca_{1-3x/2}Yb_xCu_{3-y}Mg_yTi_4O_{12}$ (x = 0.05, y = 0.05 and 0.30) prepared using a modified sol–gel method and sintered at 1070 °C for 4 h were investigated by Boonlakhorn *et al.* [107] They observed that Grain sizes of all co-doped samples were smaller than that of the un-doped CCTO sample. The authors concluded that the decrease in grain size of the co-doped CCTO ceramics was an important factor in reducing tanδ. Enhanced resistivity of each GB layer was due to Mg^{2+} doping.

Rhouma *et al.* [108] synthetized $Ca_{1-x}Sr_xCu_{3-y}Ni_yTi_4O_{12}$ for (x and y =0 or 0.1), they found that Sr and Ni substitution leads to a ceramic densification and cubic grain form. They noticed that the dielectric permittivity increases (44,410) and the dielectric loss decreases (0.07) at low frequency of 1 kHz. In order to explain the grain growth, Raman spectra (Figure I-**39**) measurements were carried out for a good determination of grain and grain boundaries. The three main modes (44 cm^{-1}, 510 cm^{-1}, 576 cm^{-1}) appeared confirming the presence of CCTO at grains and grain boundaries, they found that CuO and TiO_2 exist as secondary phase on grain boundaries of the doped ceramics, which enhance the formation of liquid phase leading to grain boundary mobility and a grain growth.

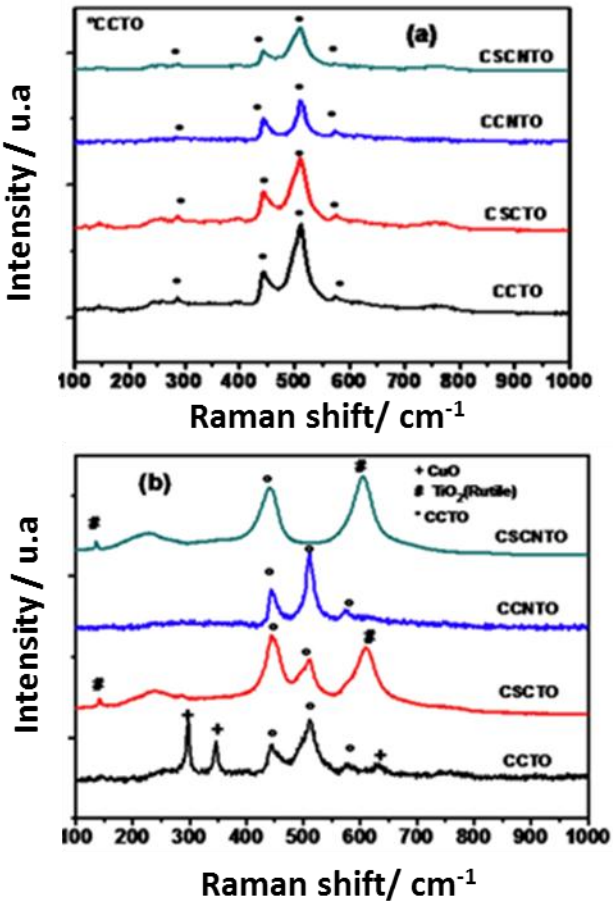

Figure I-39 : Raman Spectra (a) on grains and on grain boundaries (b). Reprinted from (Rhouma et al.). Copyright 2017 Elsevier [108]

In order to enhance dielectric properties of CCTO, lee *et al.* [109] suggested forming an electrical path for a contact network. Normally it is an artificial formation in which metallic materials used as micro capacitors to immigrate between thin dielectric layers in the ceramic materials. In CCTO ceramics a metastable phase is required for this electric path. As their previous study they noticed the formation of metastable phase after sintering at 1125°C/2h. This phase is formed when there is not enough energy to complete the sintering reaction. Usually silver or nickel are the representative migration material, lee *et al.* choose silver [109]. First they sintered CCTO at 1050°C for 0.5, 2 and 12h, metastable phase is formed in the 2h sintered CCTO ceramics, and it is the liquid Cu phase. EDS analysis is used to approve the formation of metastable phase, by studying the stoichiometric report in different regions of the material. In order to study the effect of Ag migration into CCTO (Figure I-40), after sintering a

post heating at 700°C/1h was employed to Ag coated-CCTO. Dielectric studies applied on CCTO ceramics showed that the permittivity increases after post-heating to about $565.9x10^3$ at 1KHz.

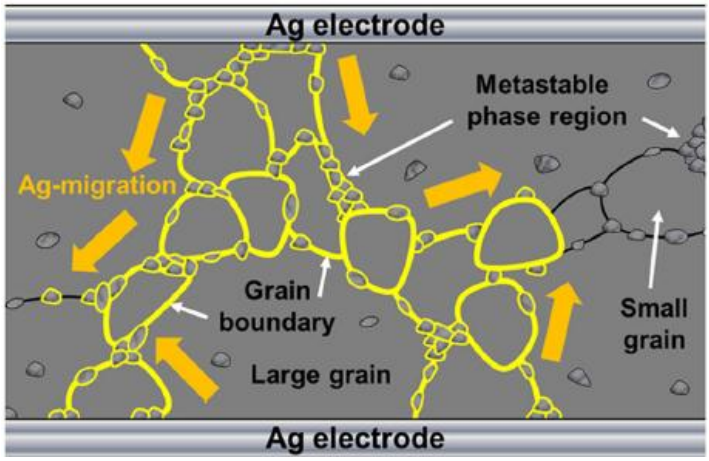

Figure I-40 : Schematic of the Ag-migration phenomenon into metastable phase including grain boundary for the 2 h sintered $CaCu_3Ti_4O_{12}$ ceramics. Reprinted from Springer Nature/ scientific reports (Lee et al). Copyright © 2018, Springer Nature [109]

The effect of co-doping CCTO on microstructure, permittivity (ε_r) and loss tangent ($\tan\delta$) are resumed in Table I-4. From these results, we can conclude that adding Yttrium to CCTO together with another dopant element can suppress the grain growth. Co-doping CCTO with Yttrium (Y) and Aluminum (Al) for instance yields a CCTO with a high dielectric constant ($2*10^4$) and a low dielectric loss ($\tan\delta$=0.048).The results are explained by the following equation I-3:

$$\varepsilon' = \varepsilon_{gb} \left(d/t\right) \qquad \textbf{(I-3)}$$

Where (d) is the grain size and (t) is the grain boundary thickness. From SEM we see that grain size decreases after co-doping and grain boundaries are thinner so the ration (d/t) is high, which lead to a higher dielectric constant and a lower dielectric loss.

Table I-4 : dopant element, concentration, permittivity, loss tangent (tanδ) and grain size of doped CCTO ceramic

Material	Concentration	εr(10^3Hz)	tanδ(10^3-10^6)	Grain size (μm)	References
Y^{3+}/Al^{3+}	0.05	20×10^4	0.048	2-5	[105]
Bi/Al	1% mol	4,020	10^{-1}	2.29-3.24	[97]
Sr/Ni	X = 0.1/0.1	44,410	0.07	35.50	[108]
Sr/Zn	x= 0.05/0.1	29,664	0.049	0.74	[103]
La/Zn	Zn (5-10%)	8,102	0.1	3-4	[99]
Y^{3+}/Zn^{4+}	3mol%/5mol%	10,196	~0.039	1.3-3.5	[106]
Sm/Zn	x=0.05/0.1	5,313	0.041	~2	[96]
Mg/Y	x=0.05/0.05	$\sim10^4$	~0.013	~3.73	[88]
Nb^{5+}/Al^{3+}	x=0.025	4.1×10^4	0.058	~35.1	[89]
Nb^{5+}/Al^{3+}	x=0.05	2.9×10^4	0.045	~34.6	[89]
Mg/Y	x=0.05/0.05	$\sim10^4$	~0.013	~3.73	[88]
Nb^{5+}/Al^{3+}	x=0.025	4.1×10^4	0.058	~35.1	[89]
Nb^{5+}/Al^{3+}	x=0.05	2.9×10^4	0.045	~34.6	[89]
Sr/La	x=0.4/0.15	$\sim4\times10^4$	~0.05	0.6	[91]
Ni^{2+}/Zr^{4+}	x=0.05/0.1	$\sim2\times10^4$	0.026	4.75	[104]
LiF	0.5%	34,994	0.68	2.1	[92]
Yb/Mg	x=0.05/0.3	$\sim10^4$	0.018	2.32	[107]
FeNb	x=0.5	8.0×10^4	~0.8	1.9	[98]

I.5 Applications:

$CaCu_3Ti_4O_{12}$ showed exceptions dielectric properties useful for capacitors applications. Due to its outstanding structure where both atoms Ca^{2+} and Cu^{2+} with different ionic radius shared A site, CCTO can be used as well in photocatalytic application and especially in visible light. In addition CCTO is an antiferromagnetic compound; it is used to form composites with magnetic properties useful for antennas, GPS and other applications. In this section photocatalytic and magnetic properties will be reported.

I.5.1 Photocatalytic properties

Accelerated industrial development and population growth forced science to find "green solutions" to solve problem of pollutions, by using a renewable energy such as visible light. The decomposition reaction of pollutants and pharmaceutical waste occurs only upon UV lights, in which UV light shared 4% of wavelengths with visible light [8,110]. TiO_2 is acclaimed as a UV-light photocatalytic. To enhance TiO_2 performance in visible light, many approaches investigate the doping of TiO_2 with metal transitions [111–113]. While doping, a disordered structure could appear in TiO_2, limiting the efficiency of this approach. Perovskite structure ABO_3 has been investigated because A site is shared by two cations without causing a disordered lattice [8]. $CaCu_3Ti_4O_{12}$ perovskite showed a good photo-catalytic reaction against water pollutants and pharmaceutical waste [8,109,110,114,115]. As mentioned above, the specific structure of CCTO is the key of this function. It is related to photo-induced charge transition from ground state Cu^{2+},Ti^{4+} to excited state Cu^{3+},Ti^{3+} that CCTO have a visible light activity and they observed a direct band transition with a small band gap (1.52eV) [8,110]. CCTO was prepared using oxalate route to decompose pharmaceutical waste (erythrosin (dye), ciprofloxacin (antibiotic) and estriol (steroid))[110], sol-gel and solid route to break-down water pollutants such as 4-chlorophenol [8].

Kushwaha *et al.*[110] demonstrate that after 40 min of exposure a total decomposition of erythrosine dye (solution turned from pink to colorless). As shown in Figure I-41, the absorbance pic of erythrosine was observed at 525nm and starts to decrease after exposure of the pink solution to the visible light irradiation in presence of CCTO pellets.

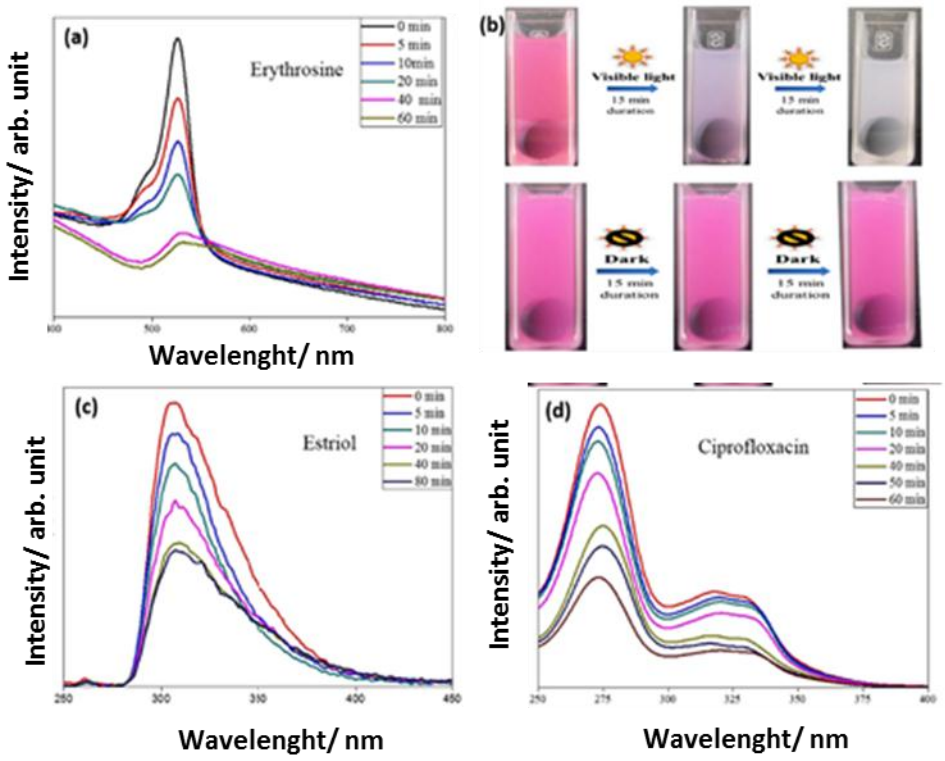

Figure I-41: (a) Change in absorbance of Erythrosine (525 nm) (b) Color change in erythrosine under dark and light (Figure drawn by author H.S. Kushwaha) (c) Change in absorbance of Ciprofloxacin (276 nm) and (d) fluorescence emission of estriol (305 nm excited at 240 nm) with time in photocatalytic degradation using CCTO pellets under visible light (λ > 420 nm). Reprinted from (Kushwaka et al). Copyright 2016 Creative Commons [110]

In 2017, *Hailili et al.*[115] used the molten salt method in order to synthetize $CaCu_3Ti_4O_{12}$. Five different salts were utilized to control the shape of crystals. By XRD, the formation of pure phase is confirmed for the five samples and no additional peaks for CuO or TiO_2 appear. It is well known that the presence of oxygen vacancy is very important for the photocatalytic behavior. For that, Electron Paramagnetic Resonance (EPR) measurements were carried out to investigate their presence in each sample. The measurements show that for all samples, the EPR signals are in the same position since all samples have the same Cu content. However samples with octahedron, nanorod and polyhedron shape samples have a large line width with high intensities in comparison with cubic shape samples indicating a high oxygen vacancy concentration. Photocatalytic test under visible irradiation are performed in the presence of tetracycline as pollutant. They deduced that with octahedron shape, the decomposition of TC

achieved 99.1 %, with higher constant k=1.1*$10^{-1}$$min^{-1}$ (first low of kinetics). These results are explained by 2 reasons: (i) the defects that enhance the active sites and (ii) an effective separation of electron-hole pairs to produce high efficiency in photocatalytic activity.

In order to enhance pollutant decomposition under visible light*, Hailili et al.*[116] synthesized a single crystal of $CaCu_3Ti_4O_{12}$ octahedron by molten salt. This crystal contains oxygen vacancies, metal deficiencies of Cu^+ and Ti^{3+} and coexposed facets of ({001},{111}).

In CCTO (perovskite type ABO_3), Ca and Cu atoms share the same A site and Cu is bonded to O atom (CuO_4) and to TiO_6 octahedron with one O atom, to form TiO6 and CuO_4 cluster. So any distortion of cluster or Ti displacement in TiO_6 causes a defect in the crystallite structure of CCTO and results in an imperfection. The defect was confirmed in EPR measurement by the presence of the characteristic pic of Ti^{3+} ($3d^1$) and Cu^+ at g value of 1.982 and 2.077 respectively which cause a distortion for Ti-O-Ti bond and generate TiO_5 distorted square structure formed from Ti^{3+} and Ti^{4+} and defects in CuO_4 planar. To characterize the heterojunctions facets, they calculate the band energy and density of states (DSO) of {001} and {111} surfaces by DFT. They deduced that there is a difference in level energy between conduction band (CB) and valence band (VB) levels of the exposed {001} and {111} facets; so facets heterojunctions can be formed. Under visible light irradiation, photoinduced electrons migrate from {001} to the exposed facets of {111} preferred as reduction sites because the electrons accumulation and {001} facets served as oxidation sites since photoinduced holes are accumulated on it. Figure I-42 showed the degradation of tetracycline under visible light in presence of CCTO with and without defect. They deduced that 99.34% from tetracycline is decomposed in the presence of defect dual CCTO with large normalized rate constant of 1.06*10^{-2} min^{-1}.

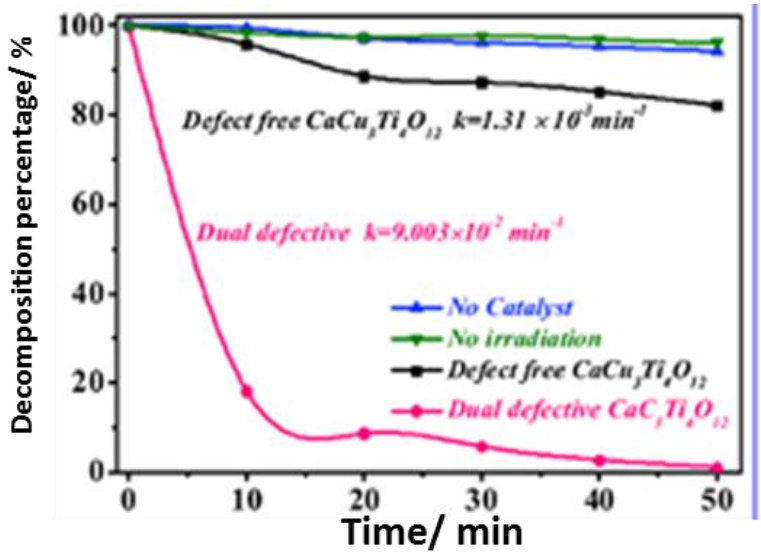

Figure I-42 : Comparison visible light degradation ratio and corresponding apparent rate constants (k) of tetracycline in the presence of octahedron shaped dual defective and defect free $CaCu_3Ti_4O_{12}$. Reprinted fom (Haillili et al.). Copyright 2019 IEEE [116].

Zhu et al. [117] tested the photo-assisted fenton-like process based on sulfate radicals using $CaCu_3Ti_4O_{12}$ as catalyst to remove pharmaceutical pollutants (ibuprofen) from water. Fenton-like process is based on sulfate radicals ($SO_4^{\cdot-}$), in which sulfate radicals with higher oxidative potential (2.5-3.1V) exhibit a higher oxidation power compared with hydroxyl radicals. Furthermore ($SO_4^{\cdot-}$) has a long life time (30-40µs) and a large range of working pH (2-9). They used molten salt synthesis to produce different shapes of CCTO catalyst by modifying sintering times. Cubic structures are formed at 775°C sintered for 6h (sample CCTO-6) and fibers are produced at 775°C sintered for 14h (sample CCTO-14). Photocatalytic behavior is tested for different systems, the ternary one (visible light/ $CaCu_3Ti_4O_{12}$ (sample-14)/peroxymonosulfate) promotes ibuprofen's removal to 91.8% in 30 min. CCTO-14 showed oxygen vacancies and production of Cu^+ since Cu^{2+} intensity decreases as shown in EPR measurement. It is related to the fact that under visible light, photogenerated-electrons are free to move into the crystallographic lattice and allow reducing Cu^{2+} to Cu^+, thus make enable peroxymonosulfate to generate sulfate radicals and reduce the rate of electron-holes recombination.

Pal et al. [118] synthesis $CaCu_3Ti_4O_{12}$-Carbon nitride composites as catalyst using low temperature thermal treatment (~150°C). They investigate the decomposition of methylene

blue in the presence of H_2O_2 activator, in the presence of LED light irradiation and the catalyst. They noticed that for 10 wt% CN in CCTO (sample: CN10CCTO), the decomposition of dye achieved 96% in 1h. Optical properties confirms charge transition from Cu^{2+}, Ti^{4+} ground states to Cu^{3+}, Ti^{3+} excited states respectively. From transient photocurrent study (Figure I-43), they showed that CN10CCTO has the highest photocurrent value, which is attributing to the efficacy of charge separation of the charge carriers leading to an enhanced photocatalytic activity.

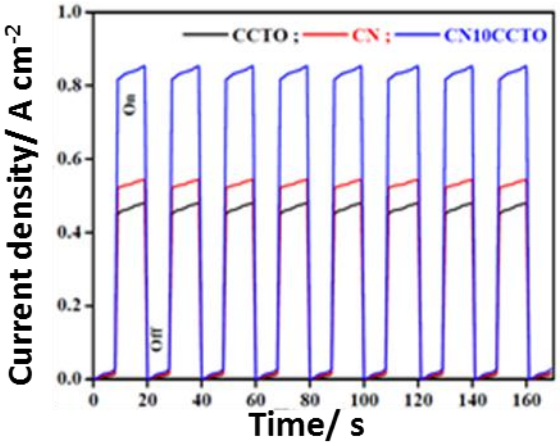

Figure I-43 : Current density vs. time plot of CCTO, CN and CN10CCTO (10 wt% CN in CCTO). Reprinted from (Pal et al.). Copyright 2019 IEEE [118].

I.5.2 Magnetic properties

A need to developed magnetic materials was the aim of researches in the 20th century. The best application is showed for materials where their coercivity and magnetization are optimized. Practical progress in magnetism largely depends on ferromagnetic materials, in which the mastery of coercivity was resulted from combined control of magnetocrystalline anisotropy and microstructure [119]. Ferromagnetic materials had a large range of magnetic dipoles that can be switched by applying a determined magnetic field [120]. The challenge is to correlate nanostructure properties and magnetic properties, and in order to explain this correlation, nanostructure materials were classified into different categories. Bulk materials or type D is one of this nanostructure materials, it is formed from grains and interfaces. With type D, the magnetic behavior cannot be predicted by applying theories for polycrystalline at nanoscales, because it is depending from grain boundaries and interaction [121].

$CaCu_3Ti_4O_{12}$ is a bulk material with a antiferromagnetic behavior below Neel temperature (T_N=25 K) studied with neutron diffraction and susceptibility measurements [122], due to spins (S=1/2) aligned antiferromagnetically on the A sites Cu^{2+} [56]. In order to enhance CCTO magnetic properties and to produce multiferroic material stable at room temperature, many investigations were performed by doping CCTO [56,122,123].

Wang et al. [58] doped CCTO ceramics using Cobalt (Co) by solid-state method. They showed from hysteresis loops, a weak ferromagnetism due to the superexchange interaction along Cu-O-Co-O-Cu path attributed to the small amount of Co substitution for the Ti site, instead of antiferromagnetic superexchange via Cu-O-Ti-O-Cu path.

Pansara *et al.* [123] synthesize $CaCu_{3-x}Ti_{4-x}Fe_{2x}O_{12}$ (x=0.0-07) using solid state reaction. From M-H loops, they conclude that the material for x=0.0-0.3 presents an antiferromagnetic behavior while x=0.5 and 0.7 present a ferromagnetic properties. To explain the influence of Fe doping on CCTO, ^{27}Fe Mossbauer spectroscopy is used to investigate the oxidation number of Fe doped into the crystallite lattice. They conclude from hyperfine interaction parameters such as isomer shift (IS), Quadruple splitting (QS) and magnetic hyperfine field (HF) that Fe is in Fe^{3+} form in which for x=0.5 and 0.7 Fe^{3+} ions prefer A'-site. Fe^{3+} in A'-site changes the superexchange interaction by increasing the Cu-Cu distance and increase the ferromagnetism by the dominant superexchange interaction through Cu(Fe)-O-Ti(Fe)-O-Cu(Fe) path.

Raval *et al.* [124] investigate the effect of ball milling, microwave assisted heating and rapid thermal cooling on magnetic properties in polycrystalline $CaCu_3Ti_4O_{12}$. Ball-milling induce curtails hybridization of empty Ti-3d orbitals with Cu-3d and O-2p orbitals and secondary phase formation. M-T curves show pure antiferromagnetic peak for unmilled sample in which Cu-Cu bond distance is 3.6963 Å, and a weak ferromagnetic peak for 16 h milling in which Cu-Cu bond is longest.

Gavrilova et al. [125] synthesized a CCTO based nanocomposite $(SrFe_{12}O_9)_x(CaCu_3Ti_4O_{12})_{1-x}$ (x=0.01, 0.03, 0.07, 0.1) using solid state method. Electron spin resonance (EPS) showed two different lineshapes between x=0.03-0.07 group and x=0.01-0.1 group. For x=0.01, two lines appear, one is due to Cu^{2+} paramagnetic signal and the second is related to ferromagnetic

signal from $CaCu_3Ti_{4-y}Fe_yO_{12}$ solid solution. The position of ferromagnetic line shifts to g=2 (H=3300 Oe) while increasing the temperature. For x=0.03 and 0.07, TEM analysis confirmed the formation of nanostructured composites where SFO inclusions are inside the matrix. These results confirm the presence of two lines by EPS, in which one is attributed to the paramagnetic behavior of CCTO and second is a ferromagnetic line from SFO component. The EPS spectra for x=0.03 and 0.07 become less symmetric with increasing temperature.

Conclusion and perspectives

Recent investigations focus on high dielectric material especially ceramics to energy storage and environmental application. Ceramics with specific dielectric properties are highly demanded because of their fast charge-discharge comparing with batteries. CCTO-perovkite is a ceramic founded in 2000, with high permittivity stable at a large range of frequencies and temperatures. In this review, an overview on the history of CCTO ceramics, the different manufacturing methods (synthesis and sintering) and the different elements used as dopant for CCTO is given. The effect of all these parameters on the microstructure and dielectric properties is discussed. The origin of high dielectric constant in CCTO ceramics is not fully understood. Many hypotheses were deducted from different studies. Intrinsic hypotheses is based on that high dielectric constant is the result of TiO_6 titled octahedral planar. By impedance spectroscopy, it was discovered that CCTO ceramics are heterogeneous, composed of semiconducting grains and insulating grain boundaries (IBLC model). Third hypothesis explain that this high dielectric constant comes from the interfacial reactions between electrodes used and the surface of the material. IBLC model is the most accepted due to that dielectric loss can be controlled with controlling grain boundaries, which allow CCTO to be useful in electronic applications. Studies focused on decreasing loss tangent with maintaining a high dielectric constant stable at large range of frequencies are summarized.

Different synthesis methods were used for the synthesis of CCTO: Solid state route, wet chemistry method at room temperature and normal pressure (sol-gel and coprecipitation), hydrothermal method (under high pressure), microwave and autocombustion methods. It is been observed that the dielectric properties highly depend on the synthesis technique. The

best dielectric properties were shown by the ceramics prepared via the solid state route despite the high temperature used. Using wet chemistry method is a better approach to obtain a homogeneous and controlled microstructure. New trend in this area should be in the direction of finding new synthesis methods such as molten salt shielded synthesis able to give a homogenous micro or nanostructures. Such techniques could help to reduce the synthesis temperature and achieve high permittivity and low loss tangent.

The use of different sintering techniques leads to different dielectric properties. Conventional sintering and spark plasma are one-step approaches for the formation of CCTO ceramics, contrariwise to microwave sintering and thermobaric treatment that need a pre-conventional sintering step. Discovering new sintering method using less energy is necessary for industrial applications of CCTO such a cold pressing sintering applied in ceramic field.

In order to enhance dielectric properties and maintain a high dielectric permittivity with a low dielectric loss, doping CCTO was one of the aims of researchers. Many atoms with different valence are chosen to be inserted into the crystalline structure in order to change the charge distribution of elements. From results showed in this review, it is clear that these elements have significant influence on dielectric properties and even on grain morphologies and boundaries. An optimal dopant could be inserted into the lattice without making distortion, but should suppress the grain growth in order to improve the dielectric properties. Till now, a huge variety of element was used as dopant for CCTO.

Because of its specific structure, several studies focused on photocatalytic function of CCTO and especially in the range of visible light for environmental issues. Pure CCTO showed an important photocatalytic performance in presence of pharmaceutical and water pollutants in visible light. CCTO showed as well an antiferromagnetic behavior based on neutron diffraction; several studies were performed in order to form multiferroic compounds, such as doping CCTO by different ferroelectric elements (Fe, Nb, Co..).

Despite his colossal dielectric properties, and to the best of our knowledge, CCTO is not used in industrial applications. In order to bring CCTO based devices on the market, more investigations

should be performed in order to tune their properties for wide range of applications such as capacitor, varistor, GPS devices, and antennas as well as as photoelectrocatalytic materials able to degrades pharmaceutical and dye pollutants.

References

[1] Y.XU, Ferroelectric Materials and their applications 1st Edition BooK.**1991**.

[2] C.J.Howard, H.T Stokes, *Acta Crystallogr. Sect. B.* **1998**,54 ,782–789.

[3] V.M.Goldschmidt - Akad, Oslo, *I. Mat-Nat. K1*, **1926**.

[4] W.Forrester, R.Hinde, *Nature*.**1945**,156 ,177.

[5] N.Banerjee, S.Krupanidhi, **2010**,2 ,688–693.

[6] M.A.Subramanian, D.Li , N.Duan, B.Reisner, A.Sleight, *J. Solid State Chem.* **2000**,151 ,323–325.

[7] D.C.Sinclair, T.B.Adams, F.Morrison, A.R.West, *Appl. Phys. Lett.* **2002**,80 ,2153–2155.

[8] J.Clark, M.Dyer, R.Palgrave, C.Ireland, J.Darwent, J.Claridge, M.Rosseinsky, *J. Am. Chem. Soc.* **2011**,133 ,1016–1032.

[9] L.Sun, R.Zhang, Z.Wang, E.Cao, Y.Zhang, L.Ju, *RSC Adv.* **2016**,6 ,55984–55989.

[10] W.Li, L.Tang, F.Xue, Z.Xin, Z.Luo, G.Du, *Ceram. Int.* **2017**,43 ,6618–6621.

[11] A.Smith, T.Calvarese, A.Sleight, M.Subramanian, *J. Solid State Chem.* **2009**,182 ,409–411.

[12] M.Cohen, J.Neaton, L.He, D.Vanderbilt , *J. Appl. Phys.* **2003**,94 ,3299–3306.

[13] M.Li, D.C.Sinclair, A.R.West, *J. Appl. Phys.* **2011**,109 ,084106.

[14] M.Li, Z.Shen, M.Nygren, A.Feteira, D.C.Sinclair, A.R.West, *J. Appl. Phys.* **2009**,106 ,104106.

[15] T.B.Adams , D.C.Sinclair, A.R.West, *Phys. Rev. B.* **2006**,73 ,94124.

[16] R.K.Pandey, W.A.Stapleton, J.Tate, A.K.Bandyopadhyay, I.Sutanto, S.Sprissler, S.Lin, *AIP Adv.* **2013**,3 ,62126.

[17] H.Ghayour, M.Abdellahi, *Powder Technol.* **2016**,292 ,84–93.

[18] H.S.Bhatti, S.T.Hussain, F.A.Khan, S.Hussain, *Appl. Surf. Sci.* **2016**,367 ,291–306.

[19] M.Ahmadipour, M.F.Ain, Z.A.Ahmad , *Nano-Micro Lett.* **2016**,8 ,291–311.

[20] G.J.Lee, E.K.Park , S.A.Yang , J.J.Park, S.D.Bu, M.K.Lee, *Sci. Rep.* **2017**,7 ,46241.

[21] H.Yu, H.Liu, H.Hao, L.Guo, C.Jin, Z.Yu, M.Cao, *Appl. Phys. Lett.* **2007**,91 ,222911.

[22] P.Thongbai, J.Jumpatam,B. Putasaeng , T.Yamwong , S.Maensiri , *J. Appl. Phys.* **2012**,112 ,114115.

[23] T.T.Fang, H.Y.Chung , S.C.Liou, *J. Appl. Phys.* **2009**,106 ,54106.

[24] N.Tripathy, K.C.Das, S.P.Ghosh, G.Bose, J.P.Kar, *IOP Conf. Ser. Mater. Sci. Eng.* **2016**,115 ,12022.

[25] B.G.Rao, D.Mukherjee, B.M.Reddy, *Nanostructures Nov. Ther.* **2017**,1–36.

[26] P.Mao, J.Wang , S.Liu, L.Zhang, Y.Zhao, L.He, *J. Alloys Compd.* **2019**,778 ,625–632.

[27] B.Zhu, Z.Wang , Y.Zhang , Z.Yu, J.Shi, R.Xiong, *Mater. Chem. Phys.* **2009**,113 ,746–748.

[28] R.Kumar, M.Zulfequar, L.Sharma, V.N.Singh, T.D.Senguttuvan, *Cryst. Growth Des.* **2015**,15 ,1374–1379.

[29] S.Patra, ethesis.nitrkl.ac.in.2009.

[30] A.Lopera, M.A.Ramirez, C.García, C.Paucar, J.Marín, *Inorg. Chem. Commun.* **2014**,40 ,5–7.

[31] C.Masingboon, S.Rungruang , *J. Phys. Conf. Ser.* **2017**,901 ,012101.

[32] R.MGerman, *Sinter. from Empir. Obs. to Sci. Princ.* **2014**,1–12.

[33] L.Jaworska, J.Cyboroń , S.Cygan, J.Laszkiewicz-Łukasik, M.Podsiadło, P.Novak, Y.Holovenko, *IOP Conf. Ser. Mater. Sci. Eng.* **2018**,329 ,012004.

[34] M.Oghbae, O.Mirzaee, *J. Alloys Compd.* **2010**,494 ,175–189.

[35] B.Barbier, C.Combettes, S.Guillemet-Fritsch, T.Chartier, F.Rossignol, A.Rumeau, T.Lebey, E.Dutarde, *J. Eur. Ceram. Soc.* **2009**,29 ,731–735.

[36] S.Krohns, P.Lunkenheimer, S.G.Ebbinghaus, A.Loidl , *J. Appl. Phys.* **2008**,103 ,084107.

[37] M.C.Ferrarelli, D.C.Sinclair, A.R.West, H.A.Dabkowska, A.Dabkowski, G.M.Luke, *J. Mater. Chem.* **2009**,19 ,5916–5919.

[38] P.Fiorenza, V.Raineri, S.G.Ebbinghaus, R.Lo-Nigro, *CrystEngComm.* **2011**,13 ,3900–3904.

[39] R.Schmidt, S.Pandey, P.Fiorenza, D.C.Sinclair, *RSC Adv.* **2013**,3 ,14580–14589.

[40] A.O.Turky, M.M.Rashad, Z.I.Zaki, I.A.Ibrahim, M.Bechelany, *RSC Adv.* **2015**,5 ,18767–18772.

[41] S.Y.Chung, I.D.Kim, S.JL.Kang , *Nat. Mater.* **2004**,3 ,774-778.

[42] R.R.Mishra, A.K.Sharma,Composites Part A. 2016,81,78-97.

[43] R.Kumar,M. Zulfequar, T.D.Senguttuvan, *J. Electroceramics*.**2019**,42,41-46.

[44] X.Ouyang, P.Cao, S.Huang , W.Zhang, Z.Huang , W.Gao, *J. Electron. Mater.* **2015**,44 ,2243–2249.

[45] P.Y.Raval, A.R.Makadiya, P.R.Pansara , P.U.Sharma, N.H.Vasoya, J.A.Bhalodia, S.Kumar, S.N.Dolia , K.B.Modi, *Mater. Chem. Phys.* **2018**,212 ,343–350.

[46] O.Guillon, J.Gonzalez-Julian , B.Dargatz, T.Kessel, G.Schierning , J.Räthel, M.Herrmann, *Adv. Eng. Mater.* **2014**,16 ,830–849.

[47] R.Kumar, M.Zulfequar, T.D.Senguttuvan, *J. Mater. Sci.: Mater. Electron.* **2015**,26,6718-6722.

[48] R.Kumar, M.Zulfequar, T.D.Senguttuvan, *J. Mater. Sci.: Mater. Electron.* **2016**,27,5233-5237.

[49] L.Ni, M.Fu, X.Ren, Y.Zhang , *J. Mater. Sci. Mater. Electron.* **2017**,28 ,10191–10198.

[50] H.Lin, X.He, Y.Gong , D.Pang, Z.Yi, *Ceram. Int.* **2018**,44 ,8650–8655.

[51] S.Zhai, E.Ito, *Geosci. Front.* **2011**,2 ,101–106.

[52] L.F.Xu, C.Mao, V.V.Marchenkov, K.Sun, T.V.Dyachkova, A.P.Tyutyunnik, Y.G.Zainulin, C.P.Yang , S.H.Liang, *Phys. Lett. A* **2018**,382 ,2861–2867.

[53] C.Mao, L.Xu, V.V.Marchenkov, T.V.Dyachkova, A.P.Tyutyunnik, Y.G. Zainulin, C.Yang, *Ceram. Int.* **2018**,44 ,20069–20074.

[54] J.W.Lee, J.H.Koh, *Ceram. Int.* **2017**,43 ,9493–9497.

[55] L.F.Xu, K.Sun, X.Feng , H.B.Xiao, R.L.Wang, C.P.Yang, *Int. J. Mod. Phys. B.* **2017**,31 ,1750133(1-10).

[56] C.Mu, Y.Song, H.Wang, X.Wang , *J. Appl. Phys.* **2015**,117 ,17B723.

[57] Z.Kafi, A.Kompany, H.Arabi, Z.A.Khorsand, *J. Alloys Compd.* **2017**,727 ,168–176.

[58] J.Wang , Z.Lu, T.Deng, C.Zhong, Z.Chen, *J. Eur. Ceram. Soc.* **2018**,38 ,3505–3511.

[59] E.Swatsitang, T.Putjuso, *J. Eur. Ceram. Soc.* **2018**,38 ,4994–5001.

[60] A.Sakthisabarimoorthi, S.A.Martin Britto Dhas, R.Robert , M.Jose, *Mater. Res. Bull.* **2018**,106 ,81–92.

[61] M.Li, Q.Liu, C.X.Li, *J. Alloys Compd.* **2017**,699 ,278–282.

[62] J.Jumpatam, B.Putasaeng , N.Chanlek, P.Kidkhunthod, P.Thongbai,S. Maensiri , P.Chindaprasirt , *RSC Adv.* **2017**,7 ,4092–4101.

[63] R.Late, H.M.Rai, S.K.Saxena, R.Kumar,A. Sagdeo, P.R.Sagdeo, *J. Mater. Sci. Mater. Electron.* **2016**,27 ,5878–5885.

[64] Z.Wang, J.Guo, W.Hao, E.Cao, Y.Zhang , L.Sun, P.Xu, *J. Electroceram.* **2018**,40 ,115–121.

[65] J.Chen, T.Li, H.Y.Dai, Z.P.Chen, *Defect Diffus. Forum* **2017**,373 ,241–244.

[66] A.Srivastava, *Am. J. Mater. Synth. Process.* **2018**,2 ,90-93.

[67] X.Huang, H.Zhang, J.Li, Y.Lai, *J. Mater. Sci. Mater. Electron.* **2016**,27 ,11241–11247.

[68] L.Sun, R.Zhang, Z.Wang, E.Cao, Y.Zhang, L.Ju, *J. Alloys Compd.* **2016**,663 ,345–350.

[69] E.Swatsitang, K.Prompa, T.Putjuso, *J. Mater. Sci. Mater. Electron.* **2018**,29 ,12639–12651.

[70] C.Wang, W.Ni, D.Zhang, X.Sun, J.Wang, H.Li, N.Zhang, *J. Electroceram.* **2016**,36 ,46–57.

[71] S.S.Kouassi,J.P.Sagou, C.Autret-Lambert, S.Dridy, M.Lethiecq, *Adv. Mater.* **2017**,6 ,57-65.

[72] S.Senda, S.Rhouma, E.Torkani, A.Megriche, C.Autret, *J. Alloys Compd.* **2017**,698 ,152–158.

[73] J.Wang, Z.Lu, T.Deng, C.Zhong, Z.Chen, *J. Am. Ceram. Soc.* **2017**,100 ,4021–4032.

[74] J.Boonlakhorn, B.Putasaeng, P.Thongbai, *Ceram. Int.* **2019**,45 ,6944–6949.

[75] W.Li, T.Zhang, S.Liu, Z.Lu, R.Xiong, *Ceram. Int.* **2017**,43 ,4366–4371.

[76] J.A.Cortés, G.Cotrim, S.Orrego, A.Z.Simões, M.A.Ramírez MA, *J. Alloys Compd.* **2018**,735 ,140–149.

[77] M.Sahu, S.Hajra, R.N.P.Choudhary, *SN Appl. Sci.* **2018**,1 ,13.

[78] S.Amhil, E.Choukri, S.Ben Moumen, A.Bourial, L.Essaleh, *Phys. B Condens. Matter* **2019**,556 ,36–41.

[79] L.Singh, B.C.Sin, I.W.Kim, K.D.Mandal, H.Chung, Y.Lee, *J. Am. Ceram. Soc.* **2016**,99 ,27–34.

[80] S.S.Kouassi, J.P.Sagou, C.Autret-Lambert, S.Dridy, A.Nautiyal, M.Lethiecq, *Int. J. Mater. Sci. Appl.* **2017**,6 ,54-64.

[81] L.Tang, F.Xue, P.Guo, Z.Xin, Z.Luo, W.Li, *Ceram. Int.* **2018**,44 ,18535–18540.

[82] R.Xue, G.Zhao, J.Chen, Z.Chen, D.Liu, *Mater. Res. Bull.* **2016**,76 ,124–132.

[83] R.Espinoza-González, E.Mosquera, *Ceram. Int.* **2017**,43 ,14659–14665.

[84] D.Xu, Y.Zhu, B. Zhang, X.Yue, L.Jiao, J.Song, S.Zhong, J.Ma, L.Bao, L.Zhang, *J. Mater. Sci. Mater. Electron.* **2018**,29 ,5116–5123.

[85] S.Senda, S.Rhouma, E.Torkani, A.Megriche, C.Autret, *J. Alloys Compd.* **2017**,698 ,152–158.

[86] X.Huang, H.Zhang, M.Wei, Y.Lai, J.Li, *J. Alloys Compd.* **2017**,708 ,1026–1032.

[87] W.Makcharoen, W.Punsawat , *Mater. Today Proc.* **2017**,4 ,6234–6238.

[88] J.Boonlakhorn, B.Putasaeng, P.Kidkhunthod, P.Thongbai, *Mater. Des.* **2016**,92 ,494–498.

[89] J.Boonlakhorn, P.Kidkhunthod, N.Chanlek, P.Thongbai, *J. Eur. Ceram. Soc.* **2018**,38 ,137–143.

[90] J.Deng, X.Sun, S.Liu, L.Liu, T.Yan, L.Fang, B.Elouadi , *J. Adv. Dielectr.* **2016**,06 ,1650009(1-9).

[91] R.Espinoza-González, S.Hevia, Á .Adrian, *Ceram. Int.* **2018**,44 ,15588–15595.

[92] T.C.Porfirio, E.N.S.Muccillo , *Ceram. Int.* **2016**,42 ,12005–12009.

[93] J.Boonlakhorn, P.Thongbai, B.Putasaeng, T.Yamwong, S.Maensiri, *J. Alloys Compd.* **2014**,612 ,103–109.

[94] H.Katayama-Yoshida, T.Nishimatsu, T.Yamamoto, N.Orita, *J. Phys. Condens. Matter* **2001**,13 ,8901–8914.

[95] A.Wen, D.Yuan, X.Zhu, J.Zhu, D.Xiao, J.Zhu, *Ferroelectrics* **2016**,492 ,1–9.

[96] J.Boonlakhorn,P.Thongbai, *Ceram. Int.* **2017**,43 ,12736–12741.

[97] L.Ren, L.Yang, C.Xu, X.Zhao, R.Liao, *J. Alloys Compd.* **2018**,768 ,652–658.

[98] L.Bai, Y.Wu, L.Zhang, *J. Alloys Compd.* **2016**,661 ,6–13.

[99] S.Rani, N.Ahlawat, R.Punia, K.M.Sangwan, P.Khandelwal, *Ceram. Int.* **2018**,44 ,23125–23136.

[100] L.Sun, Q.Ni, J.Guo, E.Cao, W.Hao,Y. Zhang , L.Ju, *Appl. Phys. A Mater. Sci. Process.* **2018**,124 ,428.

[101] J.Boonlakhorn, P.Kidkhunthod, P.Thongbai, *J. Phys. Conf. Ser.* **2017**,901 ,12078.

[102] S.Rani, N.Ahlawat, K.M.Sangwan, S.Rani, R.Punia, J.Malik, *J. Mater. Sci. Mater. Electron.* **2018**,29 ,10825–10833.

[103] S.Rani, N.Ahlawat, K.M.Sangwan, R.Punia, A.Kumar, *J. Alloys Compd.* **2018**,769 ,1102–1112.

[104] J.Guo, L.Sun, Q.Ni, E.Cao, W.Hao, Y.Zhang, Y.Tian, L.Ju, *Appl. Phys. A* **2018**,124 ,635.

[105] G.Du, F.Wei, W.Li, N.Chen, *J. Eur. Ceram. Soc.* **2017**,37 ,4653–4659.

[106] Z.Xu, H.Qiang, Y.Chen, Z.Chen, *Mater. Chem. Phys.* **2017**,191 ,1–5.

[107] J.Boonlakhorn, P.Kidkhunthod, P.Thongbai, S.Maensiri, *Ceram. Int.* **2016**,42 ,8467–8472.

[108] S.Rhouma, S.Saîd, C.Autret ,D.Almeida, S.Didry, M.El Amrani, A.Megriche, *J. Alloys Compd.* **2017**,717 ,121–126.

[109] J.W.Lee, G.H.Lee, D.J.Shin , J.Kim, S.J.Jeong, J.H.Koh, *Sci. Rep.* **2018**,8 ,1392.

[110] H.S.Kushwaha, N.A.Madhar, B.Ilahi, P.Thomas, A.Halder, R.Vaish, *Sci. Rep.* **2016**,6 ,18557.

[111] M.Nasr, S.Balme, C.Eid, R.Habchi, P.Miele, M.Bechelany, *J. Phys. Chem. C* **2017**,121 ,261–269.

[112] M.Nasr, C.Eid, R.Habchi, P.Miele, M.Bechelany, *ChemSusChem* **2018**,11 ,3023–3047.

[113] M.Nasr, R.Viter, C.Eid, R.Habchi, P.Miele, M.Bechelany, *New J. Chem.* **2017**,41 ,81–89.

[114] A.Sen, K.K.Chattopadhyay, *J. Mater. Sci. Mater. Electron.* **2016**,27 ,10393–10398.

[115] R.Hailili, Z.Q.Wang, Y.Li, Y.Wang, V.K.Sharma, X.Q.Gong, C.Wang, *Appl. Catal. B Environ.* **2018**,221 ,422–432.

[116] R.Hailili, Z.Q.Wang, X.Q.Gong , C.Wang, *Appl. Catal. B Environ.* **2019**,254 ,86–97.

[117] Y.Zhu, T.Wang , W.Wang, S.Chen, E.Lichtfouse, C.Cheng, J.Zhao, Y.Li, C.Wang, *Environ. Chem. Lett.* **2019**,17 ,481–486.

[118] K.Pal, A.Mondal, R.Jana , P.P.Ray, A.Gayen, *Appl. Surf. Sci.* **2019**,467–468 ,543–553.

[119] J.M.D.Coey, *J. Alloys Compd.* **2001**,326 ,2–6.

[120] P.Mandal, M.J.Pitcher, J.Alaria, H.Niu, P.Borisov, P.Stamenov, J.B.Claridge, M.J.Rosseinsk, *Nature* **2015**,525 ,363.

[121] D.L.Leslie-Pelecky, R.D.Rieke, *Chem. Mater.* **1996**,8 ,1770–1783.

[122] A.Koitzsch, G.Blumberg, A.Gozar, B.Dennis, A.P.Ramirez, S.Trebst, S.Wakimoto, *Phys. Rev. B* **2002**,65 ,052406.

[123] P.R.Pansara, P.Y.Raval, N.H.Vasoya, S.N.Dolia, K.B.Modi, *Phys. Chem. Chem. Phys.* **2018**,20 ,1914–1922.

[124] P.Y.Raval, P.R.Pansara, A.R.Makadiya, N.H.Vasoya, S.N.Dolia, K.B.Modi, *Ceram. Int.* **2018**,44 ,17667–17674.

[125] T.P.Gavrilova, J.A.Deeva, I.V.Yatsyk, A.R.Yagfarova , I.F.Gilmutdinov, N.M.Lyadov, F.O.Milovich, T.I.Chupakhina, R.M.Eremina, *Phys. B Condens. Matter* **2018**,536 ,303–309.

Part II : Materials and Methods

Part II: Materials and Methods

II.1 Introduction

This chapter is divided into three sections. In the first section we will present the preparation of the two dimensional (2D) materials: the hexagonal boron nitride nanosheets and the graphene oxide. In the second part we will discuss the preparation of pure phase $CaCu_3Ti_4O_{12}$ (CCTO) and composites CCTO with 2D materials. The last section will focus on the characterization methods used to characterize the obtained composites.

II.2 Two Dimensional Materials

II.2.1 Hexagonal boron nitride nanosheets (h-BN)

Hexagonal Boron Nitride (h-BN) is a white ceramic material. It has a layered structure similar to that ofgraphite; it is therefore sometimes referred to as 'white graphene'. h-BN is a lattice alternately arranged by B and N atoms in a two-dimensional plane by hexagonal lattice formation, displaying a honeycomb structure. The N and B atoms are combined by a sp^2 orbital to form a strong σ bond combined by weak interlayer Van der Waals forces [1]. Hexagonal boron nitride (h-BN) is very attractive for many applications, particularly, as protective coating, dielectric substrates, transparent membranes, or deep ultraviolet emitters. The h-BN used in all the experiments was PHPP325B COMBAT® powder purchased by Saint Gobain. The material appearance is a white powder with particle size around 3 µm. It possesses a surface area of 60 m^2/g and an apparent density of 2.2. Each h-BN nanosheets shows charracteristics similar to graphene; it is therefore sometimes refered to as 'white graphene'.

II.2.1.1 Exfoliation method

h-BN nanosheets (h-BN) (figure II-1) were prepared using liquid phase exfoliation with the assistance of an ultrasounds device (model SONOPLUS HD 3100, 100W, 20 kHz) with a microtip

of diameter 3 mm (MS73). In 100 mL of water, 1.0 g of pristine h-BN was added. The solution was heated up to 80 °C, then 20 g of gelatin from porcine skin (gel strength 300, Type A, purchased from Sigma Aldrich) were added, the mixture was kept under stirring at the same temperature until the complete dissolution of the gelatin.

Ultrasonic acoustic cavitation has been used in the production of 2D nanosheets such as graphene, transition metal dichalcogenides or boron nitride from bulk layered materials in liquid solutions. It is widely used because it can concentrate the acoustic energy in small volumes. The acoustic cavitation concerns physical effects of high energy including the formation, growth and implosive collapse of bubbles at high ultrasonic intensities in a liquid medium. However, the high speed jets and intense shock waves can diminish the size of the nanosheets or generates defects on the surfaces. An ultrasonic homogenizer consists essentially of three components: the high-frequency (HF) generator, the ultrasonic converter (UW), and the functioning tip. The HF generator first transforms the alternating supply voltage from 50-60 Hz into a HF voltage of 20 kHz. If this voltage is applied to a suitable oscillator inside the ultrasonic converter, it is possible to transform electric oscillations into mechanical oscillations of same frequency. The mechanical oscillation is transmitted by the ultrasonic converter through sonoprobes and is transmitted into the sample through the horns connected in between. The working intensity transmitted into the medium increases in inverse proportion with the diameter of the sonoprobe area. The smallest tips transmit the largest power per measure of area in maximum oscillation amplitudes of several tenths of a millimeter [2], [3] (Figure II-2).

The dispersion was kept in a bath at 50 °C to avoid the gelatin solidification and it was sonicated (figure II-2) for 3 hours at 65 % amplitude with pulse off/on 0.5 – 1 s. After the sonication, the yellowish suspension was subsequently centrifuged twice. In a first step, the solution was centrifuged at 3000 rpm for 30 min. Then, the supernatant was collected and subjected to a second centrifugation step at 6000 rpm for 30 min. The speed during the centrifugation plays an important role in the obtained h-BN lateral size, because the large nanosheets will be separated from the thinner ones during this centrifugation steps. The supernatant, where are

the lightest nanosheets, was collected and dried at 60 °C overnight. The resultant material was heated up to 600 °C under air atmosphere to remove the gelatin.

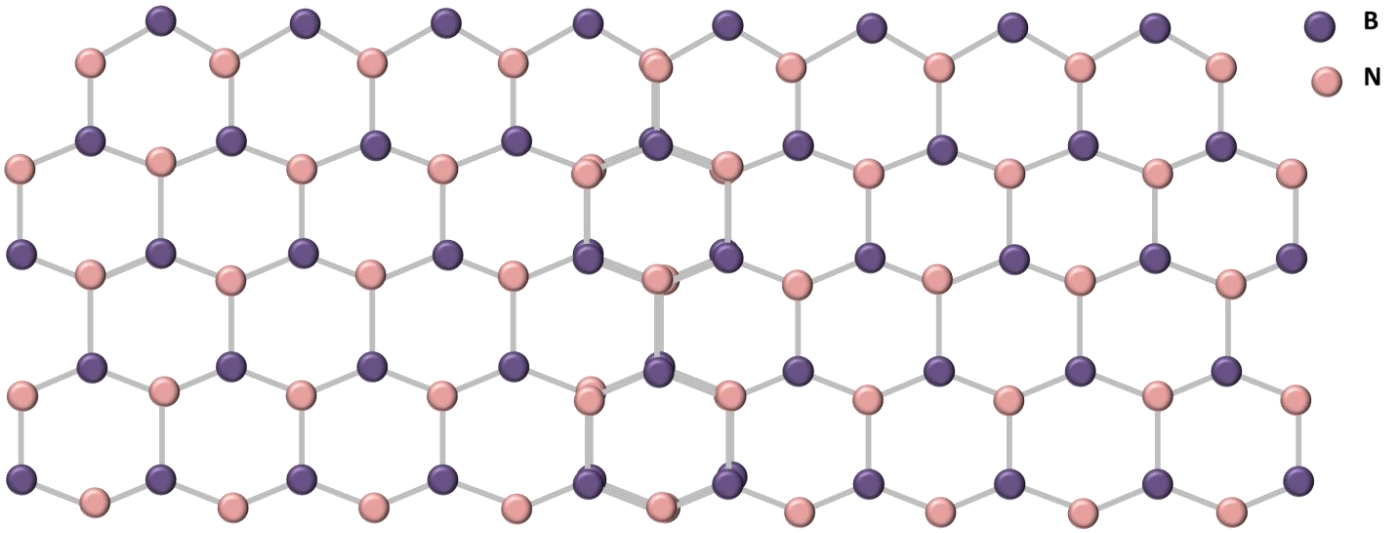

Figure II-1: Boron Nitride nanosheets

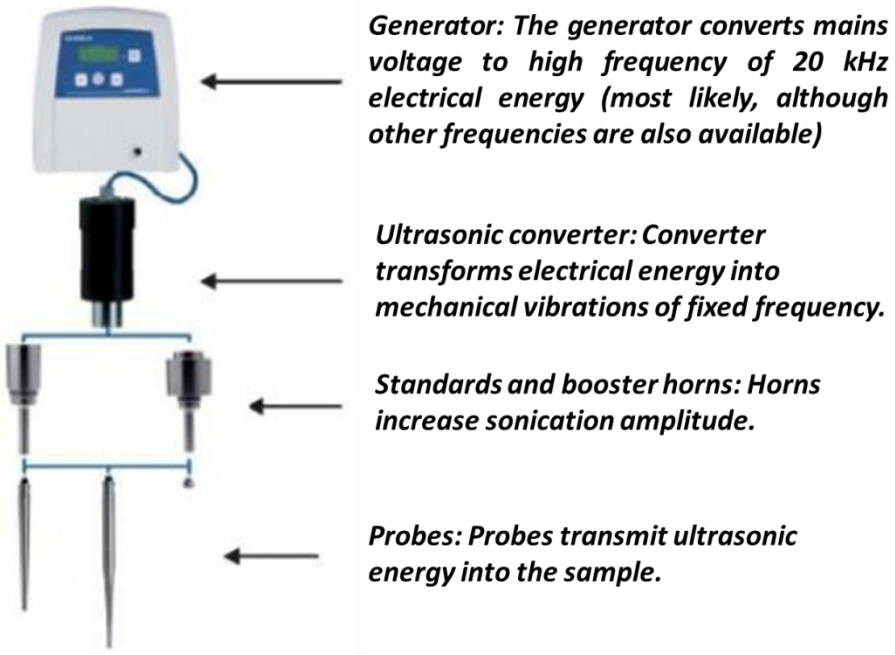

Figure II-2: Schematic representation of ultrasonic device with its different parts

II.2.2 Graphene Oxide

Graphene oxides nanosheets (Figure II-3) are prepared by graphite oxidation. The degree of oxidation and post-process induce the chemical exfoliation of flakes of graphitic stack into mono and few-layers sheets. It was prepared for the first time by Brodie in 1859 [4], though many commercially implemented methods today rely on modifications to Hummer method [5].The structure of GO is hardly characterized due to its non-stoichiometric structure and dependence on preparation parameters. According to existing direct imaging evidence, GO is considered to have long-range order in sp^2 lattice.

The graphene oxide used is prepared trough modified Hummer's method from graphite flakes [5], using the materials mentioned below in table II-1. All chemical products were purchased from Sigma Aldrich and used without purification.

Table II-1: Chemical materials purshased from Sigma Aldrich used for graphene oxide nanosheets preparation

Materials	CAS Number	Description
Graphite powder	7782-42-5	<20 µm, >99.95%, trace metal basis
Hydrochloric Acid (HCl)	8647-01-0	ACS reagent, 37%
Sulfuric Acid (H_2SO_4)	7664-93-9	99.99%
Phosphoric Acid (H_3PO_4)	7664-38-3	85%-99%, trace metal basis
Hydrogen Peroxide (H_2O_2)	7722-84-1	≥30%
Potassium Permanganate ($kMnO_4$)	7722-64-7	ACS reagent, ≥99.0%

In mixed solution of concentrated acid H_2SO_4:H_3PO_4 (9:1; 400 ml), 3g of graphite were added. Then 18g of $KMnO_4$ is added to the mixture gradually, with stirring for 12h. After that the temperature of the mixture is cooled down to room temperature, 3mL of H_2O_2 were added. A brown precipitate appears, indicating the exfoliation of graphene oxide from graphite. After one hour of sintering, GO was separated from acidic solution by centrifugation at 6000 rpm (2697 G) for 10 minutes. The resultant precipitate was washed with hydrochloric acid (30%) and absolute ethanol. Finally, the obtained powder was dried at 50°C for 24 hours to obtain the pure graphene oxide.

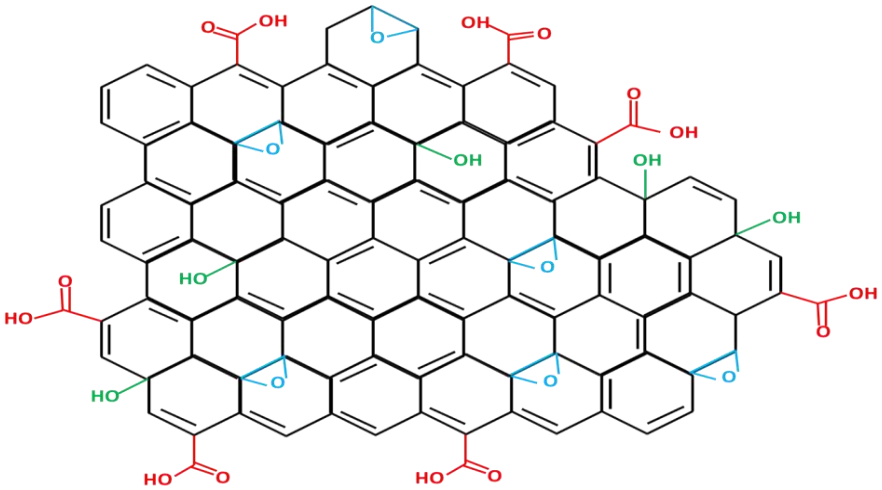

Figure II-3: Graphene oxide nanosheets

II.3 Preparation of pure $CaCu_3Ti_4O_{12}$ (CCTO) and its composites

The synthesis of CCTO powders was done through a solid-state reaction followed by a calcination step in order to obtain well-crystallized pure phase powders without residual phases.

II.3.1 Calcium copper titanate compounds

$CaCu_3Ti_4O_{12}$ (CCTO) powders were prepared from powders mixture of calcium carbonate ($CaCO_3$, Alfa Aesar, 98%), Copper oxide (CuO, Alfa Aesar, 98%), and titanium (IV) dioxide (TiO_2 anatase; Sigma Aldrich, 99.5%) powders, that were mechanically milled at room temperature under air atmosphere in an alumina container with a stoichiometric ratio. The milling was performed during 5 hours using an automatic planetary grinding machine Fritsch P700 at 350 rpm, without any solvent, with a ball-to-powder weight ratio equal to 10. The obtained black powders were then calcinated in air at 900°C for 3 hours.

The powders obtained after calcination were mixed with different weight percentages of 2D materials nanosheets, h-BN and graphene oxide, (%wt = 1,3 and 6), grounded in an agate mortar to obtain a homogeneous mixture and then pressed into pellets.

II.3.2 Sintering of CCTO composites

Solid state sintering is a technique of consolidating powders to produce dense materials using a thermal energy below the melting points of all solid phases [6]. Conventional sintering process is the method used in this work to obtain the final pellets.

Conventional sintering process is widely used to consolidate powder particles by heating a compacted pellet at high temperature and lower than the melting point of the desired compound. This process leads to a dense material with increasing in the mechanical strength and reduces the porosity in ceramics. Conventional sintering process implicates the material transport by diffusion. This diffusion is the movement of atoms or vacancies along the surface, grain boundary or through the material (Figure II-4).

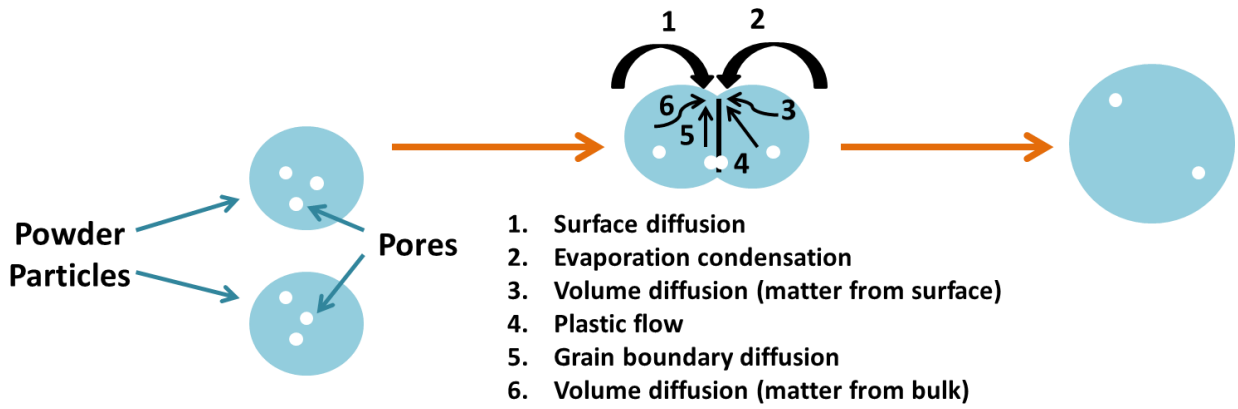

Figure II-4: Diffusion mechanisms that occur during a sintering process

During this process the shape and the size of the pores changes. The size of the pores will start to decrease as the specific area increases. This will lead to a reduction in the volume of the pores thus increasing the densification of the material. A grain growth that depend on the temperature and time of sintering is observed too [7].

The calcined powders of pure CCTO and wt% h-BN; GO: CCTO were mixed with a Polyvinyl Alcohol PVA (80%) binder aqueous solution and pressed into pellets of 10 mm diameter. Finally these green pellets were placed on titanium foil and sintered in air at 1100°C for 3h (Figure II-5).

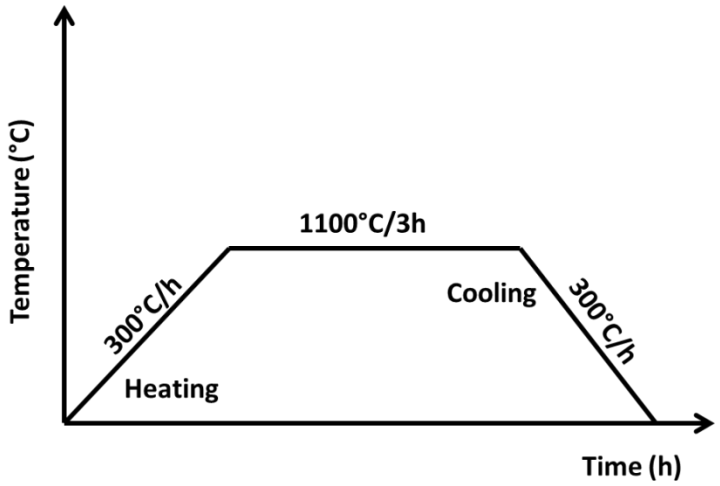

Figure II-5: One-step sintering cycle used in this investigation

II.4 Characterization techniques

A brief description of the different characterization methods used is listed below in this section. They were used to investigate the macro and microstructure of the prepared compounds as well as their optical, photoelectrochemical, dielectric and magnetic properties.

II.4.1 X-Ray diffraction

X-ray diffraction (XRD) is a characterization method used to identify the crystalline phases present in a material. It is a non-destructive method. The physical phenomenon of XRD expresses the result of the fundamental interaction between an electromagnetic wave, X-rays, and the ordered matter [8]–[10].

The crystallographic profiles of the prepared ceramics were determined using PANAalytical X'pert Pro diffractometer with Cu-K radiation (λ=1.540598 Å) at 45kV and 30mA. The measurement of the intensity is plotted against 2θ angles between incident and scattered radiation. The data were obtained over 10° to 75° 2θ range with a 0.016 step size at 0.55 sec/step. After XRD measurement and collecting the data, a profile matching on the prepared ceramics was performed with the use of the FULLPROF software [11], [12].

II.4.2 Scanning Electron Microscopy

To obtain high resolution images of the sample surface, scanning electron microscopy (SEM) is used (figure II-6). This technique is based on detecting the backscattered (BSE) and secondary (SE) electrons. Secondary electrons occur due to inelastic interactions between the primary electron beam and the sample and contain lower energy than the backscattered electrons. Secondary electrons are very beneficial for the inspection of the topography of the sample's surface.

The BSE are the result of quasi-elastic interactions between the incident electrons and the sample and provide qualitative information on the chemical contrast of the sample under study [13]–[15]. Moreover, some of SEM machines are equipped with an energy dispersive X-ray spectroscopy (EDX), which gives information about the element composition and dispersion on the surface of the studied sample.

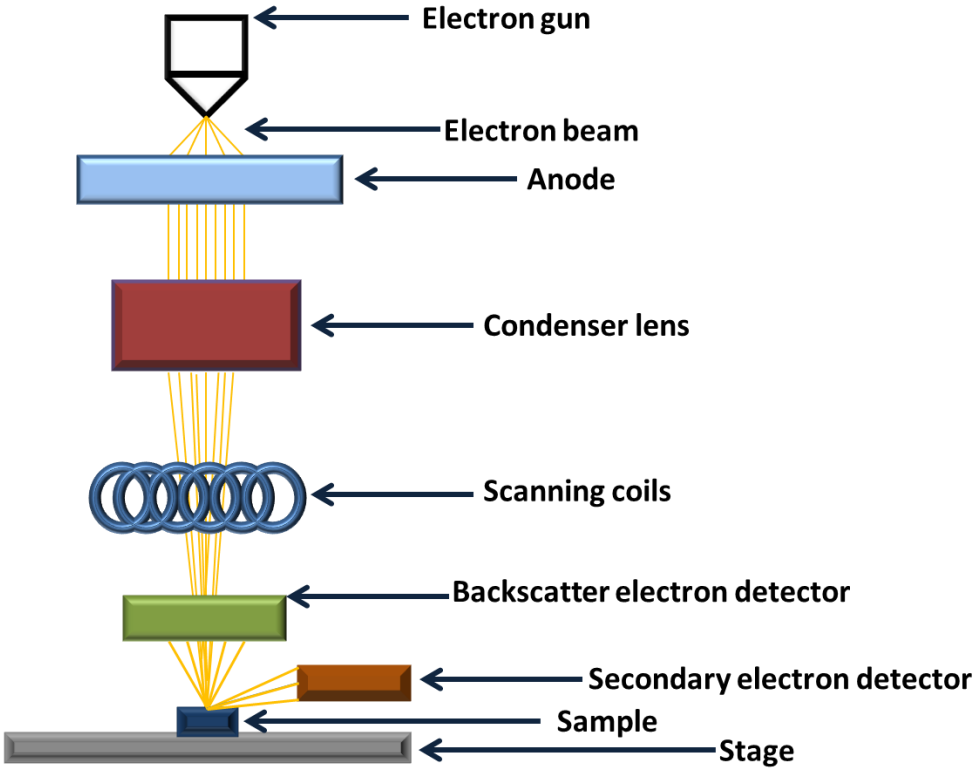

Figure II-6 : Schematic illustration of the different part of scanning electron microscopy

The microstructure and elemental mapping of the ceramics were performed on the surface of the pellets by using a Hitachi S4800 SEM system. It is equipped with a secondary and backscattered electron detector with an acceleration voltage from 0.1 kV to 30 kV. To carry out the analysis, the samples were attached to sample holder using conductive carbon tape.

II.4.3 Raman spectroscopy

Raman spectroscopy is a technique based generally on the inelastic diffusion of a monochromatic light. The monochromatic light could be emitted from a laser in the visible, near infrared or ultraviolet ranges. This technique is used to detect the vibrational and rotational mode in the materials. It is widely used to provide a defined profile in which the molecular units can be identified for any structure. First the sample is illuminated by a laser, this interaction with the sample surface creates a cloud of electrons or 'virtual state' which is not a stable state; the photon is directly re-radiated as dispersed light. The peak position showed in a Raman spectrum shows the specific vibrational mode of each molecular component involved in the material. In front of the peak positions, their width and shifting from their position can give information about the size effects and the induced stress inside the crystal [16].

Raman spectroscopy was used to characterize CCTO and its composites in order to study the influence of 2D materials nanosheets on the structure. The spectra were obtained from a Sentera model, using wavelength λ=532 nm and a power of 10 mW. The ceramics were deposited onto a glass slide to perform the analysis.

II.4.4 X-ray photoelectron spectroscopy

X-ray photoelectron spectroscopy (XPS) is a technique used to determine quantitative atomic composition by measuring the binding energy of samples. The binding energy is given by analyzing the electrons of photoelectrons emitted from the surface after it being bombarded with X-rays under vacuum. The energy of these electrons is characteristic of the atom being bombarded and thus allows determining the elements. XPS is used also to determine oxygen-containing functional groups on the surface of studied sample [17], [18].

In this work we studied the electronic state of elements and the oxygen-containing in prepared composites by using a XPS monochromatic X-ray, source: Al-Kalpha, 1486.6 eV with a resolution FHWM at 0.45 eV. The data were treated with origin software.

II.4.5 Ultraviolet-Visible diffuse reflectance spectroscopy

Ultraviolet-Visible diffuse reflectance spectroscopy (UV-Vis) is an important technique for optical properties characterization. It is a very simple rapid and low cost method. It is based on a quantitative analytical of absorbance change as a function of wavelength near ultraviolet (180-390 nm) or visible (390-780 nm) ranges. This absorbance relates to the excitation of studied samples from a ground state to an excited state. The wavelength of absorption is lower when high energy is needed for this excitation and higher when less energy is required (figure II-7) [19], [20]. The band gap of the studied materials can be evaluated from the diffuse reflectance spectra using Kubelka-Munk relation:

$$\alpha h\nu^{x}=A(h\nu-E_g)$$

Where α is the absorption coefficient, ν is light frequency and E_g is direct for x=1/2 and indirect for x=2.

In this work we used a UV-Vis spectrophotometer Jasco (model: V-570) equipped with a diffuse reflectance (DR) attachment (Shimadzu IRS-2200).

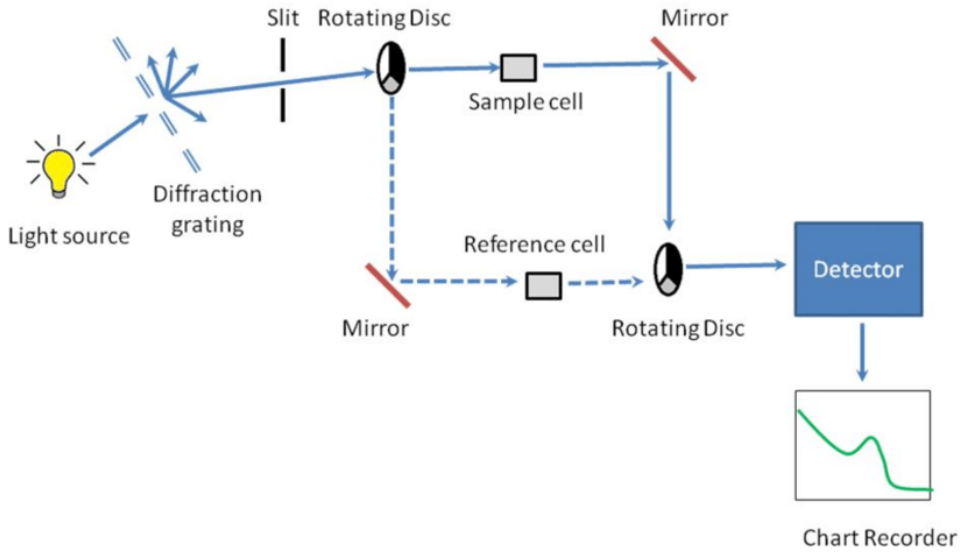

Figure II-7 : Schematic diagram of UV-Vis Spectrophotometer, reproduced from reference [21]

II.4.6 Photoluminescence spectroscopy

Photoluminescence (PL) is a spectroscopic method (Figure II-8) with which it is possible to analyze semiconductor or insulating materials, providing information on the material properties, such as surface defects (acceptors and donors) and the recombination rate between generated electron-holes. The principle of this method is to excite electrons with photon energy from the valence band to the conduction band, these electrons will return to the lower band with emission of a photon. All measurements are calculated basing of this emitted photon [22], [23].

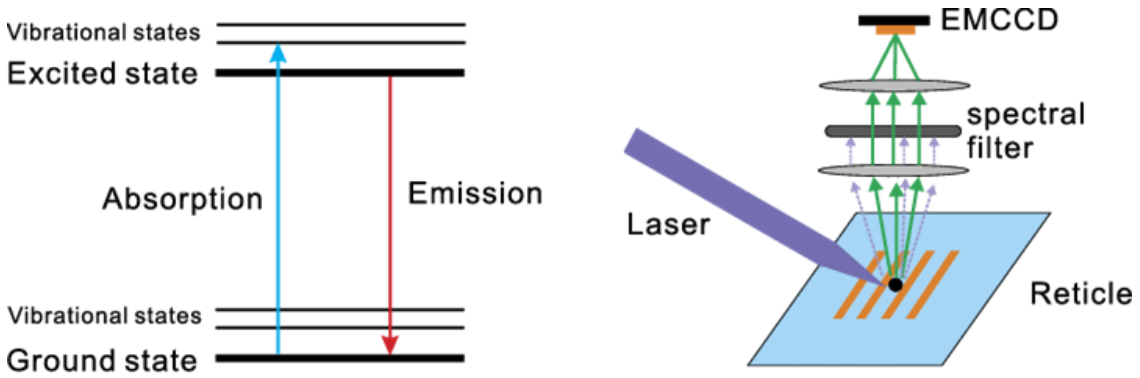

Figure II-8 : Principle of the photoluminescence process; schematic view of the working principle for inspection based on the photoluminescence, reproduced from reference [24]

The optical properties of ceramics were characterized using a PL spectroscopy (350-900 nm) at room temperature. After excitement with a nitrogen Nd:YAG laser (266 nm, 10 mW, 1 kHz), PL was recorded with an optical fiber spectrometer (Ocean Optics usb2000).

II.4.7 Photoelectrochemical Cell

Photoelectrochemical cell (PEC) is a photocurrent-generated device formed from an electrolyte, and a photoactive semiconductor electrode. The characterizations can be performed in a three electrodes cell, where the prepared sample is the working electrode, a Platinum (Pt) wire is the

counter electrode, and Ag/AgCl (saturated KCl) is the reference electrode in the presence of aqueous solution (NaOH, KCl, or Na_2SO_4) (Figure II-9). The interface of semiconductor-electrolyte is irradiated by different light source (UV or visible light irradiation) to generate electron-holes active species. The responses are attributed as linear and cyclic scan voltammetry and have been carried out using a Potentiostat. It is generally known that the transfer and separation of photoinduced electron-holes are reflected by the photocurrent transient [25]–[27].

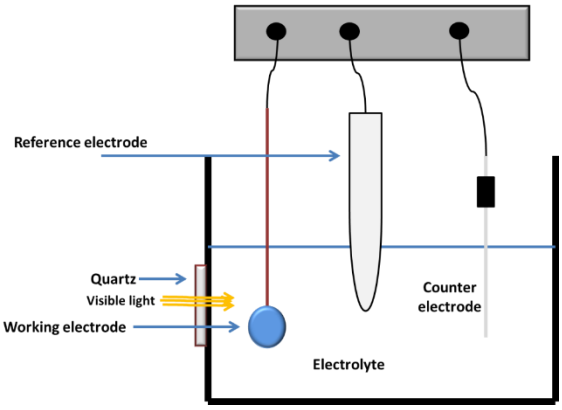

Figure II-9: Schematic illustration of the composition of photoelectrochemical cell

We used in our study a photoelectrochemical cell made from quartz glass for light diffusion, where the composites ceramics are the working electrode; Pt wire is the counter electrode, and Ag/AgCl (saturated KCl) is the reference electrode in 1M KOH solution. All electrodes are connected to a Potentiostat from *Solartron*© type. The light source used is a visible light lamp (150 W, $\lambda \geq 400$ nm). The given data were treated by *CorrWare*© (*CorrView*©).

II.4.8 Electrochemical Impedance Spectroscopy

Electrochemical impedance spectroscopy is a technique used to investigate the interface between electrolytes and electrodes. A small sinusoidal variation is applied to the potential at the working electrode, and the resulting current is analyzed in the frequency domain. The real and imaginary components of the impedance give information about the kinetic and mass transport properties of the cell, as well as the surface properties through the double layer capacitance (interface electrolyte-electrode) [28]–[30]. The results of this analysis are usually represented by a Nyquist diagram, which represents the evolution of the opposite of the

imaginary part of the complex impedance as a function of the real part of the complex impedance over a frequency range (Figure II-10). The obtained data should be fitted and treated with an equivalent circuit.

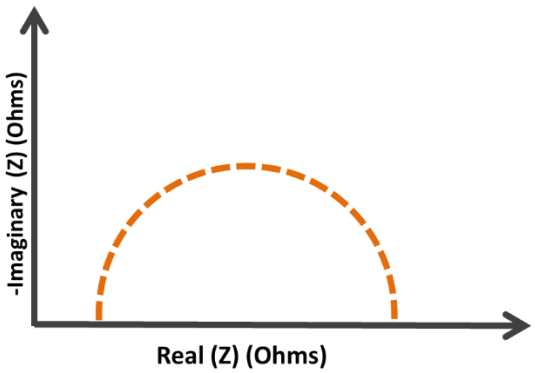

Figure II-10: Schematic illustration presents the results given after electrochemical impedance measurement

In this study, the major parameter derived from the EIS curve is the transfer resistance of charge at the electrode-electrolyte interface. It provides information on the evolution of mobility charge carriers following irradiation. The measurements were performed in the three electrode cell connected to *Solartron*© Potentiostat in dark and under visible light irradiation, using *ZPlot*© software (*ZView*©).

II.4.9 Dielectric Spectroscopy

Dielectric spectroscopy (DS) is used for dielectric permittivity and dielectric losses measurement as a function of frequency or temperature (Figure II-11). This technique can be applied to all non-conducting materials. It is useful technique for the electrical characterization of non-conducting or semi-conducting materials, up to their crystalline structure and microstructure. This technique is very sensitive to dipolar species as well as localized charge in the material, which allows determining the strength, kinetics and interactions properties of the measured material [31].

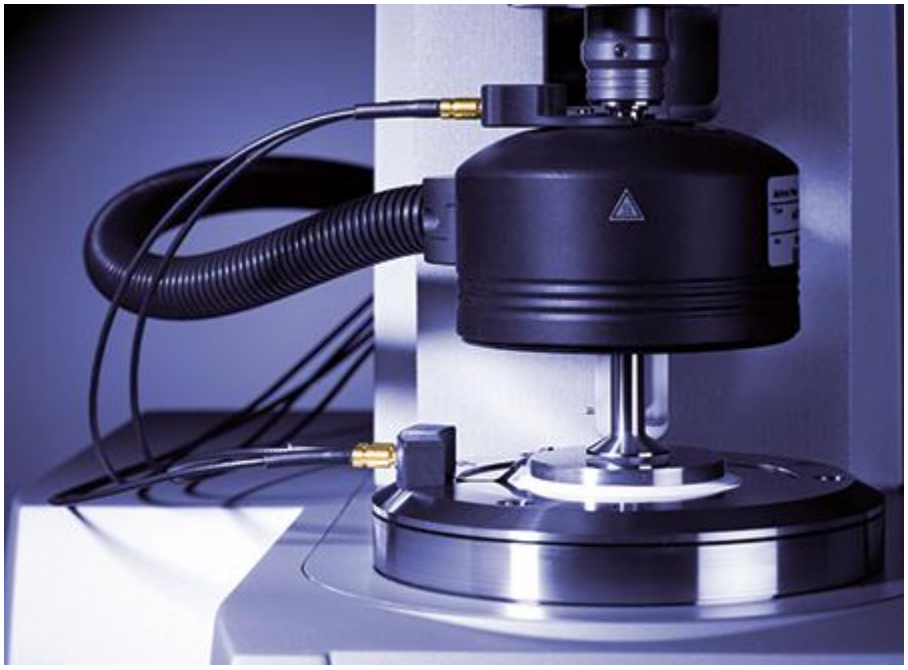

Figure II-11: a photograph of the used electrode for dielectric investigation

Dielectric spectroscopy used in this study is a Potentiostat equipped with a gold electrode, thus no need to paint the sample surface with a conductive paint. The measurements were performed only as function of frequency range (10^6-1 Hz) at room temperature.

II.4.10 Superconducting Quantum Interference Devices

Superconducting Quantum Interference Devices (SQUID) is a very sensitive, non-destructive magnetometer to measure low fields. These measurements could be performed on chemical molecular compound (transition metal complex), solid materials, nanoparticles and thin layers. It allows the study of the magnetic properties as a function of the temperature and/or the magnetic field, which makes possible to determine the magnetic nature (paramagnetic, antiferromagnetic, or ferromagnetic) of the studied materials. Briefly, the measurement consists on the travel of the sample through a series of coil to induce the current. These induce current pass through a second coil and induce a magnetic flux, in which this flux is detected by SQUID (Figure II-12). Several measurements could be performed using SQUID, such as the susceptibility (as a function of the temperature), hysteresis cycles, and relaxations study [32], [33].

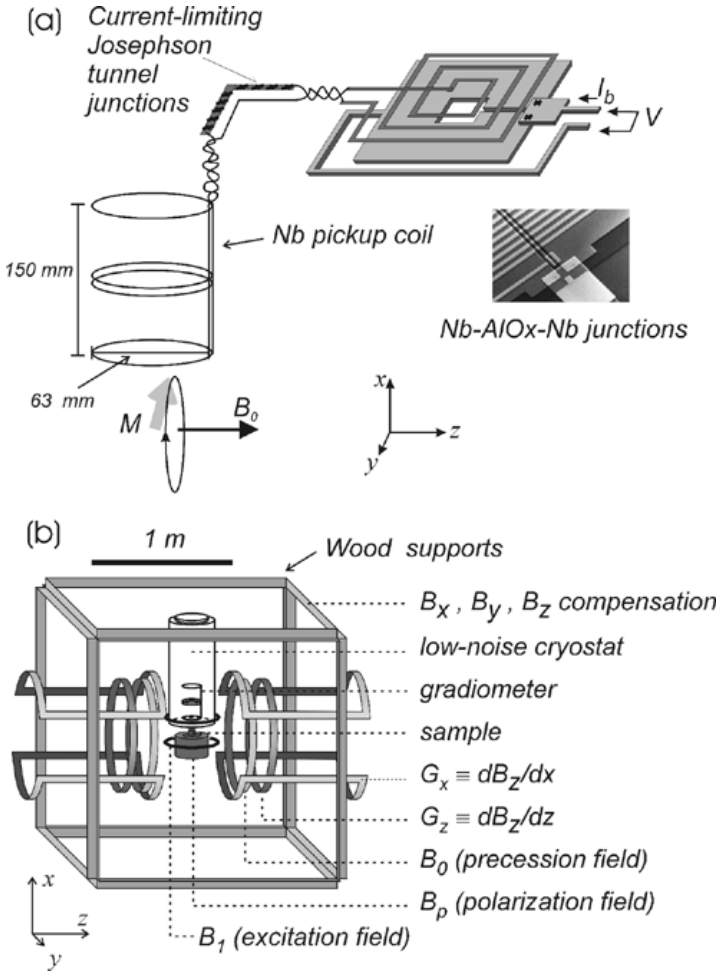

Figure II-12: (a) Measurement principle for SQUID-detected MRI. (b) Configuration of the SQUID MRI system showing magnetic field and gradient coils and the liquid helium dewar, reproduced from reference [34]

In our work, we studied the susceptibility (χ) as a function of temperature at a constant field (500 Oe) in order to determine the magnetic nature of the ceramics. The samples were putted in a small capsule (4mm of diameter), then placed in a room of 9 mm of diameter. The measurements were realized under reduced pressure of Helium. The SQUID equipment used is ''SQUID MPMS-XL''.

I.5 Conclusion

This chapter provides the information about the different chemicals used for the exfoliation of 2D materials (h-BN and GO nanosheets) and the preparation of CCTO and its composites. The protocol for the exfoliation of 2D materials is also described in this chapter. The preparation methods of CCTO powders and the ceramic CCTO with different weight percentage of h-BN and GO nanosheets, as well as the used techniques were presented in this section. The information about the different physico-chemical techniques used for the characterization of the obtained materials was briefly described.

The next chapter will be dedicated to the preparation of CCTO with different percentage weight of hexagonal boron nitride nanosheets (h-BN) in order to investigate their performance as active photoelectrode for water splitting application. Therefore it will include the characterization of obtained ceramics composite by the experimental techniques described briefly in this chapter.

References:

[1] K. Watanabe, T. Taniguchi, and H. Kanda, "Direct-bandgap properties and evidence for ultraviolet lasing of hexagonal boron nitride single crystal," *Nat. Mater.*, vol. 3, no. 6, pp. 404–409, 2004.

[2] Y. Hernandez *et al.*, "High-yield production of graphene by liquid-phase exfoliation of graphite," *Nat. Nanotechnol.*, vol. 3, no. 9, pp. 563–568, 2008.

[3] H. Xu, B. W. Zeiger, and K. S. Suslick, "Sonochemical synthesis of nanomaterials," *Chem. Soc. Rev.*, vol. 42, no. 7, pp. 2555–2567, 2013.

[4] B. C. Brodie, "XIII. On the atomic weight of graphite," *Philos. Trans. R. Soc. London*, vol. 149, pp. 249–259, Jan. 1859.

[5] W. S. Hummers and R. E. Offeman, "Preparation of Graphitic Oxide," *J. Am. Chem. Soc.*, vol. 80, no. 6, p. 1339, Mar. 1958.

[6] S.-J. L. Kang, *Sintering: densification, grain growth and microstructure*. Elsevier, 2004.

[7] M. Randall, "German., 1996. Sintering Theory and Practice." John Wiley and Sons, Inc.

[8] W. Clegg, "2.4 - X-ray Diffraction," J. A. McCleverty and T. J. B. T.-C. C. C. I. I. Meyer, Eds. Oxford: Pergamon, 2003, pp. 57–64.

[9] A. K. Chatterjee, "8 - X-Ray Diffraction," V. S. Ramachandran and J. J. B. T.-H. of A. T. in C. S. and T. Beaudoin, Eds. Norwich, NY: William Andrew Publishing, 2001, pp. 275–332.

[10] S. T. Misture and R. L. Snyder, "X-ray Diffraction," K. H. J. Buschow, R. W. Cahn, M. C. Flemings, B. Ilschner, E. J. Kramer, S. Mahajan, and P. B. T.-E. of M. S. and T. Veyssière, Eds. Oxford: Elsevier, 2001, pp. 9799–9808.

[11] J. Rodríguez-Carvajal, "FullProf," *CEA/Saclay, Fr.*, 2001.

[12] L. W. Finger, D. E. Cox, and A. P. Jephcoat, "A correction for powder diffraction peak asymmetry due to axial divergence," *J. Appl. Crystallogr.*, vol. 27, no. 6, pp. 892–900, Dec. 1994.

[13] G. E. Lloyd, "Atomic number and crystallographic contrast images with the SEM: a review of backscattered electron techniques," *Mineral. Mag.*, vol. 51, no. 359, pp. 3–19, 1987.

[14] J. I. Goldstein, D. E. Newbury, J. R. Michael, N. W. M. Ritchie, J. H. J. Scott, and D. C. Joy, *Scanning electron microscopy and X-ray microanalysis*. Springer, 2017.

[15] H. Seiler, "Secondary electron emission in the scanning electron microscope," *J. Appl. Phys.*, vol. 54, no. 11, pp. R1–R18, Nov. 1983.

[16] N. Colthup, *Introduction to infrared and Raman spectroscopy*. Elsevier, 2012.

[17] R. W. Welker, "Chapter 4 - Size Analysis and Identification of Particles," R. Kohli and K. L. B. T.-D.

in S. C. and C. Mittal, Eds. Oxford: William Andrew Publishing, 2012, pp. 179–213.

[18] H. Konno, “Chapter 8 - X-ray Photoelectron Spectroscopy,” M. Inagaki and F. B. T.-M. S. and E. of C. Kang, Eds. Butterworth-Heinemann, 2016, pp. 153–171.

[19] G. P. Holmes-Hampton, W.-H. Tong, and T. A. Rouault, “Chapter Fifteen - Biochemical and Biophysical Methods for Studying Mitochondrial Iron Metabolism,” in *Mitochondrial Function*, vol. 547, A. N. Murphy and D. C. B. T.-M. in E. Chan, Eds. Academic Press, 2014, pp. 275–307.

[20] S. Venkatachalam, “Chapter 6 - Ultraviolet and visible spectroscopy studies of nanofillers and their polymer nanocomposites,” S. Thomas, D. Rouxel, and D. B. T.-S. of P. N. Ponnamma, Eds. William Andrew Publishing, 2016, pp. 130–157.

[21] A. Bordoloi, *A DETAILED STUDY ON OPTICAL AND PHYSICAL PROPERTIES OF RICE AND ITS BY-PRODUCTS*. 2018.

[22] D. R. Baer and S. Thevuthasan, “Chapter 16 - Characterization of Thin Films and Coatings,” P. M. B. T.-H. of D. T. for F. and C. (Third E. Martin, Ed. Boston: William Andrew Publishing, 2010, pp. 749–864.

[23] Z. Batool *et al.*, “Chapter 7 - Bismuth-containing III–V semiconductors: Epitaxial growth and physical properties,” M. B. T.-M. B. E. Henini, Ed. Oxford: Elsevier, 2013, pp. 139–158.

[24] A. Gao, P. Rizo, L. Scaccabarozzi, C. Lee, V. Banine, and F. Bijkerk, “Photoluminescence-based detection of particle contamination on extreme ultraviolet reticles,” *Rev. Sci. Instrum.*, vol. 86, p. 63109, Jun. 2015.

[25] S. Ghosh and R. N. Basu, “Chapter 4 - Nanoscale Characterization,” in *Micro and Nano Technologies*, S. Mohapatra, T. A. Nguyen, and P. B. T.-N. M.-M. O. H. N. Nguyen-Tri, Eds. Woodhead Publishing, 2019, pp. 65–93.

[26] B. Bajorowicz *et al.*, “4 - Application of metal oxide-based photocatalysis,” in *Metal Oxides*, A. B. T.-M. O.-B. P. Zaleska-Medynska, Ed. Elsevier, 2018, pp. 211–340.

[27] M. R. Pai, A. M. Banerjee, A. K. Tripathi, and S. R. Bharadwaj, “14 - Fundamentals and Applications of the Photocatalytic Water Splitting Reaction,” S. Banerjee and A. K. B. T.-F. M. Tyagi, Eds. London: Elsevier, 2012, pp. 579–606.

[28] T. Lopes, L. Andrade, H. A. Ribeiro, and A. Mendes, “Characterization of photoelectrochemical cells for water splitting by electrochemical impedance spectroscopy,” *Int. J. Hydrogen Energy*, vol. 35, no. 20, pp. 11601–11608, 2010.

[29] M. E. Orazem and B. Tribollet, *Electrochemical impedance spectroscopy*. John Wiley & Sons, 2017.

[30] D. D. Macdonald, “Reflections on the history of electrochemical impedance spectroscopy,”

Electrochim. Acta, vol. 51, no. 8, pp. 1376–1388, 2006.

[31] F. Kremer and A. Schönhals, *Broadband dielectric spectroscopy*. Springer Science & Business Media, 2012.

[32] R. L. Fagaly, "Superconducting quantum interference device instruments and applications," *Rev. Sci. Instrum.*, vol. 77, no. 10, p. 101101, Oct. 2006.

[33] D. Drung, R. Cantor, M. Peters, H. J. Scheer, and H. Koch, "Low-noise high-speed dc superconducting quantum interference device magnetometer with simplified feedback electronics," *Appl. Phys. Lett.*, vol. 57, no. 4, pp. 406–408, Jul. 1990.

[34] M. Mossle *et al.*, "SQUID-detected in vivo MRI at microtesla magnetic fields," *Appl. Supercond. IEEE Trans.*, vol. 15, pp. 757–760, Jul. 2005.

Part III : h-BN/$CaCu_3Ti_4O_{12}$ ceramics composites for enhanced electrocatalytic behavior under visible light irradiation

Part III: h-BN/$CaCu_3Ti_4O_{12}$ ceramics composites for enhanced electrocatalytic behavior under visible light irradiation

Abstract

Photoelectrochemical water splitting under visible light has attracted attention for renewable hydrogen production. Despite prevalent investigations, many challenges still hindered an efficient energy conversion, such as enhancing the reaction efficiency in visible light. Thus controlling the photoelectrode materials is an essential step in designing new materials for water splitting. $CaCu_3Ti_4O_{12}$ (CCTO) has received great attention as photocatalyst under visible light due to its combined band gap as result of the presence in its structure of TiO_2 active in UV light and CuO active under visible light. In this work a cubic CCTO with different amount of exfoliated hexagonal boron nitride has been synthesized. The produced materials were characterized by X-ray diffraction (XRD), X-ray photoelectron spectroscopy (XPS), Raman and scanning electron microscopy (SEM). Physico-chemical characterizations demonstrate that bore and nitrogen co-doped CCTO and causes an increase in grain boundaries thickness, and thus leads to shift peaks in XRD and Raman spectra. In order to investigate the optical properties, UV-Vis diffuse reflectance spectroscopy and photoluminescence were used. UV-Vis spectra showed a decrease of the bang gap value after adding boron nitride nanosheets into CCTO. The electrochemical performance and the resistivity of the obtained materials were performed using electrochemical impedance spectroscopy in dark and under visible light exposition. The onset potential recorded for CCTO with 3% of boron nitride nanosheets (Eg=2.9), is around 0.5V and the current generation is 16 times more than pure phase of CCTO. This work focused on fabricating the semiconductor structures for the next generation of photoelectrocatalyst. It showed that CCTO with 3% of boron nitride nanosheets can be considered as an active electrocatalyst under visible light irradiation for water splitting.

Key words: *Water splitting, Photoelectrochemical, Visible light, $CaCu_3Ti_4O_{12}$ perovskite, Hexagonal boron nitride nanosheets (h-BN)*

Graphical abstract

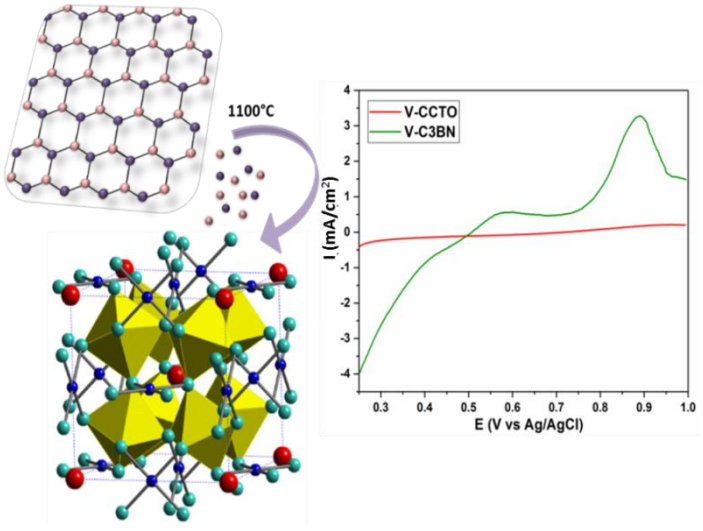

III.1 Introduction

Hydrogen production become a challenge as a source of renewable energy, and considerable efforts are currently undertaken to enriche its production. Hydrogen production can be carried out by several process such as chemical conversion of biomass and photoelectrochemical water splitting [1]–[3]. Chemical conversion of biomass are mainly classified into two categories, the thermochemical technology found on gasification and pyrolysis of raw materials such as coal, methanol, wood and gasoline to produce hydrogen [3]–[5] and the thermobiological technology. This process is based on photosynthetic activity of bacteria and green algae [6]–[9]. Chemical conversion of biomass is widley used but it is limited by the reaction parameters control, such as temperature, heating/cooling rate, and the type of catalyst [10].

The Photoelectrochemical cell (PEC) is an advanced devices for water splitting technology . Several investigations focused to improve PEC cell efficiency for energy storage and hydrogen production.. The main limit is that photoelectrocatalysts are active in UV light range which is only 4% from the received solar energy [2], [11]. Oxygen evolution reaction (OER) and oxygen reduction reaction (ORR) are the principle electrochemical process that cover a wide range of electrochemistry conversion for energy storage and conversion devices [12]–[14]. The thermodynamic differences between mechanisms reduce the probability to use one catalyst in ORR and OER voltage scale [15].

Noble metals such as platinum appear as very interested alternative and showed very good efficiency in acidic solution but its poor catalytic performance in alkaline solution, its high cost and its low abundance limit their applications [16], [17].

Recent investigations focused on spinel materials as promissing candidates due to their chemical stability and specific optoelectronic properties. Spinel ferrites MFe_2O_4 ($M=Zn^{2+}$, Mg^{2+}, and Ca^{2+}) are widley investigated because their conduction and valence band levels that can potentielly be tuned via band hybridization with the M^{2+} states [18]–[21]. The aim of this combination is to bring the flat band gap potential closer to the hydrogen evolution potential with lowest onset voltage for water splitting. However these materials have not shown a

significantly lower flat band potential and the onset potential is similar to that of Fe_2O_3 [22], [23].

Metal oxides such as RuO_2 and MnO_2 play as well a significant role as catalysts of the oxygen evolution reaction (OER) and oxygen reduction reaction (ORR) in alkaline media. These oxides present an excellent behavior for OER mechanisms, but their high cost, poor stability, and their environmental issues limit their use [24]–[26]. Ather oxides such as TiO_2 and WO_3 electrodes are easy to prepare and remerkably stable in electrochemical cell, but their wide band gap limit their activity under solar light for photoelectrochemical behavior [27]–[31]. Studies were then conducted to mix semiconductors by doping or forming composites to reduce the band gap value able to photoinduced electrons under visible light exposition [32]–[40]. However all these efforts did not succeed till now to create a highly active PEC cell.

ABO_3 perovskite oxides have gained attention due to their electrocatalytic behavior. In general they are composed from different oxides characterised by different band gap energy. This combination of band gap energy improve their photoelectrocatalytic efficiency. The structure of $CaCu_3Ti_4O_{12}$-CCTO (space group I*m3*) can be derived from an ideal cubic perovskite structure ABO_3 by superimposing a body centered ordering of Ca^{2+} and Cu^{2+} that share the A site, and Ti^{4+} is on B site. Due to the different ionic radius between Cu and Ca atoms, a tilting of TiO_6 octahedral planar appears [41]. This distortion forms a square planar oxide environment convenient to Jahn-Teller distorted Cu^{2+}. TiO_2 is an active photocatalyst in UV light and CuO is a good absorption component of visible light, thus merging properties in complex oxide $CaCu_3Ti_4O_{12}$ can enhance its properties under visible light exposition leading to photo-generate an electron-hole free movement in the ordered crystallographic sublattices of the complex oxide [42]. Recently, $CaCu_3Ti_4O_{12}$ was used as photocatalyst for the decomposition of dye and pharmaceutical waste [43]–[47]. It was found that the synthesis route used to prepare CCTO powder has a big influence on the properties of the obtained material.

$CaCu_3Ti_4O_{12}$ is established for the first as time as photo-electrocatalysis by Kushwaha et al. [43]. They conclude that under light irradiation the current density increase to 0.97 mA/cm^2. In a second study [48] they accomplished an electrochemical investigation and concluded that CCTO in octahedral shape shows a good performance for the decomposition of pollutants under

visible light. They found that for crystallite size of 26 nm CCTO synthesized using oxalate precursor route exhibit a bifunctional electrocatalytic activity (in OER and ORR range) with an onset potential of 0.83V. Investigations focused on that synthesis method leading to different powders structures [49] of CCTO and changing the electronic state of the material by doping [49] result to a different electrocatalysts behavior.

However the high recombination rate excited electron-hole limit the photocatalysis of all oxides in general and specialy CCTO. The separation between e-/h+ must be fast, and the recombination rate is decelerated by the high generation of current density [43]. Introducing material with different band gap is an efficient method to enhance the fast separation of electron-hole. One of the approaches that could be used to enhance this e-/h+ separation is the introducing of 2D materials in CCTO structures.

Among all two dimensional (2D), boron nitride nanosheets (h-BN) attracted attention because its outstanding properties [50]–[52]. BN is insulator with a wide ban gap (5.2 eV) depending on the synthesis method [53]. Boron nitride presents useful properties such as high chemical stability and thermal conductivity. Recent studies showed that hexagonal boron nitride nanosheets (h-BN) present a semiconducting and electronic transport similar to those of metals or metal oxides [54], [55].

In this paper, we prepared a new photoelectroactive CCTO/h-BN nanocomposite active under visible light. Different percentages of BN nanosheets were added to CCTO powders (1, 3 and 6 wt% BN), and then pellets were prepared by a one-step conventional sintering at high temperature. The crystallinity and phase detection of prepared samples were investigated by XRD and Raman techniques. Surface morphology and oxidation state of elements are detected by SEM and XPS respectively. Optical properties are studied using UV-Vis and photoluminescence spectroscopies. Finally we evaluated the electrochemical activity (Cyclic and linear voltammetry measurements) and the resistivity (Electrochemical Impedance Spectroscopy) of samples in Dark and under visible light irradiation in alkaline solution.

III.2 Experimental Section

III.2.1 Materials

Titanium (IV) Oxide (TiO_2- CAS Number: 13463-67-7, 99.5%), Potassium Hydroxide (KOH-CAS Number: 01900-20-08,≥85%) and gelatine from porcine skin(CAS Number: 9000-70-8) were purchased from Sigma Aldrich. Calcium Carbonate ($CaCO_3$-CAS Number: 471-34-1, 98%) and Copper (II) Oxide (CuO-CAS Number: 1317-38-0, 98%) were purchased from Alfa Aesar. BN nanosheets were prepared from commercial BN (Saint Gobain, 95%, 325 mesh). All chemicals were used without any further purification.

III.2.2 Exfoliation of BN

Boron nitride nanosheets were elaborated from commercial boron nitride powder with gelatin as reported elswhere [56]. 20 g of porcine skin gelatine was dissolved in 80 mL of hot water (75 °C). After dissolution of gelatine, 1 g of BN was added to the solution. The mixture was kept overnight in an ultrasonic homogenizer at 50°C and it was sonicated for 3 hours at 65 % amplitude with pulse off/on 0.5 – 1 s. Exfoliated BN was collected from last precipitates by centrifugation at 6000 rpm for 30 minutes and the supernatant was collected to repeat the separation process for. The precipitates were dried at 80 °C for 48 hours and then calcined at 600 °C for 2 hours in air with a heating rate of 5 °C/min to obtain the pure exfoliated BN.

III.2.3 Preparation of $CaCu_3Ti_4O_{12}$ Pellets

First a stoichiometric mixture of the starting materials ($CaCO_3$, TiO_2 and CuO) was mixed by ball milling using Alumina (Al_2O_3) balls and jar for 5h. Second the mixture was calcined at 900°C for 3h to obtain pure CCTO powders. Then calcined powders were pressed into pellets (d=10 mm, e=1-2 mm) by uniaxial hydraulic compression at 3.5T. In final step CCTO pellet was sintered in air at 1100°C for 3h.

III.2.4 Preparation of CCTO (1%BN), CCTO (3%BN) and CCTO (6%BN)

$CaCu_3Ti_4O_{12}$/ x%h-BN ceramics (x% =1, 3 and 6) were prepared using solid state reaction method**.** The calcined powders were mixed and ground with different percentage of h-BN nanosheets and pressed into pellets with 10mm of diameter and 1-2 mm in thickness by a uniaxial hydraulic compression at 3.5T. Finally these pellets were sintered in air at 1100°C for 3h. The obtained pellets are labeled CCTO, C1BN, C3BN and C6BN corresponding to pure phase of $CaCu_3Ti_4O_{12}$, CCTO (1%BN), CCTO (3%BN) and CCTO (6%BN) respectively.

III.2.5 Characterizations of pellets

The crystalline phase of the obtained pellets was analyzed by X-ray diffraction (XRD), using a PANAlytical Xpert-PRO diffractometer equipped with an Xcelerator detector using Ni-filtered Cu-radiation with wavelength of 1.54 A. The scan step size of all prepared pellets was fixed at 0.0167°/step and the time per step was 0.55 sec/step. Rietveld refinement was performed using the FULLPROF program [57] and profile function 7 (Thompson-Cox-Hastings pseudo-Voigt convoluted with axial divergence asymmetry function)[57]. The morphology of all ceramics was studied via scanning electron microscopy (SEM), where images were taken with a Hitachi S4800, Japan. Elemental mapping were performed with a Zeiss EVO HD15 microscope coupled with an Oxford X-MaxN EDX detector. Raman spectra were measured by the dispersive Raman spectroscopy (Model Sentera,Bruker, Germany) using 532 nm laser [doubled Nd:YAG laser (neodymium-doped yttrium aluminum garnet)] and a power of 10 mW. In order to investigate the oxidation state of elements in pellets X-ray photoelectron spectroscopy (XPS) was performed using XPS: monochromatic X-ray source: Al-Kalpha, 1486.6 eV - Resolution FWHM 0.45 eV.

The band gab of pellets was measuring from UV–vis spectra. These spectra were measured by a UV–vis spectrophotometer (Jasco model V-570) equipped with a diffuse reflectance (DR) attachment (Shimadzu IRS-2200). Room temperature photoluminescence (PL) was measured in the range of 350–900 nm. After excitement with a nitrogen Nd:YAG laser (266 nm, 10 mW, 1 kHz), PL was recorded with an optical fiber spectrometer (Ocean Optics usb2000).

III.2.5.1 Electrochemical Measurement

Electrochemical measurements for ORR and OER were carried out in a three- electrode system using 1 M KOH as the electrolyte in dark and under visible light exposition using 500W linear halogen lamp (the visible light source is in the range of 420-600 nm). CCTO and h-BN (x%)/CCTO pellets with a diameter of 10mm was used as working electrode, Ag/AgCl as reference electrode and platinum wire as counter electrode. Electrochemical Impedance spectroscopy measurements in dark and under visible light irradiation were performed at room temperature in the frequency range of 0.01Hz to 10^6 kHz with voltage bias of 20 mV amplitude.

III.3 Results and discussions

Pellets from pure phase of CCTO and with different amounts of hexagonal boron nitride (x=1, 3 and 6%) were synthesized using mecanosynthesis method, followed by sintering step at 1100°C for 3h. The crystallinity and morphology of pellets are characterized by XRD, SEM, XPS and Raman. The optical properties were investigated using UV-Vis and photoluminescence measurements. Finally, in order to study the performance of obtained materials under visible light and their resistivity, electrochemical measurements (cyclic and linear voltammetry) and impedance spectroscopy were performed in a system of three electrodes in 1M of KOH solution.

III.3.1 Physico-chemical characterization

The XRD data of the samples sintered at 1100°C for 3h under air are shown in figure III-1. The reflections of XRD patterns of examined materials can be indexed to the cubic structure of $CaCu_3Ti_4O_{12}$ (space group *Im*-3) as a main phase and monoclinic CuO (space group *C*2/*c*) as minor phase. Rietveld refinement of XRD patterns revealed that the grains of sintered samples are preferentially grown along the [422] direction. The lattice parameter *a* of $CaCu_3Ti_4O_{12}$ phase in CCTO sample found to be 7.3914 (1), which is in good agreement with previously reported value for pure $CaCu_3Ti_4O_{12}$ [58]. On the other hand, the addition of BN resulted in a slight increase in the lattice parameter of $CaCu_3Ti_4O_{12}$ phase (*a* = 7.3937 (1), 7.3934 (1) and 7.3952 (1) Å for C1BN, C3BN and C6BN sample, respectively). This increase in the lattice parameter can be

explained by the incorporation of B or N in the lattice of $CaCu_3Ti_4O_{12}$, as confirmed by XPS results. The change in the cation stoichiometry of $CaCu_3Ti_4O_{12}$ could be another reason for this increase as the amount of the secondary CuO phase increased with the addition of GO nanosheets. Previous studies showed that Cu deficiency and the partial reduction of Cu^{2+} and Ti^{4+} cations lead to the expansion of CCTO phase [57]. As it can be seen in Figure 1, the intensities of XRD reflections corresponding to CuO phase are drastically changed with the addition of h-BN, indicating the change in the amount of CuO phase on the surface of sintered samples. It was difficult to quantify precisely the amount of CuO phase in the samples by Rietveld refinement due to the strong preferred orientations observed for $CaCu_3Ti_4O_{12}$ phase. However, the amount of CuO phase on the pellet surface can be quantified by calculating the intensities ratio of the (211) reflection for $CaCu_3Ti_4O_{12}$, which does not suffer from preferred orientation, and (11-1) reflection for CuO. The intensities ratio CCTO (211)/CuO (11-1) increases with increasing Boron nitride nanosheets.

Moreover, no characteristic XRD reflections corresponding to any of crystalline BN phase are observed in the XRD patterns of all samples. In contrast, XPS analysis revealed the presence of elemental boron and nitrogen in the sintered samples as will be showed later. These results might be due to the presence of h-BN phase is present in a very small amount of crystalline phase to be detected by XRD measurements in the presence of highly crystalline $CaCu_3Ti_4O_{12}$ and CuO phases. The incorporation of B or N in the lattice of $CaCu_3Ti_4O_{12}$ and CuO phases could be another reason due to the oxidation of boron nitride nanosheets at high temperature under air, as confirmed by XPS results.

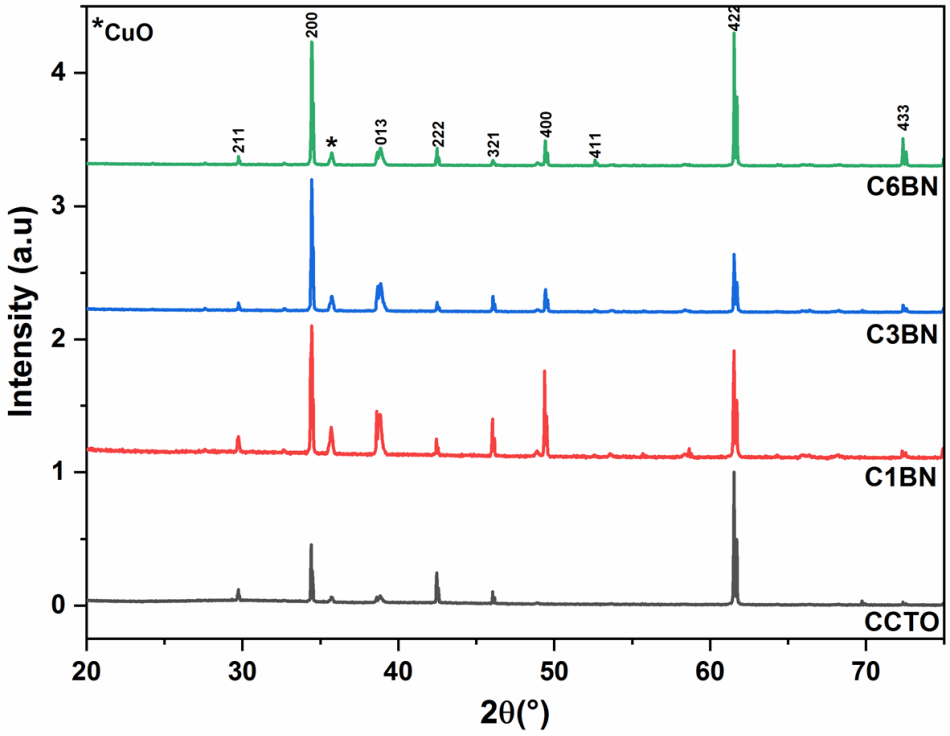

Figure III-1 : X-ray diffraction patterns of CCTO, C1BN, C3BN and C6BN ceramics sintered at 1100°C/3h.

The morphology and microstructure of the obtained ceramics were examined using SEM. Figure III-2 shows the microstructural evolution of CCTO ceramics sintered at 1100°C for 3h under air after adding 1,3 and 6% of BN nanosheets. The presence of two regions is noticed in all the ceramics : the grain region and the grain boundaries region. The grain diameter and the thickness of the grain boundaries region are highly influenced by the addition of h-BN nanosheets. For the pure CCTO ceramic the grain size obtained using ImajJ, Java-based image processing software is 104.9 ±0.5 µm. The grain sizes decreases to 101.1±0.3 µm, 63.8±0.3 µm and 64.4±0.5 µm for C1BN, C3BN and C6BN respectively.

It is well known that during the sintering process, the mass diffusion of ions takes place through the grain boundaries region. The added elements (dopant, nanosheets or nanofillers) can melt or react with the present major phase and form a eutectic liquid phase. In ceramics, the liquid phase is mainly present between the grains making it easier for the ions to diffuse. The temperature of eutectic liquid phase for the system CuO-TiO_2 is between 900 and 950°C, depending from CuO/TiO_2 ratio in which CuO phase transforms into liquid during the sintering treatment[59]. XRD studies showed that adding boron nitride nanosheets to CCTO leads to the

formation of CuO phase. The amount of CuO increases with the increase of the percentage of h-BN nanosheets. The presence of the CuO phase will create a liquid phase during the sintering process that increases the thickness of the grain boundaries region. From the SEM images, we can notice an increase in the grain boundaries thickness and a decrease in the grain size with the addition of h-BN nanosheets. The thickness of the grain boundaries region increases with the increase in the percentage of h-BN nanosheets. This is mainly due to the increase in the amount of CuO phase after adding the nanosheets.

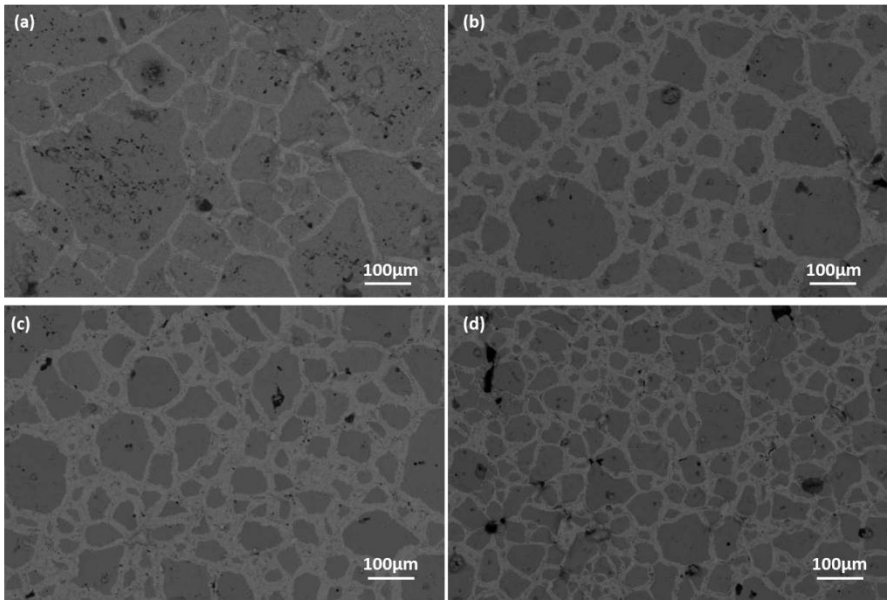

Figure III-2 : Scanning electron micrographs of the pellets (a) CCTO, (b) C1BN, (c) C3BN, (d) C6BN sintered at 1100°C/3h

Figure III-3 shows the SEM/EDX mapping images of CCTO (Figure III-3a), C1BN (Figure III-3b) and C3BN (Figure III-3c). It confirms the presence of all major elements (Ca, Ti, Cu and O). It is clear that ading boron nitride nanosheets leads to increase the ratio of Copper at grain boundaries. Thus confirms that adding boron nitride nanosheets enhance the formation of a liquid phase originated from the eutectic phase TiO_2-CuO. Using SEM/EDX mapping could not detect the dispersion of h-BN nanosheets because B and N are a light element and EDX is not sensetive to these elements.

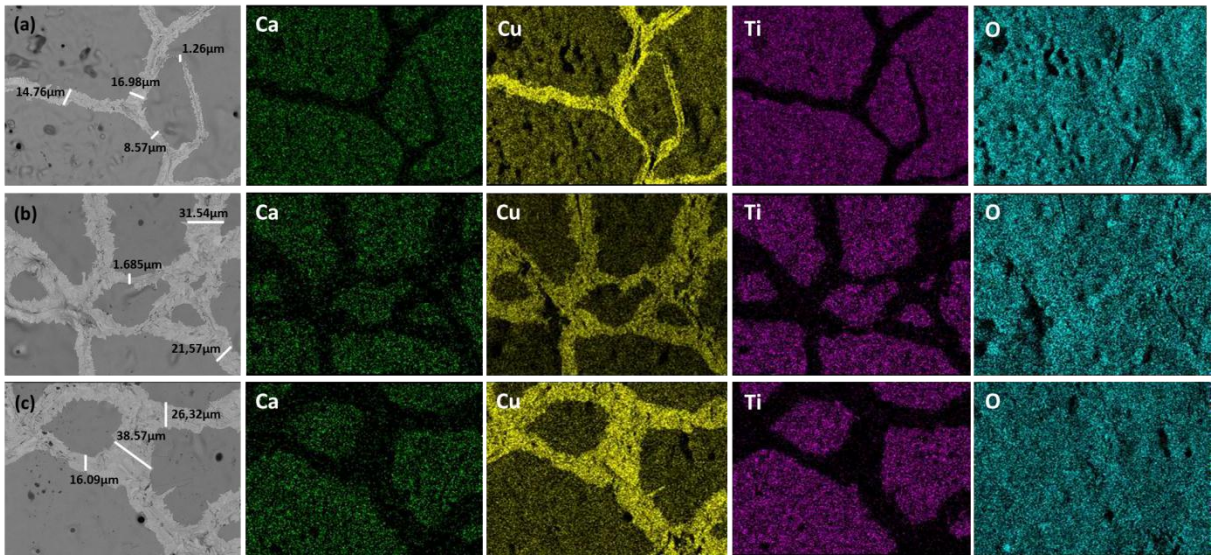

Figure III-3 : SEM/EDX mapping of (a) CCTO, (b) C1BN and (c) C3BN ceramics.

High resolution XPS analysis of pure and composite CCTO has been carried out to know the oxidation states of the constituent elements and to confirm the presence of oxygen vacancies responsible of a good electrochemical behavior. The XPS scan shows the presence of Ti 2p, Cu 2p, and O 1s at their corresponding binding energies in pure CCTO and the presence of Ti 2p, Cu 2p, O 1s, B 1s and N 1s in CCTO-BN composites (Figure III-4). Figure III-4a shows XPS data of oxygen atoms for CCTO composite, it indicates an increase in the distortion of anatase lattice with the increase of h-BN percentage in CCTO matrix. As shown in Figure III-4a, O1s spectrum can be fitted with four peaks 528.9±0.0053, 530.4±0.026, 531.8±0.012, and 533.2±0.133 eV corresponding to O-(Cu/Ca), O-Ti, O-Lattice and O-H_2O respectively, as seen that for composites peaks are slightly shifted to higher binding energy (ev). The ratios of O-B/O-Lattice that refers to the surface oxygen vacancies, increase from 0.35 for CCTO to 0.39 and 0.47 for C1BN and C3BN respectively suggesting that increasing the amount of boron nitride nanosheets increase the surface defects of the material. A slight shift of peaks to a lower binding energy is observed for $Ti^{4+}$and Cu^{2+} (Figure III-4). Shifting of peaks are maybe due to the segregation of Cu on grain boundaries, in which the segragation increases the surface stress and lead to produce an effective pressure to raise the force constants [60], [61]. In addition to that the shifting confirm the partial reduction of Ti^{4+} and Cu^{2+} with the creation of oxygen vacancies and the insertion of B and N in TiO lattice. In B1s XPS spectra (figure III-4e) the peak corrsponding to B-N bond in

boron nitride nanosheets appears peak C1BN material; from XPS spectra of C1BN it can be conclude that Boron nitride nanosheets are not involved into CCTO lattice. With increasing BN amount, four different peaks appear for C3BN material at 187.8±0.124, 190.1±0.092, 192.1±0.106 and 195±0.179 ev corresponding to TiB_2 [62], B-N bond in BN nanosheets, B-O bonds due to a defects in BN layers [63], and B-O-Ti bond respectively. Referring to XPS data, Boron nitride nanosheets is decomposed, oxidized and incorporated in TiO_2 lattice. In figure III-4f two peaks at around 400±0.5 eV and 401.8±0.21 ev appears. These peaks are related to the intertitial nitrogen in form Ti-O-N (Ti-N-O linkages) and the oxidized nitrogen on the surface respectively [64] in C1BN and C3BN materials. A peak refered to B-N bond in Boron nitride nanosheets appears for C1BN [65] confirming that 1% of boron nitride was not enough to insert bore and nitrogen atom into the lattice. Boron nitride nanosheets reacted in different way according to their amount. As seen from XPS data, Bore and nitrogen atomes are highly inserted in CCTO lattice for 3% of boron nitride nanosheets (figure 4e and 4f), with default residual of boron nitride in comparison to C1BN according to the composition ratio . The characteristic peak of intertial Bore into TiO_2 lattice for C1BN material can not be fitted due to the small amount of boron nitride naosheets.

Thus the observed shift of Ti 2p peaks is due to defects in TiO_2 lattice resulting from the substitution of oxygen atom (Pauling electronegativity ~3.44) by a lower electronegativity atoms, B (2.04) and N (3.04) leading to an increase in electrons surroding the Ti atoms [62].

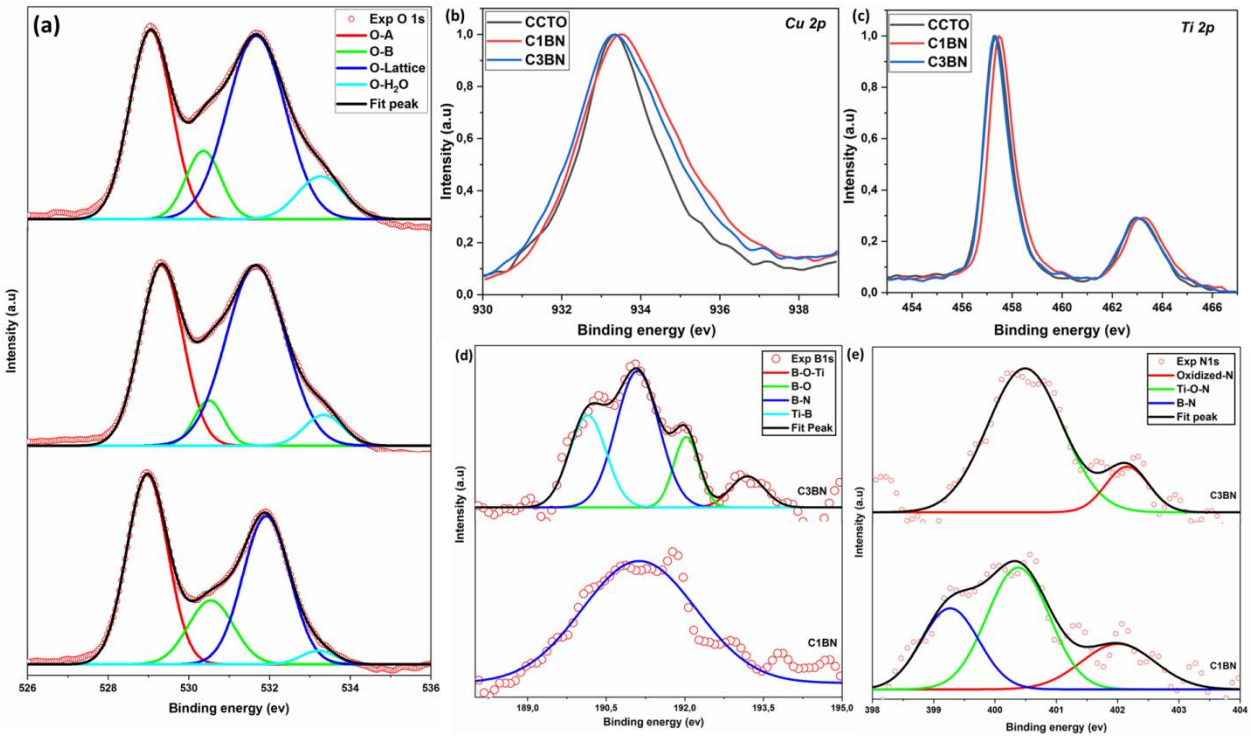

Figure III-4 : High resolution XPS Spectra of (a) O 2s, (b) Cu 2p, (c) Ti 2p, (d) B 1s, and (e) N 1s spectra, of CCTO, C1BN, and C3BN.

Pure CCTO and h-BN/CCTO were further studied by confocal Raman analysis. In order to confirm the crystalline quality and the presence of the different phases in the obtained materials, Raman spectra were recorded between 50 and 600 cm^{-1}. Figure III-5 shows the Raman spectra of the grain and grain boundaries regions for the ceramics CCTO, C1BN, C3BN and C6BN. In general, the position of the Raman modes frequencies in metal oxides is affected by the effective charge, the asymmetry, the bond length of the participating atoms and the vibrational modes of atoms. Three main modes close to 445, 506 and 570 cm^{-1} are essential to determine CCTO [66]. All mentioned modes (P7, 8 and 9) are related to TiO_6 clusters. P7 and P8 modes appear in all samples and in both regions corresponding to wavelenght near to 445cm^{-1} and 506cm^{-1} respectively related to TiO_6 clusters in the Ag symmetries. These two modes are slightly shifted to an emission of high energy for 1, 3 and 6% BN samples resulted from a stress generated in c axix produced by B^{3+} and N^{3-} ions introduced in TiO lattice. The third mode P9 close to 570 cm^{-1} (Fg symmetrie) is an antistretching mode Ti-O-Ti for the TiO_6 octahedras and

appears only for CCTO, C3BN and C6BN samples, which mean that the amount of polarization strenght has been influenced by doping because the Raman scattering intensity is determined by amount of polarization strenght [67]. Figure III-5ii shows Raman spectra on grain boundaries; as reported grain boundaries are dominated by CuO. For all samples TiO_2 phase appears. P7 and P8 modes characteristic of CCTO phases are present in different intensity for C1BNand C6BN.

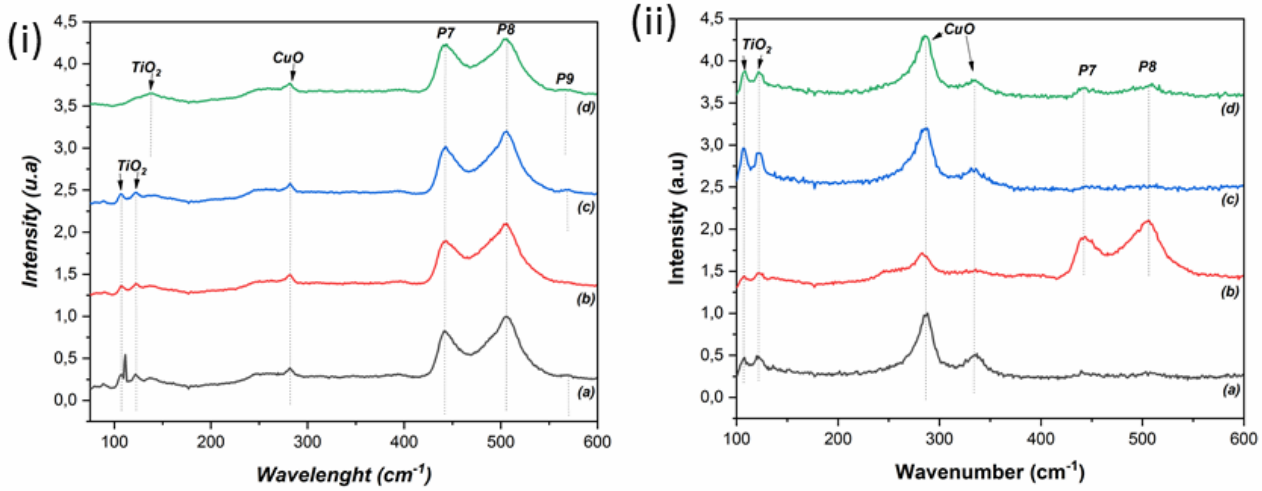

Figure III-5 : Raman shifts on i-grains and ii-grain boundaries of (a) CCTO, (b) C1BN, (c) C3BN and (d) C6BN pellets.

III.3.2 Optical properties

Photoluminescence spectroscopy is used to study the efficiency of charge carrier trapping, migration and transfer. It is used in order to understand the recombinaition between electrons and holes in which a lower recombination rate induce a lower PL intensity. Figure III-6 shows the PL spectra for pure and BN doped CCTO.

The emission spectra have four significant peaks, centered at 390, 480, 700 and 800 nm. UV peak is related to band-band transitions with involvement of phonon [68]. UV emission can be related to band-band transitions or exciton emission [69]–[71]. Liu showed that intensity of excitonic emission depends on surface-to-volume ration of TiO_2 nanoparticles. The increase of the nanoparticle volume resulted in increase of defect emission. In the present work, the UV intensity increased for low concentration of BN doping and then decreased. The changes of UV PL can be related to change of lattice constants and lattice strain after BN doping [72], [73].

Emission, centered at 480 nm is related to self-trapped excitons and oxygen vacancies. Emission bands in NIR region correspond to surface defects [74]. Low intensities of Vis-NIR bands point to high ratio of surface recombination and charge separation.

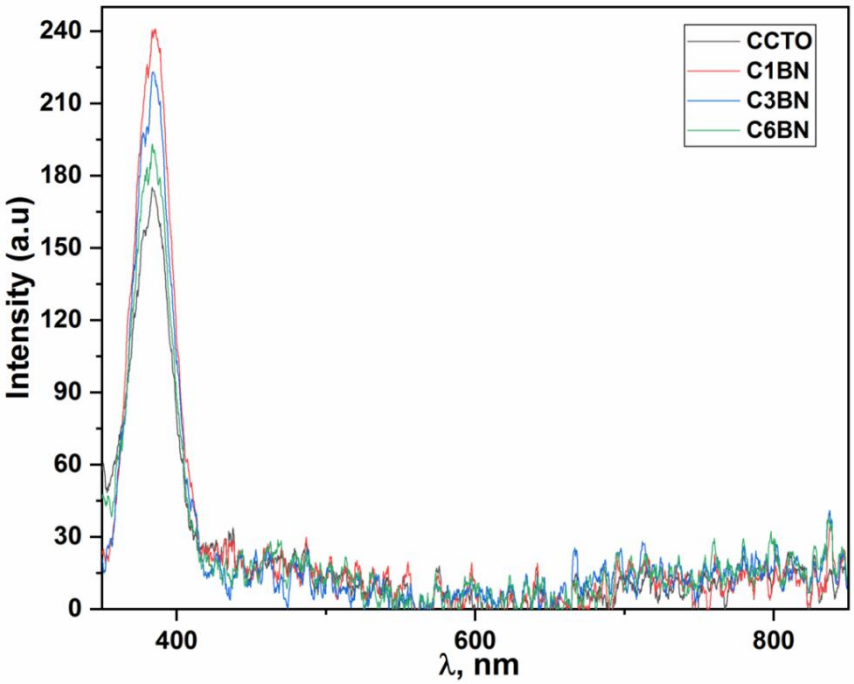

Figure III-6 : Photoluminescence spectra of pure CCTO ceramics, C1BN, C3BN, and C6BN composites ceramics

The optical properties of materials were explored as well by UV-Vis diffuse reflectance spectroscopy and presented in Figure III-7. Since CCTO is a complex perovskite, it can present two band gap in direct and indirect transition [41].

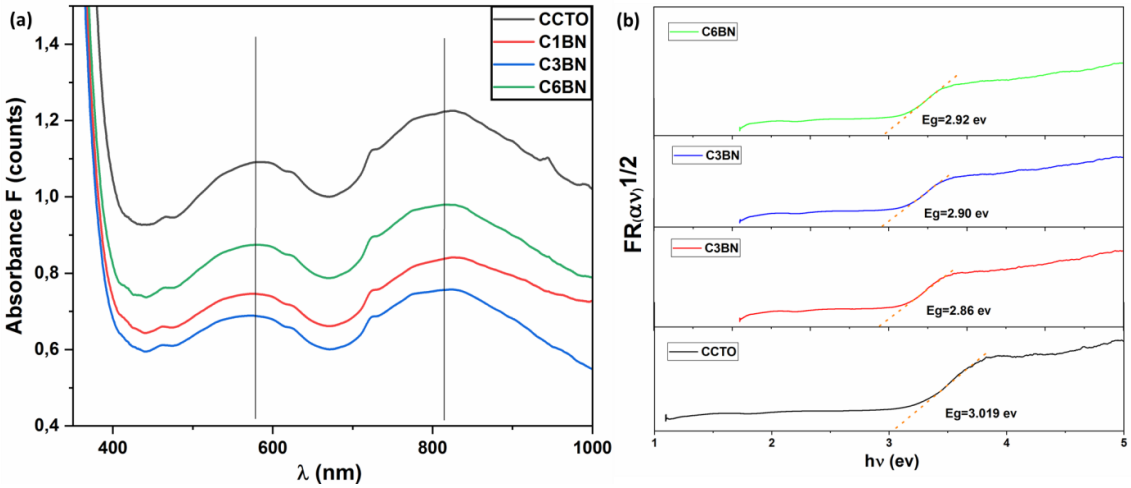

Figure III-7 : (a) Band gap calculation from reflectance spectra and (b) Reflectance spectra of CCTO, C1BN, C3BN, and C6 BN ceramics.

The optical absorption spectra of all materials show the presence of two absorption, at around 450nm and at 680nm which are related to the hybridized valence band (VB) from Cu 3d−O 2p to conduction band (CB) with Ti−3d states (Figure III-7a). In CCTO, the higher energy absorption edge arises due to direct transition from Cu *3d*- O *2p* hybridized valance band to the Ti-*3d* conduction band and the lower energy absorption is attributed as transition between valance band and unoccupied Cu *3d* band.

The absorption peak arround 575nm corresponding to 2.1 eV is refered to the transition between V_o (oxygen vacancies level) and VB and VC. There are slight shift of peaks due to the surface defects and the minor lattice expansion which is beneficial for photoelectroactivity under visible light exposition.

The UV-Vis spectra shows a higher intensity for the composites material and we can notice a slight shift in the wavelengths indicating a change in the band-gap after the addition of Boron Nitride nanosheets to CCTO perovskite.

The optical band gap Eg of the samples was determined by Kubelka-Munk remission function according to the following equation [53]:

$$(\alpha h\nu)^{1/2} = A(h\nu - Eg) \qquad (\textbf{III-1})$$

Where α is the absorption coefficient, ν is light frequency and Eg is the direct transition band gap.

The obtained Eg values for CCTO, C1BN, C3BN and C6BN are 3.01 , 2.86, 2.90 and 2.93 eV respectively (Figure III-7a), which indicate a red shift in the band gap of the material with increasing the boron nitride nanosheets percentage. The band gap of composites could be affected by the presence of oxygen vacancies, and B and N ions in Ti-O bond linkage responsible. Thus the defect level between CB and VB is important to a better photo-electrocatalytic of the semi-conductor in visible light. B^{3+} and N^{3+} ions incorporated in TiO lattice can form a shallow level inside the band gap resulting in the decreasre of band gap energy and extend the spectral response to the visible region [68].

III.3.3 Electrochemical performances

Electrochemical properties of synthesized CCTO samples (CCTO, C1BN, C3BN and C6BN) were measured in dark and under visible exposition using three electrode systems in 1M KOH solution. All curves were recorded at a scan rate of 20 $mV.s^{-1}$ in the potential range of 0.25-1V (Figure III-8a). Current density increases while increasing the percentage of nanofillers and after their exposure to visible light irradiation.

III.3.3.1 Capacitive characterization:

From cyclic voltammetry (CV) and a charge-discharge (CD) cycling, the capacitive behavior of a material can be estimated. The specific capacitance (SC) based on CV and CD cycling can be calculated as follows [75]:

i- $SC(CV)(F\ g\text{-}1) = {Q(c)}/{[scan\ rate * m(g)]}$

ii- $SC(CD)(F.g^{-1}) = {[i(A) * \Delta t(s)]}/{[\Delta E(V) * m(g)]}$

Where Q is anodic charge, i the discharge current in ampere, Δt the discharge time in second corresponding to the voltage difference (ΔE) in volt, and m is the electrode mass in gram (active material).

CCTO activity is measured in ORR range in dark and under visible light exposition as shown in figure III-8a. The behavior of CCTO is different before and after irradiation. It seems inactive in dark without any oxydation or reduction peaks. it can be seen that under visible light a reduction peak appears at 0.47 V vs. AgCl/Ag with no identifiable peak at anodic current. It can be explained by the high resistance of the material at high voltage. Under visible light exposition the photogenareted current increase and CCTO showed a pseudocapacitive behavior.

It is clear that materials behavior change after adding nanofillers and under visible light irradiation, the larger integral area indicates the higher areal capacitance. The rectangular nature of CV curve for the composite C3BN (Figure III-8b) measured in dark and under visible

light showed symmetric anodic and cathodic halves without redox peaks thus indicates the ideal pseudocapacitive nature of material (high reversibility and high pulse charge discharge property) [76]. The behavior of CCTO is different before and after irradiation; it can be seen that under visible light a reduction peak appears at 0.47 V vs. AgCl/Ag with no identifiable peak at anodic current. The distortion of CV curves shape indicates that the electrode does not store charge uniformly.

The behavior of the same samples was measured in OER range between 1 and 2.4 V vs. Ag/AgCl in 1M KOH using the three electrodes system. From figure III-8c, it can be seen that electroactivity of CCTO change after adding 3% of boron nitride nanosheets. A reduction peak appears and the cathodic current is generated. Under visible light C3BN exhibit a larger reduction peak at slightly lower potential. The linear behavior of all sample at anodic potential (>1.4V) suggests that the electrodes could be oxidatively stable in this scanning potential range and that the resistance of the material at high potential becomes higher. This behavior is explained by many factor one of them is the presence of CuO at grain boundaries. According to XRD and XPS results, Cu-defects on grain boundaries appeared after sintering and during cooling can act as acceptors, besides the n-type semiconductor grains [77]. It is well known that CuO is used as an active agent in electrochemical reaction, especially in their micro and nanoscale because they can generate an intracellular reactive oxygen species such as hydrogen peroxide [78]. The best behavior is given for C3BN with a pseudocapacitive behavior in dark and under exposure of visible light, because of the presence of more than phase (TiB_2, B-O-Ti, and oxygen vacancies) known as semiconducting and good electronic transport agents comparable to metals or metal oxides [53], [79]. The higher photocurrent density was observed under the light illumination from LSV current in OER and ORR range (Figure III-9a,b) for C3BN pellets which was attributed as light harvesting ability and narrow band gap of the composite. The interband electron transition due to photon absorption during visible light irradiation results into the generation of photocurrent and four fold increase of current density. LSV and cyclic voltammetry showed that the C3BN can be used effectively as photocatalyst and photoelectrode materials. The onset in ORR range is at 0.5V.

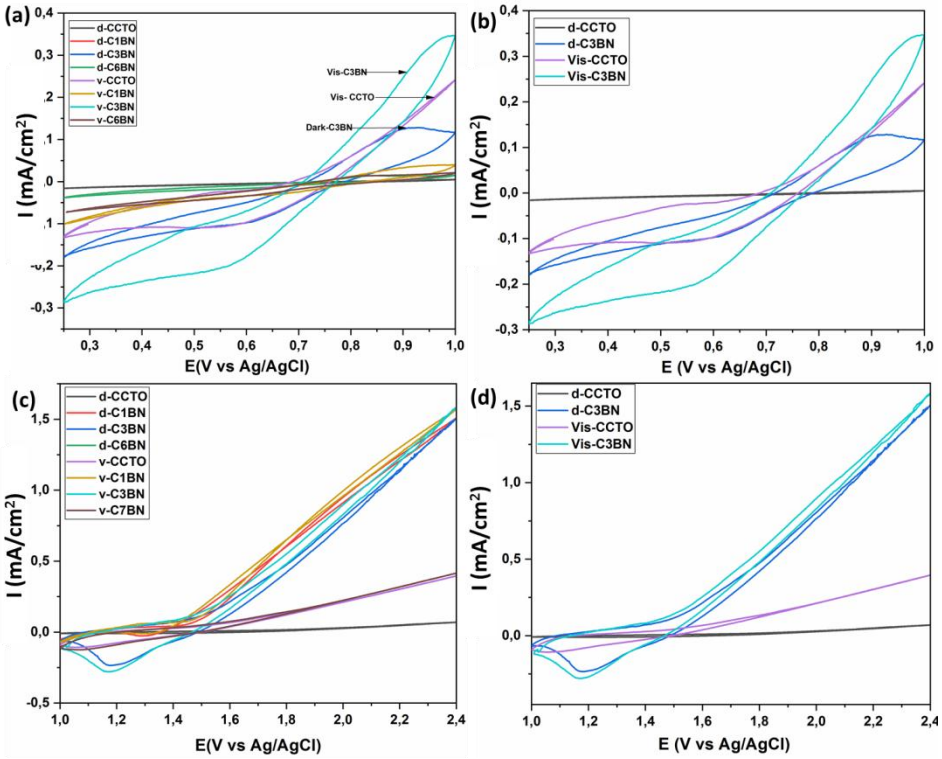

Figure III-8: CV curves (a) CCTO, C1BN, C3BN, and C6 BN ceramics in dark and under visible light in ORR range. (b) CCTO and C3BN in dark and under visible light in ORR range. (c) CCTO, C1BN, C3BN, and C6 BN ceramics in dark and under visible light in OER range. (In 1M KOH vs Ag/AgCl)

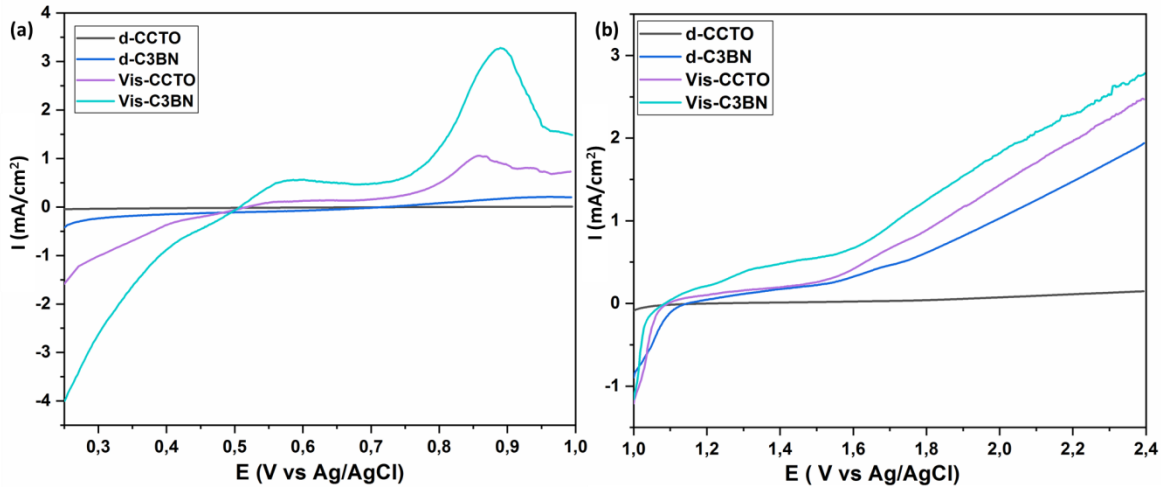

Figure III-9: LSV curves of CCTO, C1BN, C3BN, and C6BN ceramics in dark and under visible light irradiation in 1M KOH vs Ag/AgCl in (a) ORR range and (b) OER range.

Electrochemical impedance spectroscopy (EIS) is used to evaluate the electrical conductivity and capacitive characteristics of electrode materials. Figure III-10 (a,bc,d) shows the Nyquist plots of our materials in the applied potential range of 0.4V-0.6V vs. Ag/AgCl under dark and visible light.

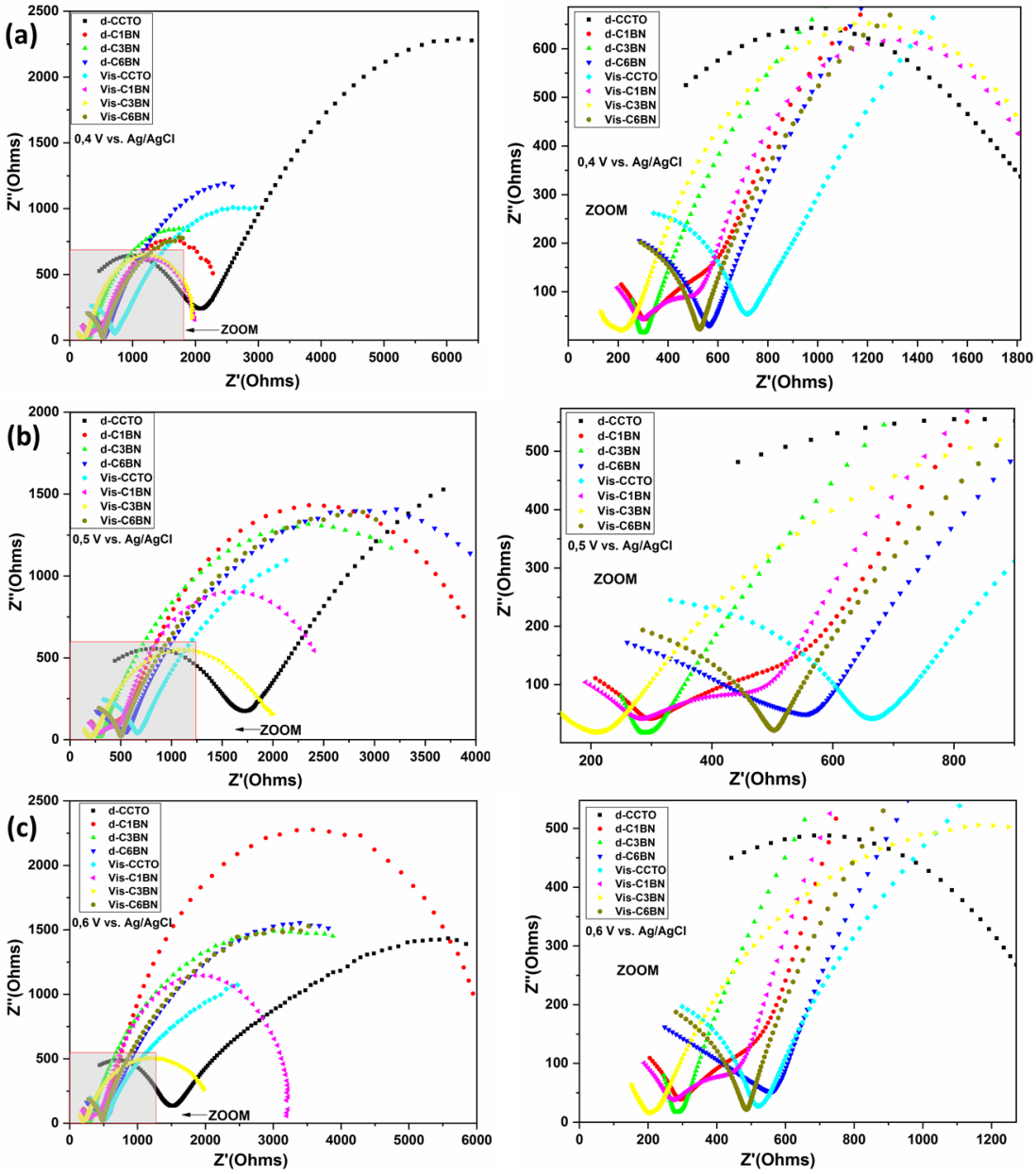

Figure III-10 : The Nyquist plot of CCTO, C1BN, C3BN, and C6BN ceramics in dark and under visible light irradiation at (a) 0.4V vs. Ag/AgCl, (b) 0.5V vs. Ag/AgCl and (c) 0.6V vs. Ag/AgCl.

As shown in Figure III-10 all Nyquist plots showed a small semi-circle in high and medium frequencies and a large semi-circle in low frequency region but the arc diameter change for different material. The larger semi-circle is showed for pure CCTO, it can be seen that the resistance decrease after adding nanosheets and after their exposure to visible light irradiation For quantitative analysis, experimental data of impedance spectra have been fitted to the model depicted by the equivalent circuit shown in Figure III-11. In the model of figure III-11, R_1 is the resistance of electrolyte (1M KOH solution). The parallel combination of the interfacial charge transfer resistance (R_2 and R_3 resistance of grains boundaries and grain respectively) and the constant phase element (CPE) is also included in this circuit. The CPE instead of a capacitor is taken in consideration for frequency dispersion. R_2 and R_3 values are mentioned in Table III-2. The resistances decrease after adding boron nitride nanosheets maybe related to the formation of conducting CuO phases at grain boundaries and the presence of surface defects as oxygen vacancies due to the B-N codoped TiO_2 lattice. This finding indicates that the formation of Ti synergetic bond with N and B atoms produce more accessible active sites and multi charged electrons for electrochemical reactions [80], [81].

Table III-1 : EIS parameters in all materials

	R_2		R_3	
	Dark	**Visible**	**Dark**	**Visible**
CCTO	**1871±5.05**	**815.1±16.81**	**7486±4.681**	**4476±16.56**
CCTO (1%BN)	**594.8±19.41**	**363.8±7.696**	**3382±12.95**	**2074±5.17**
CCTO (3%BN)	**744.7±3.95**	**344±55.22**	**4303±2.378**	**1869±11.36**
CCTO (6%BN)	**4608±4.906**	**585.6±14.38**	**1492±107.5**	**4564±2.469**

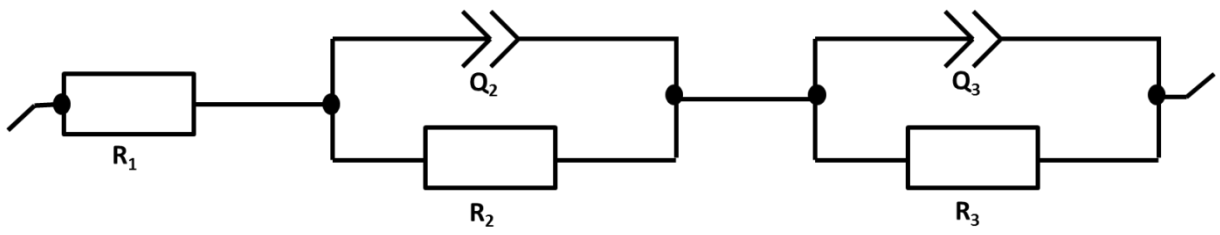

Figure III-11 : EIS equivalent circuit for the impedance behavior.

First step of oxygen reduction reaction takes place when the oxygen molecules are absorbed on the surface of the catalysts and it reduced into O^{2-}. The lowest resistance is given for C3BN under visible light which is in agreement with CV curves. The EIS analysis confirms that the C3BN under visible light has better charge transport properties which results into improved electrocatalytic activity during oxygen reduction reaction.

Under visible light exposition, CCTO behavior change and the current density start to increase. A reduction peak appear leading to decrease CCTO resistance. The infinite transmissive diffusion process start to increase at dark after adding BN nanosheets. . Best behavior was recorded to C3BN under visible light as shown from CV curves in ORR range (Figure III-8a), and the lowest resistance as shown from Nyquist plots, due to the increased adsorption of O^{2-} on the catalysts surface. The lowest charge transfer resistance results into higher production of the peroxide ion (HO^{2-}). The adsorption of HO^{2-} on the catalysts surface is the second step of the oxygen reduction reaction. As presented in figure III-12 (C3BN), the resistance increases while decreasing the applied potential because of the adsorbed peroxide ion on the electrode surface. In the last step of oxygen reduction, the peroxide species are further reduced into H_2O. From equation (1) the capacitive behavior can be calculated using the parameters given by fitting Nyquist plots, whereas the capacitive behavior increase from $1.11*10^{-2}$ to $5.3*10^{-2}$ for CCTO in Dark and CCTO_3BN under exposure of visible light respectively.

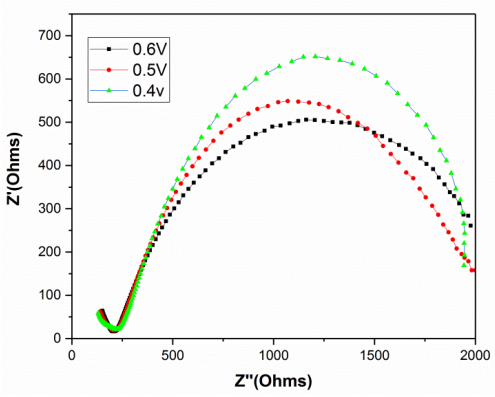

Figure III-12 : The Nyquist plot of C3BN at 0.4V, 0.5V and 0.6V vs Ag/AgCl.

III.4 Conclusion

Investigations focused to find an active photoelectrode under visible light irradiation to ameliorate the photoelectrochemical cell efficiency. In this study we prepared $CaCu_3Ti_4O_{12}$ ceramics with different amount of hexagonal boron nitride nanosheets (1, 3, and 6%). Using Reitveld refinement of XRD data, the formation of pure crystalline phase for all CCTO based materials with small amount of CuO as second phase is detected. The characteristic peaks of h-BN nanosheets are not detected due to the oxidation of h-BN at high temperature. SEM/EDX mapping and Raman spectroscopy showed the segregation of CuO phase on grain boundaries that increase with increasing h-BN weight percentage in the lattice. XPS spectra confirm the incorporation of bore (B) and nitrogen (N) into CCTO lattice. The B and N co-dopant CCTO enhance the partial reduction of Cu^{2+} and Ti^{4+} which is seen by the shift of peaks to lower binding energy, and thus leads to create oxygen vacancy on the surface for charge compensation. The described microstructure of co-doped CCTO materials showed a red shift in band gap energy value detected by UV-Vis spectra. Furthermore, electrochemical measurement were performed in dark and under visible light exposure, they showed that the incorporation of h-BN nanosheets in CCTO lattice enhance the materials efficiency. The photocurrent generation is enhanced 16 times for CCTO with 3% of h-BN under visible light irradiation compare to CCTO. This activity is induced by the presence of new bond in CCTO lattice after the insertion of B and N elements (Ti-O-N and Ti-B-O) and the generated oxygen vacancy on the surface. The conductivity of studied materials was measured using an impedance spectroscopy. The measurements showed that the insertion of co-doped elements and CuO segragtation on grain boundaries acting as n-type semiconductor enhance the electron conductivity on the interface between materials surface and the electrolyte.

References

[1] A. Demirbaş, “Biomass resource facilities and biomass conversion processing for fuels and chemicals,” *Energy Convers. Manag.*, vol. 42, no. 11, pp. 1357–1378, 2001.

[2] K.-H. Ye *et al.*, “Enhancing photoelectrochemical water splitting by combining work function tuning and heterojunction engineering,” *Nat. Commun.*, vol. 10, no. 1, p. 3687, 2019.

[3] M. J. Wornat, R. H. Hurt, N. Y. C. Yang, and T. J. Headley, “Structural and compositional transformations of biomass chars during combustion,” *Combust. Flame*, vol. 100, no. 1, pp. 131–143, 1995.

[4] Y. Li, W. Liu, Z. Zhang, X. Du, L. Yu, and Y. Deng, “A self-powered electrolytic process for glucose to hydrogen conversion,” *Commun. Chem.*, vol. 2, no. 1, p. 67, 2019.

[5] P. H. Moud, E. Kantarelis, K. J. Andersson, and K. Engvall, “Biomass pyrolysis gas conditioning over an iron-based catalyst for mild deoxygenation and hydrogen production,” *Fuel*, vol. 211, pp. 149–158, 2018.

[6] X. Qi, Y. Ren, P. Liang, and X. Wang, “New insights in photosynthetic microbial fuel cell using anoxygenic phototrophic bacteria,” *Bioresour. Technol.*, vol. 258, pp. 310–317, 2018.

[7] V. Nagy *et al.*, “Water-splitting-based, sustainable and efficient H2 production in green algae as achieved by substrate limitation of the Calvin–Benson–Bassham cycle,” *Biotechnol. Biofuels*, vol. 11, no. 1, p. 69, 2018.

[8] K.-Y. Show, Y. Yan, M. Ling, G. Ye, T. Li, and D.-J. Lee, “Hydrogen production from algal biomass – Advances, challenges and prospects,” *Bioresour. Technol.*, vol. 257, pp. 290–300, 2018.

[9] N. Fakhimi, A. Dubini, O. Tavakoli, and D. González-Ballester, “Acetic acid is key for synergetic hydrogen production in Chlamydomonas-bacteria co-cultures,” *Bioresour. Technol.*, vol. 289, p. 121648, 2019.

[10] A. Demirbaş, “Gaseous products from biomass by pyrolysis and gasification: effects of catalyst on hydrogen yield,” *Energy Convers. Manag.*, vol. 43, no. 7, pp. 897–909, 2002.

[11] A. G. Tamirat, J. Rick, A. A. Dubale, W.-N. Su, and B.-J. Hwang, “Using hematite for photoelectrochemical water splitting: a review of current progress and challenges,” *Nanoscale Horiz.*, vol. 1, no. 4, pp. 243–267, 2016.

[12] B. Pivovar, “Catalysts for fuel cell transportation and hydrogen related uses,” *Nat. Catal.*, vol. 2, no. 7, pp. 562–565, 2019.

[13] L. Hui *et al.*, “Overall water splitting by graphdiyne-exfoliated and -sandwiched layered double-

hydroxide nanosheet arrays," *Nat. Commun.*, vol. 9, no. 1, p. 5309, 2018.

[14] A. E. Baumann, D. A. Burns, B. Liu, and V. S. Thoi, "Metal-organic framework functionalization and design strategies for advanced electrochemical energy storage devices," *Commun. Chem.*, vol. 2, no. 1, p. 86, 2019.

[15] Y. Jiao, Y. Zheng, M. Jaroniec, and S. Z. Qiao, "Design of electrocatalysts for oxygen- and hydrogen-involving energy conversion reactions," *Chem. Soc. Rev.*, vol. 44, no. 8, pp. 2060–2086, 2015.

[16] D. T. Tran, H. T. Le, T. L. Luyen Doan, N. H. Kim, and J. H. Lee, "Pt nanodots monolayer modified mesoporous Cu@CuxO nanowires for improved overall water splitting reactivity," *Nano Energy*, vol. 59, pp. 216–228, 2019.

[17] S. Sun *et al.*, "Photoinduced composite of Pt decorated Ni(OH)2 as strongly synergetic cocatalyst to boost H2O activation for photocatalytic overall water splitting," *Appl. Catal. B Environ.*, vol. 243, pp. 253–261, 2019.

[18] R. A. Henning *et al.*, "Characterization of MFe2O4 (M = Mg, Zn) Thin Films Prepared by Pulsed Laser Deposition for Photoelectrochemical Applications," *J. Phys. Chem. C*, vol. 123, no. 30, pp. 18240–18247, Aug. 2019.

[19] N. Guijarro *et al.*, "Evaluating spinel ferrites MFe2O4 (M = Cu, Mg, Zn) as photoanodes for solar water oxidation: prospects and limitations," *Sustain. Energy Fuels*, vol. 2, no. 1, pp. 103–117, 2018.

[20] T. K. Sahu, A. K. Shah, G. Gogoi, A. S. Patra, M. S. Ansari, and M. Qureshi, "Effect of surface overlayer in enhancing the photoelectrochemical water oxidation of in situ grown one-dimensional spinel zinc ferrite nanorods directly onto the substrate," *Chem. Commun.*, vol. 54, no. 74, pp. 10483–10486, 2018.

[21] S. Chandrasekaran *et al.*, "Spinel photocatalysts for environmental remediation, hydrogen generation, CO2 reduction and photoelectrochemical water splitting," *J. Mater. Chem. A*, vol. 6, no. 24, pp. 11078–11104, 2018.

[22] Y. Guo, Y. Fu, Y. Liu, and S. Shen, "Photoelectrochemical activity of ZnFe2O4 modified α-Fe2O3 nanorod array films," *RSC Adv.*, vol. 4, no. 70, pp. 36967–36972, 2014.

[23] K. J. McDonald and K.-S. Choi, "Synthesis and Photoelectrochemical Properties of Fe2O3/ZnFe2O4 Composite Photoanodes for Use in Solar Water Oxidation," *Chem. Mater.*, vol. 23, no. 21, pp. 4863–4869, Nov. 2011.

[24] J. Zhang, Z. Zhao, Z. Xia, and L. Dai, "A metal-free bifunctional electrocatalyst for oxygen

reduction and oxygen evolution reactions," *Nat. Nanotechnol.*, vol. 10, p. 444, Apr. 2015.

[25] M. Shao, Q. Chang, J.-P. Dodelet, and R. Chenitz, "Recent Advances in Electrocatalysts for Oxygen Reduction Reaction," *Chem. Rev.*, vol. 116, no. 6, pp. 3594–3657, Mar. 2016.

[26] N.-T. Suen, S.-F. Hung, Q. Quan, N. Zhang, Y.-J. Xu, and H. M. Chen, "Electrocatalysis for the oxygen evolution reaction: recent development and future perspectives," *Chem. Soc. Rev.*, vol. 46, no. 2, pp. 337–365, 2017.

[27] W. Li *et al.*, "WO3 Nanoflakes for Enhanced Photoelectrochemical Conversion," *ACS Nano*, vol. 8, no. 11, pp. 11770–11777, Nov. 2014.

[28] F. Cao, G. Oskam, G. J. Meyer, and P. C. Searson, "Electron Transport in Porous Nanocrystalline TiO2 Photoelectrochemical Cells," *J. Phys. Chem.*, vol. 100, no. 42, pp. 17021–17027, Jan. 1996.

[29] I. S. Cho *et al.*, "Branched TiO2 Nanorods for Photoelectrochemical Hydrogen Production," *Nano Lett.*, vol. 11, no. 11, pp. 4978–4984, Nov. 2011.

[30] Y. Lu *et al.*, "Self-hydrogenated shell promoting photocatalytic H2 evolution on anatase TiO2," *Nat. Commun.*, vol. 9, no. 1, p. 2752, 2018.

[31] L. Sun, Y. Wang, F. Raziq, Y. Qu, L. Bai, and L. Jing, "Enhanced photoelectrochemical activities for water oxidation and phenol degradation on WO3 nanoplates by transferring electrons and trapping holes," *Sci. Rep.*, vol. 7, no. 1, p. 1303, 2017.

[32] J. Su, X. Feng, J. D. Sloppy, L. Guo, and C. A. Grimes, "Vertically Aligned WO3 Nanowire Arrays Grown Directly on Transparent Conducting Oxide Coated Glass: Synthesis and Photoelectrochemical Properties," *Nano Lett.*, vol. 11, no. 1, pp. 203–208, Jan. 2011.

[33] Y. Liu, J. Li, W. Li, Y. Yang, Y. Li, and Q. Chen, "Enhancement of the Photoelectrochemical Performance of WO3 Vertical Arrays Film for Solar Water Splitting by Gadolinium Doping," *J. Phys. Chem. C*, vol. 119, no. 27, pp. 14834–14842, Jul. 2015.

[34] K. Li, Z. Huang, X. Zeng, B. Huang, S. Gao, and J. Lu, "Synergetic Effect of Ti3+ and Oxygen Doping on Enhancing Photoelectrochemical and Photocatalytic Properties of TiO2/g-C3N4 Heterojunctions," *ACS Appl. Mater. Interfaces*, vol. 9, no. 13, pp. 11577–11586, Apr. 2017.

[35] J. Su, L. Guo, N. Bao, and C. A. Grimes, "Nanostructured WO3/BiVO4 Heterojunction Films for Efficient Photoelectrochemical Water Splitting," *Nano Lett.*, vol. 11, no. 5, pp. 1928–1933, May 2011.

[36] S. Sakthivel, M. Janczarek, and H. Kisch, "Visible Light Activity and Photoelectrochemical Properties of Nitrogen-Doped TiO2," *J. Phys. Chem. B*, vol. 108, no. 50, pp. 19384–19387, Dec. 2004.

[37] T. Zhang *et al.*, “Iron-doping-enhanced photoelectrochemical water splitting performance of nanostructured WO3: a combined experimental and theoretical study,” *Nanoscale*, vol. 7, no. 7, pp. 2933–2940, 2015.

[38] A. A. Murashkina *et al.*, “Influence of the Dopant Concentration on the Photoelectrochemical Behavior of Al-Doped TiO2,” *J. Phys. Chem. C*, vol. 122, no. 14, pp. 7975–7981, Apr. 2018.

[39] X. Zhang, Y. Liu, S.-T. Lee, S. Yang, and Z. Kang, “Coupling surface plasmon resonance of gold nanoparticles with slow-photon-effect of TiO2 photonic crystals for synergistically enhanced photoelectrochemical water splitting,” *Energy Environ. Sci.*, vol. 7, no. 4, pp. 1409–1419, 2014.

[40] Q. Liu, D. Ding, C. Ning, and X. Wang, “Black Ni-doped TiO2 photoanodes for high-efficiency photoelectrochemical water-splitting,” *Int. J. Hydrogen Energy*, vol. 40, no. 5, pp. 2107–2114, Feb. 2015.

[41] D. C. Sinclair, T. B. Adams, F. D. Morrison, and A. R. West, “CaCu3Ti4O12: One-step internal barrier layer capacitor,” *Appl. Phys. Lett.*, vol. 80, no. 12, pp. 2153–2155, Mar. 2002.

[42] J. H. Clark *et al.*, “Visible Light Photo-oxidation of Model Pollutants Using CaCu3Ti4O12: An Experimental and Theoretical Study of Optical Properties, Electronic Structure, and Selectivity,” *J. Am. Chem. Soc.*, vol. 133, no. 4, pp. 1016–1032, Feb. 2011.

[43] H. S. Kushwaha, N. A. Madhar, B. Ilahi, P. Thomas, A. Halder, and R. Vaish, “Efficient Solar Energy Conversion Using CaCu3Ti4O12 Photoanode for Photocatalysis and Photoelectrocatalysis,” *Sci. Rep.*, vol. 6, p. 18557, Jan. 2016.

[44] J.-W. Lee, G.-H. Lee, D.-J. Shin, J. Kim, S.-J. Jeong, and J.-H. Koh, “Ag-migration effects on the metastable phase in CaCu3Ti4O12 capacitors,” *Sci. Rep.*, vol. 8, no. 1, p. 1392, 2018.

[45] A. Sen and K. K. Chattopadhyay, “Nanostructured CaCu3Ti4O12 for environmental remediation through visible light active catalysis,” *J. Mater. Sci. Mater. Electron.*, vol. 27, no. 10, pp. 10393–10398, 2016.

[46] R. Hailili, Z.-Q. Wang, X.-Q. Gong, and C. Wang, “Octahedral-shaped perovskite CaCu3Ti4O12 with dual defects and coexposed {(001), (111)} facets for visible-light photocatalysis,” *Appl. Catal. B Environ.*, vol. 254, pp. 86–97, Oct. 2019.

[47] R. Hailili *et al.*, “Oxygen vacancies induced visible-light photocatalytic activities of CaCu3Ti4O12 with controllable morphologies for antibiotic degradation,” *Appl. Catal. B Environ.*, vol. 221, pp. 422–432, Feb. 2018.

[48] H. S. Kushwaha, A. Halder, P. Thomas, and R. Vaish, “CaCu3Ti4O12: A Bifunctional Perovskite Electrocatalyst for Oxygen Evolution and Reduction Reaction in Alkaline Medium,” *Electrochim.*

Acta, vol. 252, pp. 532–540, 2017.

[49] S. Maity, M. Samanta, A. Sen, and K. K. Chattopadhyay, "Investigation of electrochemical performances of ceramic oxide CaCu3Ti4O12 nanostructures," *J. Solid State Chem.*, vol. 269, pp. 600–607, 2019.

[50] M. Weber *et al.*, "Enhanced electrocatalytic performance triggered by atomically bridged boron nitride between palladium nanoparticles and carbon fibers in gas-diffusion electrodes," *Appl. Catal. B Environ.*, vol. 257, p. 117917, 2019.

[51] D. Gonzalez Ortiz, C. Pochat-Bohatier, J. Cambedouzou, M. Bechelany, and P. Miele, "Pickering emulsions stabilized with two-dimensional (2D) materials: A comparative study," *Colloids Surfaces A Physicochem. Eng. Asp.*, vol. 563, pp. 183–192, 2019.

[52] M. Bechelany, A. Brioude, S. Bernard, P. Stadelmann, D. Cornu, and P. Miele, "Boron nitride multiwall nanotubes decorated with BN nanosheets," *CrystEngComm*, vol. 13, no. 21, pp. 6526–6530, 2011.

[53] M. Nasr *et al.*, "High photodegradation and antibacterial activity of BN–Ag/TiO2 composite nanofibers under visible light," *New J. Chem.*, vol. 42, no. 2, pp. 1250–1259, 2018.

[54] M. Öner, A. A. Çöl, C. Pochat-Bohatier, and M. Bechelany, "Effect of incorporation of boron nitride nanoparticles on the oxygen barrier and thermal properties of poly(3-hydroxybutyrate-co-hydroxyvalerate)," *RSC Adv.*, vol. 6, no. 93, pp. 90973–90981, 2016.

[55] V. Thangaraj *et al.*, "Fluorescence Quenching of Sulfo-rhodamine Dye over Graphene Oxide and Boron Nitride Nanosheets," *Eur. J. Inorg. Chem.*, vol. 2016, no. 13-14, pp. 2125–2130, May 2016.

[56] J. Biscarat, M. Bechelany, C. Pochat-Bohatier, and P. Miele, "Graphene-like BN/gelatin nanobiocomposites for gas barrier applications," *Nanoscale*, vol. 7, no. 2, pp. 613–618, 2015.

[57] J. Jumpatam *et al.*, "Improved giant dielectric properties of CaCu3Ti4O12 via simultaneously tuning the electrical properties of grains and grain boundaries by F− substitution," *RSC Adv.*, vol. 7, no. 7, pp. 4092–4101, 2017.

[58] R. Schmidt, S. Pandey, P. Fiorenza, and D. C. Sinclair, "Non-stoichiometry in 'CaCu3Ti4O12' (CCTO) ceramics," *RSC Adv.*, vol. 3, no. 34, pp. 14580–14589, 2013.

[59] M. A. de la Rubia, J. J. Reinosa, P. Leret, J. J. Romero, J. de Frutos, and J. F. Fernández, "Experimental determination of the eutectic temperature in air of the CuO–TiO2 pseudobinary system," *J. Eur. Ceram. Soc.*, vol. 32, no. 1, pp. 71–76, 2012.

[60] S. V Bobylev and I. A. Ovid'ko, "Stress-driven migration of deformation-distorted grain boundaries in nanomaterials," *Acta Mater.*, vol. 88, pp. 260–270, 2015.

[61] D. Magnfält, A. Fillon, R. D. Boyd, U. Helmersson, K. Sarakinos, and G. Abadias, “Compressive intrinsic stress originates in the grain boundaries of dense refractory polycrystalline thin films,” *J. Appl. Phys.*, vol. 119, no. 5, p. 55305, Feb. 2016.

[62] Y. H. Lu, Z. F. Zhou, P. Sit, Y. G. Shen, K. Y. Li, and H. Chen, “X-Ray photoelectron spectroscopy characterization of reactively sputtered Ti–B–N thin films,” *Surf. Coatings Technol.*, vol. 187, no. 1, pp. 98–105, 2004.

[63] D. Zhao, Y. Yu, C. Cao, J. Wang, E. Wang, and Y. Cao, “The existing states of doped B3+ ions on the B doped TiO2,” *Appl. Surf. Sci.*, vol. 345, pp. 67–71, 2015.

[64] L. Li *et al.*, “Framework Cu-doped boron nitride nanobelts with enhanced internal electric field for effective Fenton-like removal of organic pollutants,” *J. Mater. Chem. A*, vol. 7, no. 12, pp. 6946–6956, 2019.

[65] A. A. Nada, M. F. Bekheet, R. Viter, P. Miele, S. Roualdes, and M. Bechelany, “BN/GdxTi(1-x)O(4-x)/2 nanofibers for enhanced photocatalytic hydrogen production under visible light,” *Appl. Catal. B Environ.*, vol. 251, pp. 76–86, Aug. 2019.

[66] S. Orrego, J. A. Cortés, R. A. C. Amoresi, A. Z. Simões, and M. A. Ramírez, “Photoluminescence behavior on Sr2+ modified CaCu3Ti4O12 based ceramics,” *Ceram. Int.*, vol. 44, no. 9, pp. 10781–10789, Jun. 2018.

[67] S. Rani, N. Ahlawat, K. M. Sangwan, R. Punia, and A. Kumar, “An approach for correlating electrically heterogeneous structure to enhanced dielectric properties of Sr and Zn co-substituted CaCu3Ti4O12 ceramics,” *J. Alloys Compd.*, vol. 769, pp. 1102–1112, Nov. 2018.

[68] M. H. Reilly, “Temperature dependence of the short wavelength transmittance limit of vacuum ultraviolet window materials—II theoretical, including interpretations for U.V. spectra of SiO2, GeO2, and Al2O3,” *J. Phys. Chem. Solids*, vol. 31, no. 5, pp. 1041–1056, 1970.

[69] L. Kernazhitsky *et al.*, “Room temperature photoluminescence of anatase and rutile TiO2 powders,” *J. Lumin.*, vol. 146, pp. 199–204, 2014.

[70] S. Mathew *et al.*, “UV-Visible Photoluminescence of TiO2 Nanoparticles Prepared by Hydrothermal Method,” *J. Fluoresc.*, vol. 22, no. 6, pp. 1563–1569, 2012.

[71] B. Liu, L. Wen, and X. Zhao, “The photoluminescence spectroscopic study of anatase TiO2 prepared by magnetron sputtering,” *Mater. Chem. Phys.*, vol. 106, no. 2, pp. 350–353, 2007.

[72] M. Tsega and F. B. Dejene, “Influence of acidic pH on the formulation of TiO2 nanocrystalline powders with enhanced photoluminescence property,” *Heliyon*, vol. 3, no. 2, p. e00246, 2017.

[73] M. Tsega and F. B. Dejene, “Tailoring luminescence properties of a sol–gel drivenTiO2

nanoparticles by ammonia treatment," *Mater. Res. Express*, vol. 4, no. 3, p. 35018, 2017.

[74] I. Iatsunskyi *et al.*, "Study on Structural, Mechanical, and Optical Properties of Al2O3–TiO2 Nanolaminates Prepared by Atomic Layer Deposition," *J. Phys. Chem. C*, vol. 119, no. 35, pp. 20591–20599, Sep. 2015.

[75] T. Shinomiya, V. Gupta, and N. Miura, "Effects of electrochemical-deposition method and microstructure on the capacitive characteristics of nano-sized manganese oxide," *Electrochim. Acta*, vol. 51, no. 21, pp. 4412–4419, 2006.

[76] C.-C. Hu and T.-W. Tsou, "Ideal capacitive behavior of hydrous manganese oxide prepared by anodic deposition," *Electrochem. commun.*, vol. 4, no. 2, pp. 105–109, Feb. 2002.

[77] L.-T. Mei, H.-I. Hsiang, and T.-T. Fang, "Effect of Copper-Rich Secondary Phase at the Grain Boundaries on the Varistor Properties of CaCu3Ti4O12 Ceramics," *J. Am. Ceram. Soc.*, vol. 91, no. 11, pp. 3735–3737, Nov. 2008.

[78] G. Zampardi *et al.*, "Electrochemical Behavior of Single CuO Nanoparticles: Implications for the Assessment of their Environmental Fate," *Small*, vol. 14, no. 32, p. 1801765, Aug. 2018.

[79] F. Huang *et al.*, "Facile Synthesis, Growth Mechanism, and UV−Vis Spectroscopy of Novel Urchin-like TiO2/TiB2 Heterostructures," *Cryst. Growth Des.*, vol. 9, no. 9, pp. 4017–4022, Sep. 2009.

[80] D. Hassen *et al.*, "Nitrogen-doped carbon-embedded TiO2 nanofibers as promising oxygen reduction reaction electrocatalysts," *J. Power Sources*, vol. 330, pp. 292–303, Oct. 2016.

[81] K. Zhang, X. Wang, T. He, X. Guo, and Y. Feng, "Preparation and photocatalytic activity of B–N co-doped mesoporous TiO2," *Powder Technol.*, vol. 253, pp. 608–613, Feb. 2014.

Part IV : Using 2D Graphene Oxide nanosheets to create oxygen vacancies on $CaCu_3Ti_4O_{12}$ surface

Part IV: Using 2D Graphene Oxide nanosheets to create oxygen vacancies on $CaCu_3Ti_4O_{12}$ surface

Abstract

Photoelectrochemical cells are promised devices for hydrogen production via sunlight energy. One of the important challenges in this area is to design photoactive electrodes able to absorb visible light. A good photoelectrochemical behavior depends on the presence of surface active sites and competent to photogenerate current at the lower potential for water splitting. Recent investigations in this field are focusing on perovskite materials such as $CaCu_3Ti_4O_{12}$ (CCTO) as visible light active electrode due its outstanding structure in which CCTO enclose in its structure a visible light absorbance component (CuO) and an ultra violet irradiation recipient (TiO_2). The presence of Surface defects such as oxygen vacancies is mainly responsible for trapping electrons. Therefore we prepared here CCTO with different amount of graphene oxide nanosheets (GO). Physico-chemical characterization of the materials was investigated using X-Ray diffraction (XRD), X-ray photoelectron (XPS), Raman, and scanning electron microscopy (SEM). It showed that the heat treatment of the nanocomposites at high temperatures and the elimination of GO nanosheets lead to the reduction of Ti^{4+} to Ti^{3+} and Cu^{2+} to Cu^{+}, causing a segregation of copper on grain boundaries regions and to a shift of XRD and Raman peaks . The band gap red shift of prepared materials and their optical properties were also investigated using UV-Vis diffuse reflectance and photoluminescence spectroscopies. Electrochemical performance and materials resistivity are measured in dark and under visible light irradiation. CCTO with 3% of GO nanosheets showed 50% higher photocurrent generation than pure phase of CCTO. It showed that CCTO (3%GO) can be a new photoactive electrode for water splitting under visible light.

Key words: *Water splitting, Photoelectrochemical cell, Perovskite $CaCu_3Ti_4O_{12}$, 2D Graphene oxide, Ti^{4+} reduction, Cu^{2+} reduction.*

Graphical abstract

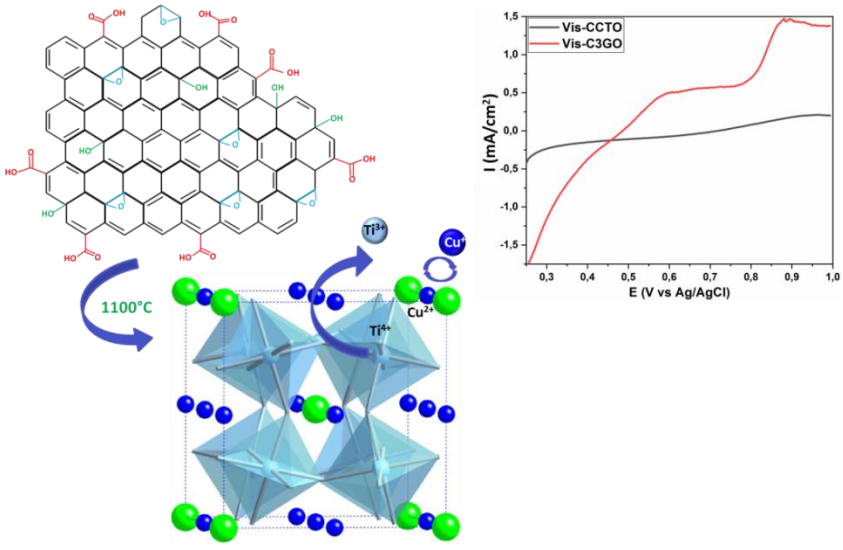

IV.1 Introduction

Currently, a high amount of the global primarily energy need is met by burning fossil fuels. This directly impact the environment and put modern society in front of insufficient energy sources [1], [2]. To address these issues, new renewable energy systems are needed. Hydrogen is an efficient energy carrier that can combine with oxygen in a fuel cell to produce electricity without generating pollutants [3]–[7]. However, the main methods to produce hydrogen comes from steam reforming of natural gas, in which the production demand a consumption of natural resources and production of carbon dioxide as byproduct [8]–[11]. Photoelectrochemical water splitting systems are studied widely, due to their efficient hydrogen production, without pollutant generation [12]–[15]. The produced hydrogen from PEC cells is still in default in comparison to the traditional method; especially that it is limited by the used photoelectrodes. To achieve solar-water-splitting, PEC system employs photoactive semiconductors able to absorb solar light to produce electrons and holes and generate the photovoltage needed to split water [16]–[20].

Since that photoelectrochemical performance depends largely from the stability and efficiency of photoelectrodes, large number of catalysts has been investigated including composites. Noble-metals-based such as Platinum, oxides based Ruthenium (RuO_2) and Iridium (IrO_2) were used as electrodes and show excellent efficiency [21]–[26]. The activity of such photoelectrodes is limited by their instability in alkaline solution, high cost and poor abundant. Carbon-based materials (graphene, graphene oxide, g-C_3N_4) achieve considerable attention due their chemical and optical properties [27], [28]. Nevertheless, their intrinsic inconvenient of bulks such as low surface and high recombination efficiency of photogenerated electron-holes pairs limit the carbon based materials performance under visible light [29]–[33]. Spinel materials known as metal oxide ($A'B'_2O_4$; A'=alkaline-earth and/or transition metals, B'=group 13 elements and /or transition metals) had been investigated due to their enhanced electrocatalytic activity under visible light [34], [35]. However, a lack of fundamental concept about limiting factors has prohibited important advance in their performance.

Perovskite materials (ABO_3 where A= Alkaline earth and or/transition metals and B= transition metals) was widely studied due to its bifunctional electrocatalytic behavior [36]–[38]. Among them, $CaCu_3Ti_4O_{12}$ (CCTO) known as high dielectric material is a double perovskite with a cubic structure ($A'ABO_3$), where A' and A site are occupied by Ca^{2+} and Cu^{2+} and Ti^{4+} is localized at B site [39]. CCTO structure is characterized by incorporating of Ti^{4+} and the open-shell Cu^{2+} into the perovskite without any doping. A distortion of TiO_6 octahedra in the structure forms a square planar structure to produce Jahn-Teller distortion in Cu^{2+}[40]. However the strong covalence bonding of oxygen atom with A'-Cu and B-Ti ions enhance the charge transfer between them, which is a key in electrocatalytic activity [41]. Since those photocatalytic and photoelectrochemical performances of a catalyst mainly depend on light absorption, CCTO is chosen like a candidate because it is a combination from TiO_2 catalyst highly active under UV light irradiation and CuO able to absorb visible light [42], [43].

However the electrocatalytic performance of these materials is still poor due to their large band gap, low active sites and weak electrical conductivity. Recently many defect engineering studies are focusing on the creation of oxygen vacancies in order to obtain superior electrocatalytic performance for these materials. It is known that oxygen vacancies are catalytically active sites and their presence in materials is able to regulate its electronic structure and serve as reactive species [44]–[47]. Hailili *et al.* [48] prepared by molten salt synthesis method different CCTO morphology (cube, polyhedron, nanorod and octahedron). They found that octahedron and nanorod morphologies exhibit the best behavior under visible light, attributed to the high abundant of oxygen vacancies on the surface. Since that the presence of Ti^{3+} enhance the photoelectrochemical and photocatalytic behaviors, thus several investigations focused on Ti^{3+} self doped in TiO_2/ graphene composites in presence of reductant agent [49]–[51].

In this paper we prepared CCTO with different amount of graphene oxide nanosheets (1, 3, and 6%) using a low cost and scalable approach. Graphene nanosheets are known as 2D high surface materials, useful for fabricating inorganic composites due to their electronic property, high transparency, and flexible structure [52]–[54]. [55]. Partially oxidized graphene is favorable for its optical, conductive and chemical properties. The oxidized graphene is

functionalized by carboxylic acid, hydroxyl, and epoxide groups to form the graphene oxide (GO) [56]. GO materials could be insulating or conductive depending on the oxidation degree (C/O ratio) [57], [58]. Furthermore, graphene oxide has been found to be either a p-type or n-type semiconductor [59]. Several investigations used modified graphene in inorganic composites for electronic, photoelectrocatalytic, and photocatalytic application [60]–[62].

In this investigation the materials were formed as pellets in one easy sintering step. The oxidation of GO nanosheets at high temperature into CCTO lattice changes the electronic structure of the material and creates oxygen vacancies on the surface which enhances the photoelectrochemical behavior. The prepared materials were then fully characterized. The crystallinity and vibrational modes of the material were investigated using XRD and Raman spectroscopy. The morphology and element distribution were analysed by scanning electron microscopy. XPS was employed to study the electronic structure of the materials. Optical properties were performed using PL and UV-Vis spectroscopies. Finally we evaluate electrochemical activities (cyclic and linear voltammetry) and the conductivity (impedance measurement) in dark and under visible light irradiation.

IV.2 Experimental Section

IV.2.1 Materials

Titanium (IV) Oxide (TiO_2- CAS Number: 13463-67-7, 99.5%), Potassium Hydroxide (KOH-CAS Number: 01900-20-08, ≥85%), Graphite (CAS Number: 7782-42-5, graphite pulver <20 Micron, synthetic), Sulfuric acid (H_2SO_4, CAS Number: 7664-93-9, 95-98%), Phosphoric acid (H_3PO_4, CAS Number: 7664-38-2, 99%), Potassium Permanganate($KMnO_4$, CAS Number: 7722-64-7, 99.0%), Hydrolic acid (HCl, CAS Number: 7647-01-0, 36.2%), and Absolute Ethanol (CAS Number: 64-17-5, 99.94%) were purchased from Sigma Aldrich. Calcium Carbonate ($CaCO_3$-CAS Number: 471-34-1, 98%) and Copper (II) Oxide (CuO-CAS Number: 1317-38-0, 98%) were purchased from Alfa Aesar. All chemicals were used without any further purification.

IV.2.2 Synthesis of Graphene Oxide (GO)

Graphene oxide was synthesized from natural graphite powder, following modified Hummer's method [63], [64]. Briefly, 3g of graphite were dispersed in concentrated H_2SO_4:H_3PO_4 (9:1, 400 mL) solution. Then, 18 g of $KMnO_4$ were added gradually to the mixture and it was stirred for 12 h. Later on, the mixture was cooled down to room temperature and 3 mL of H_2O_2 were added. A brown precipitate was observed; showing that exfoliation of graphene oxide from graphite was being carried out. After one hour stirring, the GO was separated by centrifugation at 6000 rpm for 10 minutes and the supernatant was decanted away. The resultant precipitates were washed several times with 30% hydrochloric acid and absolute ethanol. Finally, the obtained powder was dried at 50°C for 24 hours to obtain the pure graphene oxide.

IV.2.3 Preparation of $CaCu_3Ti_4O_{12}$ pellets

In an alumina jar (Al_2O_3), a stoichiometric amount of precursors (TiO_2 (1.56g), CuO (1.16g), and $CaCO_3$ (0.48g) is mixed with alumina balls according to a defined ratio (precursors/ball = 1/9), in a ball milling machine for 5h. Then the mixture was calcined at 900°C for 3h to obtain CCTO powders. Powders are then pressed into a mold with 10 mm of diameter and 1-2mm of thickness to form pellets using hydraulic press (3.5T) at room temperature. At the final step the pellet was sintered at 1100°C for 3h.

IV.2.4 Preparation of CCTO (1%GO), CCTO (3%GO), and CCTO (6%GO)

After powders calcination at 900°C for 3h, a pure phase of CCTO is obtained. CCTO powders were mixed with different amount (x) of graphene oxide (GO) nanosheets (%x=1, 3, and 6%) using solid state method. The mixture was then molded into pellets (d=10 mm and e= 1-2mm) using hydraulic press at 3.5T at room temperature. The as-prepared pellets finally were sintered at 1100°C for 3h to obtain CCTO (1%GO), CCTO (3%GO), and CCTO (6%GO) labeled C1GO, C3GO, and C6GO respectively.

IV.2.5 Characterizations of pellets

The crystalline phase of the obtained pellets was analyzed by X-ray diffraction (XRD), using a PANAlytical Xpert-PRO diffractometer equipped with an Xcelerator detector using Ni-filtered Cu-radiation with wavelength of 1.54 A. The scan step size of all prepared pellets was fixed at 0.0167°/step and the time per step was 0.55 sec/step. Rietveld refinement was performed using the FULLPROF program and profile function 7 (Thompson-Cox-Hastings pseudo-Voigt convoluted with axial divergence asymmetry function). The morphology of all ceramics was studied via scanning electron microscopy (SEM), where images were taken with a Hitachi S4800, Japan. Elemental mapping were performed with a Zeiss EVO HD15 microscope coupled with an Oxford X-MaxN EDX detector. Raman spectra were measured by the dispersive Raman spectroscopy (Model Sentera,Bruker, Germany) using 532 nm laser [doubled Nd:YAG laser (neodymium-doped yttrium aluminum garnet)] and a power of 10 mW. In order to investigate the oxidation state of elements in pellets, X-ray photoelectron spectroscopy (XPS) was performed using XPS: monochromatic X-ray source: Al-Kalpha, 1486.6 eV - Resolution FWHM 0.45 eV.

The band gab of pellets was measuring from UV–vis spectra. These spectra were measured by a UV–vis spectrophotometer (Jasco model V-570) equipped with a diffuse reflectance (DR) attachment (Shimadzu IRS-2200). Room temperature photoluminescence (PL) was measured in the range of 350–900 nm. After excitement with a nitrogen Nd:YAG laser (266 nm, 10 mW, 1 kHz), PL was recorded with an optical fiber spectrometer (Ocean Optics usb2000).

IV.2.5.1 Electrochemical Measurement

Electrochemical measurements for oxygen reduction reaction (ORR) and oxygen evolution reaction (OER) were carried out in a three- electrode system using 1 M KOH as the electrolyte in dark and under visible light exposition using 500W linear halogen lamp (the visible light source is in the range of 420-600 nm). CCTO and GO (x%)/CCTO pellets with a diameter of 10 mm was used as working electrode, Ag/AgCl as reference electrode and platinum wire as counter electrode. Electrochemical Impedance spectroscopy measurements in dark and under visible

light irradiation were performed at room temperature in the frequency range of 0.01Hz to 10^6 kHz with voltage bias of 20 mV amplitude.

IV.3 Results and discussions

The obtained pellets were synthesized using mecanosynthesis method followed by sintering step at 1100°C for 3h. Pellets are formed from pure phase of CCTO and CCTO with different amount of graphene oxide nanosheets (%x=1, 3, and 6%). The crystallinity and morphology of pellets are characterized by XRD, SEM, XPS and Raman. The optical properties were investigated using UV-Vis and photoluminescence measurements. Finally, in order to study the performance of obtained materials under visible light and their resistivity, electrochemical measurements (cyclic and linear voltammetry) and impedance spectroscopy were performed in a system of three electrodes in 1M of KOH solution

IV.3.1 Physico-Chemical characterizations

XRD patterns of CCTO and CCTO/x%GO (x=1, 3 and 6% of graphene oxide nanosheets) pellets sintered at 1100°C for 3h were recorded in figure IV-1. The XRD reflections in the measured patterns of all materials can be assigned to the cubic structure of $CaCu_3Ti_4O_{12}$ (space group *Im*-3) as a main phase and monoclinic CuO (space group *C*2/*c*) as minor phase. No additional XRD reflections attributed to GO nanosheets or any of other crystalline carbon/carbides phases were observed in the XRD pattern of all materials, which suggests the oxidations of GO nanosheets as well as any carbon residuals at this high temperature. It can be clearly seen that the intensities of XRD reflections corresponding to $CaCu_3Ti_4O_{12}$ phase differ slightly for different samples, suggesting preferred orientations of crystallites. Moreover, these XRD reflections are shifted to lower two theta angles for the GO containing samples, indicating the increase in the lattice parameters of $CaCu_3Ti_4O_{12}$ phase in these samples. Rietveld refinement of XRD patterns confirmed this increase in lattice parameter *a* from 7.3914(1) Å for CCTO sample to 7.3922 (1), 7.3927 (1) and 7.3942 (1) Å for C1GO, C3GO and C6GO, respectively. This increase in the lattice parameter with the addition of GO can be explained by the partial reduction of smaller cations such as Cu^{2+} and Ti^{4+} to larger Cu^{+} and Ti^{3+} during the oxidation process of GO. It has been

reported that several transition elements can be reduced by CO oxidation [65] that might be formed during the thermal oxidation of GO. The change in the cation stoichiometry of $CaCu_3Ti_4O_{12}$ could be another reason for this increase as the amount of the secondary CuO phase increased with the addition of GO nanosheets according to Rietveld refinement. These results are in good agreement with previous studies showed that Cu deficiency and the partial reduction of Cu^{2+} and Ti^{4+} cations can lead to the expansion of CCTO phase [66].This finding suggests that the samples sintered in the presence of GO nanosheets may contain a defect-rich CCTO phase.

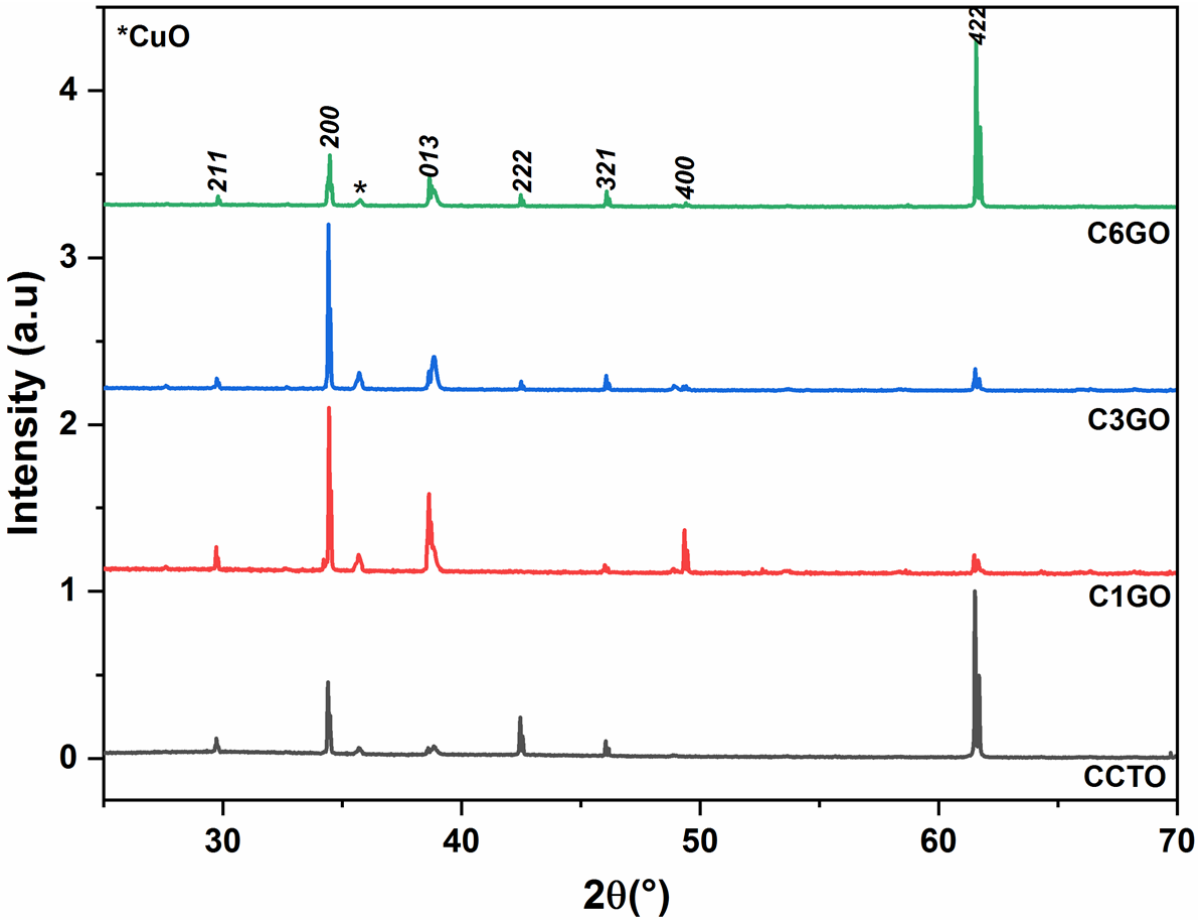

Figure IV-1 : X-ray diffraction patterns of CCTO, C1GO, C3GO and C6GO ceramics sintered at 1100°C/3h.

Surface morphology of CCTO, C1GO, C3GO and C6GO are shown in Figure IV-2a, IV-2b, IV-2c and IV-2d respectively. It is clearly seen that grain and grain boundary growth change after

adding different amount of graphene oxide nanosheets. The grain sizes are reduced progressively after adding GO nanosheets and it can be explained by the increase of grain boundaries thickness. Normally at around 950°C, the eutectic point of CuO-TiO_2 (liquid phase) appears at the surface of the materials. At this point, the atoms can migrate and diffuse easily between grains and grain boundaries. Thus adding GO nanosheets to the lattice enhance surface defects such as oxygen vacancies as it will be shown later from XPS analysis (Figure 4d) and leads to the free migration of atoms on the surface. This phenomena will increase grain boundaries thickness and reduce grain size comparing to the pure CCTO.

SEM EDX mapping, can confirm these results. As shown in Figure IV-3a, IV-3b and IV-3c corresponding to CCTO, C1GO and C3GO, all major elements (Ca, Cu, Ti and O) exist with a homogenous distribution. It is clearly seen that CuO phase are located at grain boundaries and their amount increases after the incorporation of GO nanosheets which is in accordance with XRD and SEM results.

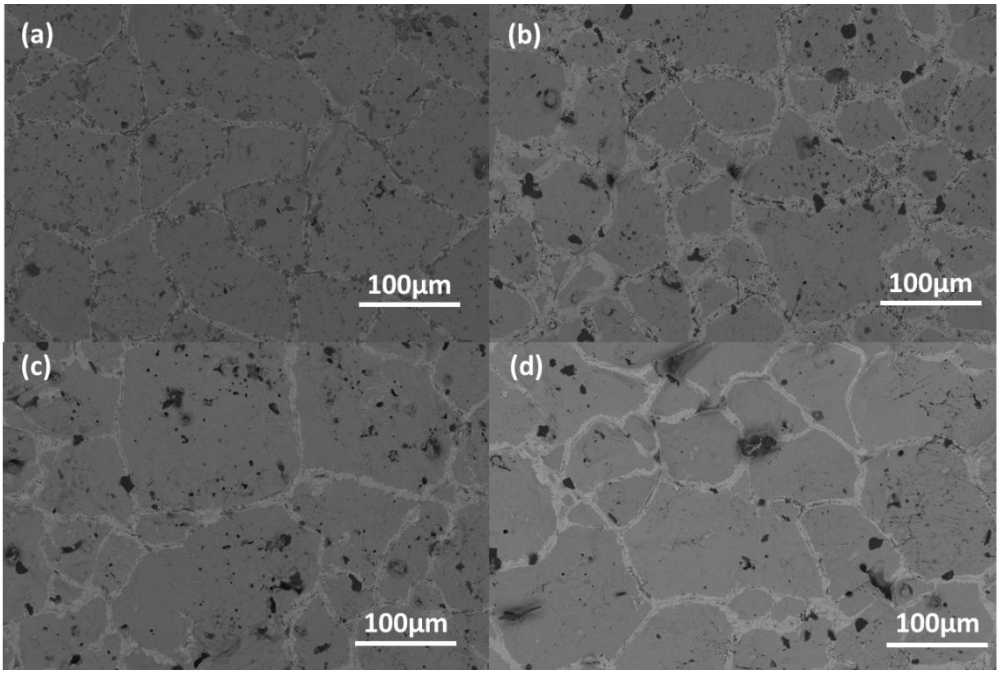

Figure IV-2 : Scanning electron micrographs of the pellets (a) CCTO, (b) C1GO, (c) C3GO, (d) C6GO sintered at 1100°C/3h

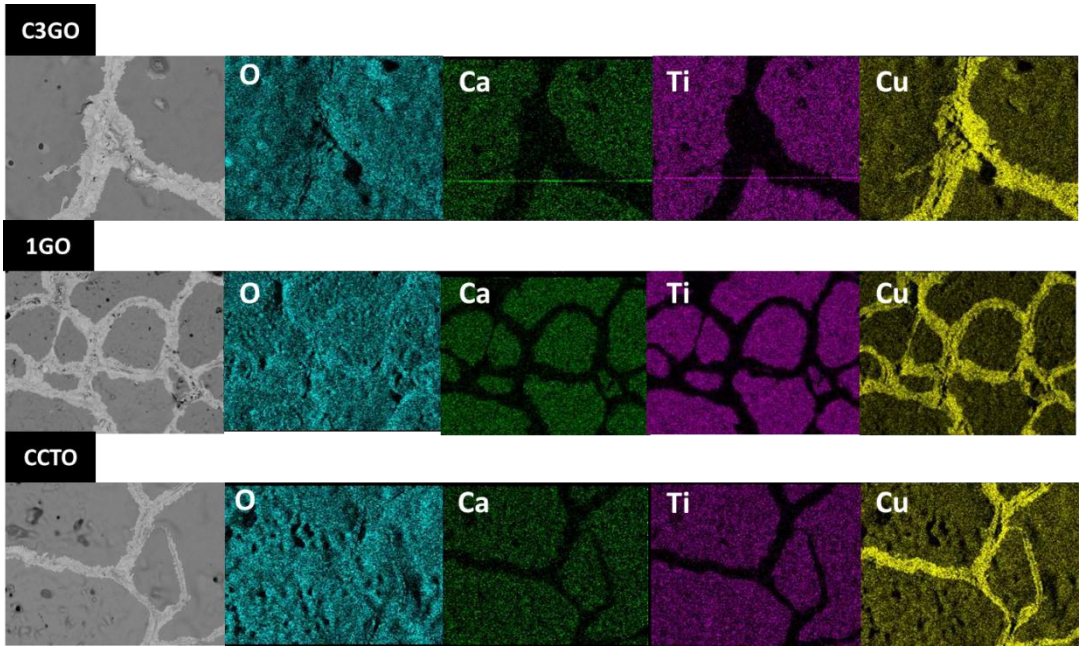

Figure IV-3 : SEM EDX mapping of (a) CCTO, (b) C1GO and (c) C3GO ceramics.

High resolution X-ray photoelectron spectroscopy (XPS) analysis of materials CCTO, C1GO and C3GO has been investigated, to elucidate their chemical composition and chemical states. Figure IV-4a, IV-4b, and IV-4c show the high resolution XPS spectra of O 1s, Ti 2p, and Cu 2p respectively.

In Figure IV-4a the spectrum of O 1s is shown, where four peaks are observed at arround 528.9±0.008 , 530.5±0.072, 531.9±0.026 and 533.2±0.158 eV and are fitted to O-(Cu/Ca), O-Ti, O-Lattice and O-H_2O respectively. Oxygen vacancies on the surface can be estimated using the ratio (O-A+O-B)/(O-Lattice). The values of the ratio are 0.35, 0.24 and 0.56 for CCTO, C1GO and C3GO respectively. As shown from obtained values, oxygen vacancies on the surface vary and increase remarkably for C3GO. The shift of binding energy is due to lattice parameter chaging and oxygen vacancies present in the material as defect, resulting from GO nanosheets oxydation. The crystal structure of CCTO is made up of corner sharing TiO_6 octahedra and CuO_4 square planes. Every TiO_6 (Ti^{4+}) octahedron is corner-shared with six different CuO_4 (Cu^{2+}) square planes, and each square plane with eight different TiO_6 octahedra [67]. Thus any distortion and state chagement can affect the hole structure.

Figure IV-4b showed XPS spectra of Ti 2p in CCTO, C1GO and C3GO. CCTO showed two peaks at 458.1 eV and 463.9 eV corresponding to Ti^{4+} with line separation between Ti $2p_{1/2}$ and Ti $2p_{3/2}$ at about ˜5.63 eV, which is consistent with the standard binding energy of TiO_2 [68]. Adding GO nanosheets and their oxidation at high temperature lead to the reduction of Ti^{4+} to Ti^{3+} as seen by XRD. Results are confirmed with XPS, as seen from figure 4b, a shift to lower binding energy is observed after adding GO nanosheets indicating an influence of GO oxidation on electronic state of Ti element, in which Ti^{4+} can be substitute by Ti^{3+} cations. The highest oxygen vacancy ratio is showed for C3GO, which is in agreement with the binding shift value by 0.4 observed in Ti 2p spectrum (figure IV-4b). Oxygen vacancies must be formed arrounf Ti^{3+} for charge compensation [69].

Figure IV-4c showed XPS spectra of Cu 2p for all materials. A width peak is located at 934.1 eV referring to Cu^{2+} in CCTO. A shifting to lower binding energy is observed after GO nanosheets incorporation, thus can be related to the reduction of Cu^{2+} to Cu^{+} as mentioned from XRD results. The incorporation of GO nanosheets leads to CuO segregation at grain boundaries as seen in Figure IV-2b (SEM/EDX mapping), which mean the decomposition of CuO from CCTO lattice and thus creation of cation vacancies [66]. The oxidation of GO nanosheets and the presence of Ti element on grain boundaries (as seen below in Figure IV-5ii) results in monovalent copper due to the charge neutrality [70].

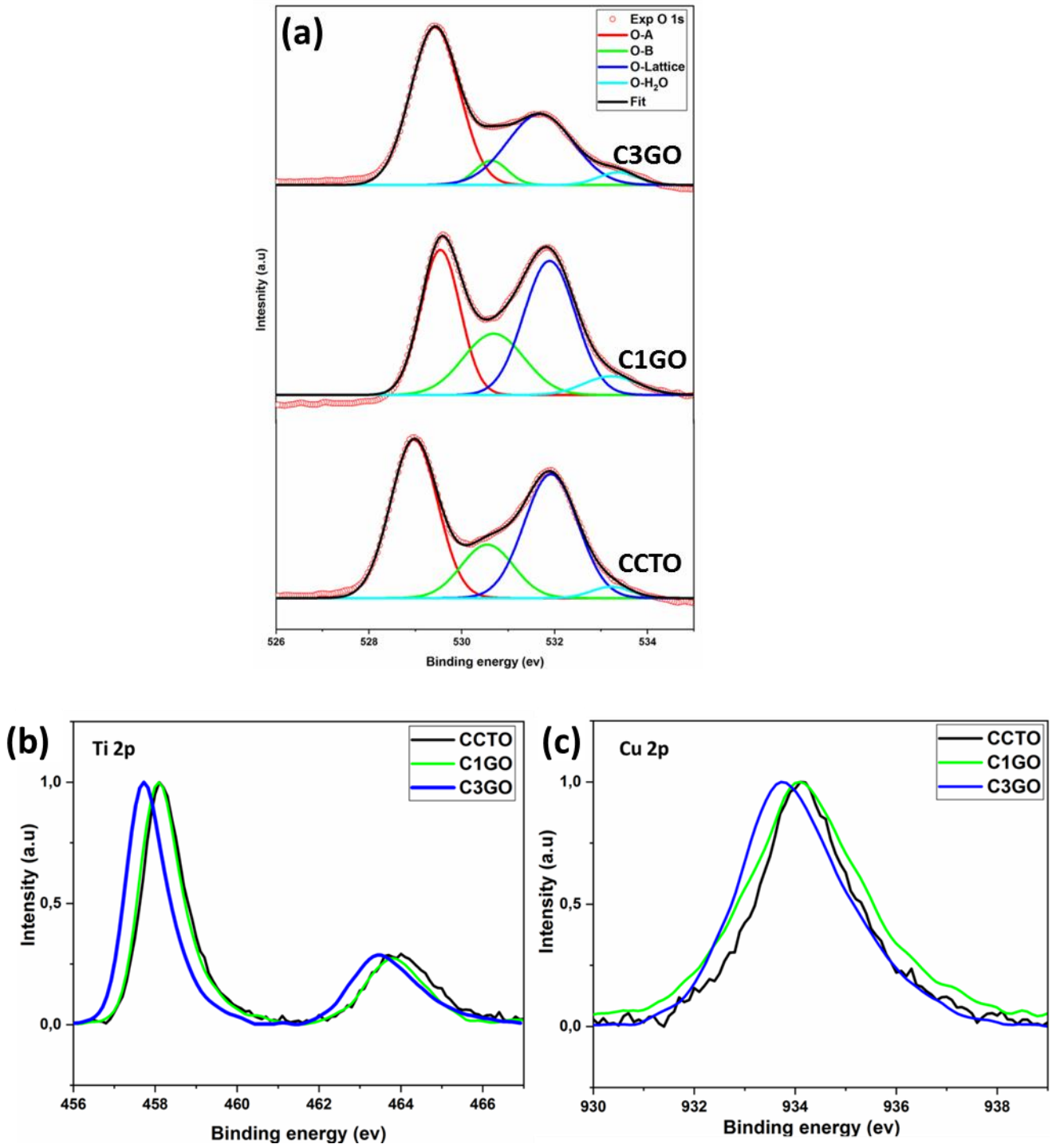

Figure IV-4 : High resolution XPS Spectra of (a) O1s, (b) Ti 2p, and (c) Cu 2p of CCTO, C1GO, and C3GO, ceramics

Raman spectroscopy is used to determine vibrational modes of molecules. In this part, Raman spectroscopy is used to investigate the effect of GO nanosheets on the crystal structure of CCTO materials. Acccording to the litterature CCTO exhibit three main active bands in Raman

spectroscopy at 445, 506 and 570 cm^{-1} [71]. Raman spectroscopy for CCTO, C1GO, C3GO and C6GO is recorded between 100 and 600 cm^{-1} on grain and grain boundaries in figure IV-5i and IV-5ii respectively.

Figure IV-5i presents Raman band on grains and it showed the three main band related to TiO_6 clusters (modes P7,8 and 9 corresponding to 445, 506, and 570 cm^{-1} respectively). P7 and 8 modes appeared at high intensity, refer to TiO_6 clusters (Ag symmetrie), the third mode (P9) corresponding to Ti-O-Ti antistretshing (Fg symmetrie) mode is present at very low intensity but it increases slightly after adding graphene oxide nanosheets, maybe due to the changement in the amount of polarization states [72]. From Figure IV-5ii, it can be seen that CuO modes appear at high intenisty which confirms that CuO phase is located at the grain boundaries. For C3GO, P7 and P8 modes appears at low intesity. The slight shift of modes for C3GO and C6GO is due to the significant defects generated in the lattice such as oxygen vacancies and the formation of Ti^{3+} in TiO_2 lattice [73]–[75].

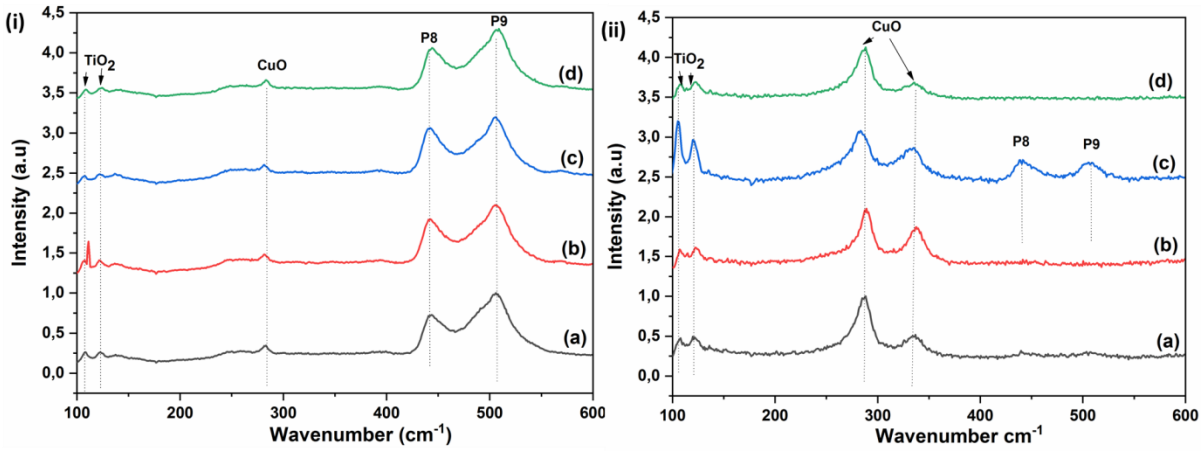

Figure IV-5 : Raman shifts on i-grains and ii-grain boundaries of (a) CCTO, (b) C1GO, (c) C3GO and (d) C6GO pellets.

IV.3.2 Optical properties:

In order to investigate the effect of defects made in CCTO materials as result of GO nanosheets oxidation, on the optical band gap, UV–Vis diffuse reflectance measurements were performed. Figure IV-6 showed two absorbance bands at around 1.6 and 2.9 eV corresponding to the hybridized valence band (VB) Cu 3d-O2p and to the conduction band (CB) Ti-3d states

respectively [48]. The optical band gap E_g of the samples was determined (Figure 6a) by Kubelka-Munk remission function according to the following equation (equation IV-1)

$$\alpha h\nu^{1/2} = A(h\nu - E_g) \qquad \textbf{(IV-1)}$$

Where α is the absorption coefficient, *v* is light frequency and E_g is an direct transition band gap. The E_g obtained values (Figure IV-6b) are 3.066, 3.052, 3.036 and 3.031 eV corresponding to CCTO, C1GO, C3GO and C6GO respectively. This little decrease of the band gap energy can be related to the crystallinity or the formation of electronic energy levels within energy band gap [76], [77]. In our study crystallite sizes did not vary between different materials even after GO nanosheets incorporation, thus the first reason can be discarded. Therefore, forming mid band gap energy levels in GO materials is due to oxygen vacancies formation and Ti^{4+} reducing to Ti^{3+} for charge compensation. The electronic transition from valence band to oxygen level then to Ti^{3+} then to conduction band cause a red shift in adsorption edge showing reduced band gap [78]. The intensity of absorbance band increases after adding GO nanosheets indicating an increase in different sources of disorder such as oxygen vacancy states above the valence band [79].

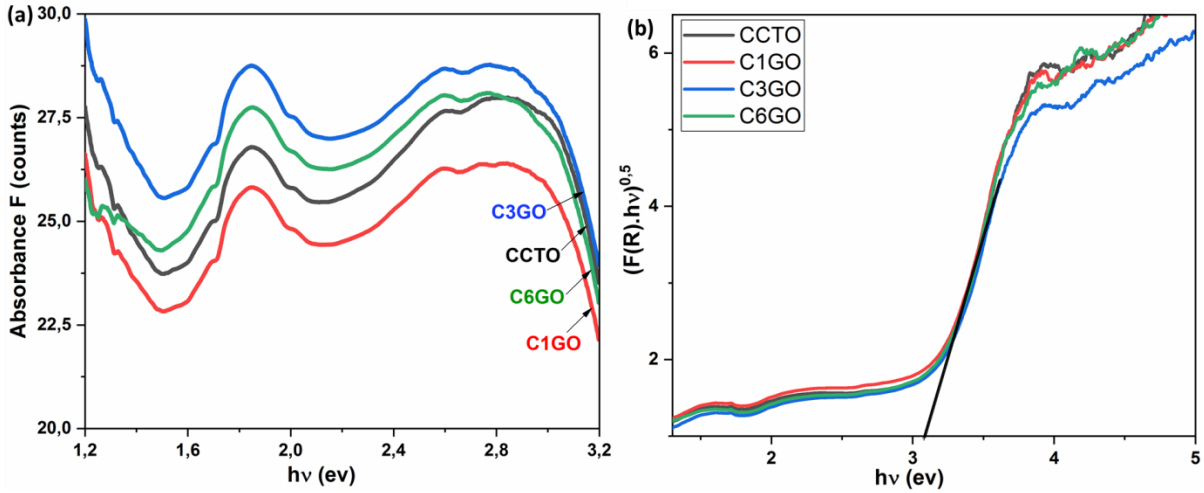

Figure IV-6 : (a) Reflectance spectra and (b) Band gap calculation from reflectance spectra of CCTO, C1GO, C3GO and C6GO

The photoluminiscence measurements were used to be correlated with electronic and structural properties of oxides [80]. PL spectra of CCTO, C1GO, C3GO and C6GO materials at room temperature are shown in Figure IV-7. Similar spectra shape indicates the same electronic band structure for all materials.

UV part of emission spectra shows band-to-band transitions in TiO_2 (peak, centered at 385 nm). The observed decrease of intenity is related to GO addings and photoinduced charge transfer between TiO_2 and oxygen vacancies. Visible emission in TiO_2 is formed by self trapped excitons and surface defects such as oxygen vacancies [81]. The low intenity in visible emisson could be attributed to an efficient separation of photogenerated surfaces between the volume and the surface [82].

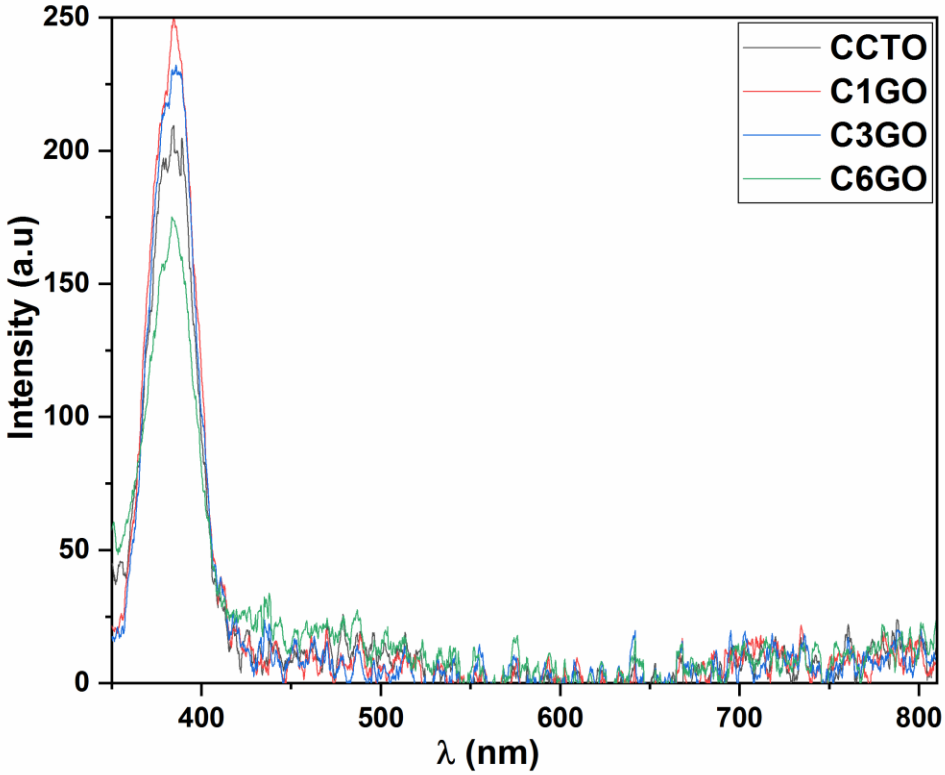

Figure IV-7 : Photoluminescence spectra of pure CCTO , C1GO, C3GO, and C6GO

IV.3.3 Electrochemical behavior

CCTO pellets with different amount of GO nanosheets are used as electrodes in 1M KOH solution to investigate their photoelectrochemical behavior. CCTO without and with GO nanosheets were considered as working eletrode, Pt as counter electrode and Ag/AgCl as a reference. Cyclic voltammetry curves are recorded in Figure IV-8. Figure IV-8a shows CV curves for the different samples between 1 V and 2.4 V in oxygen evolution range (OER range vs Ag/AgCl). CCTO material in dark (d-CCTO) seems inactive as seen from Figure IV-8a. After light exposition, the activity of CCTO is enhanced and start to generate photocurrent. It is clear that the generation of current increase with adding GO nanosheets in dark and under visible light exposition. CCTO3GO under visible light, showed two peaks of oxidation and a small peak of reduction (Figure IV-8b). There is no hysteris form due to that for voltages higher than 1.6 V, the resistivity of materials increases. It may be related to the formation of an insulator layer on surface defects at high voltage.

Figure IV-8c recorded cyclic voltammetry curves in the range of oxygen reduction reaction between 0.25 V-1 V (ORR range vs Ag/AgCl). Different behavior is showed in this range, in which CCTO (v-CCTO) is only active and generate photocurrent after visible light exposition. The electrochemical activity of these materials after incorporation of GO nanosheets still poor with no sigificant difference except for C3GO materials.

CCTO with 3% of graphene oxide nanosheets is electrochemically active in dark (d-C3GO) and under visible light exposition (v-C3GO) (Figure IV-8d). The photoelectrochemical behavior for CCTO pellets depend largely from surface properties. Different activities of these CCTO based materials is related to surface properties. Oxygen vacancies and Ti^{3+} act as n-type semiconducting and they are considered as an effective candidates to reduce band gap energy to attend the visible light region [83], [84]. Ti^{3+} and oxygen vacancies leads to form localized states below the conduction band, and thus expand the visible light absorbtion [78]. These different behavior of CCTO based materials can be explained by the effect of GO oxidation on electronic structure. As seen before in XPS spectra; different amount of GO nanosheets leads to eletronic state changement. C3GO showed the highest oxygen vacancies ratio and wide shift

(by 0.4) in Ti 2p and Cu 2p spectra. Thus, the presence of Ti^{3+}, Cu^{+} and oxygen vacancies in different ratio enhances the photoelectrochemical behavior in comparison to other materials.

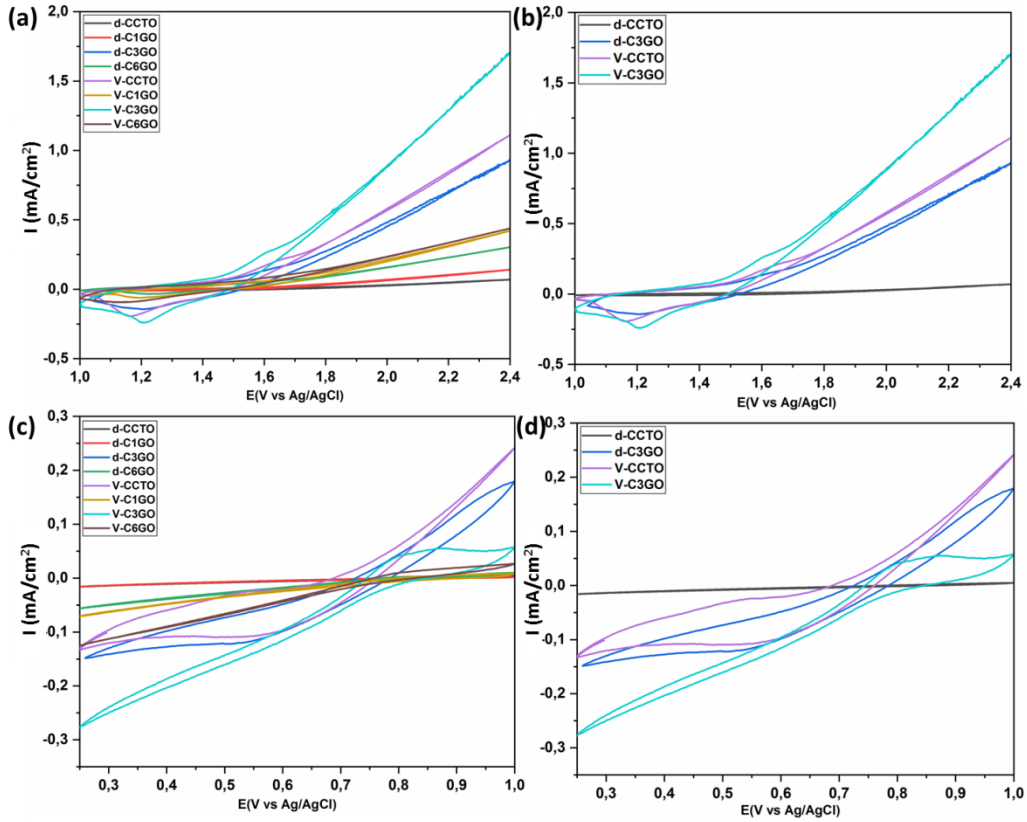

Figure IV-8 : CV curves of CCTO, C1GO, C3GO, and C6GO ceramics in (a) OER range and (c) ORR range in dark and under visible light. (In 1M KOH vs Ag/AgCl)

To demonstrate the enhanced electron transfer in active materials, the photoelectrochemical activity of materials in dark and under visible light was analyzed by measuring the photocurrent, using linear sweep voltammetry (LSV). These results are presented in Figure IV-9a and IV-9b in OER and ORR ranges respectively. The high photocurrent value indicates a strong capacity to generate and transfer photogenerated charge carries and thus enhance the photoelectrochemical activity [85]. In dark, the current density for CCTO and C3GO is recorded at an onset potential of 0.01 $A.cm^{-2}$ and 0.25 $A.cm^{-2}$ in OER and ORR range respectively (Figure IV-9a and IV-9b). After visible light exposition, the photocurrent generation from C3GO increases by 50% in comparison to CCTO. The photocurrent increase in two ranges with

increasing bias voltage, indicates that the photoinduced electron-hole-recombination is embeded to accelerate electrons transfer [85].

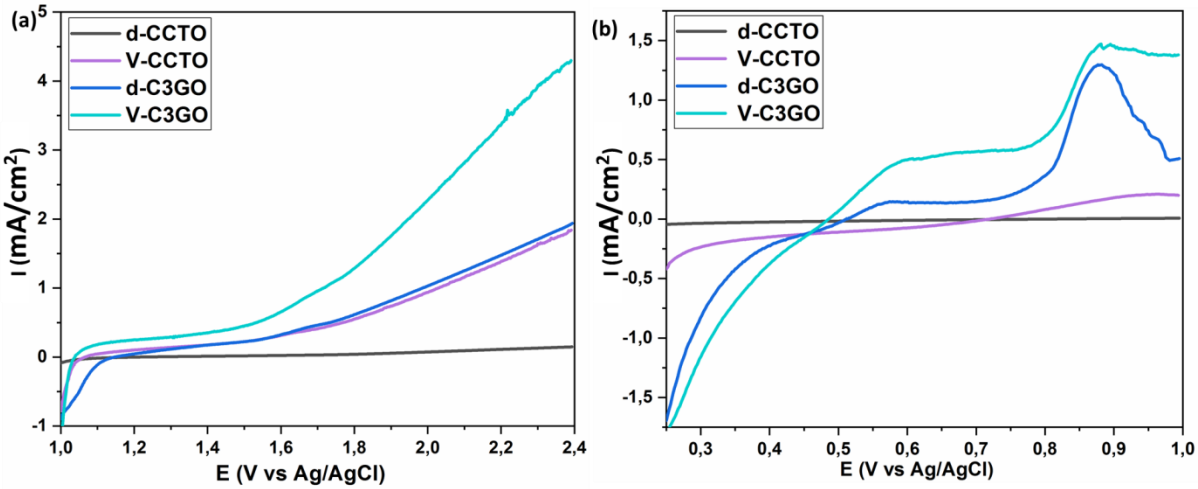

Figure IV-9 : LSV curves of CCTO and C3GO in dark and under visible light irradiation in 1M KOH vs Ag/AgCl in (a) OER range and (b) ORR range.

Electrochemical impedance spectroscopy (EIS) is used to study the resistivity of CCTO based materials. Figure IV-10a, IV-10b and IV-10c presents the Impedance spectra of these materials in dark and visible light for 0.4 V, 0.5 V and 0.6 V Vs Ag/AgCl reference electrode in 1M KOH solution. CCTO is caracterised by two semi circles one at high frequency corresponding to grain boundaries and the second at low frequency corresponding to grains. Which mean that the rate of charge transfer for photoelectrocatalytic acitivity is depending from the grains and grain boundaries behavior. The seperation of photogenerated hole-electron is an important step for semiconductor in order to improve photocatalytic and photoelectrocatalytic performances. The smallest arc radiuses refered to all material under visible light exposition leading to high rate of charge transfer thus higher the efficiency of charge separation [86], [87]. Therefore, the enhanced photocatalytic performance is mainly attributed to the increase of the charge separation efficiency due to the broadening of the valence band (VB) width induced by surface oxygen–vacancy states and Ti^{3+} states. Since those grain boundaries regions affect the photoelectrochemical behavior as shown from impedance spectroscopies shape, it can be concluded that the performance of these materials under visible light exposition is enhanced by

the presence of CuO segregation at grain boundaries. It is debated in the literature that surface defects could be on CuO phase due to the generation of oxygen vacancies. Thus might promote the formation of such reactive oxygen species. In addition the redox activity of the CuO nanoparticles has a critical role to enhance the oxidation mechanism [88], [89]. In addition those electrons are trapped in TiO_2 lattice in mid gap states as Ti^{3+} ions, known as superficial donors of conduction electrons.

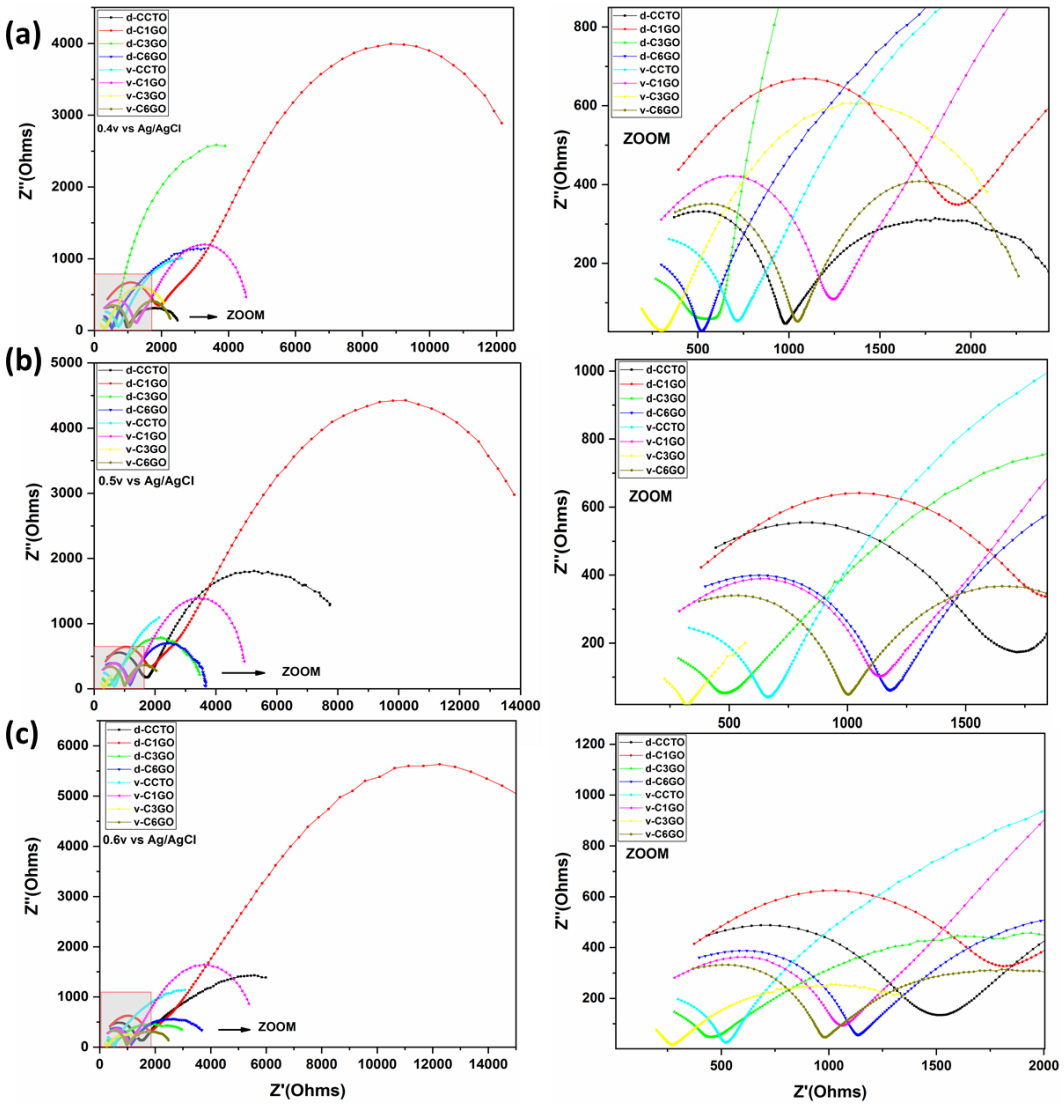

Figure IV-10 : The Nyquist plot of CCTO, C1GO, C3GO, and C6GO ceramics in dark and under visible light irradiation at (a) 0.4 V vs Ag/AgCl, (b) 0.5 V vs Ag/AgCl and (c) 0.6 V vs Ag/AgCl.

For quantitative measurement, plots of electrochemical impedance spectroscopy where fitted to the model of an equivalent circuit (Figure IV-11). In the model of Figure IV-11, R_1 is the

resistance of electrolyte (1M KOH solution). The parallel combination of the interfacial charge transfer resistance (R_2 and R_3 resistance of grains boundaries and grain respectively) and the constant phase element (CPE) is also included in this circuit. The CPE instead of a capacitor is taken in consideration for frequency dispersion. R_2 and R_3 values are mentioned in Table IV-1. As shown in Table IV-1, the resistivity of the CCTO based materials decreases under visible light exposition thus lead to higher charge conductivity.

Table IV-1 : Electrochemical impedance spectroscopy parameter in all materials

	R_2 (Ohm)		R_3 (Ohm)	
	Dark	**Visible**	**Dark**	**Visible**
CCTO	**1861±5.05**	**743.2±16.81**	**7475±4.681**	**4401±16.56**
C1GO	**5131±63.43**	**1134±3.02**	**10443±39.51**	**4672±1.78**
C3GO	**1468±227.3**	**389.3±88.15**	**3483±2.447**	**1316±4.108**
C6GO	**1155±5.04**	**940.7±5.49**	**2528±1.812**	**1353±0.84**

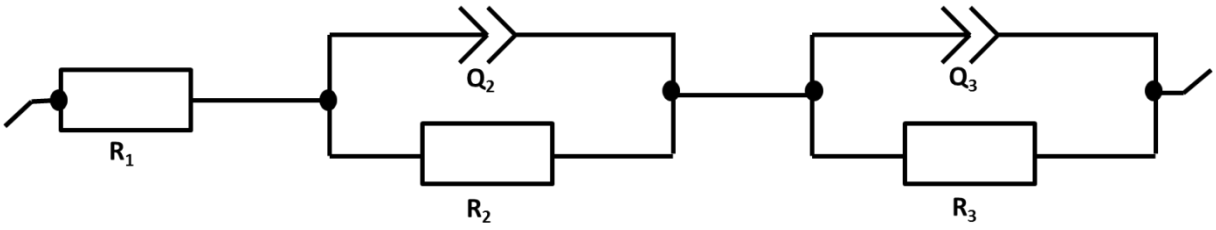

Figure IV-11 : EIS equivalent circuit for the impedance behavior

IV.4 Conclusion

In order to enhance photoelectrochemical cell, investigations focused on searching an active photoelectrodes under visible light. In this work we prepared $CaCu_3Ti_4O_{12}$ based material with different amount of graphene oxide nanosheets (1, 3, and 6%). By XRD, pure CCTO phase of CCTO were observed for all CCTO based materials with the presence of small amount of CuO as second phase as detected by Rietveld refinement. A slight shift to lower angle indicates the replacement of Ti^{4+} and Cu^{2+} by larger cations Ti^{3+} and Cu^{+} respectively. The segregation of CuO phase at grain boundaries is showed by SEM. SEM/EDX mapping and Raman spectroscopy confirms that CuO phase segregation increases at grain boundaries with increasing GO nanosheets amount in CCTO lattice. Since the electronic state affects directly the photoelectrochemical behavior, XPS spectra were performed for CCTO, C1GO and C3GO. It showed that the reduction impact of Ti^{4+} and Cu^{2+} and oxygen vacancy distribution on the surface increases with the percentage of GO. It is noticed that incorporation of 2D nanosheets leads to a red shift of band gap energy. Electrochemical measurement was performed in 1M KOH solution in dark and under visible light exposition. An enhancement by 50% of photocurrent generation is recorded for C3GO in comparison to CCTO under visible light irradiation. This activity is induced by the presence of Ti^{3+} and oxygen vacancies below the conduction band, and thus widened C3GO visible-light absorption. Furthermore, the conductivity of electrons is measured by impedance spectroscopy. It showed that the impedance decreases after GO incorporation and under exposure to visible light. The conduction mechanism inside the n-type semiconductor might be primarily attributed to electron hopping in Ti^{4+}-O-Ti^{3+} and oxygen vacancies.

References

[1] S. J. A. Moniz, S. A. Shevlin, D. J. Martin, Z.-X. Guo, and J. Tang, "Visible-light driven heterojunction photocatalysts for water splitting – a critical review," *Energy Environ. Sci.*, vol. 8, no. 3, pp. 731–759, 2015.

[2] A. Kudo and Y. Miseki, "Heterogeneous photocatalyst materials for water splitting," *Chem. Soc. Rev.*, vol. 38, no. 1, pp. 253–278, 2009.

[3] H. Ishaq, I. Dincer, and G. F. Naterer, "Performance investigation of an integrated wind energy system for co-generation of power and hydrogen," *Int. J. Hydrogen Energy*, vol. 43, no. 19, pp. 9153–9164, 2018.

[4] S. F. Yin, B. Q. Xu, X. P. Zhou, and C. T. Au, "A mini-review on ammonia decomposition catalysts for on-site generation of hydrogen for fuel cell applications," *Appl. Catal. A Gen.*, vol. 277, no. 1, pp. 1–9, 2004.

[5] J. Kim *et al.*, "Hybrid-solid oxide electrolysis cell: A new strategy for efficient hydrogen production," *Nano Energy*, vol. 44, pp. 121–126, 2018.

[6] D. R. Barcellos, M. D. Sanders, J. Tong, A. H. McDaniel, and R. P. O'Hayre, "BaCe0.25Mn0.75O3−δ—a promising perovskite-type oxide for solar thermochemical hydrogen production," *Energy Environ. Sci.*, vol. 11, no. 11, pp. 3256–3265, 2018.

[7] T. Kodama, Y. Kondoh, R. Yamamoto, H. Andou, and N. Satou, "Thermochemical hydrogen production by a redox system of ZrO2-supported Co(II)-ferrite," *Sol. Energy*, vol. 78, no. 5, pp. 623–631, 2005.

[8] R. Łukajtis *et al.*, "Hydrogen production from biomass using dark fermentation," *Renew. Sustain. Energy Rev.*, vol. 91, pp. 665–694, 2018.

[9] M. L. Dieuzeide, M. Laborde, N. Amadeo, C. Cannilla, G. Bonura, and F. Frusteri, "Hydrogen production by glycerol steam reforming: How Mg doping affects the catalytic behaviour of Ni/Al2O3 catalysts," *Int. J. Hydrogen Energy*, vol. 41, no. 1, pp. 157–166, 2016.

[10] Y. C. Sharma, A. Kumar, R. Prasad, and S. N. Upadhyay, "Ethanol steam reforming for hydrogen production: Latest and effective catalyst modification strategies to minimize carbonaceous deactivation," *Renew. Sustain. Energy Rev.*, vol. 74, pp. 89–103, 2017.

[11] R. D. Cortright, R. R. Davda, and J. A. Dumesic, "Hydrogen from catalytic reforming of biomass-derived hydrocarbons in liquid water," *Nature*, vol. 418, no. 6901, pp. 964–967, 2002.

[12] T. Hisatomi and K. Domen, "Reaction systems for solar hydrogen production via water splitting with particulate semiconductor photocatalysts," *Nat. Catal.*, vol. 2, no. 5, pp. 387–399, 2019.

[13] H. Dotan *et al.*, "Decoupled hydrogen and oxygen evolution by a two-step electrochemical–chemical cycle for efficient overall water splitting," *Nat. Energy*, vol. 4, no. 9, pp. 786–795, 2019.

[14] S. K. Saraswat, D. D. Rodene, and R. B. Gupta, "Recent advancements in semiconductor materials for photoelectrochemical water splitting for hydrogen production using visible light," *Renew.*

Sustain. Energy Rev., vol. 89, pp. 228–248, 2018.

[15] Q. Wang *et al.*, "Oxysulfide photocatalyst for visible-light-driven overall water splitting," *Nat. Mater.*, vol. 18, no. 8, pp. 827–832, 2019.

[16] Y. Lu *et al.*, "Self-hydrogenated shell promoting photocatalytic H2 evolution on anatase TiO2," *Nat. Commun.*, vol. 9, no. 1, p. 2752, 2018.

[17] A. M. Rassoolkhani *et al.*, "Nanostructured bismuth vanadate/tungsten oxide photoanode for chlorine production with hydrogen generation at the dark cathode," *Commun. Chem.*, vol. 2, no. 1, p. 57, 2019.

[18] A. Bin Yousaf, M. Imran, S. J. Zaidi, and P. Kasak, "Highly Efficient Photocatalytic Z-Scheme Hydrogen Production over Oxygen-Deficient WO3–x Nanorods supported Zn0.3Cd0.7S Heterostructure," *Sci. Rep.*, vol. 7, no. 1, p. 6574, 2017.

[19] I. Poli *et al.*, "Graphite-protected CsPbBr3 perovskite photoanodes functionalised with water oxidation catalyst for oxygen evolution in water," *Nat. Commun.*, vol. 10, no. 1, p. 2097, 2019.

[20] W. Ma, H. Ma, Y.-Y. Peng, H. Tian, and Y.-T. Long, "An ultrasensitive photoelectrochemical platform for quantifying photoinduced electron-transfer properties of a single entity," *Nat. Protoc.*, vol. 14, no. 9, pp. 2672–2690, 2019.

[21] X. Li *et al.*, "Light Illuminated α−Fe2O3/Pt Nanoparticles as Water Activation Agent for Photoelectrochemical Water Splitting," *Sci. Rep.*, vol. 5, p. 9130, Mar. 2015.

[22] J. N. Tiwari *et al.*, "Multicomponent electrocatalyst with ultralow Pt loading and high hydrogen evolution activity," *Nat. Energy*, vol. 3, no. 9, pp. 773–782, 2018.

[23] L. Qin, G. Wang, and Y. Tan, "Plasmonic Pt nanoparticles—TiO2 hierarchical nano-architecture as a visible light photocatalyst for water splitting," *Sci. Rep.*, vol. 8, no. 1, p. 16198, 2018.

[24] W. Q. Zaman, W. Sun, Z. Zhou, Y. Wu, L. Cao, and J. Yang, "Anchoring of IrO2 on One-Dimensional Co3O4 Nanorods for Robust Electrocatalytic Water Splitting in an Acidic Environment," *ACS Appl. Energy Mater.*, vol. 1, no. 11, pp. 6374–6380, Nov. 2018.

[25] M. Zhang, J. Chen, H. Li, P. Cai, Y. Li, and Z. Wen, "Ru-RuO2/CNT hybrids as high-activity pH-universal electrocatalysts for water splitting within 0.73 V in an asymmetric-electrolyte electrolyzer," *Nano Energy*, vol. 61, pp. 576–583, 2019.

[26] Z. U. Rahman, N. Wei, M. Feng, and D. Wang, "TiO2 hollow spheres with separated Au and RuO2 co-catalysts for efficient photocatalytic water splitting," *Int. J. Hydrogen Energy*, vol. 44, no. 26, pp. 13221–13231, 2019.

[27] Y. Che *et al.*, "Bio-inspired Z-scheme g-C3N4/Ag2CrO4 for efficient visible-light photocatalytic hydrogen generation," *Sci. Rep.*, vol. 8, no. 1, p. 16504, 2018.

[28] S. Mahzoon, S. M. Nowee, and M. Haghighi, "Synergetic combination of 1D-2D g-C3N4 heterojunction nanophotocatalyst for hydrogen production via water splitting under visible light irradiation," *Renew. Energy*, vol. 127, pp. 433–443, 2018.

[29] L. Shen *et al.*, “Black TiO2 nanobelts/g-C3N4 nanosheets Laminated Heterojunctions with Efficient Visible-Light-Driven Photocatalytic Performance,” *Sci. Rep.*, vol. 7, p. 41978, Feb. 2017.

[30] Z. Zhang, K. Liu, Z. Feng, Y. Bao, and B. Dong, “Hierarchical Sheet-on-Sheet ZnIn2S4/g-C3N4 Heterostructure with Highly Efficient Photocatalytic H2 production Based on Photoinduced Interfacial Charge Transfer,” *Sci. Rep.*, vol. 6, p. 19221, Jan. 2016.

[31] N. Mao, “Investigating the Heteronjunction between ZnO/Fe2O3 and g-C3N4 for an Enhanced Photocatalytic H2 production under visible-light irradiation,” *Sci. Rep.*, vol. 9, no. 1, p. 12383, 2019.

[32] J. Chu, X. Han, Z. Yu, Y. Du, B. Song, and P. Xu, “Highly Efficient Visible-Light-Driven Photocatalytic Hydrogen Production on CdS/Cu7S4/g-C3N4 Ternary Heterostructures,” *ACS Appl. Mater. Interfaces*, vol. 10, no. 24, pp. 20404–20411, Jun. 2018.

[33] J. Xu, Y. Qi, C. Wang, and L. Wang, “NH2-MIL-101(Fe)/Ni(OH)2-derived C,N-codoped Fe2P/Ni2P cocatalyst modified g-C3N4 for enhanced photocatalytic hydrogen evolution from water splitting,” *Appl. Catal. B Environ.*, vol. 241, pp. 178–186, 2019.

[34] H.-Y. Wang, Y.-Y. Hsu, R. Chen, T.-S. Chan, H. M. Chen, and B. Liu, “Ni3+-Induced Formation of Active NiOOH on the Spinel Ni–Co Oxide Surface for Efficient Oxygen Evolution Reaction,” *Adv. Energy Mater.*, vol. 5, no. 10, p. 1500091, May 2015.

[35] H. Yang, F. Hu, Y. Zhang, L. Shi, and Q. Wang, “Controlled synthesis of porous spinel cobalt manganese oxides as efficient oxygen reduction reaction electrocatalysts,” *Nano Res.*, vol. 9, no. 1, pp. 207–213, 2016.

[36] J. G. Lee *et al.*, “A New Family of Perovskite Catalysts for Oxygen-Evolution Reaction in Alkaline Media: BaNiO3 and BaNi0.83O2.5,” *J. Am. Chem. Soc.*, vol. 138, no. 10, pp. 3541–3547, Mar. 2016.

[37] W. T. Hong *et al.*, “Charge-transfer-energy-dependent oxygen evolution reaction mechanisms for perovskite oxides,” *Energy Environ. Sci.*, vol. 10, no. 10, pp. 2190–2200, 2017.

[38] D. Chen *et al.*, “Preferential Cation Vacancies in Perovskite Hydroxide for the Oxygen Evolution Reaction,” *Angew. Chemie Int. Ed.*, vol. 57, no. 28, pp. 8691–8696, Jul. 2018.

[39] M. A. Subramanian, D. Li, N. Duan, B. A. Reisner, and A. W. Sleight, “High Dielectric Constant in ACu3Ti4O12 and ACu3Ti3FeO12 Phases,” *J. Solid State Chem.*, vol. 151, no. 2, pp. 323–325, May 2000.

[40] J. H. Clark *et al.*, “Visible Light Photo-oxidation of Model Pollutants Using CaCu3Ti4O12: An Experimental and Theoretical Study of Optical Properties, Electronic Structure, and Selectivity,” *J. Am. Chem. Soc.*, vol. 133, no. 4, pp. 1016–1032, Feb. 2011.

[41] M. Mizumaki, T. Saito, H. Shiraki, and Y. Shimakawa, “Orbital Hybridization and Magnetic Coupling of the A-Site Cu Spins in CaCu3B4O12 (B = Ti, Ge, and Sn) Perovskites,” *Inorg. Chem.*, vol. 48, no. 8, pp. 3499–3501, Apr. 2009.

[42] H. S. Kushwaha, A. Halder, P. Thomas, and R. Vaish, “CaCu3Ti4O12: A Bifunctional Perovskite Electrocatalyst for Oxygen Evolution and Reduction Reaction in Alkaline Medium,” *Electrochim.*

Acta, vol. 252, pp. 532–540, 2017.

[43] H. S. Kushwaha, N. A. Madhar, B. Ilahi, P. Thomas, A. Halder, and R. Vaish, "Efficient Solar Energy Conversion Using CaCu3Ti4O12 Photoanode for Photocatalysis and Photoelectrocatalysis," *Sci. Rep.*, vol. 6, p. 18557, Jan. 2016.

[44] Z. Xiao *et al.*, "Filling the oxygen vacancies in Co3O4 with phosphorus: an ultra-efficient electrocatalyst for overall water splitting," *Energy Environ. Sci.*, vol. 10, no. 12, pp. 2563–2569, 2017.

[45] X. Li *et al.*, "Confined distribution of platinum clusters on MoO2 hexagonal nanosheets with oxygen vacancies as a high-efficiency electrocatalyst for hydrogen evolution reaction," *Nano Energy*, vol. 62, pp. 127–135, Aug. 2019.

[46] W. Yang *et al.*, "Oxygen vacancies confined in ultrathin nickel oxide nanosheets for enhanced electrocatalytic methanol oxidation," *Appl. Catal. B Environ.*, vol. 244, pp. 1096–1102, May 2019.

[47] X. Miao *et al.*, "The role of oxygen vacancies in water oxidation for perovskite cobalt oxide electrocatalysts: are more better?," *Chem. Commun.*, vol. 55, no. 10, pp. 1442–1445, 2019.

[48] R. Hailili *et al.*, "Oxygen vacancies induced visible-light photocatalytic activities of CaCu3Ti4O12 with controllable morphologies for antibiotic degradation," *Appl. Catal. B Environ.*, vol. 221, pp. 422–432, Feb. 2018.

[49] F. Zuo, L. Wang, T. Wu, Z. Zhang, D. Borchardt, and P. Feng, "Self-Doped Ti3+ Enhanced Photocatalyst for Hydrogen Production under Visible Light," *J. Am. Chem. Soc.*, vol. 132, no. 34, pp. 11856–11857, Sep. 2010.

[50] Y. Ji *et al.*, "Surface Ti3+/ Ti4+ Redox Shuttle Enhancing Photocatalytic H2 Production in Ultrathin TiO2 Nanosheets/CdSe Quantum Dots," *J. Phys. Chem. C*, vol. 119, no. 48, pp. 27053–27059, Dec. 2015.

[51] J. Pan *et al.*, "The enhancement of photocatalytic hydrogen production via Ti3+ self-doping black TiO2/g-C3N4 hollow core-shell nano-heterojunction," *Appl. Catal. B Environ.*, vol. 242, pp. 92–99, 2019.

[52] L. Zhi and K. Müllen, "A bottom-up approach from molecular nanographenes to unconventional carbon materials," *J. Mater. Chem.*, vol. 18, no. 13, pp. 1472–1484, 2008.

[53] S. Sun, L. Gao, and Y. Liu, "Enhanced dye-sensitized solar cell using graphene-TiO2 photoanode prepared by heterogeneous coagulation," *Appl. Phys. Lett.*, vol. 96, no. 8, p. 83113, Feb. 2010.

[54] R. R. Nair *et al.*, "Fine Structure Constant Defines Visual Transparency of Graphene," *Science (80-.).*, vol. 320, no. 5881, pp. 1308 LP – 1308, Jun. 2008.

[55] V. Thangaraj *et al.*, "Fluorescence Quenching of Sulfo-rhodamine Dye over Graphene Oxide and Boron Nitride Nanosheets," *Eur. J. Inorg. Chem.*, vol. 2016, no. 13-14, pp. 2125–2130, May 2016.

[56] X. Zhou *et al.*, "In Situ Synthesis of Metal Nanoparticles on Single-Layer Graphene Oxide and Reduced Graphene Oxide Surfaces," *J. Phys. Chem. C*, vol. 113, no. 25, pp. 10842–10846, Jun. 2009.

[57] D. Wang *et al.*, “Self-Assembled TiO2–Graphene Hybrid Nanostructures for Enhanced Li-Ion Insertion,” *ACS Nano*, vol. 3, no. 4, pp. 907–914, Apr. 2009.

[58] D. W. Boukhvalov and M. I. Katsnelson, “Modeling of Graphite Oxide,” *J. Am. Chem. Soc.*, vol. 130, no. 32, pp. 10697–10701, Aug. 2008.

[59] X. Wu, M. Sprinkle, X. Li, F. Ming, C. Berger, and W. A. de Heer, “Epitaxial-Graphene/Graphene-Oxide Junction: An Essential Step towards Epitaxial Graphene Electronics,” *Phys. Rev. Lett.*, vol. 101, no. 2, p. 26801, Jul. 2008.

[60] H. H. El-Maghrabi, E. A. Nada, F. S. Soliman, Y. M. Moustafa, and A. E.-S. Amin, “One pot environmental friendly nanocomposite synthesis of novel TiO2-nanotubes on graphene sheets as effective photocatalyst,” *Egypt. J. Pet.*, vol. 25, no. 4, pp. 575–584, 2016.

[61] D. Choi *et al.*, “Li-ion batteries from LiFePO4 cathode and anatase/graphene composite anode for stationary energy storage,” *Electrochem. commun.*, vol. 12, no. 3, pp. 378–381, 2010.

[62] B. Seger and P. V Kamat, “Electrocatalytically Active Graphene-Platinum Nanocomposites. Role of 2-D Carbon Support in PEM Fuel Cells,” *J. Phys. Chem. C*, vol. 113, no. 19, pp. 7990–7995, May 2009.

[63] S. Nagarajan *et al.*, “Porous Gelatin Membrane Obtained from Pickering Emulsions Stabilized by Graphene Oxide,” *Langmuir*, vol. 34, no. 4, pp. 1542–1549, Jan. 2018.

[64] T. X. H. Le, M. Bechelany, S. Lacour, N. Oturan, M. A. Oturan, and M. Cretin, “High removal efficiency of dye pollutants by electron-Fenton process using a graphene based cathode,” *Carbon N. Y.*, vol. 94, pp. 1003–1011, 2015.

[65] M. F. Bekheet, L. Schlicker, A. Doran, K. Siemensmeyer, and A. Gurlo, “Ferrimagnetism in manganese-rich gallium and aluminium spinels due to mixed valence Mn2+–Mn3+ states,” *Dalt. Trans.*, vol. 47, no. 8, pp. 2727–2738, 2018.

[66] J. Jumpatam *et al.*, “Improved giant dielectric properties of CaCu3Ti4O12 via simultaneously tuning the electrical properties of grains and grain boundaries by F− substitution,” *RSC Adv.*, vol. 7, no. 7, pp. 4092–4101, 2017.

[67] M.-H. Whangbo and M. A. Subramanian, “Structural Model of Planar Defects in CaCu3Ti4O12 Exhibiting a Giant Dielectric Constant,” *Chem. Mater.*, vol. 18, no. 14, pp. 3257–3260, Jul. 2006.

[68] R. Sanjinés, H. Tang, H. Berger, F. Gozzo, G. Margaritondo, and F. Lévy, “Electronic structure of anatase TiO2 oxide,” *J. Appl. Phys.*, vol. 75, no. 6, pp. 2945–2951, Mar. 1994.

[69] K. Li, Z. Huang, X. Zeng, B. Huang, S. Gao, and J. Lu, “Synergetic Effect of Ti3+ and Oxygen Doping on Enhancing Photoelectrochemical and Photocatalytic Properties of TiO2/g-C3N4 Heterojunctions,” *ACS Appl. Mater. Interfaces*, vol. 9, no. 13, pp. 11577–11586, Apr. 2017.

[70] C. Wang, H. J. Zhang, P. M. He, and G. H. Cao, “Ti-rich and Cu-poor grain-boundary layers of CaCu3Ti4O12 detected by x-ray photoelectron spectroscopy,” *Appl. Phys. Lett.*, vol. 91, no. 5, p. 52910, Jul. 2007.

[71] S. Orrego, J. A. Cortés, R. A. C. Amoresi, A. Z. Simões, and M. A. Ramírez, “Photoluminescence

behavior on Sr2+ modified CaCu3Ti4O12 based ceramics," *Ceram. Int.*, vol. 44, no. 9, pp. 10781–10789, Jun. 2018.

[72] H. Dai *et al.*, "Effect of BiFeO3 doping on the structural, dielectric and electrical properties of CaCu3Ti4O12 ceramics," *Appl. Phys. A*, vol. 119, no. 1, pp. 233–240, 2015.

[73] B. Peng *et al.*, "Achieving Ultrafast Hole Transfer at the Monolayer MoS2 and CH3NH3PbI3 Perovskite Interface by Defect Engineering," *ACS Nano*, vol. 10, no. 6, pp. 6383–6391, Jun. 2016.

[74] M. Mehta *et al.*, "Hydrogen treated anatase TiO2: a new experimental approach and further insights from theory," *J. Mater. Chem. A*, vol. 4, no. 7, pp. 2670–2681, 2016.

[75] Y. Zhang *et al.*, "Ti3+ Self-Doped Blue TiO2(B) Single-Crystalline Nanorods for Efficient Solar-Driven Photocatalytic Performance," *ACS Appl. Mater. Interfaces*, vol. 8, no. 40, pp. 26851–26859, Oct. 2016.

[76] M. Sathish, B. Viswanathan, R. P. Viswanath, and C. S. Gopinath, "Synthesis, Characterization, Electronic Structure, and Photocatalytic Activity of Nitrogen-Doped TiO2 Nanocatalyst," *Chem. Mater.*, vol. 17, no. 25, pp. 6349–6353, Dec. 2005.

[77] X. Wang *et al.*, "Synthesis, structural characterization and evaluation of floating B-N codoped TiO2/expanded perlite composites with enhanced visible light photoactivity," *Appl. Surf. Sci.*, vol. 349, pp. 264–271, Sep. 2015.

[78] B. Bharti, S. Kumar, H.-N. Lee, and R. Kumar, "Formation of oxygen vacancies and Ti3+ state in TiO2 thin film and enhanced optical properties by air plasma treatment," *Sci. Rep.*, vol. 6, p. 32355, Aug. 2016.

[79] Y. Lv, W. Yao, R. Zong, and Y. Zhu, "Fabrication of Wide–Range–Visible Photocatalyst Bi2WO6−x nanoplates via Surface Oxygen Vacancies," *Sci. Rep.*, vol. 6, p. 19347, Jan. 2016.

[80] G. Blasse and B. C. Grabmaier, "How Does a Luminescent Material Absorb Its Excitation Energy? BT - Luminescent Materials," G. Blasse and B. C. Grabmaier, Eds. Berlin, Heidelberg: Springer Berlin Heidelberg, 1994, pp. 10–32.

[81] B. J. Jin, H. S. Woo, S. Im, S. H. Bae, and S. Y. Lee, "Relationship between photoluminescence and electrical properties of ZnO thin films grown by pulsed laser deposition," *Appl. Surf. Sci.*, vol. 169–170, pp. 521–524, Jan. 2001.

[82] A. A. Chaaya *et al.*, "Tuning Optical Properties of Al2O3/ZnO Nanolaminates Synthesized by Atomic Layer Deposition," *J. Phys. Chem. C*, vol. 118, no. 7, pp. 3811–3819, Feb. 2014.

[83] X. Lin, M. Sun, Y. Yao, and X. Yuan, "In situ construction of N/Ti3+ codoped triphasic TiO2 layer on TiO2 nanotube arrays to improve photoelectrochemical performance," *Electrochim. Acta*, vol. 291, pp. 319–327, 2018.

[84] J. Shao *et al.*, "In situ synthesis of carbon-doped TiO2 single-crystal nanorods with a remarkably photocatalytic efficiency," *Appl. Catal. B Environ.*, vol. 209, pp. 311–319, Jul. 2017.

[85] J. Wang and W.-D. Zhang, "Modification of TiO2 nanorod arrays by graphite-like C3N4 with high visible light photoelectrochemical activity," *Electrochim. Acta*, vol. 71, pp. 10–16, 2012.

[86] H. Liu, X. Z. Li, Y. J. Leng, and W. Z. Li, “An Alternative Approach to Ascertain the Rate-Determining Steps of TiO2 Photoelectrocatalytic Reaction by Electrochemical Impedance Spectroscopy,” *J. Phys. Chem. B*, vol. 107, no. 34, pp. 8988–8996, Aug. 2003.

[87] W. H. Leng, Z. Zhang, J. Q. Zhang, and C. N. Cao, “Investigation of the Kinetics of a TiO2 Photoelectrocatalytic Reaction Involving Charge Transfer and Recombination through Surface States by Electrochemical Impedance Spectroscopy,” *J. Phys. Chem. B*, vol. 109, no. 31, pp. 15008–15023, Aug. 2005.

[88] G. Applerot *et al.*, “Understanding the Antibacterial Mechanism of CuO Nanoparticles: Revealing the Route of Induced Oxidative Stress,” *Small*, vol. 8, no. 21, pp. 3326–3337, Nov. 2012.

[89] B. Fahmy and S. A. Cormier, “Copper oxide nanoparticles induce oxidative stress and cytotoxicity in airway epithelial cells,” *Toxicol. Vitr.*, vol. 23, no. 7, pp. 1365–1371, Oct. 2009.

Part V : Investigation of dielectric and magnetic properties of the CCTO based composites

Part V: Investigation of dielectric and magnetic properties of the CCTO based composites

V.1 Introduction

A large number of dielectric materials have been studied so far. $CaCu_3Ti_4O_{12}$ is an ABO_3 material type that has attracted great interest due to its dielectric constant of about 10^4-10^5 at temperature from 100 to 600 K without any phase transition [1]. It is now established that the origins of such high permittivity values are due to an extrinsic effect of internal barrier layer capacitance (IBLC) mechanism which is the development of Schottky barriers at insulating grain boundaries (GB) between n-type semiconducting grains [2].

Furthermore, a sample-electrode interface effect has been suggested to explain the origin of the high permittivity value in single crystal of CCTO [3]. However, the mechanisms responsible of the great permittivity and exceptional properties of this material are still not fully understood.

The aim of this part of the thesis is to give brief background information of the basics of dielectric materials and their applications. Firstly, a brief introduction on capacitors and a description of the dielectric behavior (dielectric constant and dielectric losses) will be given. Most of the collected information come from three books: L. Pardo [4], B . Jaffe [5], and A. J. Moulson [6]. Secondly, the dielectric properties of the prepared materials will be described.

A dielectric material is an electrical insulating material that can support charges without conducting it. This material presents two opposites charges called electric dipole separated by a certain distance on the atomic sale, in which this separation gives rise to a dipole moment. Once an external electric field is applied on the dielectric material, a certain force will be exerted on the electric dipole that will try to align it with the applied external electric field, this is called polarization. The polarization is maintained when the center of the electron cloud does

not longer coincide with the nucleus, in which the electron cloud moves in one direction and the nucleus moves on the other direction.

V.1.2 Generalities on capacitors

In this part we will briefly describe the capacitors, the dielectric constant and the dissipation factor.

V.1.2.1 Capacitor

A capacitor is an electronic device that stores electric charge in an electric field. It is usually composed of two conducting plates separated by an insulator or dielectric material. In capacitors, charge on one conductor plate will exert a force on the charge carriers within the other conductor plate, attracting opposite polarity charge and repelling like polarity charges, thus an opposite polarity charge will be induced on the surface of the other conductor. The conductors thus hold equal and opposite charges on their facing surfaces and the dielectric develops an electric field (Figure V-1)

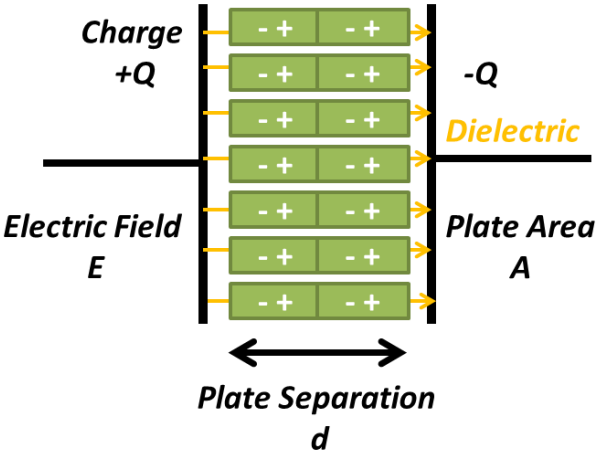

Figure V-1 : Charge separation in a capacitor

When a voltage is applied trough the capacitor, the plates will have opposite charges, and an electric field will be present between them. A capacitor is characterized by its capacitance C. C

of an electrostatic system is the ratio of the quantity of separated charge (Q) to the potential difference applied between the two conductor plates.

$$C = \frac{Q}{V} \qquad \textbf{(V-1)}$$

The unit of the capacitance is the Farad (Coulomb/V).

The capacitance of capacitor can be affected by many factors:

- It is directly proportional to the area (A) of the conductive plates
- It is inversely proportional to the separation (d) between the plates
- It is directly proportional to the dielectric constant or permittivity of the material between the plates.

$$C = \frac{\varepsilon A}{d} \qquad \textbf{(V-2)}$$

Therefore, in a capacitor, the highest capacitance is achieved with a high permittivity dielectric material, large plate area, and small separation between the plates.

V.1.2.2 Dielectric constant

The dielectric constant can be defined as the ability of a material to be polarized in response to an applied electrical field. Dielectric constant or relative permittivity is the ratio of material permittivity to the permittivity of a vacuum (equation 3). It represents the capacity of storage of a material. The more polarized is the material in the presence of an electrical field the more it will show a high dielectric constant.

$$\varepsilon_r = \frac{\varepsilon}{\varepsilon_0} \qquad \text{(V-3)}$$

Where ε_r is the relative permittivity, ε is the permittivity of the dielectric medium, and ε_0 is the permittivity of a vacuum.

V.1.2.3 Dissipation factor or dielectric loss

The ideal dielectric material can support the orientation and shifting of dipole moments with the minimal dissipation of energy in the form of heat. This heat is originated from an electric field able to polarize charges in the material and this polarization is enabling to follow the fast reversals of the electric field. Thus results in the dissipation of power within the dielectric material.

The next section will present our work on CCTO materials and composites CCTO with 2D materials nanosheets (hexagonal boron nitride and graphene oxide nanosheets). CCTO based Composites were investigated using X-Ray Diffraction (XRD), Scanning electron microscopy (SEM) and an impedance spectroscopy (IS measurements) to obtain the dielectric constant, dielectric loss and impedance behavior.

V.1.3 Synthesis of pure CCTO and CCTO composites

$CaCu_3Ti_4O_{12}$ (CCTO) was synthesized by mecanosynthesis at room temperature using stoichiometric proportions of $CaCO_3$, CuO, and TiO_2 precursors. The milling process was performed in planetary ball mill machine using a 50 ml Al_2O_3 jar and 15 balls Al_2O_3 of 10 mm diameter, where the balls to powder mass ratio was 9:1. First, precursors were milled for 5h with a rotation speed at 350 rpm. Second step is the calcination process of powders at 900°C for 3h to obtain the pure phase of CCTO. Powders then are mixed with 5% of APV (Alcohol Polyvinyl) solution and pressed using hydraulic equipment (3.5T) at room temperature. The as-prepared pellets obtained (10mm of diameter and 1 mm of thickness) were sintered at 1100°C for 3h and 6h. All prepared pellets were polished to remove the surface layer.

In order to investigate the influence of 2D nanosheets on the dielectric behavior of CCTO ceramics, Boron Nitride nanosheets (BNNs) were incorporated in the material. After calcination of CCTO at 900°C for 3h, BNNs were added to the powders in different mass ratio (1%, 3% and 6%) and mixed by solid state reaction using agate mortar and pestle. The mixed powders were recuperated to form pellets at high temperature 1100°C for 3 and 6h. The same preparation process is repeated to synthesize CCTO with graphene oxide nanosheets. The obtained

materials were polished to remove the surface layer and then characterized by X-ray diffraction (XRD) and dielectric spectroscopy for permittivity and losses tangent measurements as function of frequency (10^6-1 Hz).

V.1.4 Results and discussions:

The XRD patterns of the undoped and boron nitride nanosheets codoped CCTO (BN-CCTO) ceramics sintered at 1100°C for 3h and 6h are shown in Figure V-2i and Figure V-2ii respectively. All the peaks appearing in the XRD patterns of Figure V-2i are attributed to the cubic lattice of CCTO. A small amount of CuO is observed for CCTO with 3% of BN. All the XRD patterns of the composites ceramics (%wt BN-CCTO) sintered at 1100°C for 3 hours show a slight shift to smaller 2θ compared to undoped CCTO. This result can be explained by the fact that the atoms of Bore (B) and nitrogen (N) were inserted inside the CCTO lattice.

XRD patterns of Figure V-2ii showed that 6 h sintering was not enough to achieve the materials crystallinity. Especially for CCTO with 1 and 3% of BN, in which almost CCTO phase tends to be amorphous because of the intensity decreasing in characteristic peak (200) diffraction. After adding 6% of boron nitride nanosheets the crystallinity seems to be maintained. It is maybe due to the liquefaction phase of CuO at 950°C.

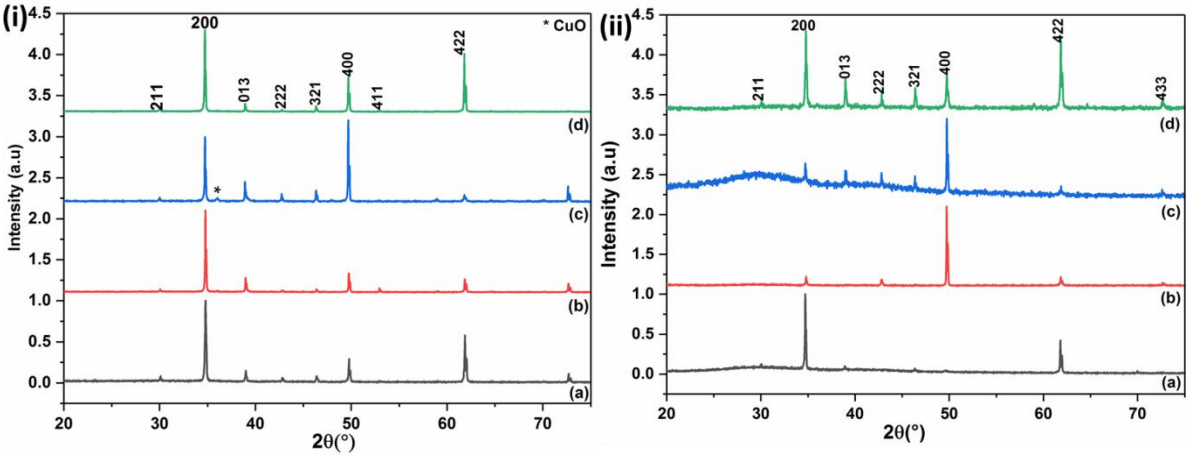

Figure V-2 : Showed XRD patterns of polished materials after sintering at 1100°C for (i) 3h, and (ii) 6h of (a) CCTO, (b) 1BN, (c) 3BN, and (d) 6BN

Figure V-3 shows the dielectric properties of sintered pellets at 1100°C for 3 and 6 hours. The pellets sintered at 3 hours (Figure V-3a) show modest room temperature ε' only. It is evident that the permittivity increases with the increase of the amount of BN in CCTO. The relative permittivity of undoped CCTO is equal to 4500 at low frequencies while it increases to 5000 for 6% wt BN at the same frequencies (Figures V-12-S1 and V-12-S2). It is clear that the dielectric constant decreases with increasing frequency for pure and BN doped CCTO. The decrease of dielectric constant in the high frequency region (1 kHz) is due to a transition from grain dielectric response to grain boundary dielectric response. The improvement in the dielectric constant after adding BN to CCTO can be explained by the change in the grain and the grain boundaries characteristics. The presence of CuO oxide seems to play an important role. It might be doping the grain boundary thus modifying the permittivity value. The melting of the copper oxide phase during the sintering treatment probably favors the wetting of the shell of the grain leading to a multilayered material. Hence, the charge carriers' concentration at the different interfaces changes with the presence of a Cu amount. The insertion of B and N in the CCTO lattice might have changed the grain characteristics.

Figure V-3c presents the losses tangent of ceramics; it shows almost the same behavior and value for undoped and co-doped materials with high loss values especially at low frequencies as reported [7], [8]. The dielectric permittivity and dielectric loss factor diagrams showed a relaxation at low frequencies likely originated from the sample-electrode effect.

Figure V-3b shows the change in the dielectric constant with frequency for pellets sintered at 1100°C for 6 hours. The pellets sintered at 6 hours show modest room temperature ε' only. These values are higher compared to the pellets sintered for 3 hours. An increase in the sintering time leads to an increase in the dielectric constant. In this case also the permittivity decreases with the increase in the frequency. The dielectric permittivity at high frequencies is almost the same for all materials sintered for 6h, and slightly higher than those sintered for 3h. As mentioned in the literature, increasing sintering time leads to an increase in dielectric properties, which is the case for dielectric permittivity and losses (Figure 3d).

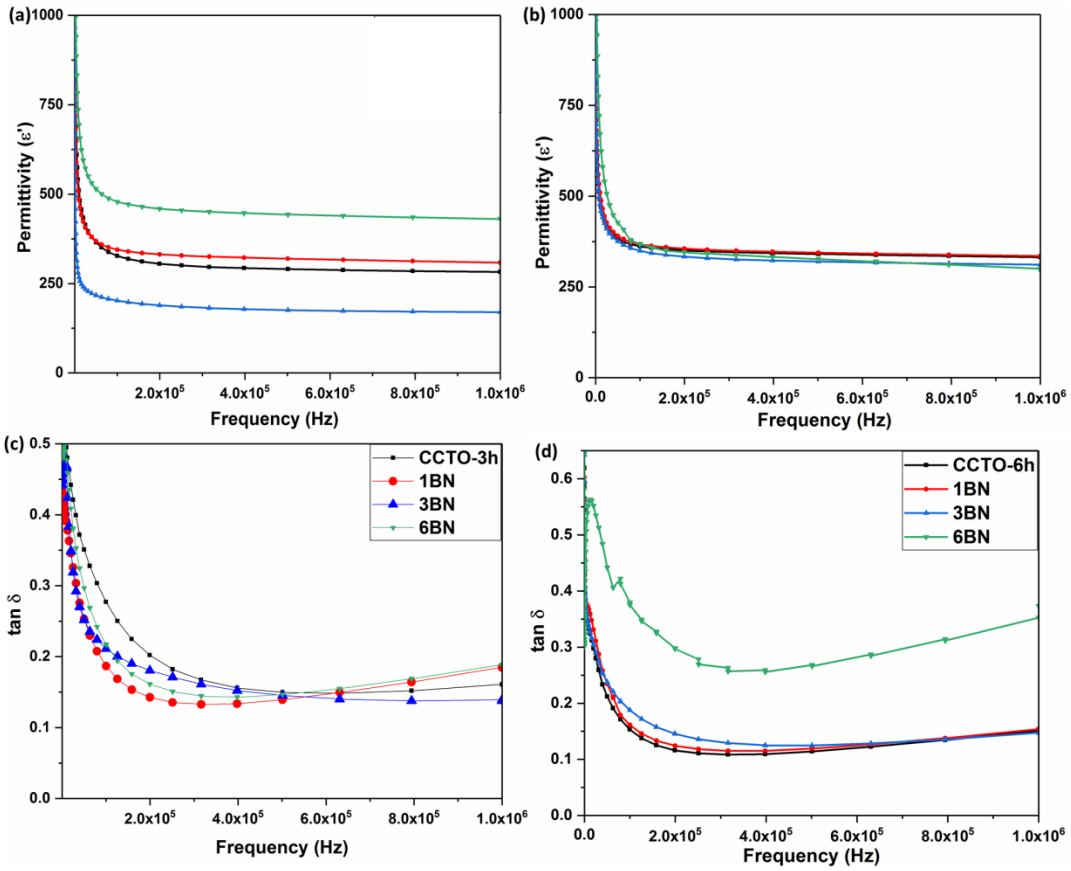

Figure V-3 : Showed the dielectric permittivity of h-BN/CCTO ceramics sintered at (a) 3h and (b) 6h, and the dielectric loss of h-BN/CCTO ceramics sintered at (c) 3h and (d) 6h.

To elucidate the influence of co-doping and sintering time on dielectric properties of CCTO ceramics, the behavior of domain responses were studied using an impedance spectroscopy. Figure V-4 shows the Z^* plots for all samples sintered at 1100°C for 3 and 6h at RT. A non-zero intercept on the Z' axis at low frequencies was observed indicating an electrical response of the semi-conducting grains [9]. It showed that the semi-circle of CCTO response decreases with increasing sintering time in comparison to CCTO-3h. In contrast the impedance of co-doped materials sintered for 6h increases in comparison to those sintered for 3h.

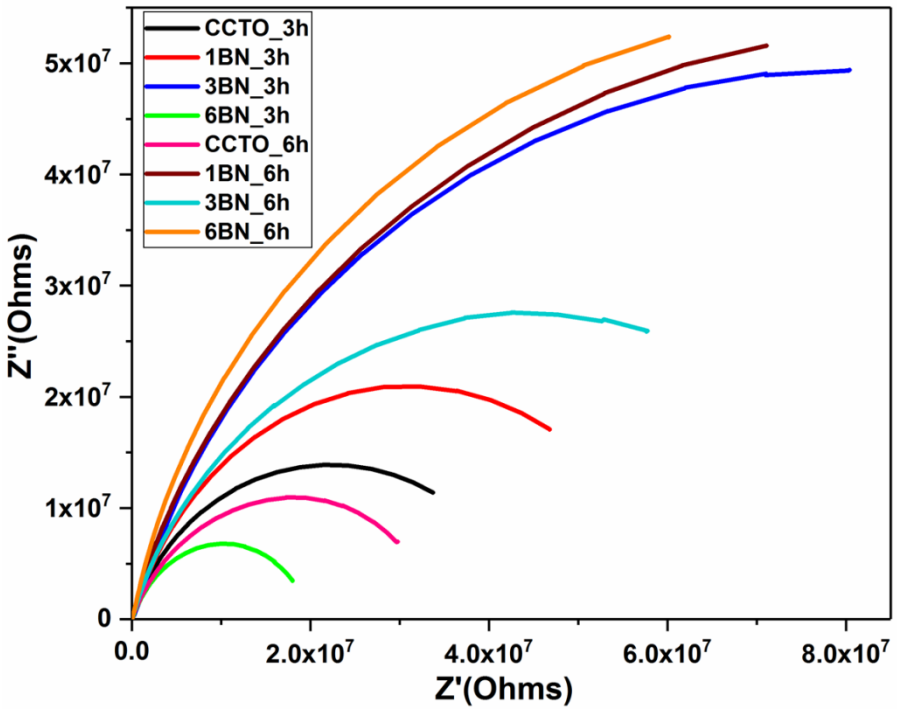

Figure V-4 : Impedance spectroscopy of h-BN/CCTO composites sintered at 3 and 6h

Furthermore, 2D Graphene Oxide nanosheets (GONs) are added to CCTO powder after calcination, in different weight percentages (1, 3, and 6%). They were mixed using agate mortar and pestle; powders were then pressed into pellet forms and then sintered at 1100°C for 3 and 6h. The pellets surface was polished to eliminate the first layer.

The crystal structure and phase composition of all the sintered ceramic samples were studied. The XRD patterns for all samples sintered at 1100°C for 3 and 6h are shown in Figure V-5i and V-5ii respectively. The patterns confirm the formation of single phase CCTO for all ceramic materials sintered for 3h, with a slight decrease in 3GO sample crystallinity (Figure 5i). In Figure 5ii, the XRD patterns showed that the crystallinity of CCTO sintered at 6h decreases. The crystallinity starts to be maintained after GO incorporation with formation of secondary phases (CuO and TiO_2).

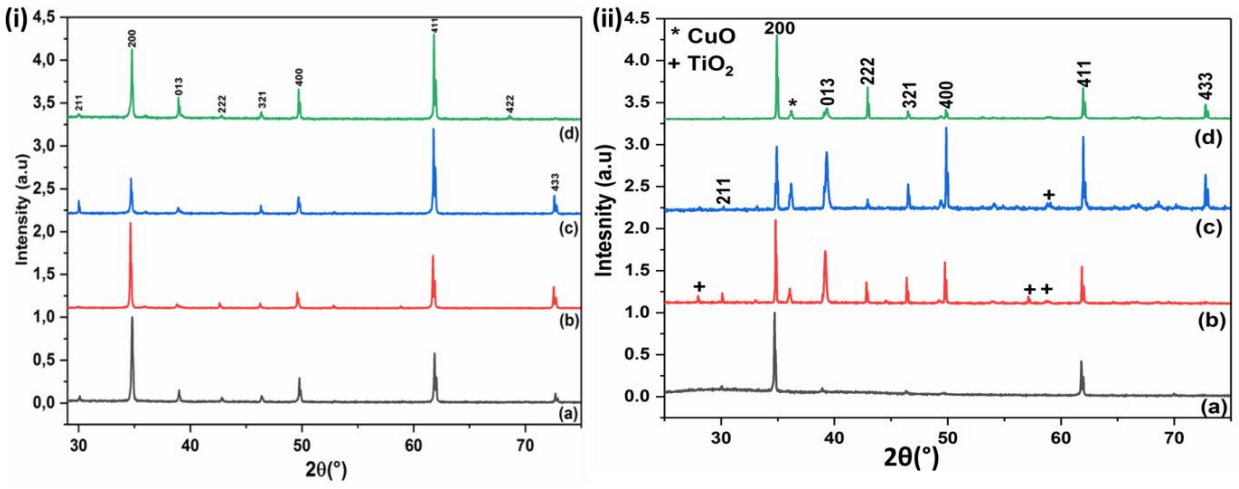

Figure V-5: XRD patterns of polished materials after sintering at 1100°C for (i) 3h and (ii) 6h of (a) CCTO, (b) 1GO, (c) 3GO and (d) 6GO

The frequency dependence of permittivity and dielectric loss for materials sintered for 3 and 6h is shown in Figure V-6. As seen from the inset of Figure V-5a and V-5b, at low frequencies, the dielectric start from ε'~5900 for CCTO-3h and ε'~1500 for CCTO-6h (Figures V-12-S3 and V-12-S4).

We can observe that an increase in the sintering time leads to a slight decrease of the dielectric permittivity (Figure V-6b). Significant changes of dielectric permittivity as function of frequency happen starting from the frequency at $\sim 10^4$ for pure phase of CCTO and composite materials sintered at different times, with different percentage weights. We can notice a decrease in the dielectric constant with the increase of frequency for all the samples. There is a rapid drop at around $\sim 10^4$ Hz followed by a stable value for the dielectric constant at intermediate and high frequency.

CCTO sample sintered at 3h showed a dielectric plateau with ε' value of ~ 5900 (Figures V-12-S3) observed at low frequencies, followed by a rapid drop of ε' at intermediate and high frequencies to the bulk dielectric value of ~ 350. With adding graphene oxide nanosheets, different plateau appears at low frequencies depending on the added amount. CCTO with 1% GO (1GO) nanosheets sintered for 3h showed the higher permittivity in comparison to other composites at intermediate and high frequency ε'=350. In the case of sintered composites for

6h, CCTO with 6%GO (6GO) showed the higher dielectric permittivity ε'~140 in comparison to other materials. Figure V-6c presents the dielectric loss of ceramics sintered for 3h; it shows almost the same behavior and value for all materials with high loss values especially at low frequencies. In Figure V-6d the dielectric loss of all ceramics sintered for 6h are present, it showed a high dielectric loss and higher than those recorded for the 3h sintered materials. The dielectric permittivity and dielectric loss factor diagrams showed a relaxation at low frequencies likely originated from the sample-electrode effect. All this fact indicated that graphene oxide incorporation plays a significant role in bulk to change the dielectric properties but in a symmetric way.

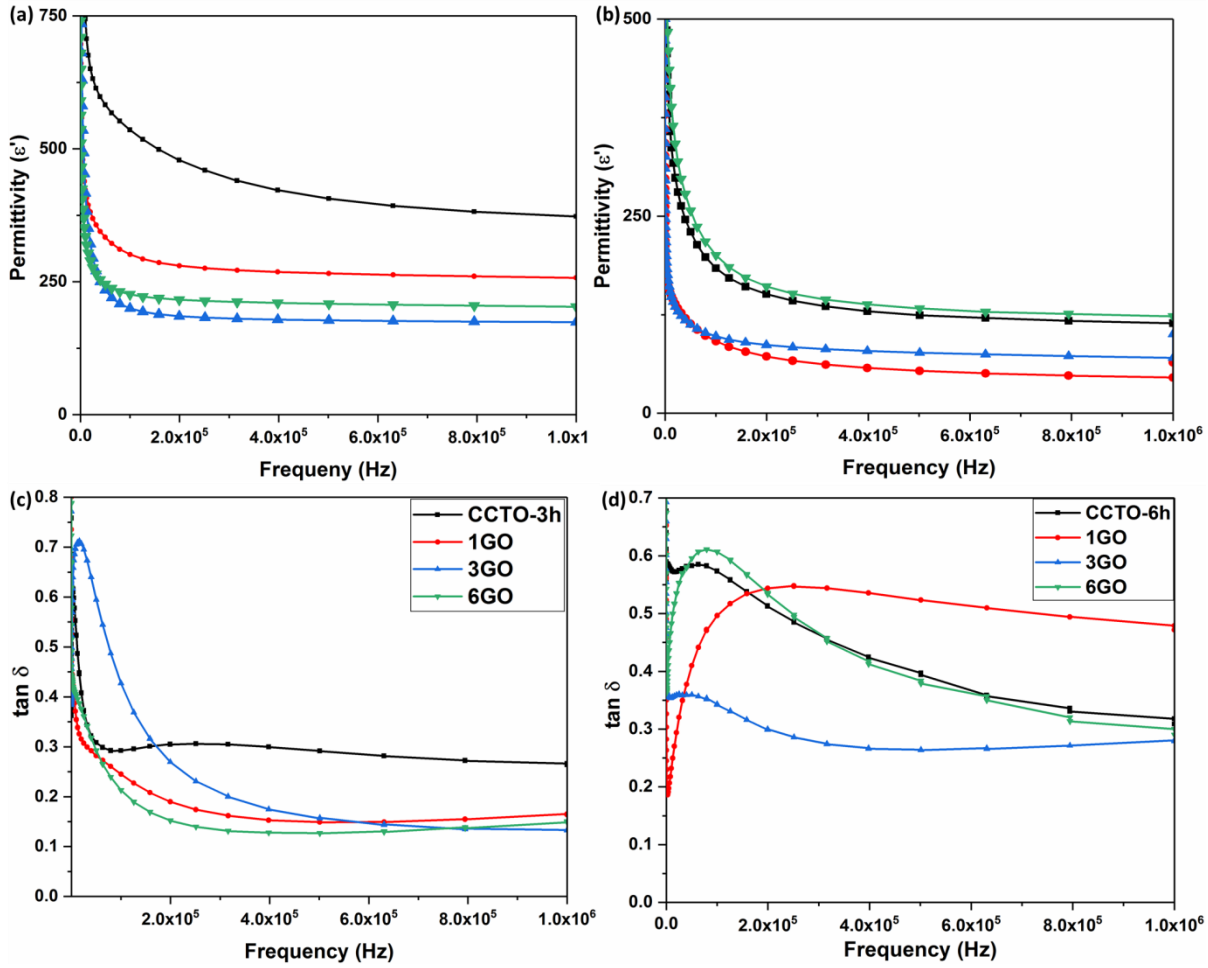

Figure V-6 : Showed the dielectric permittivity of GO/CCTO ceramics sintered at (a) 3h and (b) 6h, and the dielectric loss of GO/CCTO ceramics sintered at (c) 3h and (d) 6h.

Furthermore, to study the materials resistance, an impedance analysis is applied to the materials surface. Figure V-7 showed the impedance spectroscopy measurement for all materials sintered at 3 and 6h. It showed that the semi-circle of CCTO decreases after 6 hours of sintering. In contrast the semi-circle increases for samples with GO nanosheets sintered at 6h.

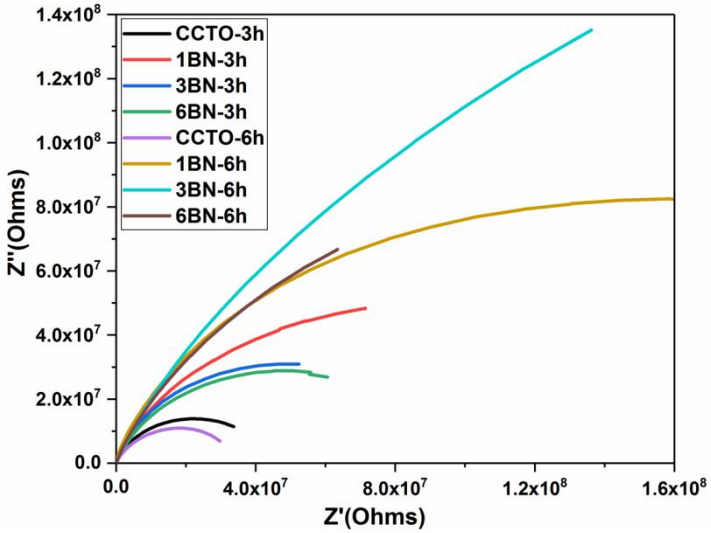

Figure V-7 : Impedance spectroscopy of materials h-BN/CCTO composites sintered at 3 and 6h.

V.1.5 Discussion and Conclusion

In general, the dielectric properties of CCTO are explained by the presence of two electrically different regions in the pellets. The first region is a semiconducting region which is the grains and the second region is an insulating one represented by the grain boundaries[10]–[12]. The main focus of recent studies is to maintain a high permittivity for the CCTO while decreasing its dielectric loss.

In this study we added to different type of 2D materials to CCTO and the obtained materials were sintered at 1100°C for 3 and 6 hours. XRD results showed that the materials sintered at 1000°C for 3 hours are single phase CCTO and highly crystalline. For the materials sintered for 6 hours the crystallinity of the materials decreases especially after the addition of the 2D

materials. Secondary phases appear in the composites, CuO and TiO_2. Figure V-8, V-9 and Figure V-10 showed the surface of CCTO and CCTO composites.

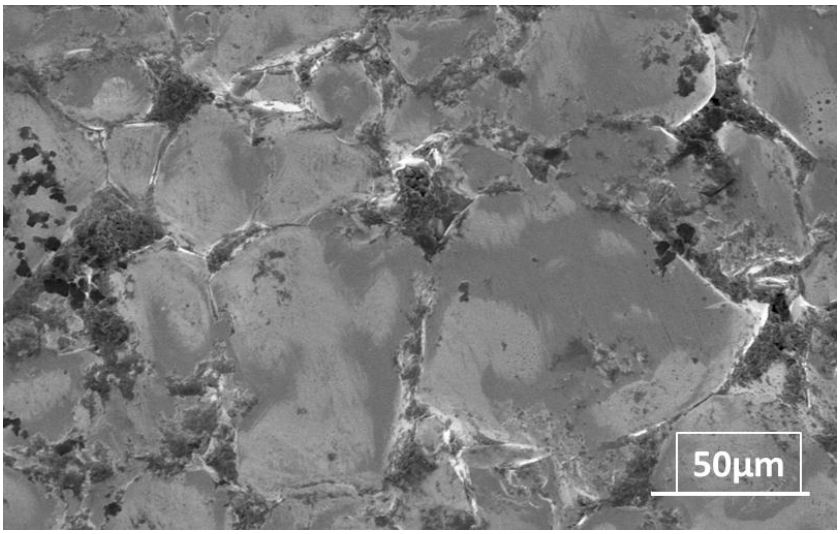

Figure V-8 : SEM of CCTO sintered at 1100°C for 3h

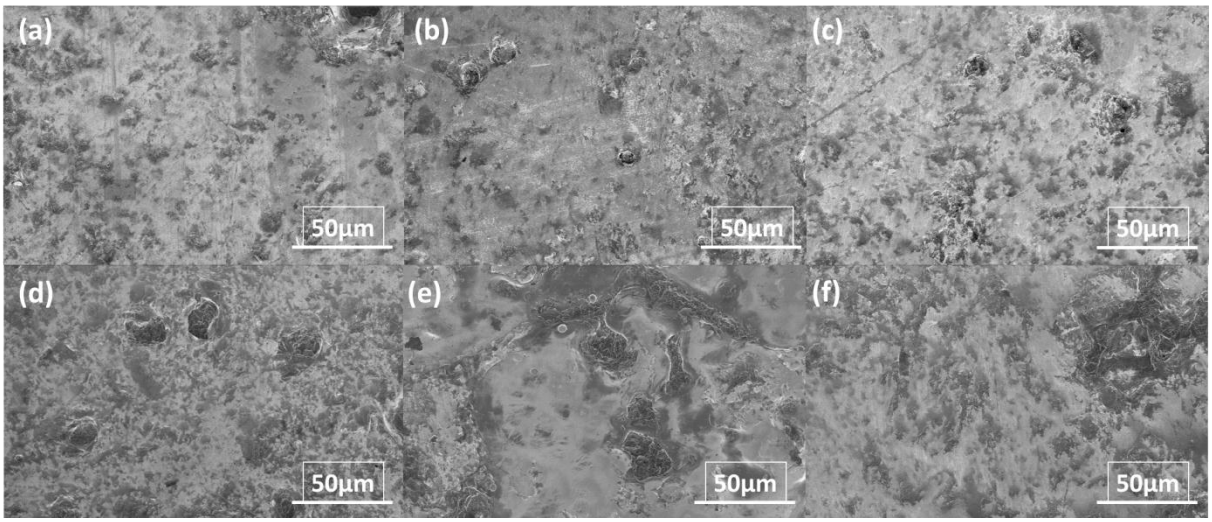

Figure V-9 : SEM of (a) CCTO (1BN), (b) CCTO (3BN), (c) CCTO (6BN), (d) CCTO (1GO), (e) CCTO (3GO), and (d) CCTO (6GO) sintered at 1100°C for 3h.

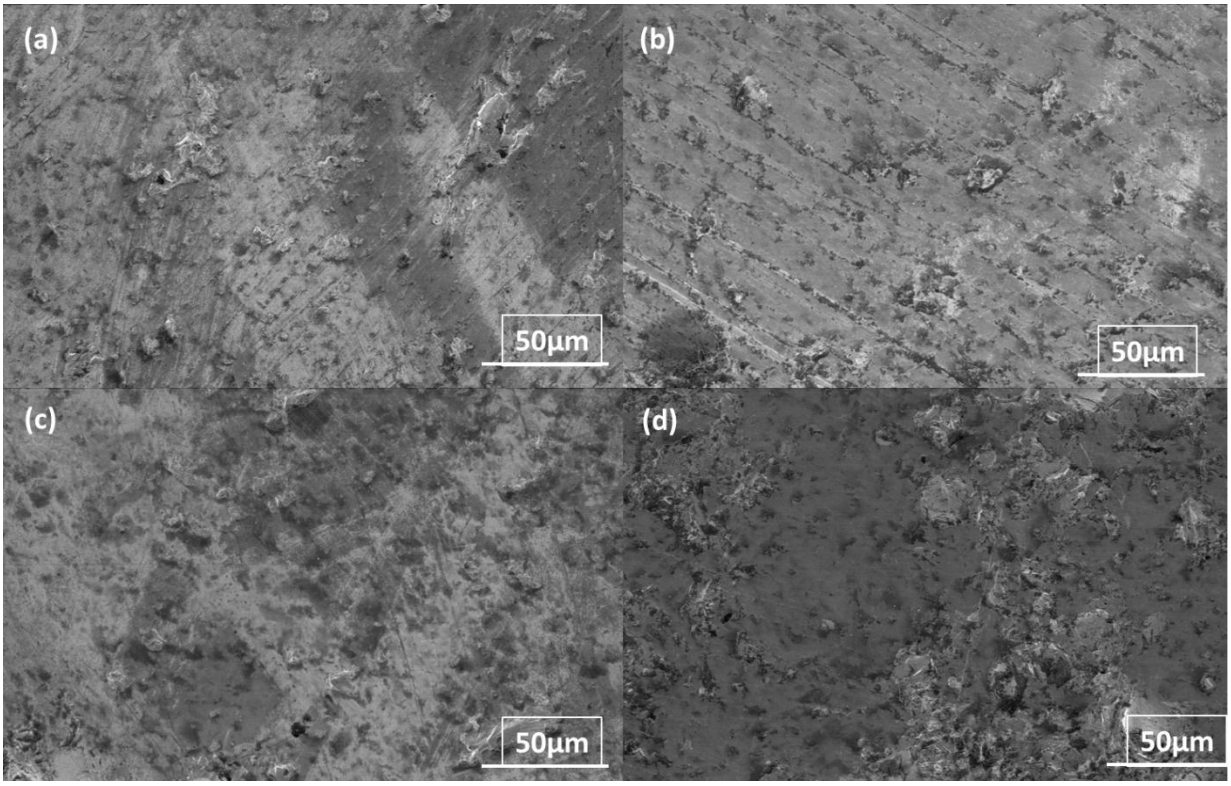

Figure V-10 : : SEM of (a) CCTO, (b) CCTO (1BN), (c) CCTO (3BN), and (d) CCTO (6BN) sintered at 1100°C for 6h.

According to previous studies, the dielectric permittivity response as frequency function in CCTO could be divided into two plateau. At low frequency the behavior refer to grain boundaries region and at high frequency the response is from grains [13]. In this study the behavior of all materials at different sintering time seems the same, the dielectric start at high value (ε'~1500-5000) then decreases rapidly to lower values. This result can be explained by the fact that polished CCTO and it composites are acting like a single phase of CCTO in which there is no real grain boundaries region (Figures V-8, V-9, and V-10). Thus the electrical behavior of the materials is dominated by the grains response. The rapid decrease in the dielectric constant can be due to the relaxation at the material-electrode contact [14].

At intermediate and high frequencies, the permittivity stays constant for all materials, the increasing or decreasing in value is related to the structure and grain contents. The high dielectric loss over the frequency range is maybe due to the relatively more coarse-grained microstructure of theses ceramics [15].

Furthermore, to understand the electrical behavior, an impedance spectroscopy measurement is performed for all ceramics. Normally the impedance spectroscopy measurements reflect the response of the grain boundaries at low frequency and the grains response at high frequency (non-zero intercept) [16], [17]. Until now a full impedance study of single crystal has not been done. Studies suggest that the absence of a clear grain boundary make the defects between grains to behave as a thin grain boundary [18]. In general when the sintering time increases the radius of the semi-circle of the impedance decreases, which is the case for pure phase of CCTO in this work. The behavior of other materials is influenced by the effect of 2D nanosheets incorporation. The shape of curves for composites sintered at 6h is more linear than semi-circle. This shape indicates that the material is highly conductive. Thus can be explained by the amorphous phases formed at high temperature and due to the presence of CuO conductive phase [3], [19].

Finally, the preparation method has a big influence on dielectric properties of $CaCu_3Ti_4O_{12}$ ceramics. To obtain high dielectric permittivity, the powders should be calcined for a long time and well milled for more diffusion and collision between precursors. The sintering step is the most important because at this stage the microstructure will take the form into grains and grain boundaries, since that these two parts influence the dielectric properties of ceramics. As seen from previous chapter, 2D materials could control the grain boundary composition and thickness according to the added amount, but they transform to conductive regions. So we polished the surface to eliminate the conductive layer and to study the dielectric behavior of the bulk. 2D materials and especially h-BN nanosheets could be used to form a dielectric material but the amount and synthesis should be controlled to enhance the domination of h-BN layer at grain boundaries.

V.2 Magnetization experiment

Composite materials draw attention due to that the combining materials create a new structure with intermediate properties [20], [21]. They exhibit unexpected new physical properties, which can depend on the synthesis method and the internal structure of the composite. With regard

to the magnetic properties, CCTO showed an antiferromagnetic transition at T~25 k, explained in terms of a double primitive cell in which each Cu–Cu nearest neighbor pair has antiparallel spins [22]. Cu defective and substituted sample showed enhanced dielectric properties in comparison to the pure ceramics [23], [24].

In this work we synthesize CCTO, CCTO with 6% of graphene oxide nanosheets (CCTO_6GO) and CCTO with 6% of boron nitride nanosheets (CCTO_6BN) using one easy step sintering at 1100°C for 3h (unpolished surfaces) in order to investigate their magnetization.

Figure V-11 (a)-(c) displays thermal variation of magnetization registered at ZFC (Zero Field Cooled) states in an externally applied magnetic field of 500 Oe for the prepared samples. The ZFC magnetization curves of all studied material showed the classical antiferromagnetic transition at Neel temperature (T_N) ~25 K, consistent with the thermal variation of magnetic susceptibility and specific heat measurements. Figure (d)-(f) showed the linear fit of magnetization curves, able to give information about Curie-Weiss temperature (ϑ). It is seen that the Curie-Weiss temperature is unchangeable for all ceramics ($\theta \sim$ -29 /-30 K). As mentioned before, the magnetic behavior is depended from Cu-Cu nearest neighbor so any create defective or distortion in Cu sites could affect the magnetic properties of the material, which is not the case. This is due to the fact studied before that incorporation of 2D materials does not affect Cu sites because of the segregation of CuO on grain boundaries and as seen that defects on Cu are negligible in comparison to those generated at Ti sites. In several investigations, they showed that even Ti^{4+} (μ_B=0) substitution by a ferromagnetic element with considered Bohr magneto (μ_B) could affect the magnetic behavior [25]. In this study, Ti^{4+} was replaced by bore and nitrogen (μ_B=0) and Ti^{3+} (μ_B=0) after incorporation of boron nitride and graphene oxide respectively. These results could explain the unchanged of specific magnetic parameters.

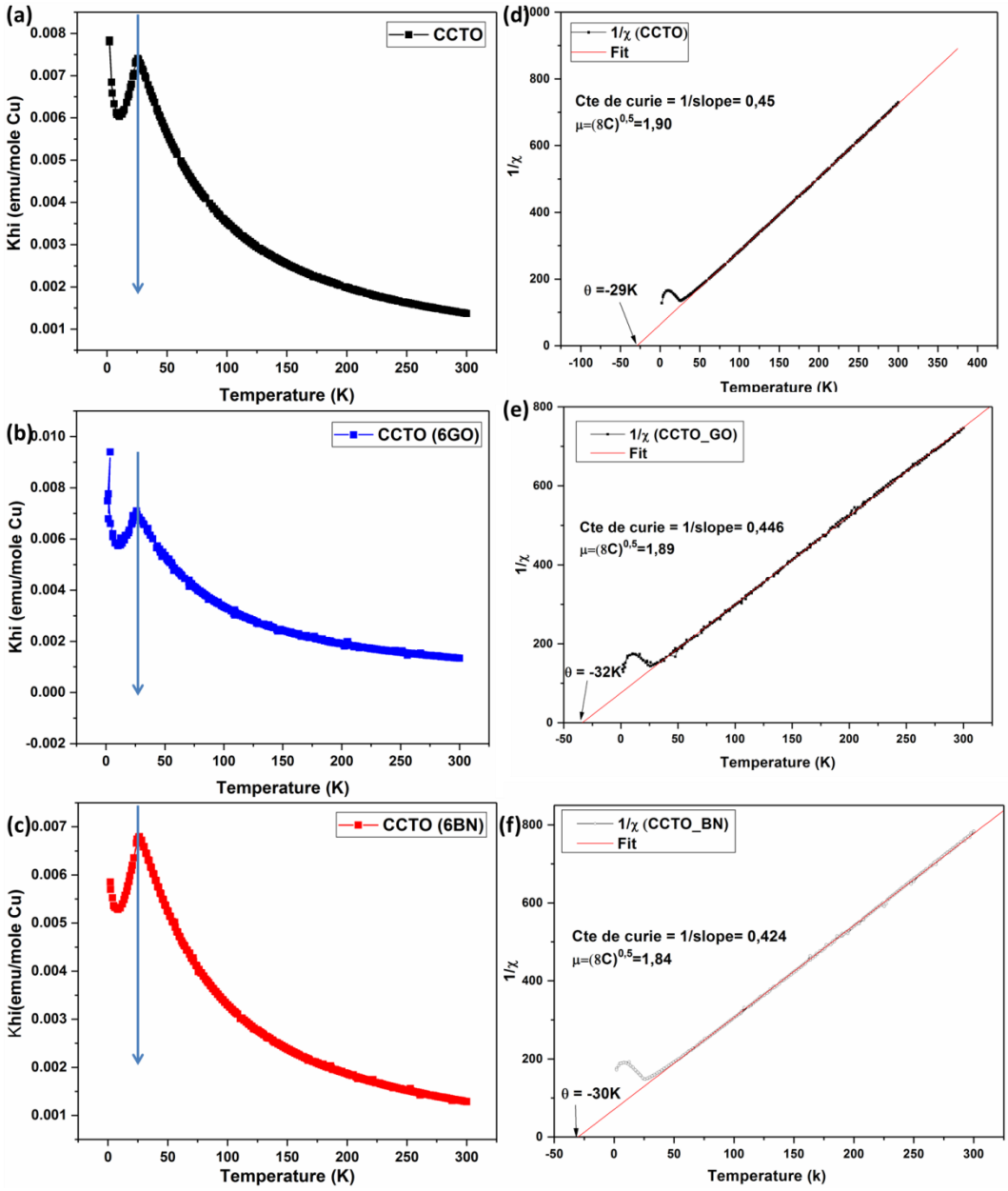

Figure V-11 : Thermal variation of magnetization in zero-field cooled mode recorded at the applied magnetic field of 500 Oe

V.3 Conclusion

CCTO composites with 2D nanosheets materials (h-BN and GO) were prepared using solid-state reaction and sintered at 1100°C for 3h and 6h. Ceramics surface were polished to eliminate the first layer. Pure phase of CCTO showed the grains and very thin grain boundaries regions. In contrast, after polishing the composites showed the morphology of one single crystal. Thus affects directly the crystallinity and the dielectric properties of the different obtained materials. Almost one response is showed for the CCTO based composites; high dielectric constant appears at very low frequency then a rapid drop is recorded due to the electrode-material effect. At intermediate and high frequencies the permittivity seems to be stable and the shown dielectric losses are very high for capacitor applications. Dielectric measurements and values are very low in comparison to the literature due to the used synthesis method, in which 3h of sintering is not sufficient for highly ceramics density.

CCTO with 6% of 2D nanosheets were used to study their magnetic behavior. Magnetic characterizations showed that these nanosheets do not affect Cu-O-Ti-O-Cu chain responsible of the magnetic behavior, in which Neel temperature is ~ 25 K for all studied materials.

References

[1] B. A. Bender and M.-J. Pan, “The effect of processing on the giant dielectric properties of CaCu3Ti4O12,” *Mater. Sci. Eng. B*, vol. 117, no. 3, pp. 339–347, 2005.

[2] S. Guillemet-Fritsch, T. Lebey, M. Boulos, and B. Durand, “Dielectric properties of CaCu3Ti4O12 based multiphased ceramics,” *J. Eur. Ceram. Soc.*, vol. 26, no. 7, pp. 1245–1257, Jan. 2006.

[3] T. B. Adams, D. C. Sinclair, and A. R. West, “Influence of Processing Conditions on the Electrical Properties of CaCu3Ti4O12 Ceramics,” *J. Am. Ceram. Soc.*, vol. 89, no. 10, pp. 3129–3135, Aug. 2006.

[4] L. Pardo and J. Ricote, *Multifunctional polycrystalline ferroelectric materials: processing and properties*, vol. 140. Springer Science & Business Media, 2011.

[5] B. Jaffe, *Piezoelectric ceramics*, vol. 3. Elsevier, 2012.

[6] A. J. Moulson, J. M. Herbert, and S. Electroceramics, “Electroceramics, John Wiley & Sons Ltd,” *Chichester, West Sussex, UK*, 2003.

[7] L. Feng, X. Tang, Y. Yan, X. Chen, Z. Jiao, and G. Cao, “Decrease of dielectric loss in CaCu3Ti4O12 ceramics by La doping,” *Phys. status solidi*, vol. 203, no. 4, pp. R22–R24, Mar. 2006.

[8] H. Tang, Z. Zhou, C. C. Bowland, and H. A. Sodano, “Synthesis of calcium copper titanate (CaCu3Ti4O12) nanowires with insulating SiO2 barrier for low loss high dielectric constant nanocomposites,” *Nano Energy*, vol. 17, pp. 302–307, 2015.

[9] T. B. Adams, D. C. Sinclair, and A. R. West, “Giant Barrier Layer Capacitance Effects in CaCu3Ti4O12 Ceramics,” *Adv. Mater.*, vol. 14, no. 18, pp. 1321–1323, Sep. 2002.

[10] P. Thongbai, J. Jumpatam, T. Yamwong, and S. Maensiri, “Effects of Ta5+ doping on microstructure evolution, dielectric properties and electrical response in CaCu3Ti4O12 ceramics,” *J. Eur. Ceram. Soc.*, vol. 32, no. 10, pp. 2423–2430, 2012.

[11] Z. Yang, Y. Zhang, G. You, K. Zhang, R. Xiong, and J. Shi, “Dielectric and Electrical Transport Properties of the Fe3+-doped CaCu3Ti4O12,” *J. Mater. Sci. Technol.*, vol. 28, no. 12, pp. 1145–1150, 2012.

[12] Q. Zheng, H. Fan, and C. Long, “Microstructures and electrical responses of pure and chromium-doped CaCu3Ti4O12 ceramics,” *J. Alloys Compd.*, vol. 511, no. 1, pp. 90–94, 2012.

[13] R. Schmidt, S. Pandey, P. Fiorenza, and D. C. Sinclair, “Non-stoichiometry in ‘CaCu3Ti4O12’ (CCTO) ceramics,” *RSC Adv.*, vol. 3, no. 34, pp. 14580–14589, 2013.

[14] M. Li, D. C. Sinclair, and A. R. West, “Extrinsic origins of the apparent relaxorlike behavior in CaCu3Ti4O12 ceramics at high temperatures: A cautionary tale,” *J. Appl. Phys.*, vol. 109, no. 8, p. 84106, Apr. 2011.

[15] A. Ibarra, R. Heidinger, and J. Mollá, “New potentials for high mechanical strength grades of polycrystalline alumina for EC waves windows,” *J. Nucl. Mater.*, vol. 191–194, pp. 530–534, 1992.

[16] D.-L. Sun, A.-Y. Wu, and S.-T. Yin, “Structure, Properties, and Impedance Spectroscopy of CaCu3Ti4O12 Ceramics Prepared by Sol–Gel Process,” *J. Am. Ceram. Soc.*, vol. 91, no. 1, pp. 169–173, Jan. 2008.

[17] M. A. Sulaiman, S. D. Hutagalung, J. J. Mohamed, Z. A. Ahmad, M. F. Ain, and B. Ismail, “High frequency response to the impedance complex properties of Nb-doped CaCu3Ti4O12 electroceramics,” *J. Alloys Compd.*, vol. 509, no. 18, pp. 5701–5707, 2011.

[18] L. Ni and X. M. Chen, “Enhanced giant dielectric response in Mg-substituted CaCu3Ti4O12 ceramics,” *Solid State Commun.*, vol. 149, no. 9, pp. 379–383, 2009.

[19] B. Wang, Y.-P. Pu, H.-D. Wu, K. Chen, and N. Xu, “Influence of sintering atmosphere on dielectric properties and microstructure of CaCu3Ti4O12 ceramics,” *Ceram. Int.*, vol. 39, pp. S525–S528, 2013.

[20] T. Pandirengan, M. Arumugam, M. Durairaj, and G. R. Thangaiyanadar Suyambulingam, “Development of performance-improved global positioning system (GPS) patch antenna based on sol-gel-synthesized dual-phase (Bi4Ti3O12)X – (CaCu3Ti4O12)1–X composites,” *Cryst. Res. Technol.*, vol. 51, no. 6, pp. 366–379, Jun. 2016.

[21] M. R. Dadfar, S. A. S. ebrahimi, and M. Dadfar, “Microwave absorption properties of 50% SrFe12O19–50% TiO2 nanocomposites with porosity,” *J. Magn. Magn. Mater.*, vol. 324, no. 24, pp. 4204–4208, 2012.

[22] Y. J. Kim, S. Wakimoto, S. M. Shapiro, P. M. Gehring, and A. P. Ramirez, “Neutron scattering study of antiferromagnetic order in CaCu3Ti4O12,” *Solid State Commun.*, vol. 121, no. 11, pp. 625–629, 2002.

[23] M. C. Mozzati, C. B. Azzoni, D. Capsoni, M. Bini, and V. Massarotti, “Electron paramagnetic resonance investigation of polycrystalline CaCu3Ti4O12,” *J. Phys. Condens. Matter*, vol. 15, no. 43, p. 7365, 2003.

[24] M. A. Subramanian, D. Li, N. Duan, B. A. Reisner, and A. W. Sleight, “High Dielectric Constant in ACu3Ti4O12 and ACu3Ti3FeO12 Phases,” *J. Solid State Chem.*, vol. 151, no. 2, pp. 323–325, May 2000.

[25] P. R. Pansara, P. Y. Raval, N. H. Vasoya, S. N. Dolia, and K. B. Modi, “Intriguing structural and magnetic properties correlation study on Fe3+-substituted calcium-copper-titanate,” *Phys. Chem. Chem. Phys.*, vol. 20, no. 3, pp. 1914–1922, 2018.

V.4 Annexes

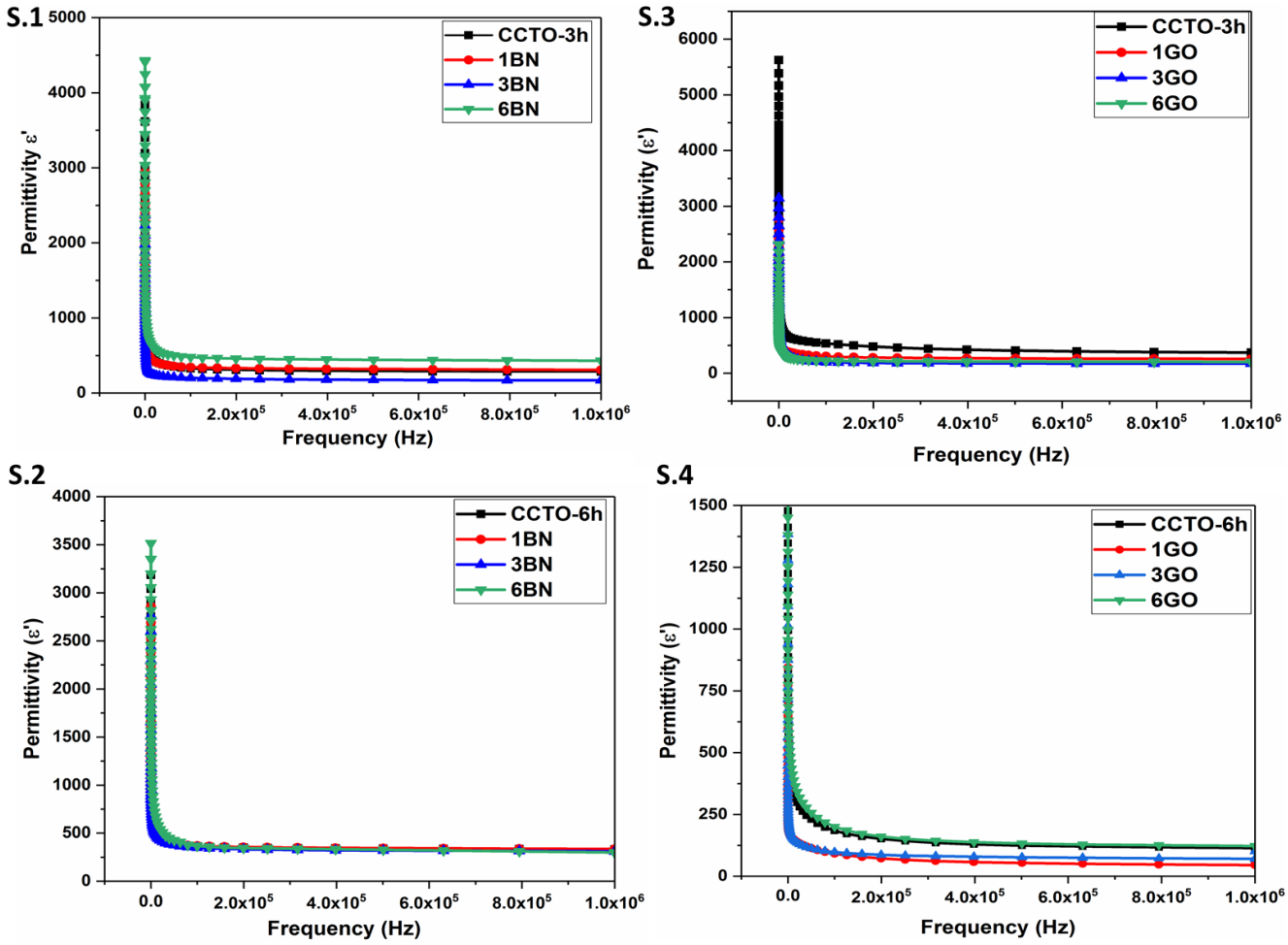

Figure V-12 : Permittivity dependence from frequency of ceramics composites with h-BN sintered at (S.1) 3h and (S.2) 6h, and of ceramics composites with GO sintered at (S.3) 3h and (S.4) 6h.

General Conclusion

General Conclusion and Perspectives

The purpose of this work was to synthesize and characterize $CaCu_3Ti_4O_{12}$ composites prepared by solid-state reaction. $CaCu_3Ti_4O_{12}$ is a perovskite oxide with a cubic lattice stable at high temperature. It was discovered and studied for several years as high dielectric material due to its colossal permittivity. Recently it was used for different photocatalytic applications, in photoelectrochemical cells and in magnetic compound owning to its specific structure. Investigations focused on two dimensional materials such as hexagonal boron nitride (h-BN) and graphene oxide nanosheets (GO) because of their interesting electrical and thermal properties. In these work 2D nanosheets materials were added to CCTO in order to enhance its photoelectrochemical, dielectric, and magnetic properties.

The first part of this study was dedicated to investigate the effect of the incorporation of hexagonal boron nitride nanosheets in the CCTO lattice in the purpose to enhance its photoelectrochemical properties. Based on different characterization techniques we showed that hexagonal boron nitride was oxidized at high temperature and this allowed the insertion of bore and nitrogen elements into TiO_2 lattice of CCTO material. This insertion created oxygen vacancies on the surface and conduct to a partial reduction of Ti^{4+} and Cu^{2+}. The electronic microstructure of composites leads to a red shift in band gap energy of materials. This was proven by photoelectrochemical and impedance measurements in which the resistivity of composites material was dropped under visible light illumination compare to pure CCTO. The activity of composites is enhanced under visible light irradiation and showed high electrons conductivity compared to the pure CCTO.

In the second part we used graphene oxide nanosheets to study their oxidation effect at high temperature on the CCTO materials. We showed that graphene oxide oxidation at high temperature lead to oxygen vacancies creation on the surface and element reduction, in which Ti^{4+} and Cu^{2+} are reduced to Ti^{3+} and Cu^{+} respectively for charge neutralization. Band gap energy is shifted to lower values due to the presence of energy band gap of oxygen vacancy below the valence band of CCTO. CCTO with GO nanosheets showed lower resistivity compared to pure

ceramics of CCTO and thus enhance their activity by 50% photocurrent generation higher than pure CCTO under visible light irradiation.

According to the obtained and discussed results, CCTO composites showed a good performance in which the photocurrent generation seen from linear voltammetry is enhanced in comparison to pure CCTO. CCTO with hexagonal boron nitride nanosheets showed two times higher activity compared to CCTO composites with graphene oxide nanosheets. That is maybe due to the efficiency of codoping in presence of cations reduction and oxygen vacancy, while for CCTO/GO composites only the reduced cations and surface oxygen vacancies interact in front of visible light irradiation.

These two parts focused on the synthesis method to incorporate 2D nanosheets materials in CCTO lattice and their effect under visible light exposure. As presented above they showed a good performance compare to pure CCTO. This study can be more enhanced by using different source of visible light energy with higher power in comparison to what has been used in this work. Since that the preparation process affects materials morphologies, the composites mixture could be performed in a ball mill machine or by using ultrasonication. During sintering the grain boundaries and grain size are highly dependent from the time and temperature, thus using a controlled sintering method such as spark plasma can be recommended.

Renewable energy is collected from resources naturally replenished on a human scale. Recently more than 20% of consumption energy came from renewable energy. There are many techniques that need to be evolved to be able to store energy from different natural resources. The expense of maintenance and the lower projection of power have limited the use of this type of energy. In order to resolve critical global issues such as water pollution, developmental capacities for clean energy supplies increases. Thus a new insight for design of advanced hybrid photocatalyst with actively chemical bonding and surface defects species has been recommended. CCTO composites could be used for many photocatalytic applications such as water treatment for dye and pharmaceutical waste decomposition due to the presence of different chemical bond and oxygen vacancy on the surface. In addition to that investigations focused on photoelectrooxidation of methanol for portable fuel cell applications could be

developed. Recently modified TiO_2 is used as an active agent, so CCTO composites enclosing different active compound can be used as well for such applications. Furthermore, different types of 2D nanosheets materials can be used to prepare CCTO composites such as graphene, Bi_2Te_3 and MoS_2 because of their high surface and outstanding opto-electrical properties. Among various nanoscale materials, 1D nanomaterials including nanowires, nanofibers, nanorods and nanotubes are recognized as a class of promising material for composites composition due to their highly active surface and could be investigated as well.

The dielectrical properties of CCTO and CCTO composite were also investigated. The dielectric properties of the polished surface of prepared composites were studied. In general and due to the sintering process, CCTO morphology presents grains and grain boundaries regions, in which the dielectric properties are highly dependent. In this study, the surface of prepared pellets was polished in order to eliminate the first layer. Only the pure phase of CCTO showed the two different regions. For h-BN and GO nanosheets based composites, no distinguish regions appeared. Dielectric measurements showed that the materials sintered at different times and after polishing performed as a single crystal, in which only the bulk response is given. The modest values of the dielectric constant obtained at room temperature can be attributed to the synthesis method, especially that the calcination and sintering time were too short to obtain dense ceramics with high dielectric constant.

The study of the magnetic properties of CCTO materials with 6%wt. of different 2D materials (without surface polishing) was also performed and showed that the incorporation of the 2D materials do not affect Neel temperature (~25K) and do not lead to magnetic properties modifications. These results come from the fact that Cu-O-Ti-O-Cu chain was not affected by the cations reduction after GO oxidation or by the B and N-codoping (non-magnetic compound) with h-BN nanosheets oxidation at high temperature.

Dielectric and magnetic properties are highly dependent on the synthesis method. In fact the crystal structure and the microstructure of the CCTO materials and these properties are highly connected. Boron nitride and graphene oxide nanosheets showed different properties depending on sintering atmosphere and conditions, thus it would be interesting to change the

conditions of sintering (Argon, nitrogen, etc.) of the ceramics in order to obtained well defined microstructures.

Abstract

Perovskite oxides exhibit a large variety of properties because of their structures and chemical compositions. Well known properties of the perovskite oxides are Ferroelectricity in $BaTiO_3$-based oxides and superconductivity in $YBa_2Cu_3O_7$. The major limit of these compounds is their phase transitions at high temperature, which lead to modify the perovskite properties. $CaCu_3Ti_4O_{12}$ (CCTO) exhibit a cubic structure stable at high temperature, it is a double-perovskite (ABO_3). CCTO was known as high dielectric material, and can play a key role in photoelectrochemical activity due to its structure. In addition, CCTO can occur a phase transition into the antiferromagnetically ordered phase below Neel temperature T_N = 25 K. On the other hand, 2D nanomaterials including graphene oxide (GO) and hexagonal boron nitrides (h-BN) were widely used due their exceptional properties.

The aim of this thesis is to investigate the photoelectrochemical, dielectric, and magnetic properties of CCTO based composites. Composites made of CCTO/GO and CCTO/h-BN ceramics were fabricated by solid-state reaction. With the addition of 2D nanosheets materials, the photoelectrochemical performance is enhanced by increasing the generation of photocurrent. CCTO with 3%wt of h-BN showed the insertion of bore (B) and nitrogen (N) into CCTO lattice, leading to Ti-B-O, Ti-N-O bonds and oxygen vacancies on the surface which reduce the bang gap energy and increase the density of generated photocurrent. With 3% of GO, Ti^{4+} and Cu^{2+} were reduced to active species Ti^{3+} and Cu^{+} respectively and oxygen vacancies were generated at the surface for charge neutralization, leading to generate photocurrent density 50% higher than pure phase of CCTO. In order to investigate 2D nanomaterials effects on magnetic properties of composites, CCTO with 6%wt of nanosheets was prepared and have shown no significant changes in Neel temperature. Finally in the last section, all composites were surface polished to investigate their dielectric properties, measurements showed a low permittivity in comparison to the literature. In conclusion, this work has shown that 2D nanosheets materials incorporation does not affect dielectric and magnetic properties, but enhance strongly the photoelectrochemical behavior of CCTO.

Résumé

Les oxydes de type pérovskites présentent différentes propriétés selon leur structure et leur composition chimique. Les principales pérovskites étudiées, $BaTiO_3$ et $YBa_2Cu_3O_7$, possèdent d'intéressantes propriétés ferroélectriques et supraconductrices. Une des limitations de ce type d'oxydes est la transition de phase à haute température qui peut modifier leurs propriétés. Le matériau $CaCu_3Ti_4O_{12}$ (CCTO) est un oxyde connu comme double perovskite (ABO_3) à structure cubique, qui a été étudié ces dernières années en tant que matériau diélectrique de permittivité élevée. De plus, CCTO subit une transition magnétique à antiferromagnétique au-dessous de la température de Néel (T_N=25K). Les propriétés du matériau CCTO sont fortement dépendantes de sa structure et offrent des possibilités d'applications photoélectrochimiques. D'un autre côté, les nanofeuillets de nitrure de bore (h-BN) et d'oxyde de graphène (GO) sont des matériaux 2D présentant des propriétés très intéressantes.

Dans le cadre de ce travail, des matériaux composites à base de CCTO et de nanofeuillets de nitrure de bore et d'oxyde de graphène ont été synthétisés et étudiés. Les céramiques composites CCTO/GO et CCTO/h-BN ont été synthétisées par réaction solide-solide. Les différentes propriétés photoélectrochimiques, diélectriques, et magnétiques ont été caractérisées. L'addition de 3% de h-BN aboutit à l'incorporation des atomes du bore et d'azote dans le réseau cristallin du CCTO et forme les liaisons Ti-B-O et Ti-N-O, et génère des lacunes d'oxygène à la surface, ce qui améliore la génération de porteurs de charges. La génération de porteurs de charges est augmentée en 50% par rapport au CCTO pur, après l'addition de 3% de GO, due à l'oxydation de GO à haute température qui réduit Ti^{4+} et Cu^{2+} en site actifs Ti^{3+} et Cu^{+} respectivement. Les propriétés magnétiques du CCTO avec 6% de nanofeuillets ont été étudiées, et ont montré que la température Néel n'était pas modifiée. Enfin, un polissage est effectué à la surface des céramiques pour étudier leurs propriétés diélectriques. Les résultats montrent des valeurs de permittivité plus basse que celles décrites dans la littérature. En conclusion, ces travaux ont démontré que l'incorporation des nanofeuillets 2D n'affecte pas les propriétés diélectriques et magnétiques, mais améliore considérablement les propriétés photoélectrochimiques du CCTO.